Photocatalytic Water Splitting for Solar Hydrogen Production and Simultaneous Decontamination of Organic Pollutants

Von der Naturwissenschaftlichen Fakultät

der Gottfried Wilhelm Leibniz Universität Hannover

zur Erlangung des Grades

Doktor der Naturwissenschaften
(Dr. rer. nat.)

genehmigte Dissertation von

Yamen AlSalka, Madjistir (Syrien)

2020

Referent: apl. Prof. Dr. rer. nat. Detlef W. Bahnemann

Korreferent: Prof. Dr. rer. nat. Jürgen Caro

Tag der Promotion: 24.06.2020

For My Mother & Father

For My Family

II

Acknowledgments

The achievement of this work would not have been possible without support by many persons whom I want to express my deepest gratitude.

To begin with, I am very grateful to my supervisor **Prof. Dr. Detlef W. Bahnemann** for the guidance, trust and scientific freedom he provided. Our discussions and his advice, motivation and immense knowledge have been enriching. His aspiration and persistence made me develop new skills and competences. He supported me, as well, to participates in many conferences and workshops to widen my research from various perspectives.

I am grateful to **Prof. Dr. Jürgen Caro** for kindly accepting to be a co-referee of this thesis and for the time he has spent for the productive revision of my PhD thesis. His outstanding experience and his scientific suggestions have raised the level of my thesis.

I am also thankful to **Prof. Dr. Ursula Rinas** for accepting to become the head of my examination committee. Her attendance and her questions have absolutely enriched the exam.

I am also thankful to **Prof. Dr. Thomas Scheper** to enable me to do my PhD at the institute of technical chemistry at Hannover University. His positive attitudes have been a motivation for me.

I express my warmest appreciation to the **Deutscher Akademischer Austauschdienst (DAAD)** for the financial supports through a full scholarship during my doctoral studies here in Germany in addition to the accompanying personal competence program.

I also would like to thank **Dr. Ralf Dillert** for our productive discussions. It has been a pleasure to share the scientific questions with you to take advantage of your knowledge.

I would also like to extend my sincere and special appreciation to **Dr. Amer Hakki** for his valuable input in terms of thoughtful scientific discussions as well as his great help throughout my PhD. His efforts and his way of discussing are greatly appreciated.

I would like to thank **Dr. Mariano Curti** for his valuable advice, productive suggestions, scientific discussions, and academic supports.

I would like to thank **Dr. Jenny Schneider**, **Dr. Irina Ivanova** and **Dr. Wegdan Ramadan** for their help during the first steps in my study and for their scientific supports.

I would like to thank **Prof. Dr. Armin Feldhoff** at the Institut für Physikalische Chemie, Universität Hannover for his support to carry out analytical characterizations.

Zusammenfassung

Zukünftige nachhaltige Energieszenarien benötigen einen verbesserten Zugang zu erneuerbaren Energiequellen und können somit dabei helfen, den Kohlenstoffdioxidfußabdruck des Energiesektors zu reduzieren. Der Traum der Implementierung eines photokatalyischen Solarsystems, das die Umwandlung von wässrigen organischen Schadstoffen in wertvolle Treibstoffe, wie z. B. H_2, ermöglicht, ist noch sehr weit von der Realisierung entfernt, vor allem aufgrund von technischen, materiellen und reaktionsmechanistischen Problemen. TiO_2 ist einer der am häufigsten verwendeten Photokatalysatoren, jedoch ist eine Modifizierung der Eigenschaften nötig, um die derzeit noch sehr enjen Grenzen seiner effektiven Nutzung zu überwinden.

In dieser Arbeit wurde eine TiO_2 Modifikation erfolgreich synthetisiert, die zur edelmetallfreien photokatalytischen H_2-Entwicklung fähig ist. Hierzu wurde das Verfahren der Evaporation-Induced Self-Assembly (EISA) mithilfe der statistischen Design of Experiment Methode optimiert. Durch die Anwendung der Ergebnisse der statistischen Versuchsplanung, z. B. durch das Kombinieren von F-108 Blockcopolymeren mit Titan(III)-chlorid als Ausgangssubstanz, wurde ein TiO_2 synthetisiert, welches photokatalytisch H_2 aus wässriger Ethanollösung entwickeln kann. Diese unrerwartete photokatalytische Aktivität lässt sich durch die Anwesenheit von neuen Defekten, z. B. Ti(II)-Spezies an der Partikeloberfläche und höchstwahrscheinlich auch auf interstitiellen Positionen, erklären. Diese Defekte führen zu einer hohen Dichte von Ladungsträgern mit längerer Lebensdauer, einer hohen Anzahl von Oberflächen-trap-Zuständen von Löchern und einer Verschiebung des Flachbandpotentials zu einem negativeren Potential. Das so synthetisierte TiO_2 wurde verwendet, um die mechanistischen Aspekte der H_2-Bildung durch die photokatalytische Reformierung von Oxalsäure zu untersuchen.

Die photokatalytische Oxidation von wässriger Oxalsäure wurde unter Verwendung verschiedener photokatalytischer Systeme unter konstanten pH-Bedingungen untersucht. Die schnelle Photooxidation von Oxalsäure auf reihem TiO_2 unter sauerstoffreichen Bedingungen wurde ohne die Detektion von Nebenprodukten erzielt, jedoch konnten 60-fach und 7-fach geringere Reaktionsraten für nicht modifiziertes TiO_2 bzw. für Pt/TiO_2 in sauerstofffreien Systemen ermittelt werden. In einem solchen System mit milderen oxidativen Eigenschaften wurde die Bildung von H_2 sowie von Nebenprodukten beobachtet.

Der Mechanismus der photokatalytischen Umwandlung von Oxalsäure wurde eingehend unter anaeroben Bedingungen unter Verwendung von selbst hergestellten mit verschiedenen Edelmetallen (Pt und/oder Au) beladenen TiO_2 Photokatalysatoren untersucht. Während die photokatalytische H_2-Entwicklung ebenfalls mit dem unmodifiziertem TiO_2 möglich ist, führt das Beladen mit Cokatalysatoren zu einer erheblichen Steigerung der Aktivität. Pt/TiO_2 zeigt dabei höhere Photoneneffizienzen als Au/TiO_2, während bimetallisches $Au-Pt/TiO_2$ keinen zusätzlichen Vorteil hat. Es wurde experimentell bestätigt, dass der Abbau von Oxalsäure über einen Oberflächen-Charge-Transfer-Mechanismus als Photo-Kolbe-Reaktion unter Bildung von $^{\bullet}CO_2^{-}$-Radikalen als Intermediate verläuft. Der Beitrag des sogenannten Current Doubling Mechanismus und der Effekt der Disproportionierungsreaktion der Radikale auf die Gesamtausbeute wird diskutiert, wobei sich ein Effizienzverlust aufgrund von Nebenreaktionen zeigt. Eine bemerkenswerte Diskrepanz zwischen der H_2-Entwicklung und der entsprechenden Oxidationsreaktion wurde in allen Fällen festgestellt, wobei Pt/TiO_2 eine um 30 % der verringerte H_2-Menge in Bezug auf die theoretisch vorhergesagten Menge zeigt. Diese Abweichung von der erwarteten Stöchiometrie kann auf (i) die Zunahme der Ladungsträgerrekombination aufgrund des Oxalsäureverbrauchs, (ii) das unvollständige Abfangen der photogenerierten Elektronen durch Pt-Nanopartikel, wie durch EPR-Spektroskopie nachgewiesen, (iii) die Bildung von Nebenprodukten, wie z. B. Formiat und Formaldehyd, in Abhängigkeit von der Art des Cokatalysators und/oder (iv) die Disproportionierung von $^{\bullet}CO_2^{-}$-Radikalen, wodurch der Beitrag des Current Doublings reduziert wird, erklärt werden.

Stichworte: Photokatalyse, H_2-Produktion, Wasserspaltung, Oxalsäure, Photoreformierung, TiO_2, Oberflächenladungstransfer, Solarkraftstoff, DoE, Statistische Versuchsplanung.

VI

Abstract

Future sustainable energy scenarios require an improved access to renewable energy sources and thuds help to reduce the carbon footprint of the energy sector. The dream concerning the implementation of a solar photocatalytic system combining the conversion of aqueous organic pollutants into value-added fuels, i.e., H_2, is still far from being realized because of technical, materials and reaction-mechanistic related issues. Titanium dioxide is one of the most widely used semiconductor photocatalysts, however, modification of its properties is required to take place to overcome the limits of its efficient exploitation.

In this thesis, TiO_2 capable of noble-metal-free photocatalytic H_2 evolution was successfully synthesized while optimizing the Evaporation-Induced Self-Assembly (EISA) method with the help of the Design of Experiment (DoE) statistical methodology. Applying the outputs of DoE, i.e., combining F-108 block copolymers with titanium(III) chloride as precursor, resulted in a TiO_2 exhibiting photocatalytic H_2 generation from aqueous ethanol solution. This unexpected photocatalytic performance is mainly attributed to the presence of new defects, i.e., Ti(II) species at the particle surface and most likely in interstitial positions. These defects resulting in a high density of charge carriers exhibiting longer lifetime, a high number of surface trapped states of holes, and a shift of the flat band potential to a more negative potential. The thus synthesized TiO_2 was used to investigate the mechanistic aspects of H_2 production *via* the photocatalytic reforming of oxalic acid.

The photocatalytic oxidation of aqueous oxalic acid was studied employing different photocatalytic systems under constant pH conditions. The fast photo-oxidation of oxalic acid on bare TiO_2 in O_2-reach conditions was achieved without the detection of by-products, however, the reaction rates were about 60-fold and 7-fold lower on bare TiO_2 and Pt/TiO_2, respectively, in O_2-free photocatalytic systems. In such a system exhibiting lower oxidative properties, the formation of H_2 and by-products was detected.

The mechanism of the photocatalytic conversion of oxalic acid has been deeply investigated in anaerobic conditions employing the self-prepared TiO_2 photocatalysts loaded with different noble metals (Pt and/or Au). While the photocatalytic H_2 evolution remarkably also occurs over bare TiO_2, the loading with a co-catalyst significantly boosts the activity. Pt/TiO_2 shows higher photonic efficiencies than Au/TiO_2, whereas bimetallic $Au-Pt/TiO_2$ has no additional advantage. The degradation of oxalic acid has been experimentally confirmed to proceed through a surface charge transfer mechanism via the photo-Kolbe reaction forming intermediate ${}^\bullet CO_2^-$ radicals. The contribution of the current doubling mechanism and the effect of the disproportionation reaction of radicals on the total yield is discussed, showing a loss of efficiency due to secondary reactions. A remarkable discrepancy between the H_2 evolution and the corresponding oxidation reaction was recorded in all cases, with Pt/TiO_2 showing ca. 30% decrease in the evolved amounts of H_2 with respect to the theoretically expected amount. This diversion can be attributed to (i) the increase in charge carriers recombination due to oxalic acid consumption, (ii) the incomplete scavenging of the photogenerated electrons by Pt nanoparticles as proved by EPR spectroscopy, (iii) the formation of by-products, i.e., formate and formaldehyde, depending on the nature of the co-catalyst, and (iv) the disproportionation of ${}^\bullet CO_2^-$ radicals, thus reducing the contribution of the current doubling.

Keywords: photocatalysis, H_2 production, water splitting, oxalic acid, photoreforming, TiO_2, surface charge transfer, solar fuel, DoE.

VIII

Table of Contents

Chapter One: Introduction

1.1. Future energy demand: facts and perspectives

For decades, humankind has powered the development of its modern society by exploiting fossil fuels without paying attention to the potential damages in sustainability. When it comes to energy, there is no dispute, that the world needs more of it—and how it is produced and used will be a critical factor in the future of the global economy and the environment. ***World energy consumption is anticipated to grow by 28% between 2015 and 2040*** [1] as shown in Figure 1-1(a). This, together with the progressive depletion of fossil fuel forces the world urgently to put a laser-like focus on its biggest challenge, i.e., meeting the rising energy demand while bringing down environmental pollution.

While coal demand is expected to remain flat through 2040 (see Figure 1-1(b)), ***renewables are believed to be the fastest-growing energy source***, with their consumption increasing by an average of 2.3% per year between 2015 and 2040 [1]. It is obvious that the development of an environmentally friendly energy economy should involve the introduction of technologies based on renewable sources of energy. The largest renewable energy resource is provided by the sun. With the average daily energy of (10^{22} J), the sun is considered the largest renewable energy resource that meets global energy demands [2]. The solar energy holds promise for a cleaner and more sustainable energy supply, especially when an efficient conversion of solar energy into chemical energy carriers is achieved.
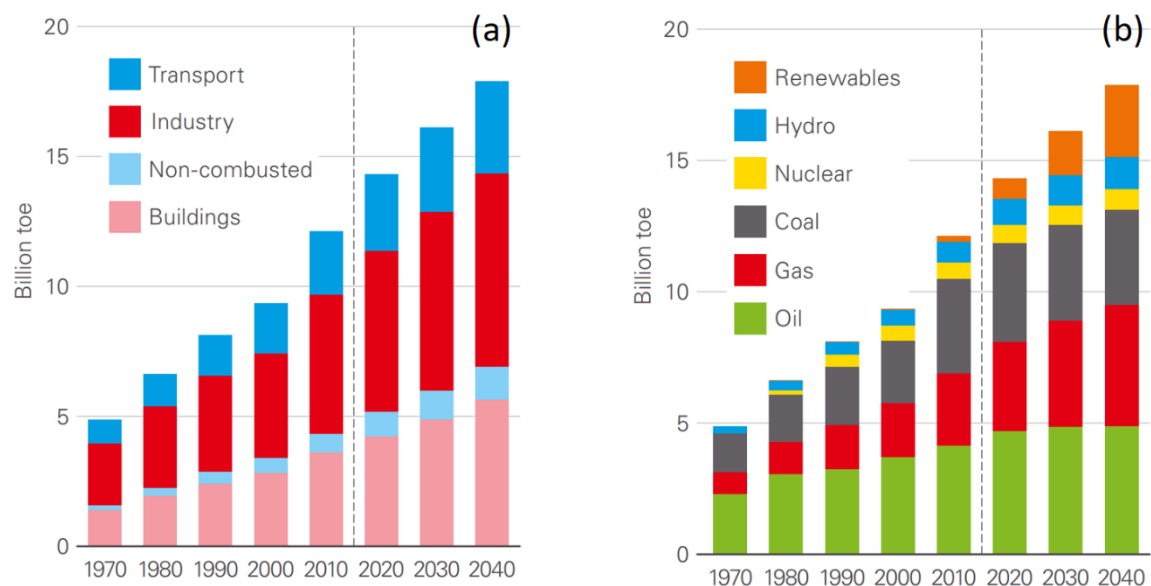
Figure 1-1 Primary energy transition through sectors (a) and fuels (b). Adapted from Ref. [3].

1.2. Molecular hydrogen: a potential sustainable fuel

Molecular Hydrogen represents an important energy carrier thanks to its energy content, i.e., 120 MJ.kg^{-1}, which is the highest value among other fuels. Therefore, H$_2$ has a huge potential for becoming one of the targeted fuels as long as it can be produced from renewable or abundant sources at low costs with the lowest harmful emissions [4, 5]. Among several methods to produce H$_2$, solar hydrogen production seems to offer an uncomplicated conversion route compared to photovoltaic technology, in which a PV cell and an electrolyzer are required [6]. H$_2$ can be generally produced via the water-splitting reaction as per one of the three methods: (1) Thermochemical water splitting by the heat collected from sunlight using solar concentrators [7], (2) Photobiological water splitting by means of aerobic or anaerobic bacteria [8], and (3) Photocatalytic water-splitting in the presence of a photocatalyst to convert the light energy into chemical energy [9].

1.3. Semiconductor-based heterogeneous photocatalytic systems

A photocatalytic system is defined, from a thermodynamic point of view, as a system, in which the photon absorption by a material facilitates a reaction with $\Delta G < 0$, i.e., the light energy is used to drive a reaction the kinetics of which would be extremely slow outside this system [6]. Such a system absorbs photons and generates accordingly charge carriers, i.e., electrons and holes, which induce a redox reaction. The light-absorbing materials are the photocatalysts, which, in the heterogeneous systems, are usually semiconductors [10]. Thus, heterogeneous photocatalysis relies on the unique properties of powdered semiconductor materials to harvest incident light and to subsequently drive surface reactions. This may provide a simple means for photochemical energy conversion into fuels [11, 12].

1.3.1. Semiconductor electronic structure

The electronic structure of a semiconductor can be explained by the band model based on the concept of molecular orbitals, in which the electronic orbitals merge and split into two bands. At 0 K, the lower band is completely filled with electrons; i.e., the valance band (VB), while the higher band is completely empty, i.e., the conduction band (CB) [13]. VB in the semiconductor is formed from the highest occupied molecular orbitals (HOMO), while CB is created from the lowest unoccupied molecular orbitals (LUMO) [14]. The region that makes up the difference in energy between the highest energy level in the VB and the lowest energy level in the CB is known as the energy bandgap (E$_g$) [15]. The origin of the band structure as a function of the number of electronic orbitals is shown in Figure 1-2.
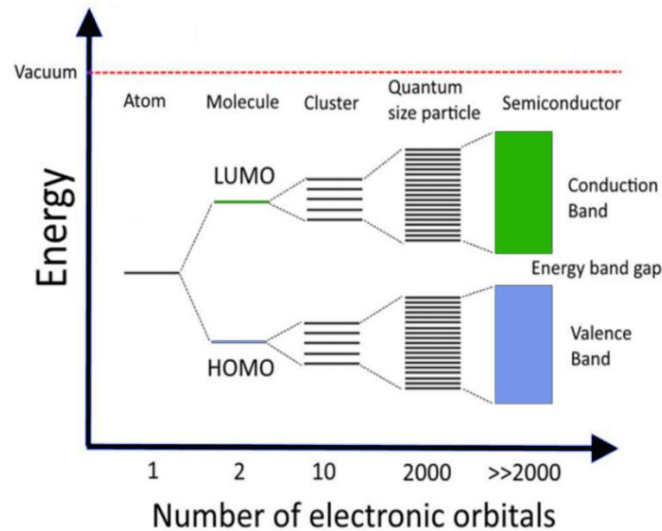
Figure 1-2 Band structure of a semiconductor as an interaction of atomic orbitals, adapted from Ref. [15].

The overlap of the CB and the VB, in the case of metals, results in a ready occupation of the vacant states in the CB. Insulators are not electrically conductive because they have a relatively large E_g, preventing the electrons to be thermally promoted to the CB [15]. If the distance between the upper edge of the VB and the lower edge of the CB is not too large, then at moderate and high temperatures a small fraction of the states near the upper edge of the VB is unoccupied and the corresponding electrons are found in the CB. Both these "thermally excited" electrons and the holes can carry electric current in the so-called semiconductor [16]. The E_g for semiconductors is sufficiently small that an energy transfer to the material may be enough for the electrons promotion from the VB to the CB [6]. The energy level diagrams for metals, semiconductors, and insulators as a function of the E_g are shown in Figure 1-3. The photo-induced properties of semiconductors arise, thus, from their unique electronic band structure which allows for the movement of electrons from the VB induced via absorbing light energy being higher or equal to E_g to occupy partially filled states in the CB.
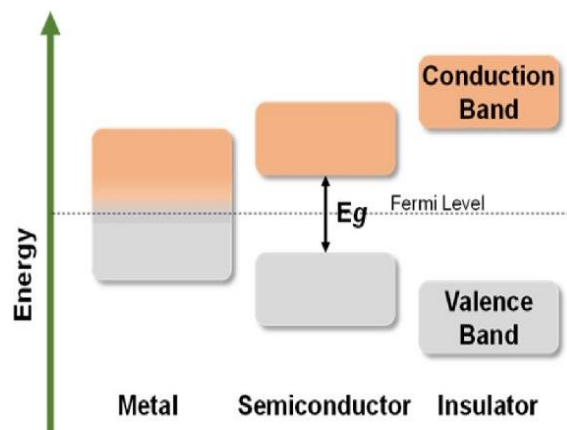
Figure 1-3 Band structures of metals, semiconductors, and insulators, reprinted from Ref. [17].

3

1.3.2. Semiconductor photocatalysis

The promotion of an electron to the CB creates an electron vacancy in the VB that is known as a positively charged hole [18]. The hole is considered as a mobile entity since it can be filled by another electron creating a vacancy in the space where it has been transferred from [19]. The electrons in the CB are also known with their mobilities being often higher than those of the holes (e.g., for Si, $\mu_{n(electrons)} = 1500 \, cm^2 \, V^{-1} \, s^{-1} > \mu_{p(holes)} = 450 \, cm^2 \, V^{-1} \, s^{-1}$ [20]). The electrons have consequently a higher diffusion coefficient, creating an electric field that is oriented to pull the electrons back toward the slower holes [21]. However, the trapping of the electrons leads to a drastic decrease in their mobilities. In the space charge region, the electron and the hole are forced to move in different directions due to the near-surface electric field. The e^-/h^+ species should then migrate to the surface of the semiconductor to react with adsorbed molecules, where holes act as oxidants (+1.0 to +3.5 V *vs* NHE), while electrons are potential reductants (+0.5 to −1.5 V *vs* NHE) [22].

Photocatalysis is considered, thus, as a multi-step-process and can be described as illustrated in Figure 1-4. It consists of the photoexcitation with electromagnetic radiation equal to or exceeding E_g (1), the separation of the charge carrier pairs (2), the diffusion of electrons and holes within the material towards the surface, and the surface charge transfer for the reduction of electron acceptors (3) and the oxidation of electron donors (4), respectively [23, 24]. Accordingly, the photo-induced electrons and holes must reach the surface of the material to react with adsorbed chemical species via surface charge transfer [25].

One of the main limitations of semiconductor photocatalysis is the recombination of photogenerated charge carriers either indirectly, i.e., *via* surface defects (5), or directly, i.e., by band-to-band recombination (6), dissipating the absorbed energy as heat [15] and affecting directly the lifetime of the electrons and holes [25]. This is highly dependent on the crystal structure that guides the photogenerated electron and hole to move independently, being influenced by their effective masses [26]. The band structure can be a limiting factor when the energy required to promote the electrons from the VB to the CB is greater than the energy associated with the irradiation. Therefore, the bandgap of the materials is the minimum thermodynamic requirement for photocatalysis [26]. To initiate redox reactions while minimizing recombination, photogenerated electrons and holes must move to a liquid junction through the solid and must react with solution species directly at the semiconductor surface [27]. Thus, a photocatalyst has to be carefully synthesized to overcome these critical issues.
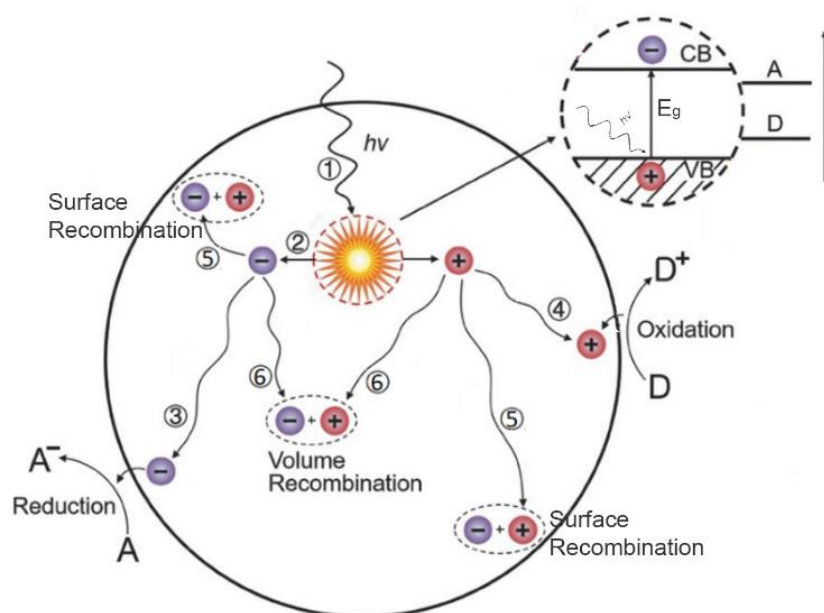
Figure 1-4 Pathways of the photogenerated charge carriers in a semiconductor photocatalyst, adapted with permission from Ref. [28].
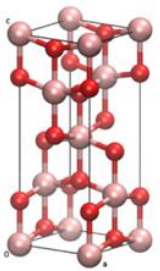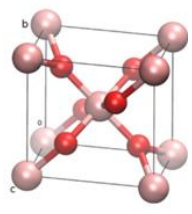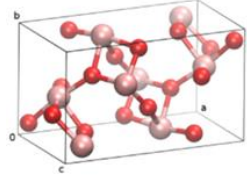
1.4. Titanium dioxide as a photocatalyst

1.4.1. General properties

One of the most widely studied semiconductors for photocatalytic applications in the last decades has been TiO_2. It is an intrinsic n-type semiconductor composed of Ti^{4+} atoms and six O_2^- coordinated together to form a TiO_6 octahedron [29]. TiO_2 exists in three crystal phases, i.e., brookite (has orthorhombic crystal structure and E_g of 3.3 eV), anatase, and rutile (both have tetragonal crystal structures and E_g of 3.2 eV, and 3.0 eV, respectively) [30]. Table 1-1 shows the properties of the different TiO_2 polymorphs.

Transition metal oxides, including TiO_2, are often nonstoichiometric, in which oxygen vacancies are the predominant defects at near-atmospheric oxygen pressure. The oxygen deficiency introduces an excess of electrons in the material resulting in an increase of the electrical conductivity, exhibiting material properties of a n-type semiconductor [31]. The surface of n-type TiO_2 contains a lot of defects, most probably oxygen vacancies (O_v) as unpaired electrons in the CB [32, 33]. These extra electrons act as donor-like states, thus creating an accumulation layer in the surface resulting in a downward band bending [34] as shown in Figure 1-5. The photocatalytic activity of TiO_2 is usually limited by the fast recombination of the photogenerated electron-hole pairs. Therefore, studying the charge carrier dynamics is of particular importance for understanding the underlying photocatalytic mechanism on TiO_2.

Table 1-1 Properties of the different TiO₂ polymorphs taken from Refs. [29, 30].

Property	Anatase TiO₂	Rutile TiO₂	Brookite TiO₂
	Tetragonal	Tetragonal	Orthorhombic
Crystal structure			
Molecules/cell	4	2	8
Crystal size (nm)	<11	>35	11-35
Lattice parameters (nm)	a=b=0.3785, c=0.9514	a=b=0.4594, c=0.2959	a=c=0.5436, b=0.9166
Space group	$I4_1/amd$	$P4_2/mnm$	Pbca
Volume/molecule (A°³)	34.061	31.2160	32.172
Density (g.cm⁻³)	3.79	4.13	3.99
Bandgap (eV)	3.26	3.05	3.3
dielectric constant $\xi(0)$	6.04	6.62	7.89
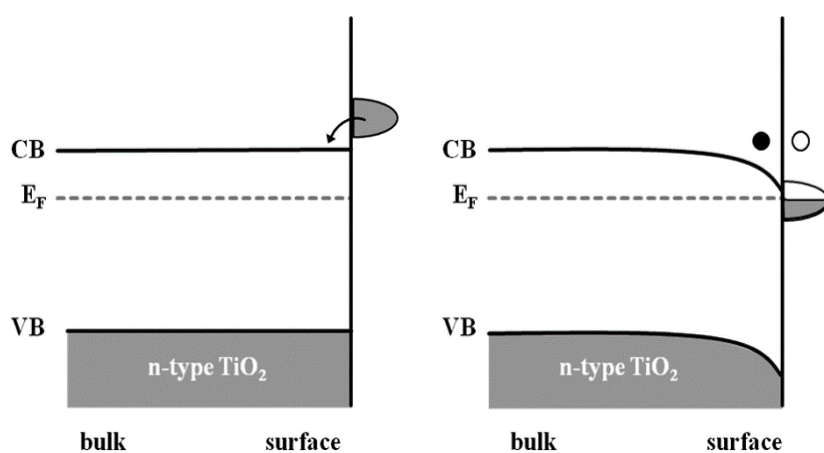
Figure 1-5 Surface band bending of n-type TiO₂ in vacuum due to the presence of donor-like surface defect states, reprinted with permission from Ref. [32].

1.4.2. The fate of the photogenerated species on irradiated TiO$_2$

Upon irradiation, the e$^-$/h$^+$ pairs are photogenerated within a few femtoseconds. Some of the charge carriers recombine easily either in the bulk or at the surface, while others, which escaped recombination, can migrate to the surface and maybe trapped before the interfacial charge transfer in redox reactions [35]. Figure 1-6 illustrates the potential pathways of charge carriers with their time scale in irradiated TiO$_2$ [22, 36] as per the following steps (Eqs. 1-1 to 1-4). In this context, the photocatalytic efficiency of TiO$_2$ is determined on the one side by the competition between charge carrier recombination and trapping (picoseconds to nanoseconds), and, on the other side, by the competition between the trapped charge carriers recombination and the interfacial charge transfer (microseconds to milliseconds) [22].

Charge carrier generation:

$$\text{TiO}_2 + h\nu \rightarrow \text{TiO}_2\,(\text{e}^-_{\text{CB}}\,/\,\text{h}^+_{\text{VB}}) \tag{1-1}$$

Charge carrier trapping:

$$\text{e}^-_{\text{CB}} + \equiv\text{Ti}^{\text{IV}}\text{OH} \rightarrow\ \equiv\text{Ti}^{\text{III}}\text{OH (shallow trapping)} \tag{1-2a}$$

$$\text{e}^-_{\text{CB}} + \equiv\text{Ti}^{\text{IV}} \rightarrow\ \equiv\text{Ti}^{\text{III}} \text{ (deep trapping)} \tag{1-2b}$$

$$\text{h}_{\text{VB}}^+ + \equiv\text{Ti}^{\text{IV}}\text{OH} \rightarrow [\text{Ti}^{\text{IV}}\text{O}^\bullet\text{H}]^+ + (\text{h}^+_{\text{tr}}) \tag{1-2c}$$

Charge carrier recombination:

$$\text{e}^-_{\text{CB}} + [\text{Ti}^{\text{IV}}\text{O}^\bullet\text{H}]^+ \rightarrow\ \text{Ti}^{\text{IV}}\text{OH} \tag{1-3a}$$

$$\text{h}+_{\text{tr}} + \equiv\text{Ti}^{\text{III}}\text{OH} \rightarrow\ \text{Ti}^{\text{IV}}\text{OH} \tag{1-3b}$$

$$\text{h}^+_{\text{tr}} + \text{Ti}^{\text{III}} \rightarrow\ \text{Ti}^{\text{IV}} \tag{1-3c}$$
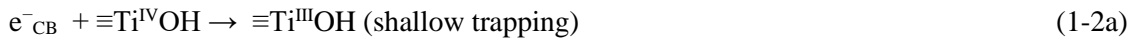
Interfacial charge transfer to the surface adsorbed acceptor (A) or donor (D)

$$\equiv\text{Ti}^{\text{III}}\text{OH} + \text{A} \rightarrow\ \equiv\text{Ti}^{\text{IV}}\text{OH} + \text{A}^{\bullet-} \tag{1-4a}$$

$$[\text{Ti}^{\text{IV}}\text{O}^\bullet\text{H}]^+ + \text{D} \rightarrow\ \equiv\text{Ti}^{\text{IV}}\text{OH} + \text{D}^{\bullet+} \tag{1-4b}$$
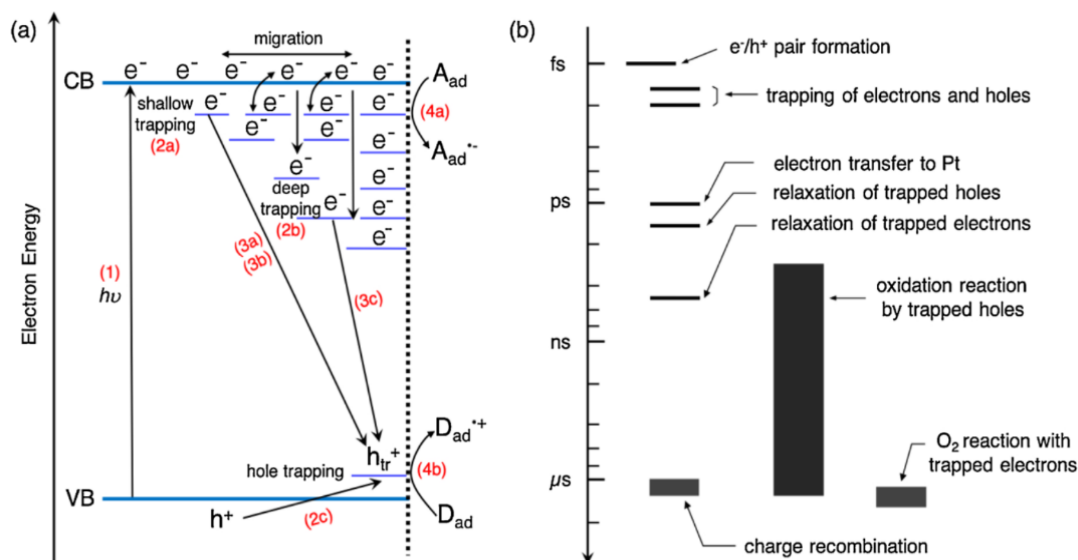
Figure 1-6 The possible charge carriers pathways on irradiated TiO₂, reprinted with permission from Ref. [35].

1.4.3. Recombination of the photogenerated charge carriers

It was found that more than 90% of the initially formed charge carriers recombine rapidly within 10 ns upon the irradiation of TiO₂ in aqueous media without any scavengers, resulting in quantum yields of photooxidation being considerably below 10% [37]. ***The optimal size for TiO₂ nanoparticles to be employed as photocatalysts has been reported to be between 10-30 nm*** [38, 39]. Such small particles are exhibiting shorter distances from the bulk to their surface and larger surface area, i.e., enabling a faster migration and trapping of the charge carriers and creating a higher number of active sites, respectively [40].

1.4.4. Trapping of the photogenerated charge carriers

The photogenerated charge carriers can be trapped in the bulk or at the surface as trapped holes, trapped electrons, or they might remain as free electrons, with the surface trapping being preferred for the subsequent redox reactions [41]. Trapped holes and electrons are found to be localized at the surface of the particles, while free electrons are distributed in the bulk as shown by Transient Absorption Spectroscopy (TAS) [42]. EPR studies demonstrated that electrons are localized in the d orbitals of Ti^{4+} while the holes are trapped at nearby lattice oxygen atoms, forming EPR-active paramagnetic Ti^{3+} and $O^{\bullet-}$ centers, respectively [43, 44].

1.4.5. Charge carrier transfer on irradiated TiO₂

Upon the generation, separation, and transport of charge carriers, e^-/h^+ pairs can induce redox reactions *via* an interfacial charge carrier transfer. However, the mismatch between short lifetimes of photogenerated charge carriers and slower kinetics of surface redox reactions negatively affects the photocatalytic activity [45]. Investigating the interfacial charge transfer dynamics at the

TiO$_2$/adsorbate interface, e.g. the TiO$_2$/H$_2$O interface, is necessary to understand the photocatalytic pathway, through which photocatalytic processes are achieved. Water layers can adsorb, physically and chemically, on the TiO$_2$ surface creating a TiO$_2$/H$_2$O interface as shown in Figure 1-7 [46], in which two kinds of Ti–OH are presented; that is, bridging hydroxyl (Ti-O-H$_2$O) groups at O sites, and terminal hydroxyl (Ti-OH) groups at Ti sites. The photogenerated holes can react either with hydroxyl groups or with H$_2$O resulting in the formation of hydroxyl radicals, $^{\bullet}$OH. Therefore, not only h$^+$ is produced by the photo-excitation of TiO$_2$ but also a hydroxyl radical can be formed on a hydrated TiO$_2$ surface.
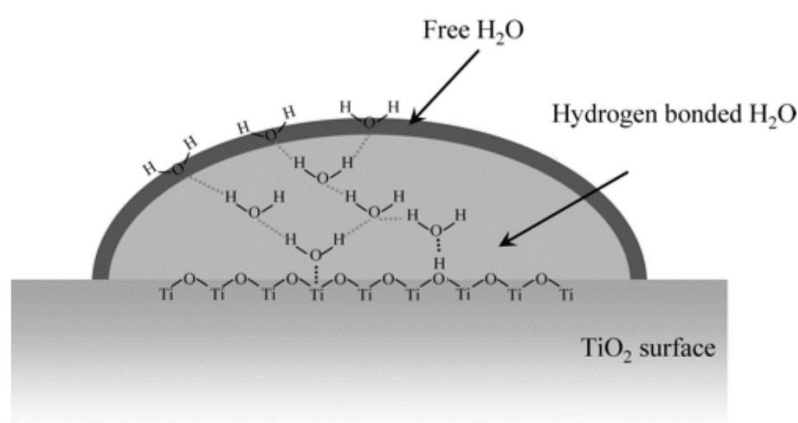
Figure 1-7 Diagram of water layers adsorbed at the TiO$_2$ surface, reprinted with permission from Ref. [47].

1.4.6. Anatase TiO$_2$ as a potential photocatalyst

Anatase is generally considered as the photocatalytically most active phase of the three TiO$_2$ polymorphs [48, 49]. This might be due to the longer lifetimes of photogenerated charge carriers as a result of its indirect bandgap transition as predicted by DFT calculations [49]. Anatase and rutile TiO$_2$ have shown differences in their respective charge carrier recombination kinetics, with a higher recombination rate for rutile [50, 51] as observed by PL measurements. In addition, different charge trapping behaviors have been observed from PL spectra for the different TiO$_2$ polymorphs [52] as illustrated in Figure 1-8. Anatase showed also shallowed-trapped electrons in addition to a higher number of free electrons having lifetimes longer than 1 ms. However, electrons in the rutile phase are found to be deeply trapped within a few picoseconds [53]. The relatively long lifetime of the free electrons in anatase is beneficial for many reduction reactions because of the low reactivity of deeply trapped electrons. The Time-Resolved Microwave Conductivity (TRMC) technique has been also applied to study the charge carrier lifetimes in anatase and rutile TiO$_2$ [54-56]. The corresponding TRMC signals for anatase and rutile are presented in Figure 1-9. Using TRMC, anatase showed longer electron lifetime in comparison to rutile as shown in this figure. Such results have been explained by a higher amount of OH groups on the anatase surface, where the holes can be trapped leading to an enhanced charge separation [57].
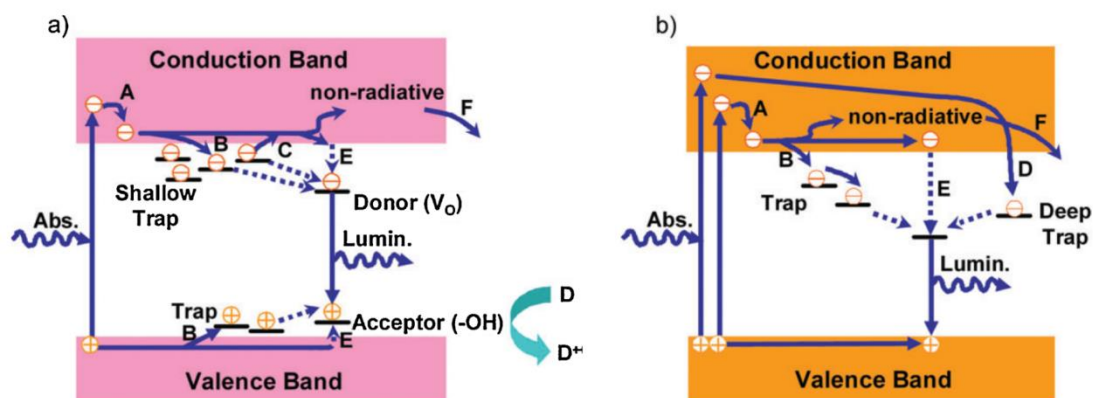
Figure 1-8 Tapping and recombination of photogenerated charge carriers in anatase (a) and rutile (b), reprinted with permission from Ref. [35].
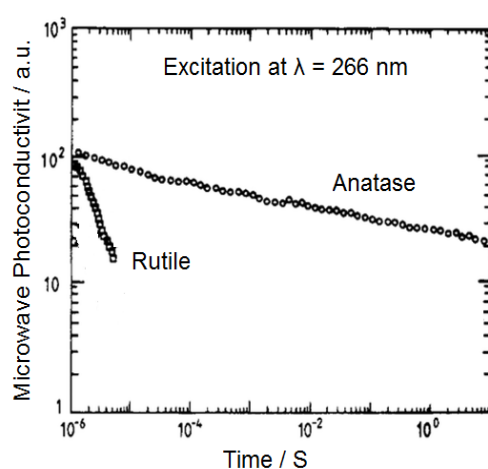
Figure 1-9 Photoconductivity of TiO$_2$ powders after a laser flash excitation at 266 nm with energies of 0.5 and 1 mJ cm^{-2} for anatase and rutile, respectively. Adapted with permission from Ref. [32].

1.4.7. Synthesis of TiO$_2$ nanoparticles

Different methods including sol−gel, surfactant-based-micelle, hydrothermal, solvothermal, chemical or physical vapor deposition, electrodeposition, sonochemical, and microwave methods have been successfully used for the synthesis of TiO$_2$ powders. In these methods, a wide range of titanium precursors (e.g., titanium chloride, titanium sulfate, and titanium alkoxides) and synthesis parameters have been applied. However, ***changing the preparation method and/or the parameters of each method, will indeed affect the structural, thermal, electronic, and optical properties of the resulting TiO$_2$ nanomaterials*** [58].

One of the methods used is the Evaporation-Induced Self-Assembly (EISA), which is based on the sol-gel methodology and known as a versatile synthesis method for mesoporous TiO$_2$ thin films and powders [59]. Mesoporous and nanoporous TiO$_2$ materials have been produced with or without the use of organic surfactant templates [60] and have shown larger specific surface areas and continuous particle frameworks, which may be beneficial in photocatalytic systems compared to separated individual

nanoparticles. These two factors, indeed, affect the photocatalytic activity of TiO_2, because such continuity can facilitate the electron transfer within the material, resulting in higher activity. ***A higher surface area will offer also more active sites for the adsorption*** of molecules, hence, inducing a higher rate of the subsequent charge transfer reactions. ***Mesoporous TiO_2 with an anatase crystalline wall is expected to behave as a high-performance photocatalyst*** [61]. The EISA method was first reported by Brinker and Ozin for the preparation of mesostructured silica thin films [62]. In this method, titanium precursors are dispersed in a solvent, e.g., alcohol, where colloidal particles, called a sol, are formed. The aggregation as a three-dimensional open network called a gel then takes place followed by the condensation around a surfactant phase (see Figure 1-10). The surfactant molecules are removed in the final step by calcination leading to the formation of a mesoporous material.

Various non-ionic and cationic surfactants have been used in the literature. Non-ionic surfactants can be categorized as diblock, i.e., they consist of two repeating units ABAB, and as triblock co-polymer surfactants being comprised of repeating ABA units [63, 64]. Such co-polymers may consist of different combinations of hydrophilic, (e.g., polyethylene oxide PEO) and hydrophobic (e.g., polypropylene PPO) components interacting in different ways with the precursor. A non-ionic surfactant that is widely used for the preparation of mesoporous TiO_2 called pluronic is a co-polymer having the formula of $[PEO]_n[PPO]_m[PEO]_n$. Examples of common pluronic co-polymers include P123 and F127 [64], where P123 has the formula $(PEO)_{20}(PPO)_{70}(PEO)_{20,}$ while F127 has the formula $(PEO)_{106}(PPO)_{70}(PEO)_{106}$ [65], respectively.

A key step of the EISA method is the removal of the surfactant by the final thermal treatment. Non-ionic co-polymer surfactants are usually removed by calcination at temperatures in the range of 300–350 °C to prevent pore wall collapsing [59]. For example, calcination at 350 °C or 400 °C has been done to remove P123 and obtain reasonable hexagonal pore ordering [66]. However, the material calcined at 400 °C showed enhanced crystallinity but reduced pore ordering with a pore diameter of 6.2 nm compared to 7.3 nm in case of the calcination at 350 °C.
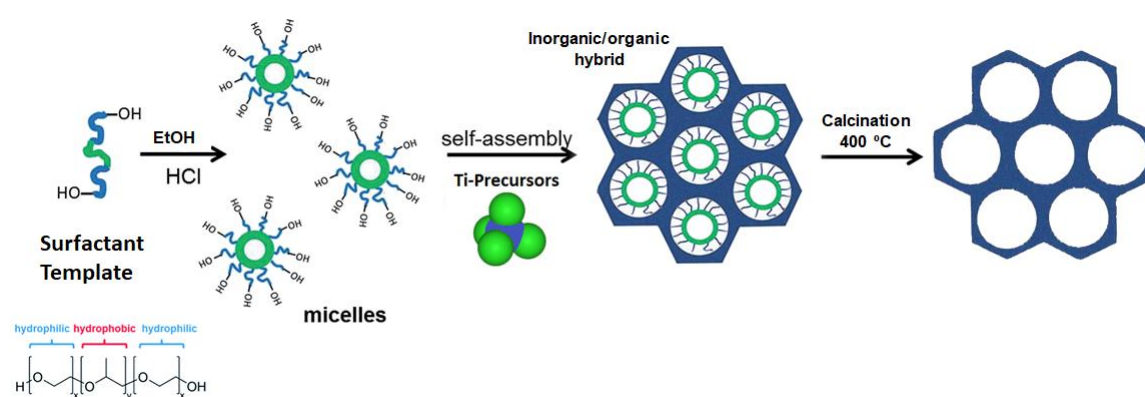
Figure 1-10 The successive steps of an EISA method [67].

The EISA method is used to produce powdered-TiO₂, however, ***the phase, the crystallinity, and the activity of the product are dependent on the nature of the surfactant, the TiO₂ precursors, the ratio of the surfactant to the titanium precursor, the amount of water, the pH, the aging time, the relative humidity (RH), and the calcination temperature*** [59, 61]. Furthermore, ***changes in the experimental conditions may show a high impact on product properties*** [59, 68].

1.5. Noble-metal modified TiO₂

In what was previously discussed, photogenerated electrons are trapped and not totally available to react at the surface, hence, TiO₂ should be modified to enhance the reactivity of photogenerated electrons. One strategy is the surface modification with noble metal nanoparticles. Bare TiO₂ has been reported as an inactive photocatalyst for H_2 production because of (1) the fast recombination of holes and electrons, which is considered to be the bottleneck of the photocatalytic activity, (2) the higher overpotential for hydrogen evolution reaction (0.05 V) [69], and (3) the necessity to employing a catalyst for the H_2 formation [70]. Hence, even in the presence of an electron donor, bare TiO₂ has shown an inability to catalyze the hydrogen evolution reaction. TAS measurements revealed that the consumption of holes by the sacrificial reagent is accompanied by the trapping of the photogenerated electrons as blue Ti^{3+} ions instead of reducing H^+ [71]. Thus, for the cathodic H_2 evolution to proceed it is highly recommended to modify TiO₂ with an appropriate co-catalyst. Noble-metal-loaded TiO₂ photocatalysts have been widely studied in the literature, in which the noble-metal NPs act as a Hydrogen Evolution Reaction (HER) catalysts.

$$2(H^+ + e^-) + * \rightarrow 2H^*$$

Volmer-Tafel mechanism

$$2H^* \rightarrow H_2 + *$$

$$H^+ + e^- + * \rightarrow H^*$$

Volmer-Heyrovsky mechanism

$$H^+ + H^+ + e^- \rightarrow H_2 + *$$
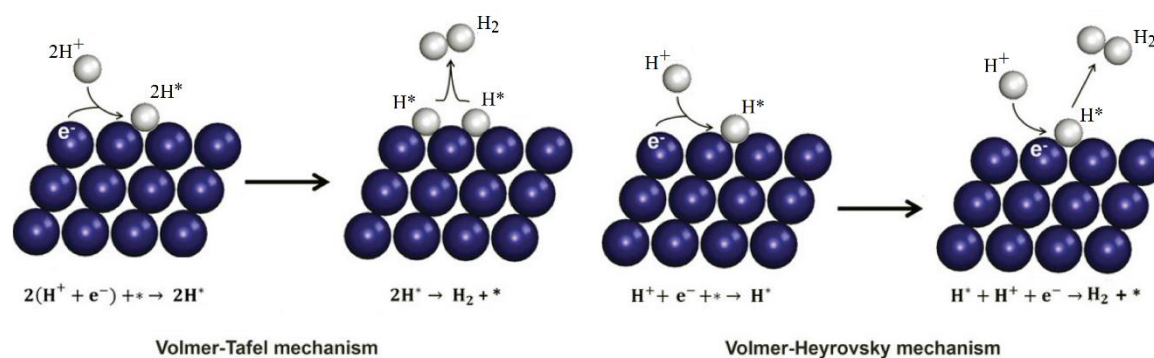
Figure 1-11 HER mechanisms on the catalyst surface in acidic solutions. The * refers to the active sites of the catalyst, H* refers to the adsorbed hydrogen atom at the active site of the catalyst. Reprinted with permission from Ref. [72]

HER on metallic platinum starts via the Volmer reaction, in which $H^{\bullet}_{ads}$ atoms are formed when the accumulated electrons in Pt transfer to the proton adsorbed H^+_{ads} and H_2O_{ads}, respectively, as described in Eqs. 1-5a and 1-5b [73]. Then the reaction proceeds via two paths, either the Heyrovsky (Eq. 1-5c) or the Tafel (Eq. 1-5d) reaction, in which $H^{\bullet}_{ads}$ react with H^+_{ads} or/and the direct recombination of two $H^{\bullet}_{ads}$ with each other, respectively [74]. In acidic solutions, the two-electron transfer reaction that occurs on the metal-catalyst surface is shown in Figure 1-11. HER on metallic

platinum has been shown to exhibit pseudo-first-order kinetics, which might be explained by the fact that the rate-determining step of the HER is the Volmer reaction [70]. Rabani et al. have shown a linear increase in the decay rate of e^-_{TiO2} with H^+ concentration at a given Pt concentration, suggesting that hydrogen is produced to a more extent by reduction of H^+ than by reduction of H_2O [70]. They have also emphasized that the presence of Pt is essential for reactions 1-5a and 1-5b to take place.

$$H^+_{ads} (Pt) + e^-(Pt) \rightarrow H^{\bullet}_{ads} (Pt) \qquad\qquad (1\text{-}5a)$$

$$H_2O_{ads}(Pt) + e^-(Pt) \rightarrow H^{\bullet}_{ads} (Pt) + OH^- \qquad\qquad (1\text{-}5b)$$

$$H^{\bullet}_{ads} (Pt) + e^-(Pt) + H^+_{ads} (Pt) + e^-(Pt) \rightarrow H_{2(g)} \qquad\qquad (1\text{-}5c)$$

$$H^{\bullet}_{ads} (Pt) + H^{\bullet}_{ads} (Pt) \rightarrow H_{2(g)} \qquad\qquad (1\text{-}5d)$$
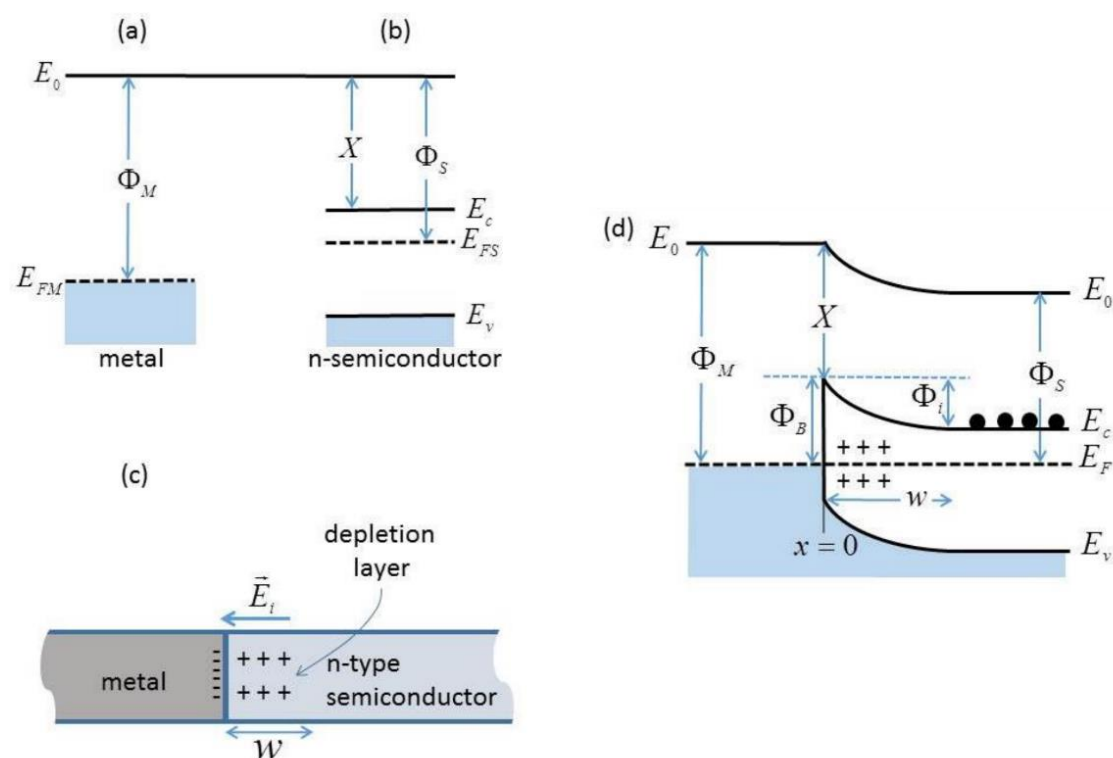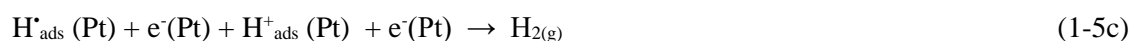
Figure 1-12 A Schottky barrier formed by a metal of high work function contacting an n-type semiconductor. (a) Metal workfunction Φ_M and Fermi energy E_{FM}. (b) Semiconductor work function Φ_S, electron affinity X and band structure with a bandgap between E_c and E_v and Fermi energy E_{FS}. (c) Charge at the metal/semiconductor (MS) junction: the negative charge at the metal surface is approximately a delta function, while the positive charge consisting entirely of immobile ionized donors extends over a distance W inside the semiconductor creating the space charge (or depletion) region. (d) Idealized equilibrium band diagram for the M/S junction. Φ_i is the energy barrier to the flow of electrons (black dots) from the semiconductor to the metal, while Φ_B is the Schottky barrier height for the electron flow in the opposite direction. W is the extension of the depletion layer. Reprinted with permission from Ref. [75].

The enhancement in the activity by modifying TiO_2 with metal NP_S is related to a better charge separation according to the Schottky barrier model. Nevertheless, an efficient transfer of photogenerated electrons across the co-catalyst/semiconductor interface is also required. Noble-

metal NPs exhibit higher Fermi level energy than TiO_2; 5.65 eV and 5.10 eV for Pt and Au, respectively [76] compared to about 4.2 eV for TiO_2 [77]. Thus, electrons can transfer from TiO_2 to the metal NPs through the interface until the thermodynamic equilibrium is reached [32]. This results in a negatively charged metal on a positively charged TiO_2, hence, a depletion layer is created at the TiO_2 surface. As a result, bands bent upwards and a Schottky barrier, i.e., the difference of the CB energy and the aligned metal Fermi level energy, is formed as shown in Figure 1-12. Schottky barrier ΦB is the barrier against electron's flow from the metal to the n-type semiconductor [75]. The thermodynamic equilibrium will be perturbed upon illumination, which allows the photogenerated electrons to continuously flow from the CB of TiO_2 to the metal NPs [32, 78]. Such a Schottky barrier facilitates electron trapping by the metal and hence provides better electron/hole separation and longer lifetime of the trapped electrons promoting the desired reduction reactions [79, 80]. Correlations between photocatalytic H_2 evolution rates and co-catalyst metal work functions have been thoroughly investigated [81, 82]. However, EPR measurements for Pt/TiO_2 showed also characteristic signals for the Ti^{3+} species, that is, the photogenerated electrons were not transferred completely to the Pt NPs, rather a certain number of them remain in the TiO_2 particle being trapped as Ti^{3+} ions [32, 44].

Scavenging the photogenerated electrons by noble-metal NPs is essential but is not the only factor. According to the Sabatier principle [83], an ideal catalyst for (HER) must exhibit an optimal interaction, i.e., binding energy, with intermediary adsorbed atomic hydrogen ($H^{\bullet}_{ads}$). The interaction should be neither too strong nor too weak. Desorption of H_2 becomes rate-limiting in case of too strong interactions, which can block the active sites for the HER reaction, while proton reduction is rate-limiting in case of weak interactions with $H^{\bullet}_{ads}$ [84]. Consequently, a volcano-type dependence between HER rates and catalyst-$H^{\bullet}_{ads}$ bond strength has been proposed [85], in which platinum seems to provide the best activity to drive the HER as shown in Figure 1-13.
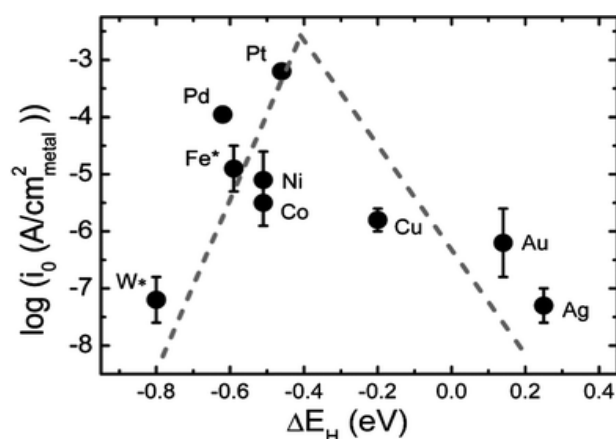
Figure 1-13 Exchange current densities, log(i_0), on monometallic surfaces plotted as a function of the calculated hydrogen binding energy, reprinted with permission from Ref. [86].

Pt/TiO$_2$ has been demonstrated to exhibit the highest photocatalytic activity among other metal-loaded TiO$_2$ [74, 87], such as Au/TiO$_2$. This has been explained by the highest work function of Pt; i.e., enhanced electrons "sinking" properties, and by its lowest overpotential for H$_2$ formation. In addition, the diagram for atomic hydrogen chemisorption energies on different metal surfaces shown in Figure 1-14 [85] confirms that the reaction at equilibrium potential is thermo-neutral over platinum, whereas this is not the case for gold. The Gibbs-free energy of the coordinate state has been considered as a reasonable descriptor of the HER activity with an optimum value of zero [88]. DFT calculations showed that Pt owns the smallest Gibbs free-energy value close to -0.09 eV compared to that of gold being 0.45 eV, indicating that Pt has the best electrocatalytic activity from the viewpoint of thermodynamics.
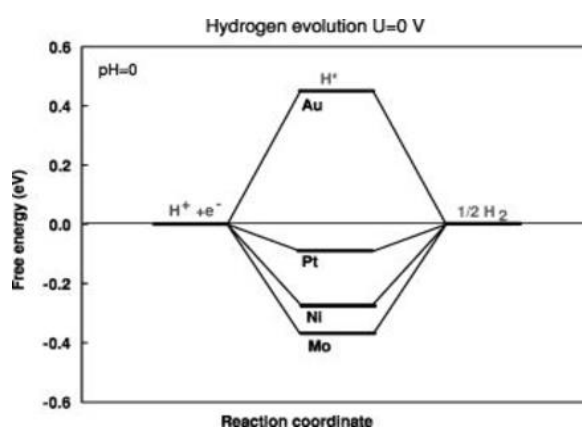
Figure 1-14 The diagram of atomic hydrogen chemisorption energies on different metal surfaces, reprinted with permission from Ref. [85].

However, some noble metal catalysts bind hydrogen with similar energies as Pt but show lower activities. Lindgren et *al.* [89] have employed a developed electronic structure method to calculate the fully potential-dependent reaction barriers. They have found that the electrochemical reaction on both metals displays similar characteristics, but the intrinsic reaction barrier on Au is significantly higher making both, the Tafel and the Heryovsky barriers on Au higher than on Pt. They claimed that the hydrogen evolution reaction proceeding from hollow sites on Au rather than the top sites on Pt. Moreover, a contradicting report [90] showed that Au/TiO$_2$ exhibited higher H$_2$ evolution from 2-propanol than Pt/TiO$_2$. This was explained by direct hydrogen abstraction from the substrate by H$^{\bullet}_{ads}$(Au) resulting in 2-propanol radical as shown in Eq. 1-6. A free radical chain reaction is induced by this abstraction because the 2-propanol radical inject its electron in TiO$_2$, which might further increase the photocatalytic activity. In addition, Au/TiO$_2$ has shown a photocatalytic activity in the visible light range due to the Surface Plasmon Resonance (SPR) effect [91]. For example, upon the excitation at $\lambda > 400$ nm, Au/TiO$_2$ showed three times higher H$_2$ evolution rates compared to Pt/TiO$_2$. This might be explained by the injection of electrons *via* two pathways; a direct one resulting in the electron-hole generation and another one related to the

electric field created by the excited plasmon. The proposed mechanisms for the visible-light H_2 production using Au–TiO$_2$ is shown in Figure 1-15.

$$H^{\bullet}_{ads}(Au) + CH_3CHOHCH_{3ads}(Au) \rightarrow Au + H_{2(g)} + CH_3{}^{\bullet}COHCH_3 \qquad (1\text{-}6)$$
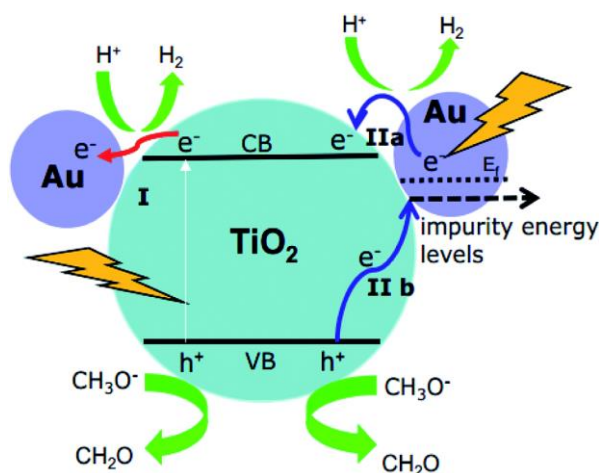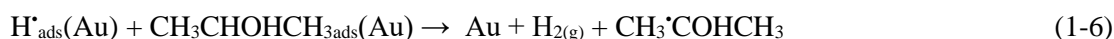
Figure 1-15 Proposed mechanisms for H$_2$ production using Au–TiO$_2$ in water/methanol mixtures (illumination with wavelength range ≥420 nm: process I + II; illumination with wavelength range ≥500 nm: process II). Reprinted with permission from Ref. [92].

Because the optimal co-catalyst loading depends also on the properties of the semiconductor, ***a universal co-catalyst modification for photocatalytic H$_2$ evolution that maximizes photocatalytic rates does not exist***. However, noble metals that depict higher work functions than their supports in general exhibit higher trapping efficiencies, thus offering a good combination of suitable electronic and catalytic properties for photocatalytic H$_2$ generation with many semiconductors [76, 81].

1.6. Photocatalytic water-splitting in heterogeneous systems

Photocatalytic H$_2$ production from water-splitting is accomplished under ambient operating conditions and consists of two half-reactions as seen in Eqs. 1-7a and 1-7b: the proton reduction and the highly demanding 4-electron water oxidation, respectively [67]. The splitting of one H_2O molecule to H_2 and ½ O_2 is accompanied by a change in free energy of $\Delta G^0 = 237.2$ kJ/mol that equals to $\Delta E^{\circ} = 1.23$ V according to the Nernst equation[93]. To drive the water-splitting photoreaction using a semiconductor, the photon energy absorbed by the semiconductor should be more than 1.23 eV (wavelengths shorter than 1000 nm), hence, it should have an E_g large enough to split water. The semiconductor is then able to convert this energy into H_2 and O_2 using electrons/holes generated under illumination provided that both, the energy of the conduction and the valance band-edges straddle the electrochemical potentials E° (H^+/H_2) and E° (O_2/H_2O) [67] (Figure 1-16). The electronic structure of TiO$_2$ matches these values rather well.
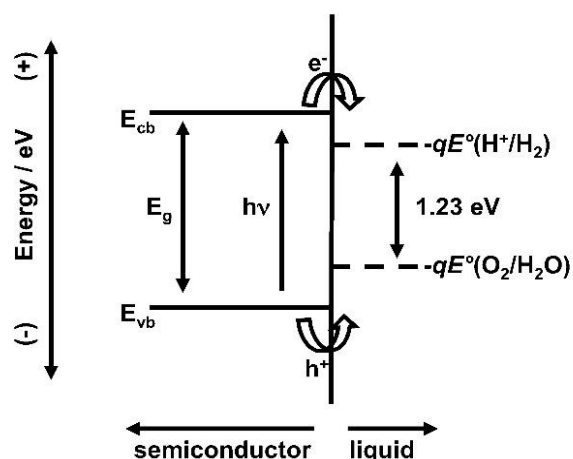
Figure 1-16 Photocatalytic splitting of water at the surface of a semiconductor under illumination, adapted with permission from Ref. [93].

$$2H^+ + 2e^- \rightarrow H_2 (\uparrow) \qquad\qquad E^0 = 0 \text{ V } vs \text{ NHE} \qquad (1\text{-}7a)$$

$$H_2O \rightarrow \tfrac{1}{2}O_2 (\uparrow) + 2H^+ + 2e^- \qquad\qquad E^0 = 1.23 \text{ V } vs \text{ NHE} \qquad (1\text{-}7b)$$
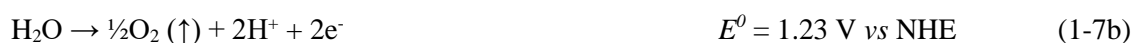
As mentioned before, the overall water-splitting reaction has a $\Delta G > 0$, i.e., the reaction absorbs energy, however, in contrast to a normal catalyst, a suitable photocatalyst can drive reactions with positive values for ΔG [94]. This is because the reduction and oxidation steps are spatially separated in photocatalysis, where both Gibbs energy changes for the reactions of electrons (ΔG_e) and holes (ΔG_h) should be negative [95] as shown in Figure 1-17. Hence, Gibbs energy change of both oxidation and reduction reactions should be negative. Consequently, the thermodynamic requirement for a photocatalytic reaction is more cathodic and more anodic energy levels of the CB bottom and VB top compared with the standard electrode potential of (H^+/H_2) and (O_2/H_2O), respectively [17, 94]. Therefore, from a thermodynamic point of view, only a few photocatalysts are capable to produce hydrogen and oxygen at the same time.
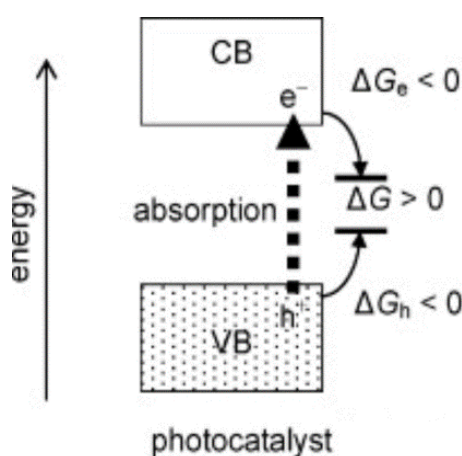
Figure 1-17 Gibbs-energy change in photocatalytic reactions, reprinted with permission from Ref. [94].

17

However, the solar photochemical conversion efficiencies of heterogeneous photocatalyst systems remain low since most systems are limited to the operation under UV light [32]. The photogenerated charge carriers can also rapidly recombine, thus turning photon energy into heat. In addition, technological measures to separate the gas mixture generated and to prevent back-reactions have to be taken [12, 96, 97]. Nevertheless, *some photocatalyst properties would enhance the hydrogen evolution* via photocatalytic water-splitting. For example, high crystallinity minimizes the bulk defects that act as recombination centers [98]. In addition, the smaller the particle size of a semiconductor is, the shorter is the diffusion length of the photogenerated carriers to the surface [99]. Another strategy is the use of co-catalysts to provide active sites for H_2 and O_2 evolution. For H_2 evolution, noble metals (Pt, Au, Pd, Rh, and Ag) or transition-metal oxides (e.g., NiO_x) have been widely used, to which the photogenerated electrons in the CB are transferred, while the photogenerated holes remain on the photocatalyst thus minimizing the probability of electron-hole recombination [67].

1.7. Hydrogen production by photoreforming

As an alternative, the coupling of H_2 evolution and photocatalytic degradation of organic substrates yielding CO_2, e.g. contaminants in water [17, 67, 74], can be achieved in the so-called photoreforming process [5]. Such a process can use solar light and wastewater as resources, while the evolved CO_2 may be recycled using the natural photosynthesis capacity [4]. In photoreforming systems, an adsorbed organic substrate is oxidized at the photocatalyst surface, whereas protons are reduced by the photogenerated CB electrons (see Eq. 1-8). The organic substrate is frequently named sacrificial reagent because it reacts irreversibly with the photogenerated holes thus preventing the undesired electron/hole recombination [67]. Photoreforming can be considered as an intermediate process between photocatalytic water-splitting and the photocatalytic oxidation of organic compounds as shown in Figure 1-18.

$$C_xH_yO_z + (2x\text{-}z)H_2O \rightarrow (2x\text{+}y/2\text{-}z)H_2 + xCO_2 \qquad (1\text{-}8)$$
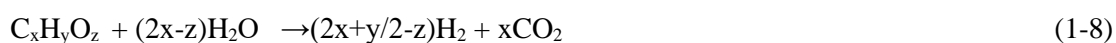
The oxidation of organic molecules on irradiated semiconductors proceeds either by the direct uptake of the photogenerated holes or via the attack of the highly reactive hydroxyl radicals generated at the surface [32]. The photocatalytically generated $^\bullet$OH radicals can abstract hydrogen atoms from the organic molecules, causing a cascade of reactions through lower molecular intermediates. This chain of oxidation reactions may end up in the complete mineralization of the substrate [100]. Organic substrates are generally characterized as stronger reducing agents compared to water, i.e., their oxidation occurs at a less positive potential. Consequently, the energetic separation of the redox half-reactions is narrowed for photoreforming compared to the overall water splitting [101]. Hence, the potentials of semiconductor band edges are met more easily

for photoreforming than for the overall photocatalytic water-splitting resulting in a larger variety of materials that are suitable for this application.
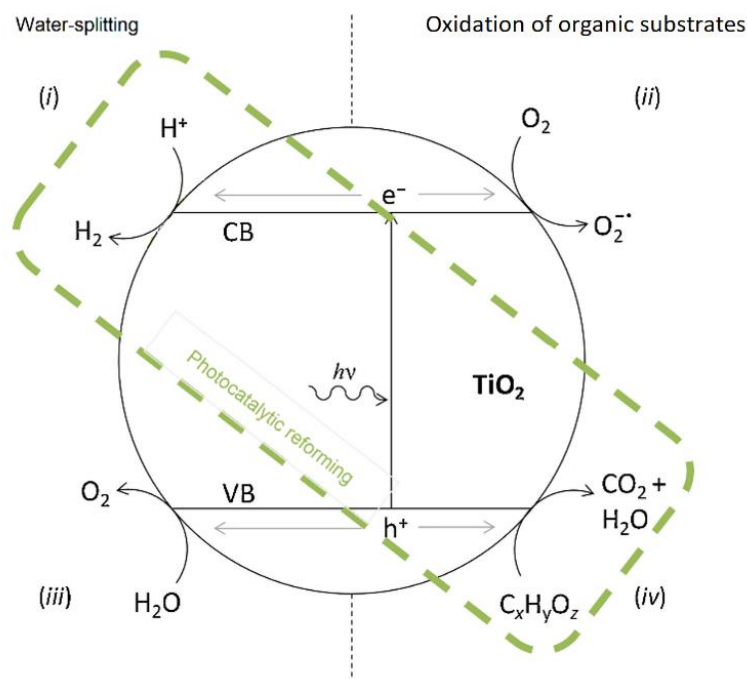
Figure 1-18 Schematic representation of photocatalytic water-splitting, photocatalytic oxidation of organics and photocatalytic reforming reactions over an irradiated TiO$_2$ photocatalyst, adapted with permission from Ref. [101].

Relatively high rates of H$_2$ evolution have been achieved using sacrificial reagents for several different photocatalytic systems. As O$_2$ is not produced in these systems, the back reaction to produce water is suppressed, avoiding a subsequent gas separation stage [57]. A wide variety of organic compounds such as alcohols, organic acids, and hydrocarbons have been employed as electron donors for photocatalytic H$_2$ generation [102]. In particular, methanol has been frequently studied since the main products are H$_2$ and CO$_2$ in a stoichiometric ratio of 3:1 with minimal formation of by-products [103]. The production of H$_2$ has been confirmed to be dependent on the concentration of the electron donor [104], as well as on the nature of the material used that can affect the kinetic reactions pathway [105]. However, *the H$_2$ yield can be negatively affected by competing for reduction reactions between H$^+$ and the intermediates formed upon the oxidation of the sacrificial reagents* [57].

It has been proved by several authors that a complete reforming of oxygenated substrates by photocatalysis at ambient temperatures is indeed possible. Kawai and Sakata demonstrated that sucrose is completely converted in the expected stoichiometry (2:1) in an aqueous suspension of a RuO$_2$-TiO$_2$-Pt photocatalyst under Xe lamp irradiation [106]. They also showed a complete acetic acid reforming on Pt/TiO$_2$ photocatalysts using a Hg lamp [107]. The catalytic pathway for the generation of H$_2$ by the aqueous-phase reforming of organic hydrocarbons might involve the

cleavage of C–C bonds as well as of C–H and/or O–H bonds. Direct hole transfer to the organic substrate adsorbed on Ti surface sites has been proposed for the C-C cleavage reaction [101].

Carboxylic acids, especially acetic acid, have also been employed as electron donors for the photocatalytic H_2 generation [108-110]. CO_2, H_2, CH_4, and C_2H_6 have been detected during the photoreforming of aqueous acetic acid solutions. ***Bare TiO₂ has shown a negligible photocatalytic activity*** while the loading with noble metals such as Pt, Rh, Au, and Ag as electron transfer catalysts has significantly improved the photocatalytic activity for H_2 production in the order of $Ag/TiO_2 <$ $Au/TiO_2 < Rh/TiO_2 < Pt/TiO_2$ [110]. The decomposition of carboxylic acids on TiO_2 has been proved to follow the photo-Kolbe mechanism [101, 111, 112]. In the case of acetic acid on irradiated TiO_2, a direct reaction between the photo-generated holes and CH_3COOH adsorbed on the TiO_2 surface results in the formation of CO_2 as reaction product and ˙CH_3 radicals as a reaction intermediate yielding the corresponding alkanes as reaction products [109, 110]. It was also reported that the photocatalytic carboxylic acid reforming produces alcohols with a lower number of carbon atoms as compared with the substrate. This was explained by the subsequent coupling of ˙CH_3 radicals with ˙OH radicals [107].

In addition, the photocatalytic reforming of dicarboxylic acids has been studied, during which the monocarboxylic acids are formed in the reaction mixture [113]. Sun et *al.* [114] observed different photocatalytic reactivity for straight-chain dicarboxylic acids with even and odd carbon numbers during TiO_2-based photocatalysis. Under identical conditions, odd-carbon-numbered-dicarboxylic acids (o-Das) showed faster degradation rates than the even-carbon-numbered-dicarboxylic acids (e-Das). Through ATR-FTIR experiments and isotopic-labeling methods, they demonstrated that the difference of reactivity was related to the difference in the coordination patterns on the TiO_2 surfaces. This determines whether the selective cleavage of the C_1-C_2 bond of the dicarboxylic acids is the predominant process. e-DAs showed strong symmetrical bidentate adsorption on the TiO_2 surface, which can resist the attack inhibiting the oxidative cleavage. On the other hand, o-DAs exhibited asymmetrical adsorption, which facilitates the C_1-C_2 bond cleavage associated with the monodentate adsorption [114]. Therefore, ***investigating the adsorption characteristics of the substrate on TiO₂ and the subsequent surface reaction mechanisms is a key factor to understand the photocatalytic reforming processes***.

However, ***contradicting reports exist regarding the pathway, through which the photoinduced radical species initiate the reaction of organic substrates on the TiO₂ surface under anaerobic conditions***. Generally, the presence of free ˙OH radicals formed by the transfer of a photogenerated hole onto a terminal OH-group is assumed [115]. Nevertheless, the computational prediction [116, 117] and the experimental studies on rutile single crystal surfaces [118] suggest that charge transfer from trapped holes at surface lattice oxygen sites to adsorbed water molecules is unlikely to happen.

Hence, the proposed photocatalytic conversion mechanisms should consider the pathways of interfacial hole transfer besides the interaction between the organic substrate and TiO_2 [119, 120].

1.8. Oxalic acid as a model compound

Oxalic acid is known to be present in the effluent of some industries, e.g., textile and metallurgy, hence, ***it is considered as a water contaminant*** [113]. On the other hand, oxalic acid has been extensively reported as an intermediate during the mineralization of a wide range of organic substrates [121]. However, ***there are contradicting reports regarding the ability to use oxalic acid as a substrate to produce H_2 over irradiated TiO_2 photocatalysts***. On the one hand, it has been predicted that oxalic acid should be unable to initiate photoreforming due to its lack of an H-atom bound to a C atom adjacent to the functional group, which is required for an H abstracting reaction [122]. On the other side, however, oxalic acid has shown good characteristics to become an efficient substrate, from which H_2 can indeed be photocatalytically produced [101].

Oxalic acid is a dicarboxylic acid of the general formula $H_2C_2O_4$ with its one-electron redox potential ($HC_2O_4^- \rightarrow HC_2O_4^{\bullet} + e^-$) being 2.1 V *vs* NHE [123, 124]. The fate of oxalic acid is found to follow the main features of a photoreforming process proceeding according to Eq. 1-9 and can generally be expected to evolve hydrogen and carbon dioxide in a 1:2 molar ratio. The presence of a metal as a co-catalyst on the surface of a photocatalyst has been shown to play an inevitable role in the pathway of the reaction [101]. Li et *al.* [113] investigated the effect of the variation of the pH, of the amount of deposited platinum and of the addition of inorganic anions on the rate of the photocatalytic hydrogen evolution over platinized Degussa P25 TiO_2 using oxalic acid as the electron donor. While ***bare TiO_2 showed no activity***, the presence of Pt enhanced the rates of the photocatalytic hydrogen evolution. These authors demonstrated also that the amount of H_2 formed is consistent with the amount of oxalate reacted as shown in Figure 1-19(a), confirming that the H_2 evolution and the degradation of oxalic acid proceed simultaneously in this photocatalytic system. H_2 production from oxalic acid showed a maximum at about pH 2.9 (see Figure 1-19(b)), where oxalic acid is mostly present as $HC_2O_4^-$. This was found to be in good agreement with a six times faster reaction between OH radicals and $HC_2O_4^-$ than with the other forms of oxalic acid, i.e., $C_2O_4^{2-}$ and $H_2C_2O_4$. However, the authors omitted to follow the formation of any by-product and found that kinetics follow a Langmuir-type behavior.

$$H_2C_2O_4 \rightarrow H_2 + 2CO_2 \tag{1-9}$$
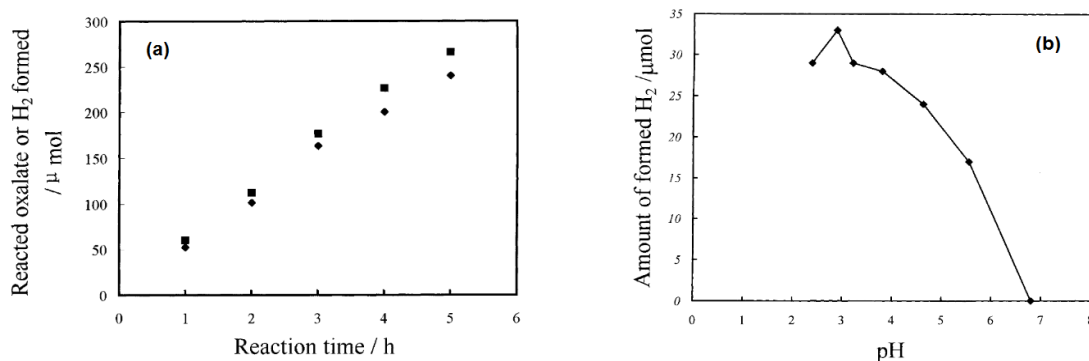
Figure 1-19 (a) Time course of (◆) produced H₂ and (■) reacted H₂C₂O₄ (4.9×10⁻³ M oxalic acid solution; 0.05 g of 0.5 wt.% Pt–P25); (b) amount of H₂ as a function of different initial pH (5.0×10⁻³ M oxalate solution; 0.02 g of 0.3 wt.% Pt–P25. Both figures are reprinted with permission from Ref. [113].

In a second paper, Li et. al. [124] investigated the photocatalytic H_2 production using aqueous Pt/TiO_2 suspension in a mixture of electron donors, i.e., oxalic acid and formic acid. In this case, the H_2 evolution was accompanied by the decomposition of oxalic acid, while no decomposition of formic acid was observed. This was attributed to the inhibition of formic acid adsorption on TiO_2 in the presence of oxalic acid.

Owing to the last conclusion, the study of oxalic acid adsorption on TiO_2 is essential, especially to understand its surface reaction mechanism. Mendive et *al.* [125] proposed the mechanistic details, and, based upon them, suggested several surface photoreactions initiated during the illumination of TiO_2 in the presence of oxalic acid. Their theoretical calculations revealed different surface complexes exhibiting different pathways and consequently different photoreactivity.
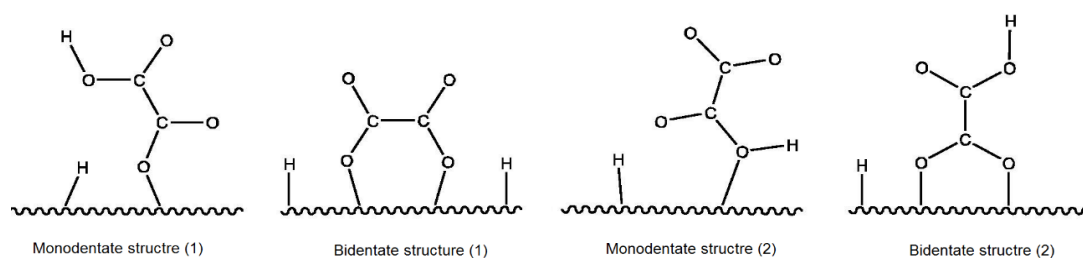
Figure 1-20 Different surface complex structures of oxalic acid on anatase-TiO₂, adapted with permission from Ref. [125].

Thanks to their ATR-FTIR studies together with their theoretical calculations executed by the MSINDO-CCM method, the adsorption of oxalic acid on anatase showed several binding structures, i.e., bidentate and monodentate structures, as shown in Figure 1-20. However, a monodentate complex appears to be the most favored on the anatase surface. These authors showed that upon irradiation, the photogenerated holes can be trapped either on O-O bonds or on the C-C bond. Nevertheless, the photogenerated electrons can be trapped either on Ti-Ti, C-C or C-O bonds. This would increase the electron densities at these atoms, as revealed from Figure 1-21, resulting in a

bond weakening and in the formation of intermediates, such as formic acid and formaldehyde, on the surface of TiO$_2$. However, ***the authors were unable to experimentally detect the formation of such products***.

Unfortunately, ***just a few reports*** have dealt with the photocatalytic reforming of oxalic acid compared to other molecules, e.g., methanol and glycerol. Moreover, ***the charge transfer mechanism occurring at the TiO$_2$/oxalic acid interface is not known to any degree of sophistication*** making such an investigation very interesting. While most of the scientific works done so far yielded ***lower H$_2$ production amounts than expected***, detailed experimental studies regarding this issue are very limited.

Monodentate structure (1)

Bidentate structure (1)

Monodentate structure (2)

Bidentate structure (2)
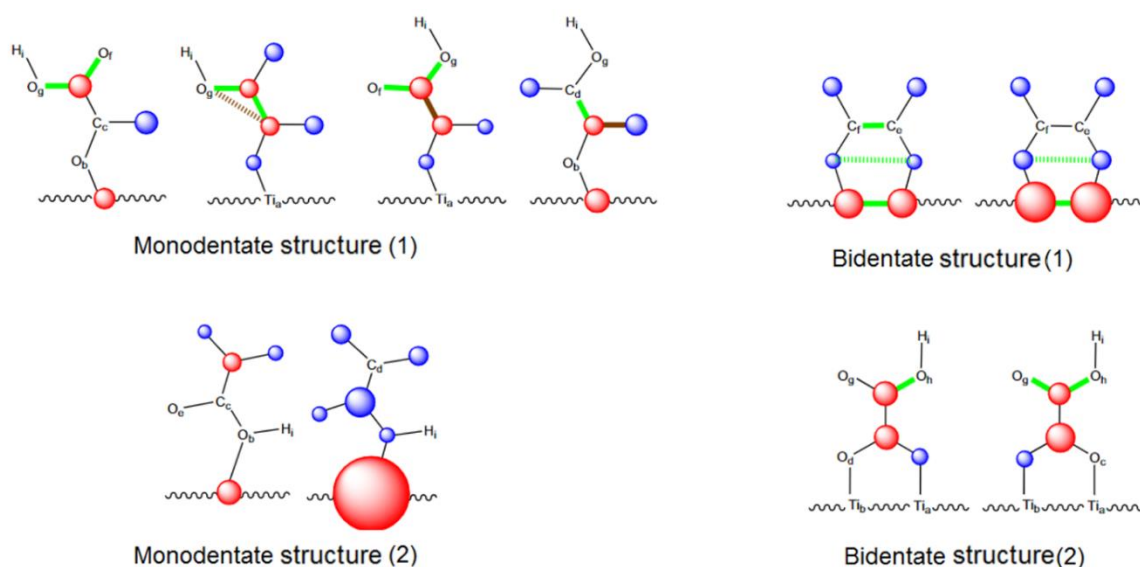
Figure 1-21 A scheme of oxalic acid molecules with red and blue circles where the atom becomes more negative and more positive, respectively; dash and thick bonds belong to the bonds that are weakened and strengthened due to the irradiation, respectively. Adapted with permission from Ref. [125] schematic representation of the molecules upon irradiation; red and blue.

1.9. The Design of Experiments approach

The design of experiments (DoE) approach is a statistical methodology with the aim to obtain the maximum amount of information employing the fewest number of experimental runs. In order to find the optimum conditions of a process, most experiments are done usually in an unsystematic way by changing the levels of one factor at a time (COST: Change One Separate factor at a Time). However, as shown by Fisher, COST does not provide much information regarding the position of the optimum parameters especially when there are interactions among the factors [126]. The most important aspect of DoE is that it provides a strict mathematical framework for changing all pertinent factors simultaneously. Using the smallest number of experimental runs, the combination between DoE and Analysis of Variance ANOVA offers the ability to identify the interaction between factors. With DoE it is also possible to optimize critical factors and identify the best

combination of values [126]. DoE can use the general full factorial design FFD, in which multiple factors are investigated simultaneously to identify the factors that have a significant effect on the response, as well as to investigate the effect of interactions. Each factor could have a different number of levels and the experiments performed at all possible combinations of the factor levels.

1.10. The scope of this thesis

Anaerobic heterogeneous photocatalysis represents a sustainable pathway to generate H_2. Yet, in the absence of O_2, the oxidants available for the oxidation of sacrificial reagents can only be formed from photogenerated holes and/or oxidants generated therefrom. However, research into the photocatalytic reforming of organic substrates still has many contradicting issues and open questions, which have been highlighted in the introduction.

Most systems investigated for the photocatalytic reforming are noble-metal-modified-TiO_2 photocatalysts. The fast charge carrier's recombination and the high over-potential of the H_2 evolution reaction turn bare TiO_2 into an inactive material. Efforts to improve photocatalytic reforming activities have been mainly devoted to the development of photocatalysts, which can be excited by visible light besides other strategies of minimizing the recombination of charge carriers. However, systematic studies on how the parameters of the synthesis method affect the reaction products are rare.

Moreover, most of the researchers pay attention to the reaction rates, but not to the total yield of the underlying photocatalytic reactions. The lack of a detailed mechanistic understanding of the photocatalytic reactions involved under these conditions has limited potential applications of this technology. Furthermore, an investigation regarding the selectivity of the photocatalyst toward the target molecule is necessary to ensure the highest yields. The oxidation of sacrificial reagents often contributes to the products that are being considered as reduction products. Hence, it becomes crucial to evaluate the fate of these substrates and their contributions to the yield of H_2 in a photocatalytic reaction. It is important, as well, to identify all products, qualitatively and quantitatively, to establish a photocatalytic mechanism involving both, the reduction as well as the oxidation pathways. These are common problems mentioned by Prof. Kamat in his editorial in ACS Energy Letter entitled *Semiconductor Photocatalysis: "Tell Us the Complete Story!"* [127]. Besides, researchers mostly do not care about the type of their reactions, i.e., a semiconductor-assisted photoreaction or a catalyzed photoreaction (photocatalytic reaction). The concept of the Turnover Number (TON) has been rarely used in publications dealing with the photocatalytic reforming reaction. This is another common issue that should be considered as mentioned by Prof. Ohtani in his review about *"Photocatalysis A to Z : What we know and what we do not know in a scientific sense"* [94].

The purpose of this thesis is to develop TiO_2-based photocatalysts which are active for the production of hydrogen *via* the photoreforming of oxalic acid and to further understanding of the mechanisms involved in promoting the reaction. The thesis is divided into two points of work:

(1) Synthesis of bare TiO_2 photocatalysts via the EISA method for a noble-metal-free photocatalytic H_2 evolution from organic substrates. In a statistical study, the effect of the type of titanium-precursor and the triblock copolymer surfactant on the prepared TiO_2 is investigated. The DoE approach is employed to optimize the synthesis procedure in a few experimental runs, in which a rarely used titanium-precursor is employed. The optimum synthesis parameters are identified by the analysis of variance (ANOVA) and applied for the synthesis of active anatase TiO_2 in powder form. The prepared photocatalysts are characterized using XRD, TEM, XPS, and UV-Vis spectroscopy to develop the relationship between high photocatalytic performance and physicochemical properties. Other properties such as flat-band potential and how the charge carrier dynamics affect the activity are also investigated.

(2) Use of the prepared TiO_2, in its bare and modified forms, for the photocatalytic H_2 evolution from oxalic acid. Oxalic acid is chosen as a model compound because of the expectation of a simple photoreforming procedure without secondary reactions. Accordingly, a study of oxalic acid degradation at constant pH values has been performed in different photocatalytic systems, i.e., oxygen-saturated and oxygen-free conditions. Additionally, the effect of different co-catalysts on the total yield of H_2 is investigated, closing the gap of knowledge between the theoretical and experimental aspects. Interestingly, the formation of several by-products during the photoreforming of oxalic acid is detected, confirming that this process is not as simple as expected. A combination of analytical techniques is applied to trace the formed by-products, e.g., ion chromatography, solid-phase EPR, and EPR spin-trap spectroscopy. A description of the photoreforming mechanism, including the degradation pathways and the nature of the adsorbate complexes at the TiO_2 surface, is consequently proposed. The effect of the current doubling mechanism and the disproportionation reaction between the formed radicals on the total yield is also discussed.

The review of the literature in the introductory **Chapter 1** should have familiarized the reader with the principles of TiO_2 photocatalysis, emphasizing its applications for the generation of H_2 as a sustainable fuel source. Besides, it highlights some open questions regarding photocatalysis, synthesis of TiO_2, and photocatalytic reforming.

Chapter 2 of this cumulative thesis includes the article entitled "*Co-Catalyst-Free Photocatalytic Hydrogen Evolution on TiO2: Synthesis of Optimized Photocatalyst through Statistical Material Science*" [67], in which the use of the Design of Experiment (DoE) approach is introduced. Such a statistical method is widely used for the optimization of processes; however, it has not been used

often in the area of material preparation. Here, DoE is employed to statistically optimize the EISA method to prepare a photo-active bare TiO_2. The use of DoE is beneficial to reduce the number of experiments and to identify the influence of the parameters studied on the synthesis method. The prepared TiO_2 has been then extensively characterized to determine its physicochemical properties in addition to the optical and the electronic ones. The prepared TiO_2 has been used for the noble-free photocatalytic H_2 evolution from ethanol.

Chapter 3 includes the article entitled "*Understanding the Degradation Pathways of Oxalic Acid in Different Photocatalytic Systems: Towards Simultaneous Photocatalytic Hydrogen Evolution*" [128], in which the use of the self-prepared TiO_2, in its bare and modified forms, for the photocatalytic oxidation of oxalic acid is presented. Understanding the anodic half-reaction, i.e., the oxidation of oxalic acid on the surface of TiO_2, indeed, forms a reliable base for the investigation of the photoreforming process. Different systems, including O_2-saturated, O_2-free, and homogenous photolysis have been used in a pH-controlled-photocatalytic system. The pH-stat technique has been used, and the concentrations of oxalic acid and by-products have been determined in the liquid phase by means of HPIC.

Chapter 4 includes the article entitled "*Photocatalytic H_2 Evolution from Oxalic Acid: Effect of Co-catalysts and Carbon Dioxide Radical Anion on the Surface Charge Transfer Mechanisms*", which presents a study of the photocatalytic reforming of oxalic acid on different noble-metal-modified-TiO_2 photocatalysts. The self-prepared TiO_2 has been modified with Pt NPs, Au NPs, and bimetals Au-Pt NPs. QMS system has been used to analyze the products in the gas phase, while HPIC has been employed to determine oxalic acid and by-products in the liquid phase. The relationship between the co-catalyst used and the kinetics of the reaction and the distribution of the by-products has been investigated. EPR-spin trap technique has been used to identify the nature of the photogenerated species resulting from the irradiation of TiO_2/oxalic acid suspensions. The contribution of the current doubling mechanism and the effect of the disproportionation reaction of radicals on the total yield is discussed, showing a loss of efficiency due to secondary reactions. An interfacial surface charge mechanism is proposed identifying the formation pathways of the by-products and clarifying the possible reasons for the lower than expected H_2 amounts reported in this thesis and previous publications.

Finally, **Chapter 5** includes a concluding discussion as well as the results of further investigations related to the work described in the previous chapters.

1.11. References

1.   Administration, U.S.E.I. *Today in Energy*. 2107   08.01.2020]; Available from: https://www.eia.gov/todayinenergy/detail.php?id=32912.
2.   Lewis, N.S. and D.G. Nocera, *Powering the planet: Chemical challenges in solar energy utilization.* Proceedings of the National Academy of Sciences, 2006. **103**(43): p. 15729-15735.
3.   Dudley, B., *The Outlook considers the energy transition through three different lenses: sectors, regions and fuels*, in *BP Energy Outlook 2019 edition*. 2019, BP p.l.c. .
4.   Shimura, K. and H. Yoshida, *Heterogeneous photocatalytic hydrogen production from water and biomass derivatives.* Energy & Environmental Science, 2011. **4**(7): p. 2467-2481.
5.   Ni, M., et al., *A review and recent developments in photocatalytic water-splitting using TiO_2 for hydrogen production.* Renewable and Sustainable Energy Reviews, 2007. **11**(3): p. 401-425.
6.   Hakki, A., et al., *Hydrogen production by heterogeneous photocatalysis.* 2018.
7.   Steinfeld, A., *Solar hydrogen production via a two-step water-splitting thermochemical cycle based on Zn/ZnO redox reactions.* International Journal of Hydrogen Energy, 2002. **27**(6): p. 611-619.
8.   Das, D. and T.N. Veziroglu, *Advances in biological hydrogen production processes.* International journal of hydrogen energy, 2008. **33**(21): p. 6046-6057.
9.   Liao, C.-H., C.-W. Huang, and J. Wu, *Hydrogen production from semiconductor-based photocatalysis via water splitting.* Catalysts, 2012. **2**(4): p. 490-516.
10.   Sivula, K. and R. Van De Krol, *Semiconducting materials for photoelectrochemical energy conversion.* Nature Reviews Materials, 2016. **1**(2): p. 15010.
11.   Takanabe, K. and K. Domen, *Toward visible light response: overall water splitting using heterogeneous photocatalysts.* Green, 2011. **1**(4): p. 313-322.
12.   Maeda, K. and K. Domen, *Photocatalytic water splitting: recent progress and future challenges.* The Journal of Physical Chemistry Letters, 2010. **1**(18): p. 2655-2661.
13.   Jiang, C., et al., *Photoelectrochemical devices for solar water splitting–materials and challenges.* Chemical Society Reviews, 2017. **46**(15): p. 4645-4660.
14.   Cao, W., *Semiconductor Photocatalysis: Materials, Mechanisms and Applications*. 2016: BoD–Books on Demand.
15.   Kisch, H., *Semiconductor Photocatalysis Principle and Applications*. 2015: Wiley-VCH.
16.   Ibach, H. and H. Lüth, *Semiconductors*, in *Solid-State Physics: An Introduction to Principles of Materials Science*. 2003, Springer Berlin Heidelberg: Berlin, Heidelberg. p. 391-482.
17.   Pichat, P., *A brief overview of photocatalytic mechanisms and pathways in water.* Water science and technology, 2007. **55**(12): p. 167-173.
18.   Friehs, E., et al., *Toxicity, phototoxicity and biocidal activity of nanoparticles employed in photocatalysis.* Journal of Photochemistry and Photobiology C: Photochemistry Reviews, 2016. **29**: p. 1-28.
19.   Hernández-Ramírez, A. and I. Medina-Ramírez, *Semiconducting Materials*, in *Photocatalytic Semiconductors: Synthesis, Characterization, and Environmental Applications*, A. Hernández-Ramírez and I. Medina-Ramírez, Editors. 2015, Springer International Publishing: Cham. p. 1-40.
20.   Barr, A., *Electrical Properties of Semiconductors*, in *Electronic Materials: From Silicon to Organics*, L.S. Miller and J.B. Mullin, Editors. 1991, Springer US: Boston, MA. p. 19-24.
21.   Fonash, S.J., *Chapter Three - Structures, Materials, and Scale*, in *Solar Cell Device Physics (Second Edition)*, S.J. Fonash, Editor. 2010, Academic Press: Boston. p. 67-120.
22.   Hoffmann, M.R., et al., *Environmental applications of semiconductor photocatalysis.* Chemical reviews, 1995. **95**(1): p. 69-96.
23.   Linsebigler, A.L., G. Lu, and J.T. Yates Jr, *Photocatalysis on TiO_2 surfaces: principles, mechanisms, and selected results.* Chemical reviews, 1995. **95**(3): p. 735-758.

24. Wang, F., Q. Li, and D. Xu, *Recent Progress in Semiconductor-Based Nanocomposite Photocatalysts for Solar-to-Chemical Energy Conversion.* Advanced Energy Materials, 2017. **7**(23): p. 1700529.

25. Mills, A. and S. Le Hunte, *An overview of semiconductor photocatalysis.* Journal of photochemistry and photobiology A: Chemistry, 1997. **108**(1): p. 1-35.

26. Takanabe, K., *Photocatalytic water splitting: quantitative approaches toward photocatalyst by design.* ACS Catalysis, 2017. **7**(11): p. 8006-8022.

27. Peter, L.M., *Photoelectrochemistry: from basic principles to photocatalysis.* 2016.

28. Habisreutinger, S.N., L. Schmidt-Mende, and J.K. Stolarczyk, *Photocatalytic Reduction of CO_2 on TiO_2 and Other Semiconductors.* Angewandte Chemie International Edition, 2013. **52**(29): p. 7372-7408.

29. Mo, S.-D. and W. Ching, *Electronic and optical properties of three phases of titanium dioxide: Rutile, anatase, and brookite.* Physical Review B, 1995. **51**(19): p. 13023.

30. Carp, O., C.L. Huisman, and A. Reller, *Photoinduced reactivity of titanium dioxide.* Progress in solid state chemistry, 2004. **32**(1-2): p. 33-177.

31. Enke, C.G., *Nonstoichiometry, diffusion, and electrical conductivity in binary metal oxides.* Materials and Corrosion, 1974. **25**(10): p. 801-802.

32. Schneider, J., et al., *Understanding TiO_2 photocatalysis: mechanisms and materials.* Chemical reviews, 2014. **114**(19): p. 9919-9986.

33. Chretien, S. and H. Metiu, *Electronic structure of partially reduced rutile TiO_2 (110) surface: where are the unpaired electrons located?* The Journal of Physical Chemistry C, 2011. **115**(11): p. 4696-4705.

34. Diebold, U., *The surface science of titanium dioxide.* Surface science reports, 2003. **48**(5-8): p. 53-229.

35. Qian, R., et al., *Charge carrier trapping, recombination and transfer during TiO_2 photocatalysis: An overview.* Catalysis Today, 2019. **335**: p. 78-90.

36. Kohtani, S., A. Kawashima, and H. Miyabe, *Reactivity of trapped and accumulated electrons in titanium dioxide photocatalysis.* Catalysts, 2017. **7**(10): p. 303.

37. Serpone, N., D. Lawless, and R. Khairutdinov, *Size effects on the photophysical properties of colloidal anatase TiO_2 particles: size quantization versus direct transitions in this indirect semiconductor?* The journal of Physical Chemistry, 1995. **99**(45): p. 16646-16654.

38. Bessekhouad, Y., D. Robert, and J.V. Weber, *Synthesis of photocatalytic TiO_2 nanoparticles: optimization of the preparation conditions.* Journal of Photochemistry and Photobiology A: Chemistry, 2003. **157**(1): p. 47-53.

39. Chae, S.Y., et al., *Preparation of size-controlled TiO_2 nanoparticles and derivation of optically transparent photocatalytic films.* Chemistry of Materials, 2003. **15**(17): p. 3326-3331.

40. Du, L., et al., *Plasmon-induced charge separation and recombination dynamics in gold−TiO_2 nanoparticle systems: dependence on TiO_2 particle size.* The Journal of Physical Chemistry C, 2009. **113**(16): p. 6454-6462.

41. Stevanovic, A. and J.T. Yates Jr, *Probe of NH_3 and CO adsorption on the very outermost surface of a porous TiO_2 adsorbent using photoluminescence spectroscopy.* Langmuir, 2012. **28**(13): p. 5652-5659.

42. Yoshihara, T., et al., *Identification of reactive species in photoexcited nanocrystalline TiO_2 films by wide-wavelength-range (400− 2500 nm) transient absorption spectroscopy.* The Journal of Physical Chemistry B, 2004. **108**(12): p. 3817-3823.

43. Howe, R.F. and M. Gratzel, *EPR study of hydrated anatase under UV irradiation.* Journal of Physical Chemistry, 1987. **91**(14): p. 3906-3909.

44. Howe, R.F. and M. Gratzel, *EPR observation of trapped electrons in colloidal titanium dioxide.* The Journal of Physical Chemistry, 1985. **89**(21): p. 4495-4499.

45. Fazio, G., et al., *Curved TiO_2 nanoparticles in water: short (chemical) and long (physical) range interfacial effects.* ACS applied materials & interfaces, 2018. **10**(35): p. 29943-29953.

46. Wu, C.-Y., et al., *Markedly enhanced surface hydroxyl groups of TiO_2 nanoparticles with superior water-dispersibility for photocatalysis.* Materials, 2017. **10**(5): p. 566.

47.   Takeuchi, M., et al., *Investigations of the Structure of H2O Clusters Adsorbed on TiO2 Surfaces by Near-Infrared Absorption Spectroscopy.* The Journal of Physical Chemistry B, 2005. **109**(15): p. 7387-7391.

48.   Augustynski, J., *The role of the surface intermediates in the photoelectrochemical behaviour of anatase and rutile TiO₂.* Electrochimica Acta, 1993. **38**(1): p. 43-46.

49.   Zhang, J., et al., *New understanding of the difference of photocatalytic activity among anatase, rutile and brookite TiO₂.* Physical Chemistry Chemical Physics, 2014. **16**(38): p. 20382-20386.

50.   Sachs, M., et al., *Evaluation of surface state mediated charge recombination in anatase and rutile TiO₂.* The journal of physical chemistry letters, 2016. **7**(19): p. 3742-3746.

51.   Knorr, F.J., C.C. Mercado, and J.L. McHale, *Trap-state distributions and carrier transport in pure and mixed-phase TiO₂: influence of contacting solvent and interphasial electron transfer.* The Journal of Physical Chemistry C, 2008. **112**(33): p. 12786-12794.

52.   Wang, X., et al., *Trap states and carrier dynamics of TiO₂ studied by photoluminescence spectroscopy under weak excitation condition.* Physical Chemistry Chemical Physics, 2010. **12**(26): p. 7083-7090.

53.   Fujishima, A., T.N. Rao, and D.A. Tryk, *Titanium dioxide photocatalysis.* Journal of photochemistry and photobiology C: Photochemistry reviews, 2000. **1**(1): p. 1-21.

54.   Schindler, K.M. and M. Kunst, *Charge-carrier dynamics in titania powders.* Journal of Physical Chemistry, 1990. **94**(21): p. 8222-8226.

55.   Carneiro, J.T., et al., *Toward a physically sound structure− activity relationship of TiO₂-based photocatalysts.* The Journal of Physical Chemistry C, 2009. **114**(1): p. 327-332.

56.   Martin, S.T., et al., *Time-resolved microwave conductivity. Part 1.—TiO₂ photoreactivity and size quantization.* Journal of the Chemical Society, Faraday Transactions, 1994. **90**(21): p. 3315-3322.

57.   Schneider, J. and D.W. Bahnemann, *Undesired Role of Sacrificial Reagents in Photocatalysis.* The Journal of Physical Chemistry Letters, 2013. **4**(20): p. 3479-3483.

58.   Yan, X. and X. Chen, *Titanium dioxide nanomaterials.* Encyclopedia of inorganic and bioinorganic chemistry, 2011: p. 1-38.

59.   Mahoney, L. and R.T. Koodali, *Versatility of Evaporation-Induced Self-Assembly (EISA) Method for Preparation of Mesoporous TiO₂ for Energy and Environmental Applications.* Materials, 2014. **7**(4): p. 2697-2746.

60.   Chen, X. and S.S. Mao, *Titanium dioxide nanomaterials: synthesis, properties, modifications, and applications.* Chemical reviews, 2007. **107**(7): p. 2891-2959.

61.   Ismail, A.A. and D.W. Bahnemann, *Mesoporous titania photocatalysts: preparation, characterization and reaction mechanisms.* Journal of Materials Chemistry, 2011. **21**(32): p. 11686-11707.

62.   Yang, H., et al., *Free-standing and oriented mesoporous silica films grown at the air–water interface.* Nature, 1996. **381**(6583): p. 589.

63.   Förster, S. and T. Plantenberg, *From self-organizing polymers to nanohybrid and biomaterials.* Angewandte Chemie International Edition, 2002. **41**(5): p. 688-714.

64.   Ortel, E., et al., *New Triblock Copolymer Templates, PEO-PB-PEO, for the Synthesis of Titania Films with Controlled Mesopore Size, Wall Thickness, and Bimodal Porosity.* Small, 2012. **8**(2): p. 298-309.

65.   Förster, S. and M. Antonietti, *Amphiphilic block copolymers in structure-controlled nanomaterial hybrids.* Advanced Materials, 1998. **10**(3): p. 195-217.

66.   Choi, S.Y., et al., *Thermally Stable Two-Dimensional Hexagonal Mesoporous Nanocrystalline Anatase, Meso-nc-TiO₂: Bulk and Crack-Free Thin Film Morphologies.* Advanced Functional Materials, 2004. **14**(4): p. 335-344.

67.   AlSalka, Y., et al., *Co-catalyst-free photocatalytic hydrogen evolution on TiO₂: Synthesis of optimized photocatalyst through statistical material science.* Applied Catalysis B: Environmental, 2018. **238**: p. 422-433.

68.   Soler-Illia, G.J.d.A.A., A. Louis, and C. Sanchez, *Synthesis and Characterization of Mesostructured Titania-Based Materials through Evaporation-Induced Self-Assembly.* Chemistry of Materials, 2002. **14**(2): p. 750-759.

69. Weber, M.F. and M.J. Dignam, *Efficiency of splitting water with semiconducting photoelectrodes.* Journal of The Electrochemical Society, 1984. **131**(6): p. 1258-1265.

70. Kasarevic-Popovic, Z., D. Behar, and J. Rabani, *Role of excess electrons in TiO₂ nanoparticles coated with Pt in reduction reactions studied in radiolysis of aqueous solutions.* The Journal of Physical Chemistry B, 2004. **108**(52): p. 20291-20295.

71. Bahnemann, D., et al., *Flash photolysis observation of the absorption spectra of trapped positive holes and electrons in colloidal titanium dioxide.* The Journal of Physical Chemistry, 1984. **88**(4): p. 709-711.

72. Hu, C., et al., *Nickel Phosphide Electrocatalysts for Hydrogen Evolution Reaction.* Catalysts, 2020. **10**(2): p. 188.

73. Erdey-Grúz, T. and M. Volmer, *Zur theorie der wasserstoff überspannung.* Zeitschrift für physikalische Chemie, 1930. **150**(1): p. 203-213.

74. Schneider, J., T.A. Kandiel, and D.W. Bahnemann, *Solar Photocatalytic Hydrogen Production: Current Status and Future Challenges*, in *Materials and Processes for Solar Fuel Production*, B. Viswanathan, V. Subramanian, and J.S. Lee, Editors. 2014, Springer New York: New York, NY. p. 41-74.

75. Di Bartolomeo, A., *Graphene Schottky diodes: An experimental review of the rectifying graphene/semiconductor heterojunction.* Physics Reports, 2016. **606**: p. 1-58.

76. Michaelson, H.B., *The work function of the elements and its periodicity.* Journal of Applied Physics, 1977. **48**(11): p. 4729-4733.

77. Xiong, G., et al., *Photoemission electron microscopy of TiO₂ anatase films embedded with rutile nanocrystals.* Advanced Functional Materials, 2007. **17**(13): p. 2133-2138.

78. Iwata, K., et al., *Carrier Dynamics in TiO₂ and Pt/TiO₂ Powders Observed by Femtosecond Time-Resolved Near-Infrared Spectroscopy at a Spectral Region of 0.9− 1.5 μm with the Direct Absorption Method.* The Journal of Physical Chemistry B, 2004. **108**(52): p. 20233-20239.

79. Yamakata, A., et al., *Photodynamics of NaTaO₃ catalysts for efficient water splitting.* The Journal of Physical Chemistry B, 2003. **107**(51): p. 14383-14387.

80. Yamakata, A., T.-a. Ishibashi, and H. Onishi, *Water-and oxygen-induced decay kinetics of photogenerated electrons in TiO₂ and Pt/TiO₂: a time-resolved infrared absorption study.* The Journal of Physical Chemistry B, 2001. **105**(30): p. 7258-7262.

81. Fu, X., et al., *Photocatalytic reforming of biomass: A systematic study of hydrogen evolution from glucose solution.* International Journal of Hydrogen Energy, 2008. **33**(22): p. 6484-6491.

82. Jang, J.S., et al., *Optimization of CdS/TiO₂ nano-bulk composite photocatalysts for hydrogen production from Na₂S/Na₂SO₃ aqueous electrolyte solution under visible light (λ≥ 420 nm).* Journal of photochemistry and photobiology A: Chemistry, 2007. **188**(1): p. 112-119.

83. Sabatier, P., *Hydrogénations et déshydrogénations par catalyse.* Berichte der deutschen chemischen Gesellschaft, 1911. **44**(3): p. 1984-2001.

84. Trasatti, S., *Work function, electronegativity, and electrochemical behaviour of metals: III. Electrolytic hydrogen evolution in acid solutions.* Journal of Electroanalytical Chemistry and Interfacial Electrochemistry, 1972. **39**(1): p. 163-184.

85. Nørskov, J.K., et al., *Trends in the exchange current for hydrogen evolution.* Journal of The Electrochemical Society, 2005. **152**(3): p. J23-J26.

86. Sheng, W., et al., *Correlating the hydrogen evolution reaction activity in alkaline electrolytes with the hydrogen binding energy on monometallic surfaces.* Energy & Environmental Science, 2013. **6**(5): p. 1509-1512.

87. Bamwenda, G.R., et al., *Photoassisted hydrogen production from a water-ethanol solution: a comparison of activities of Au-TiO₂ and Pt-TiO₂.* Journal of Photochemistry and Photobiology A: Chemistry, 1995. **89**(2): p. 177-189.

88. Dong, H., et al., *Three-dimensional nitrogen-doped graphene supported molybdenum disulfide nanoparticles as an advanced catalyst for hydrogen evolution reaction.* Scientific reports, 2015. **5**: p. 17542.

89.   Lindgren, P., G. Kastlunger, and A.A. Peterson, *A Challenge to the G~0 Interpretation of Hydrogen Evolution.* ACS Catalysis, 2019. **10**: p. 121-128.

90.   Behar, D. and J. Rabani, *Kinetics of hydrogen production upon reduction of aqueous TiO₂ nanoparticles catalyzed by Pd⁰, Pt⁰, or Au⁰ coatings and an unusual hydrogen abstraction; steady state and pulse radiolysis study.* The Journal of Physical Chemistry B, 2006. **110**(17): p. 8750-8755.

91.   Fang, J., et al., *Mesoporous plasmonic Au–TiO₂ nanocomposites for efficient visible-light-driven photocatalytic water reduction.* International journal of hydrogen energy, 2012. **37**(23): p. 17853-17861.

92.   Nie, J., et al., *New insights into the surface plasmon resonance (SPR) driven photocatalytic H₂ production of Au–TiO₂.* RSC Advances, 2018. **8**(46): p. 25881-25887.

93.   Walter, M.G., et al., *Solar Water Splitting Cells.* Chemical Reviews, 2010. **110**(11): p. 6446-6473.

94.   Ohtani, B., *Photocatalysis A to Z—What we know and what we do not know in a scientific sense.* Journal of Photochemistry and Photobiology C: Photochemistry Reviews, 2010. **11**(4): p. 157-178.

95.   Ohtani, B., *Titania Photocatalysis beyond Recombination: A Critical Review.* Catalysts, 2013. **3**(4): p. 942-953.

96.   Takata, T., et al., *Fabrication of a Core–Shell-Type Photocatalyst via Photodeposition of Group IV and V Transition Metal Oxyhydroxides: An Effective Surface Modification Method for Overall Water Splitting.* Journal of the American Chemical Society, 2015. **137**(30): p. 9627-9634.

97.   Berto, T.F., et al., *Enabling Overall Water Splitting on Photocatalysts by CO-Covered Noble Metal Co-catalysts.* The Journal of Physical Chemistry Letters, 2016. **7**(21): p. 4358-4362.

98.   Chua, C.S., et al., *The effect of crystallinity on photocatalytic performance of Co₃O₄ water-splitting cocatalysts.* Physical Chemistry Chemical Physics, 2016. **18**(7): p. 5172-5178.

99.   Kay, A., I. Cesar, and M. Grätzel, *New Benchmark for Water Photooxidation by Nanostructured α-Fe₂O₃ Films.* Journal of the American Chemical Society, 2006. **128**(49): p. 15714-15721.

100.   Park, H., et al., *Photoinduced charge transfer processes in solar photocatalysis based on modified TiO₂.* Energy & Environmental Science, 2016. **9**(2): p. 411-433.

101.   Puga, A.V., *Photocatalytic production of hydrogen from biomass-derived feedstocks.* Coordination Chemistry Reviews, 2016. **315**: p. 1-66.

102.   Chen, X., et al., *Semiconductor-based Photocatalytic Hydrogen Generation.* Chemical Reviews, 2010. **110**(11): p. 6503-6570.

103.   Kandiel, T.A., I. Ivanova, and D.W. Bahnemann, *Long-term investigation of the photocatalytic hydrogen production on platinized TiO₂: an isotopic study.* Energy & Environmental Science, 2014. **7**(4): p. 1420-1425.

104.   Bahruji, H., et al., *Rutile TiO₂–Pd photocatalysts for hydrogen gas production from methanol reforming.* Topics in Catalysis, 2015. **58**(2-3): p. 70-76.

105.   Ismail, A.A., L. Robben, and D.W. Bahnemann, *Study of the efficiency of UV and visible-light photocatalytic oxidation of methanol on mesoporous RuO₂–TiO₂ nanocomposites.* ChemPhysChem, 2011. **12**(5): p. 982-991.

106.   Kawai, T. and T. Sakata, *Conversion of carbohydrate into hydrogen fuel by a photocatalytic process.* Nature, 1980. **286**(5772): p. 474.

107.   Sakata, T., T. Kawai, and K. Hashimoto, *Heterogeneous photocatalytic reactions of organic acids and water. New reaction paths besides the photo-Kolbe reaction.* The Journal of Physical Chemistry, 1984. **88**(11): p. 2344-2350.

108.   Hamid, S., et al., *Photocatalytic conversion of acetate into molecular hydrogen and hydrocarbons over Pt/TiO₂: pH dependent formation of Kolbe and Hofer-Moest products.* Journal of catalysis, 2017. **349**: p. 128-135.

109.   Hamid, S., *Stoichiometry of the photocatalytic fuel production by the reformation of aqueous acetic acid.* 2018, Hannover: Institutionelles Repositorium der Leibniz Universität Hannover.

110.   Hamid, S., R. Dillert, and D.W. Bahnemann, *Photocatalytic Reforming of Aqueous Acetic Acid into Molecular Hydrogen and Hydrocarbons over Co-catalyst-Loaded TiO₂: Shifting the Product Distribution.* The Journal of Physical Chemistry C, 2018. **122**(24): p. 12792-12809.

111.   Mulazzani, Q.G., et al., *Interaction of formate and oxalate ions with radiation-generated radicals in aqueous solution. Methylviologen as a mechanistic probe.* The Journal of Physical Chemistry, 1986. **90**(21): p. 5347-5352.

112.   Sato, S., et al., *In situ IR observation of surface species during the photocatalytic decomposition of acetic acid over TiO₂ films.* The Journal of Physical Chemistry B, 2002. **106**(35): p. 9054-9058.

113.   Li, Y., G. Lu, and S. Li, *Photocatalytic hydrogen generation and decomposition of oxalic acid over platinized TiO₂.* Applied Catalysis A: General, 2001. **214**(2): p. 179-185.

114.   Sun, Y., et al., *An Unexpected Fluctuating Reactivity for Odd and Even Carbon Numbers in the TiO₂-Based Photocatalytic Decarboxylation of C₂-C₆ Dicarboxylic Acids.* Chemistry–A European Journal, 2014. **20**(7): p. 1861-1870.

115.   Turchi, C.S. and D.F. Ollis, *Photocatalytic degradation of organic water contaminants: mechanisms involving hydroxyl radical attack.* Journal of catalysis, 1990. **122**(1): p. 178-192.

116.   Tritsaris, G.A., et al., *Dynamics of the photogenerated hole at the rutile TiO₂ (110)/water interface: A nonadiabatic simulation study.* The Journal of Physical Chemistry C, 2014. **118**(47): p. 27393-27401.

117.   Patel, M., et al., *Water adsorption on rutile TiO₂ (110) for applications in solar hydrogen production: A systematic hybrid-exchange density functional study.* Physical Review B, 2012. **86**(4): p. 045302.

118.   Imanishi, A., et al., *Mechanism of water photooxidation reaction at atomically flat TiO₂ (rutile)(110) and (100) surfaces: dependence on solution pH.* Journal of the American Chemical Society, 2007. **129**(37): p. 11569-11578.

119.   Montoya, J.F., et al., *Comprehensive kinetic and mechanistic analysis of TiO₂ photocatalytic reactions according to the direct–indirect model:(II) Experimental validation.* The Journal of Physical Chemistry C, 2014. **118**(26): p. 14276-14290.

120.   Montoya, J.F., J. Peral, and P. Salvador, *Comprehensive Kinetic and Mechanistic Analysis of TiO₂ Photocatalytic Reactions According to the Direct–Indirect Model:(I) Theoretical Approach.* The Journal of Physical Chemistry C, 2014. **118**(26): p. 14266-14275.

121.   Franch, M.I., et al., *Photocatalytic degradation of short-chain organic diacids.* Catalysis today, 2002. **76**(2-4): p. 221-233.

122.   Bowker, M., et al., *The photocatalytic window: photo-reforming of organics and water splitting for sustainable hydrogen production.* Catalysis Letters, 2015. **145**(1): p. 214-219.

123.   Bard, A.J. and J. Ketelaar, *Encyclopedia of Electrochemistry of the Elements.* Journal of The Electrochemical Society, 1974. **121**(6): p. 212C-212C.

124.   Li, Y., G. Lu, and S. Li, *Photocatalytic production of hydrogen in single component and mixture systems of electron donors and monitoring adsorption of donors by in situ infrared spectroscopy.* Chemosphere, 2003. **52**(5): p. 843-850.

125.   Mendive, C.B., et al., *Oxalic acid at the TiO₂/water interface under UV (A) illumination: Surface reaction mechanisms.* Journal of catalysis, 2015. **322**: p. 60-72.

126.   Miller, J. and J.C. Miller, *Statistics and chemometrics for analytical chemistry.* 2018: Pearson education.

127.   Kamat, P.V. and S. Jin, *Semiconductor Photocatalysis: "Tell Us the Complete Story!".* ACS Energy Letters, 2018. **3**(3): p. 622-623.

128.   AlSalka, Y., et al., *Understanding the degradation pathways of oxalic acid in different photocatalytic systems: Towards simultaneous photocatalytic hydrogen evolution.* Journal of Photochemistry and Photobiology A: Chemistry, 2018. **366**: p. 81-90.

Chapter Two: Co-catalyst-free Photocatalytic Hydrogen Evolution on TiO₂: Synthesis of Optimized Photocatalyst through Statistical Material Science

2.1. Foreword

This chapter contains the article "Co-catalyst-free Photocatalytic Hydrogen Evolution on TiO₂: Synthesis of Optimized Photocatalyst through Statistical Material Science" by Yamen AlSalka, Amer Hakki, Jenny Schneider, and Detlef W. Bahnemann. Reproduced with permission from Applied Catalysis B: Environmental (238, 2018, 422-433, DOI: 10.1016/j.apcatb.2018.07.045). Copyright 2018 Elsevier B.V.

2.2. Abstract

An active TiO₂ for co-catalyst-free photocatalytic hydrogen evolution was successfully synthesized employing a simple Evaporation-Induced Self-Assembly (EISA) method that was developed and optimized with the help of Design of Experiment (DoE) coupled with Full Factorial Design (FFD) methodology. Coupling DoE with FFD provides a statistical tool for optimizing the synthesis process while carrying out the smallest number of experiments. This tool builds a statistical framework to determine the significance of the studied factors, i.e., titanium-precursor type, surfactant type, and surfactant quantity, along with their potential interactions, as well as with their optimum levels. The choice of the titanium-precursor type is found to be the predominant factor affecting the efficiency of TiO₂ for hydrogen gas evolution. The interaction between the precursor type and the surfactant type is also statistically significant. The statistically optimized study identifies that combining F-108 amphiphilic block copolymers with titanium(III) chloride solution leads to TiO₂ exhibiting the highest photocatalytic efficiency for the generation of molecular hydrogen. The thus prepared TiO₂ shows relatively high photocatalytic hydrogen evolution rates (1.22 mmol.h^{-1}.g^{-1}) compared to the commercially available TiO₂ photocatalysts which are not active for hydrogen generation in the absence of a co-catalyst. Significant photocatalytic reforming of ethanol is achieved over the synthesized bare TiO₂ with the formation of acetaldehyde as the main by-product in the gas phase. This unexpected photocatalytic performance is mainly attributed to the shift of flat band potential towards more negative potentials as revealed from the characterization results in addition to the high density of charge carriers exhibiting longer lifetime shown by laser transient reflectance measurements. The latter showed the presence of a high number of trapped states, which are beneficial for the photocatalytic properties.

Keywords: Photocatalysis, Molecular hydrogen evolution, TiO₂, Design of Experiment, EISA.

2.3. Introduction

Clean energy systems are increasingly required to meet the growing global energy demand and to overcome the environmental problems of our modern society. Molecular hydrogen is considered to be one of the best fuels for the future. Hence, the photocatalytic generation of hydrogen using nanoparticle photocatalysts has attracted tremendous attention because of its potential production with reasonable cost as well as due to the involvement of green processes [1]. A photocatalytic reforming of organic compounds can simultaneously be performed during the generation of molecular hydrogen, which is considered as a considerable added value of this technique [2]. However, the lack of materials that could efficiently harvest solar light is still the main obstacle hindering the transformation of this technique into practical applications.

Although TiO$_2$ absorbs mainly in the UV region, it is widely used in various photocatalytic applications because of its high reactivity, nontoxicity, low cost, stability, and resistance to photocorrosion [2, 3]. The first hydrogen gas generation through the photoelectrocatalytic splitting of water was reported by Fujishima and Honda in 1972 [2, 4]. Since this time TiO$_2$ has been extensively studied in order to enhance its photo-response by harvesting a wider range of the solar spectrum. Generally, a large surface area and high crystallinity are highly important parameters affecting the activity of the catalysts [5]. The mesoporous structure is one of the characteristics that give good catalytic specifications to the materials, as it exhibits a large surface area and pore-channels that ensure great mass diffusion within its frameworks [6]. In addition, loading noble metals and doping either with ions or with non-metals have been extensively explored to shift the light absorption of TiO$_2$ towards the visible region and to lengthen the lifetime of the photogenerated charge carriers [7]. Recently, defective TiO$_2$ has shown an enhanced visible-light absorption and improved photocatalytic performance, which has been attributed to oxygen vacancies and to the introduction of trapped states below the conduction band of the semiconductor [8].

 Evaporation-induced self-assembly (EISA), was first reported by Ozin [9] and Brinker [10], and was considered as one of the synthesis methods used to obtain thin films of mesoporous TiO$_2$. This soft-templating method is characterized by its simplicity, and efficiency [11]. It possesses several advantages compared to conventional sol-gel methods, e.g., performing the preparation under relatively mild conditions [12]. EISA process starts by dissolving block copolymer surfactant in a suitable solvent followed by adding a calculated amount of titanium precursor(s) in acidic medium to form titania-surfactant hybrid phase. This phase contains terminal hydroxyl groups that interact through H-bonding with the hydrophilic portion of the block copolymer. An aging step takes place afterward to get a condensed titania network followed by a calcination step to remove the surfactant. The main drawback of preparing TiO$_2$ by EISA method is the uncontrolled hydrolysis and

condensation of Ti^{4+} leading to the formation of poorly structured materials [11]. Adding coordinating agents, like acetylacetone, chelates Ti cations by forming metal complexes, thereby reduce the effects of a nucleophilic attack from water and lower hydrolysis kinetics [13]. Hydrolysis can also be controlled by employing a water-alcohol mixture instead of water only as a solvent because alcohols possess relatively weaker nucleophilic behavior [14]. Many studies have been conducted to discover the effect of EISA process parameters on the final product. Crepaldi et *al.* [15] tested the influence of six variables on the preparation of TiO$_2$ films including the type of surfactant, the ratio of surfactant to precursor, the quantity of water in the reaction, the humidity, and the synthesis temperature. Among these variables, the humidity during synthesis had a remarkable effect on the structure of the material. Soler–Illia and Sanchez [16] found that titanium butoxide (TBT), titanium isopropoxide (TTIP), and titanium ethoxide (TET) possessed different reaction activities toward water, hence different hydrolysis behaviors. Yang et *al.* [17] reported the production of mesoporous metal oxides, including TiO$_2$, by using metal chloride salts and P-123 surfactant. Luo et *al.* [18] obtained different phases of TiO$_2$ by changing the surfactant and the solvent used with TiCl$_4$ as a precursor. A mixture of anatase and rutile, in addition to pure rutile phase, were synthesized by employing P-123 or F-127 as surfactants while varying the solvent (methanol, ethanol, 1-butanol and 1-octanol). By tuning the amount of TiCl$_4$ in the presence of P-123, highly ordered mesoporous TiO$_2$ photocatalysts were produced in mixed phase of anatase and rutile with different ratios [19]. Bosc et *al.* [20] synthesized mesoporous anatase TiO$_2$ films using titanium(IV) isopropoxide and tri-block copolymers (Pluronic P-123, F-127). On the other hand, Masolo et *al.* [5] evaluated the effect of different titanium precursors, the calcination rate, and different ligands on the synthesized mesoporous TiO$_2$ samples. These parameters influenced the morphology and the phase content of the final products. The ratio between rutile and anatase was related to the precursor's types and their proportions. They also found that acetylacetone resulting in a narrow pore size distribution, which played a major role in the photoactivity. The calcination rate had the less influence among the studied factors on both, the crystallinity and the mesoporosity of the material. On the other hand, removing the surfactant by thermal treatments was found to be a key step in EISA process. A calcination temperature below 400 °C is preferred to be used to remove most non-ionic triblock co-polymers, because under higher temperatures the mesopore structures tend to collapse [21, 22].

In spite of the successful studies conducted previously to prepare thin films of TiO$_2$ [5], unfortunately, only a few works are addressed to the synthesis of TiO$_2$ powder through EISA method. Moreover, in most precedent works, several parameters affecting the EISA process have been changed while ignoring other factors or neglecting real optimization procedures. Conducting systematic studies defining the most important factors affecting EISA technique is also missing or

not fully discussed. Furthermore, the use of limited types of titanium precursors, in particular, the difficult handled precursor TiCl$_4$, is a common characteristic among most previous studies.

To find the optimum conditions, most experiments are usually performed by changing the levels of one factor at a time in an unsystematic way. However, this process suffers from a lack of information concerning the optimum parameters once an interaction among the studied factors is carried out. This observation was confirmed by Fischer [23], who first introduced the principles of the Design of Experiments (DoE). DoE is a statistical tool used to conduct and to plan experiments in a methodological process allowing obtaining the maximum amount of information in the fewest number of runs. The design and analysis of experiments revolve around the understanding of the effects of different variables on other variables. The dependent variable is called the response, while the independent variables are called factors, and the experiments are run at different factor values, called levels. The total number of runs in DoE is equal to the number of levels "NL" powered to the number of factors "NF" (NL^{NF}). DoE provides a strict mathematical framework by changing all pertinent factors simultaneously, in order to achieve the optimization using the fewest experimental runs [24]. When DoE is coupled with a full factorial design (FFD), multiple factors are investigated simultaneously during the test. It is possible additionally to optimize the significant factors affecting the process, determine the influence of these factors on specified responses, and specify the possible interactions between them [25].

Due to the time required to establish any normal optimization process, in addition to the high costs of consuming chemicals, we decided to benefit from the advantages of DoE to optimize the production of TiO$_2$ *via* EISA method. Through the present work, DoE coupled with the analysis of variance (ANOVA) has been applied to discover, in a systematic statistical way, the effects of several factors on EISA method. The optimum values have been then identified through the same methodology and were applied to synthesis highly active TiO$_2$ in powder form. The influence of both, the type of titanium precursor(s) and their proportions in addition to the type and quantity of the surfactant are the main core of our investigations. The use of an easy-handled titanium precursor instead of TiCl$_4$ is further discussed in detail. The material synthesized based on the optimum parameters is then characterized and compared with the commercially available photocatalysts.

2.4. Materials and Methods

2.4.1. Raw materials

All chemicals were used as received without any further purification. Titanium(IV) chloride (≥99.0%), titanium(IV) butoxide (97%), triblock copolymers pluronics F-108 and P-123, and acetylacetone (≥99%) were purchased from Sigma-Aldrich. Titanium(III) chloride 15% in HCl 10% was purchased from Merck. Methanol (≥99.9%) and ethanol (≥99.8%) were purchased from Carl-

Roth. Deionized water was obtained from Millipore Mill-Q system at a resistivity of 18.2 MΩ.cm at 25°C.

2.4.2. Preparation method

The Evaporation-Induced Self-Assembly (EISA) method was employed to prepare TiO$_2$ samples [26, 27]. In a typical synthesis, 1 g of triblock copolymer surfactant (either F-108 or P-123) was dissolved in 20 mL of ethanol under vigorous stirring followed by the addition of 1 mL of acetylacetone. Then, the calculated amounts of titanium precursor(s) were added with continuous stirring at room temperature for 2 h. The mixture was then transferred to a petri dish and heat-treated at 40°C for 24 h followed by calcination at 400°C for 12 h (at a heating rate of 4°C/min).

2.4.3. Statistical evaluation of significant factors using design of experiment (DoE)

DoE analysis was performed using Weibull ++/ALTA PRO software from Reliasoft. A general Full Factorial Design (FFD) of 16 runs was built to investigate the effects of three factors on the prepared materials: titanium-precursor type (PT), surfactant type (ST), and surfactant quantity (SQ). The photocatalytic evolution of hydrogen gas and the BET surface area were chosen as the responses to be monitored. Experimental runs were conducted in duplicate and in random order to reduce error. Generally, when all of the factors are quantitative, an alternative to replicating the combinations in the model is to apply a center point of the design and perform replicate runs at this center point. Such a procedure can improve the precision of estimates for factorial effects and provides a check on the linearity of the factor effects [28]. However, because two of the input factors, i.e. PT and ST, are qualitative factors, center point experiments are not implemented in the present study. The treatment of results was based then on the analysis of variance ANOVA using partial sum squares and 5% level of significance. Table 2-1 illustrates the FFD summary with all related variables. TiCl$_4$:Ti(OBu)$_4$ in a molar ration of (0.4:0.6) was first chosen as a precursor, to obtain TiO$_2$ in pure anatase phase, as reported in literature [26]. TiCl$_4$ was then replaced by TiCl$_3$ and mixed with Ti(OBu)$_4$ while keeping the same used molar ratio between them. Two types of triblock copolymers "surfactants", i.e., P-123 (PEO$_{19}$-PPO$_{69}$-PEO$_{19}$) and F-108 (PEO$_{132}$-PPO$_{50}$-PEO$_{132}$) were chosen because of the difference in their blocks. P-123 with 69 PPO units has a significantly lower critical micelle concentration (cmc) and lower hydrophilic-lipophilic balance value (HLB) than F-108 with 50 PPO units [29, 30].

Table 2-1 Summary of full factorial design with 3 factors in 2 levels.

Fct.	Level 1	Level 2	Resp.1	Resp.2
PT [a]	$TiCl_4:Ti(OBu)_4$	$TiCl_3:Ti(OBu)_4$	H$_2$ rate	S$_{BET}$ [d]
ST [b]	F-108	P-123	$\mu mol.h^{-1}.g^{-1}$	$m^2.g^{-1}$
SQ [c]	1 g	2 g	$\mu mol.h^{-1}.g^{-1}$	$m^2.g^{-1}$

[a] Titanium-precursor type (PT), [b] Surfactant type (ST), [c] Surfactant quantity (SQ), [d] BET surface area (S$_{BET}$)

2.4.4. Characterization

The X-ray powder diffraction (XRD) measurements were performed on a Bruker DB Advance diffractometer (Bruker AXS GmbH) with a Bragg-Brentano geometry using Cu Kα radiation. The average crystallite sizes (D) were calculated according to Scherrer's formula shown in Eq. (2-1), where K = 0.94 is Scherrer constant, λ = 0.154 nm is the x-ray wavelength of the CuKα, β is the full width of the peak measured at half maximum intensity, and θ is the Bragg's angle of the peak.

$$D = \frac{K.\lambda}{\beta.\cos\theta} \qquad\qquad (2-1)$$

The optical properties of powders were measured by recording the diffuse reflectance spectra in the range of 300–800 nm. Varian Cary 100 Bio UV/VIS spectrophotometer equipped with an integrating sphere diffusing reflectance accessory was used along with $BaSO_4$ as reference material. The measured reflectance data R were transformed to the Kubelka-Munk function f(R) [31] to determine the value of the bandgap *via* the Tauc plot.

Flat-band potential E_{fb} and the density of charge carriers (ND) were estimated by Mott–Schottky (M–S) relationship. Thin Titania films were deposited on FTO by the same EISA process utilized in this work. (M-S) measurements were conducted in a three-electrode electrochemical cell filled with KCl 0.1 mol l^{-1} at (pH 7) using IviumStat potentiostat at three different frequencies (1, 10 and 100 KHz).

Field-Emission Scanning Electron Microscopy (FE-SEM) and Energy-Dispersive X-ray Spectroscopy (EDX) measurements were carried out on a JEOL JSM-6700F field emission instrument using a secondary electron detector (SE) at an accelerating voltage of 20 kV. High-Resolution Transmission Electron Microscopy (HR-TEM) measurements were performed using Tecnai G2 F20 TMP (FEI) with an acceleration voltage of 200 kV field emission gun (FEG).

BET surface area was measured by the single-point standard Micromeritics FlowSorb II 2300 instrument equipped with a Micromeritics AutoMate 23. Adsorption/desorption isotherms were recorded using the Autosorb-iQ automated gas sorption analyzer (Quantachrome) equipped with ASiQwin data software.

2.4.5. Transient Reflectance Spectroscopy

Nanosecond diffuse reflectance laser flash photolysis spectroscopic measurements were performed as described by Schneider et *al.* [32], where the excitation of powder in a flat quartz cuvette was proceeding with a 6 ns UV-laser at 355 nm. A pulsed xenon lamp (Osram XBO; 150 W) equipped with a cut-off filter (400 nm) is focused onto the samples and the reflected light was detected between 750 and 425 nm (in 25 nm steps) by Hamamatsu PMT R928 detector. Before the analysis, each powder sample was flushed with nitrogen gas for 30 min. A terminal resistance of 50 Ω was used to facilitate a short rise time and fast observation of the signal after 40 ns, i.e., the period after which the signals related to the charge carrier were analyzed [33]. For easier processing and fitting of the transient signals, the optical reflectance changes ΔJ of the powder samples were calculated from the absorbance values as shown in Eq. (2-2), where I_0 and I are the reflected lights before and after the laser excitation, respectively.

$$\Delta J = 1 - 10^{-Abs} = \frac{I_0 - I}{I_0} \qquad (2-2)$$

2.4.6. Photocatalytic hydrogen gas evolution

The experiments of the photocatalytic evolution of hydrogen gas were carried out in a batch photocatalytic system. All experiments were performed in 10 ml crimp glass vials tightly closed with crimp cap and silicon septum. In a typical experiment, 10 mg of the photocatalyst powder was suspended into a 6 ml aqueous solution containing 4.28 mol l^{-1} of hole-scavenger (typically ethanol). All the photocatalysts were introduced following the calcination procedure to insure the decomposition of any organic surfactant. In addition, a separate photocatalytic baseline experiment has been done, in which no surfactant was used during the synthesis procedure. After purging with pure argon (>99.999%) for 15 min, the vials were horizontally fixed inside an orbital shaker placed at 30 cm distance below a 1000 W xenon lamp (Hönle UV Technology, Sol 1200) as a simulated solar light. From the measurement of the spectral irradiance in the wavelength range between 350 nm and 380 nm at the irradiated area, the photon flux was found to be I_0= 383 x 10^{-6} mol m^{-2} s^{-1}. Ignoring loss of light due to reflecting and scattering out, 1.42 x 10^{-7} mole of photons are entering the irradiated suspension per second.

The photocatalytically evolved molecular hydrogen was quantitatively determined by means of GC. For this purpose, a 50 µL gas sample was periodically taken from the headspace over the suspension using a Valco gas-tight sampling syringe equipped with a push-button valve. The gas sample was then injected into the injection port of a Shimadzu GC-8A, equipped with a TCD detector and a stainless-steel molecular sieve 5A GC column (Sigma-Aldrich). The column temperature was fixed at 80°C, while the temperatures of both, the injector and the TCD detector were maintained at 120°C. The general relative standard deviation (RSD) of the set of data ranged between 4.8 % and 6.5 % depending on the sample, where each photocatalytic test was repeated in triplicate, each in a separate reaction vial.

Acetaldehyde was also analyzed in the gas phase over the reaction mixture by head-space/GC-MS technique using GCMS-QP5000 (Schimadzu) coupled with AOC-5000 Plus head-space autosampler. A capillary RTX-Wax column (30 m x 0.32 mm, dF= 0.25 μm; Restek) was used employing parameters applied by Cordell et *al.* [34]. High-Performance Ion Chromatography (HPIC) was used to detect the products of ethanol conversion in the liquid phase. HPIC analysis was performed using a Dionex ICS-1000 with a conductivity detector and an electro-regenerator suppressor. The eluent of 9×10^{-3} mol l^{-1} of sodium carbonate was pressed through an Ion pac As9-HC 2 x 50 mm column.

2.5. Results and discussion

2.5.1. A statistical study of the factors affecting the synthesis of TiO₂

As mentioned previously, DoE suggested a design of (2^3) runs built automatically according to the studied factors. Conducting just 8 runs in duplicate, with a total of 16 runs, is found to be very convenient and quick to explore the effects of the studied factors. This feature in decreasing the number of experiments would undoubtedly reduce the errors and save time. Table 2-S1 shows the values of both responses that introduced in FFD design, which are the BET surface area and the evolved hydrogen gas. Upon changing the levels of the employed factors, the BET surface area deviated over a very small range (106 – 123 m^2 g^{-1}) in contrast to the photocatalytic evolution of hydrogen that underwent huge variations (425 - 999 µmol h^{-1} g^{-1}). These observations obviously confirm that the photocatalytic activities are significantly affected by changing the levels of the studied factors. Because the same changing in factors has a much smaller effect on the BET surface area, it suggests that the correlation between the photocatalytic activity and the surface area is less than expected. However, the photocatalytic hydrogen gas evolution was approximately decreased to half when the surfactant had been excluded during the synthesis procedure. This could be related to the decrease of the BET surface area.

The analysis of variance (ANOVA) is provided in Tables 2-2 and Table 2-S2. The goodness-of-fit statistics mentioned in these tables could be used to determine how well the model fits the data. Standard deviation values (S) of 17 and 0.7 indicate that the standard deviations between the experimental data points and the fitted values are approximately 17 µmol h^{-1} g^{-1} and 0.7 m^2 g^{-1} for the hydrogen evolution and the BET surface area, respectively. However, such low S values by themselves do not indicate that the model meets the model assumptions. The coefficient of determination R^2 is a statistical measure of how close the data are to the fitted regression line. It could be used to determine how well the model fits the data, hence measure the goodness-of-fit. The calculated values of R^2 and adjusted R^2 are more than 98.8%, which means that both regression modes account for more than 98.8% of the variance. In general, the more variance that is accounted for by the regression model the closer the data points will fall to the fitted regression line. With such high values, the regression models show very good variability and validity [35].

Table 2-2 The factors and their interaction effects on the photocatalytic hydrogen evolution (ANOVA results) in FFD.

Variation	D.F.	Sum of Squares	Mean Squares	F Ratio	P Value [a]
Model	7	6.20E+05	8.86E+04	3.05E+02	4.53E-09
PT	1	4.95E+05	4.95E+05	1.70E+03	1.30E-10
ST	1	1.15E+05	1.15E+05	3.94E+02	4.30E-08
SQ	1	6.03E+03	6.03E+03	2.08E+01	1.86E-03
PT • ST	1	3.96E+03	3.96E+03	1.36E+01	6.13E-03
PT • SQ	1	9.41E+01	9.41E+01	3.24E-01	5.85E-01
ST • SQ	1	4.10E+01	4.10E+01	1.41E-01	7.17E-01
PT • ST • SQ	1	5.40E+01	5.40E+01	1.86E-01	6.78E-01
Residual	8	2.32E+03	2.91E+02		
Pure Error	8	2.32E+03	2.91E+02		
Total	15	6.23E+05			

^{a} α = 0.05, S = 17.04, R^2 = 99.63%, R^2(adj) = 99.30%.

ANOVA results revealed that each of the studied three factors is statistically significant on both responses. This can be seen from a P value below the level of significance (α=0.05). "PT" exhibits a P value of 1.3E-10, which is the lowest P value among the whole design of the hydrogen evolution response (see Table 2-2). Titanium-precursor type, therefore, possesses the highest statistical

impact on this response. On the other hand, with its lowest value of P = 5.2E-10 (see Table 2-S2), the surfactant type "ST" is statistically the most intense factor affecting the BET surface area. However, because all the studied factors possess lower P values than the level of significance, all these factors affect statistically both responses but in different magnitudes. The rank ordering of the statistically significant factors can also be discovered from the Pareto charts provided in Figure 2-1.
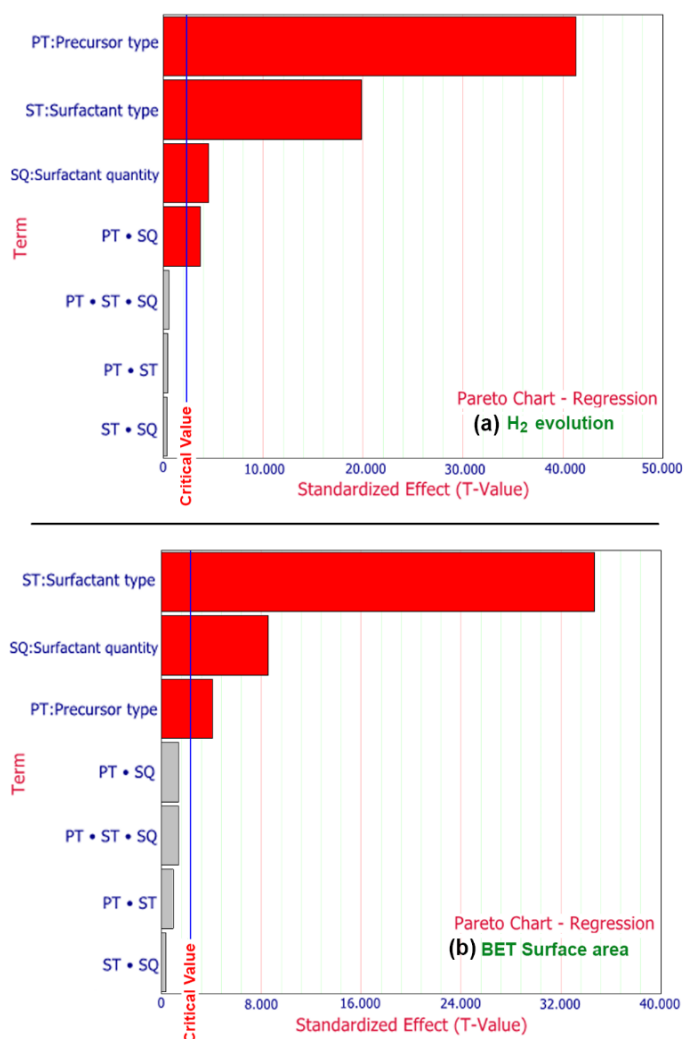
Figure 2-1 Pareto Charts delivered from Full Factorial Design and ANOVA test for hydrogen evolution (a) and BET surface area (b).

Pareto chart can be used to determine the magnitude and the importance of the effects. This chart plots a reference line to indicate which effects are statistically significant. On the Pareto chart, bars that cross the reference line are statistically significant at the 0.05 level with the current model terms. Figure 2-1 shows again that titanium-precursor type (PT) is the predominant factor affecting the hydrogen evolution followed by the effect of surfactant type. On the other hand, the surfactant type (ST) is the predominant factor affecting the surface area followed by the effect of surfactant

quantity. However, with a T-value more than 40, PT shows the most intense impact among all the studied factors. Because the Pareto chart displays the absolute value of the effects, it is able to determine which effects are larger without determining which effects increase or decrease the response. The normal probability plot of the standardized effects can be therefore used to examine the magnitude, direction and the importance of the effects on one plot. In the plots presented in Figure 2-2, effects that are further from 0 are statistically significant with greater magnitude. In the agreement with the previously mentioned conclusion, all the studied factors are statistically significant at the 0.05 level, since the colour and shape of the points differ between statistically significant (red squares), and statistically insignificant effects (blue circles). In addition, positive standardized effects increase the response when the settings change from the low value of the factor to the high value. In the case of the hydrogen evolution response, the precursor type has a positive standardized effect (see Figure 2-2 (a)). Hence, the high level of this factor, which is TiCl$_3$-based precursor, increases the hydrogen evolution. Surfactant type and surfactant quantity have in contrast negative standardized effects. Consequently, using the low levels of these factors, which are F-108 and 1 g, increases the hydrogen evolution as well. Similarly, the BET surface area increases (see Figure 2-2 (b)) when TiCl$_4$-based precursor and F-108 were used, as they are the low values of each factor (negative standardized effects). The standard deviation for BET measurement is determined to be SD = 0.61 for the sample synthesized using (TiCl$_3$:TiBu(OH)$_4$ and 1g of F-108), with a corresponding coefficient of variation of COV = 0.52 %. On the other hand, the coefficient of variation of all the 16 BET measurements is calculated to be COV = 5.69 %.

The interaction of the studied factors shown in Pareto chart and the interaction matrix plots (see Figure 2-3) was statistically insignificant in terms of BET surface area, which means that the deference in precursor type is independent of the surfactant type or its quantity and vice versa. On the other hand, the interaction between precursor type and surfactant type was the only statistically significant interaction affected the photocatalytic hydrogen evolution as observed from its P value. The interaction plots could be used to show how the relationship between one factor (e.g. PT) and a response (e.g. H$_2$ evolution) depends on the value of a second factor (e.g ST). It plots the means for each level of a factor while the level of a second factor held constant. Interaction is present when the lines are not parallel to each other. This could be slightly noticed in the case of the interaction between PT and ST shown in Figure 2-3. A plot of the response (H$_2$ evolution) of precursor type "PT" at different levels of surfactant type "ST" shows that the response is changed with the levels of PT, but the effect of PT on the response could also depend on the level of ST.
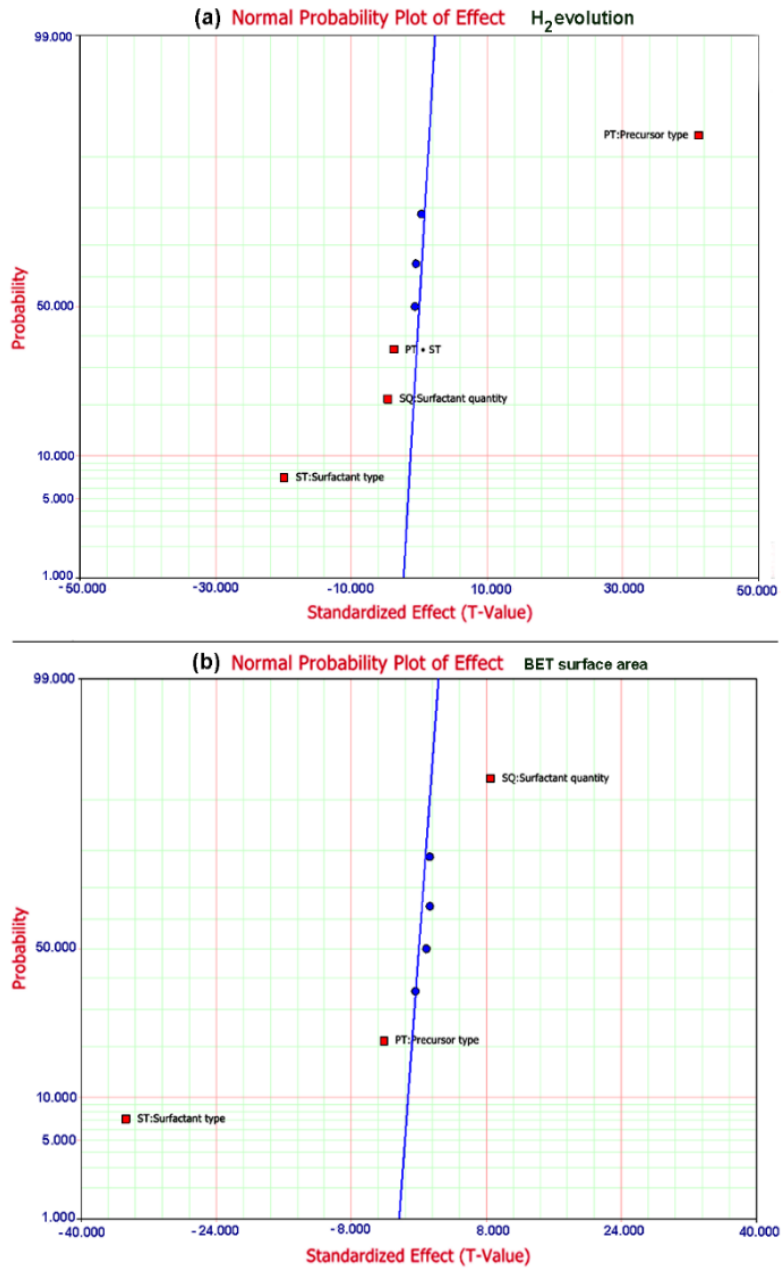
Figure 2-2 The normal probability plots delivered from ANOVA analysis showing the magnitude, direction and the importance of the effects on the hydrogen evolution (a) and the BET surface area (b).
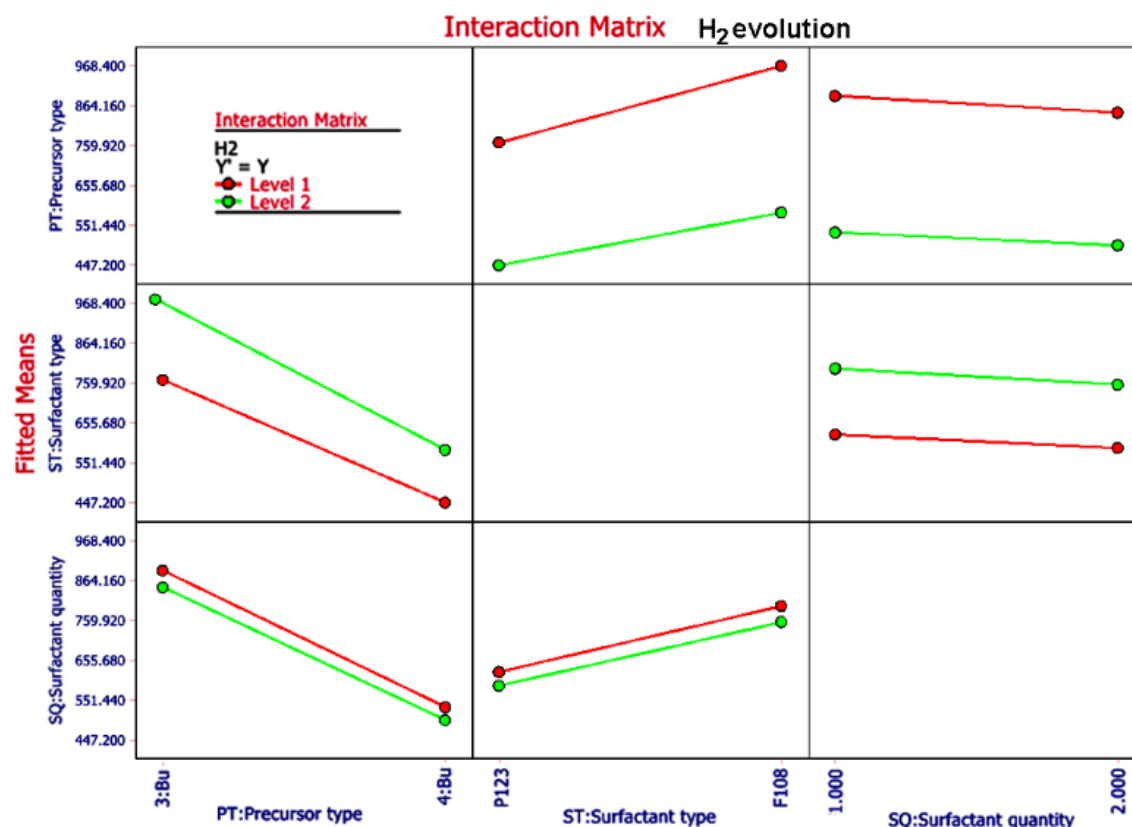
Figure 2-3 The interaction matrix delivered from ANOVA analysis related to the hydrogen evolution response.

In this instance, the photocatalytic hydrogen evolution is always higher when using a TiCl$_3$-based precursor rather than a TiCl$_4$-based precursor for TiO$_2$ synthesis as clearly shown in the term effect plot presented in Figure 2-4 (a). When the line of the term-effect plot is not horizontal, different levels of the factor affect the response differently. Figure 2-4 (a) indicates a higher evolution of hydrogen gas when F-108 rather than F-127 is used as a templating surfactant. On the other hand, the photocatalysts synthesized employing F-108 shows the highest BET surface area values, which could be related to the higher ratio of the hydrophobic PEO block resulting in higher numbers of smaller hydrophobic cores in the surfactant micelles [36]. Interestingly, while the surface area was slightly increased by increasing the amount of surfactant, the molecular hydrogen evolution was slightly decreased. However, the less horizontal the line in the term-effect plot, the greater the likelihood that the effect is statistically significant. Therefore, the effect of surfactant amount could be considered as relatively negligible; consequently, the use of less amount of surfactant will result in the same activity but lower costs.
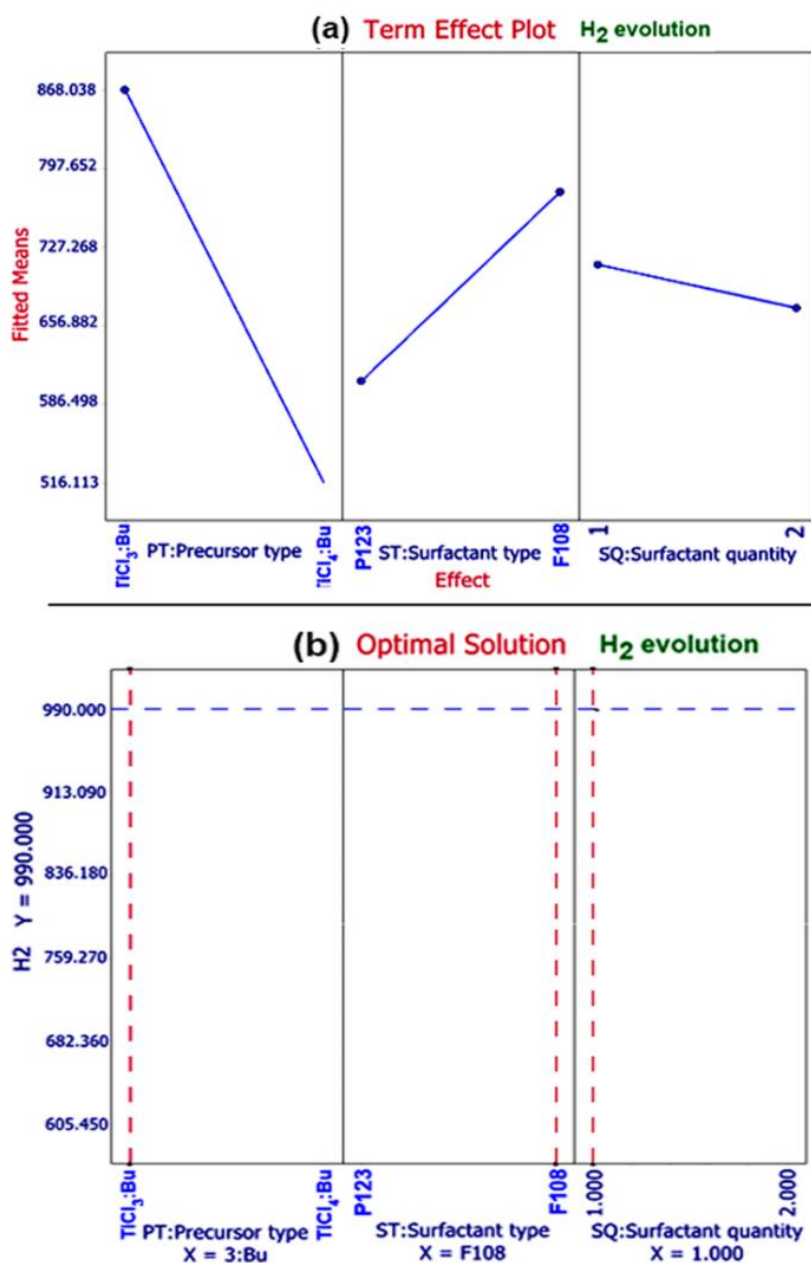
Figure 2-4 The term effect plot for the hydrogen evolution based on the statistical tests (a), and the optimal solution towards maximizing hydrogen based on ANOVA result.

Considering the previous statistical study, and based on the ANOVA outcomes, the optimization features of DoE were successfully utilized to identify the statistical optimization of factors. Figure 2-4 (b) presents the computed optimized conditions towards maximizing the photocatalytic hydrogen gas evolution. According to this figure, using TiCl$_3$ based-precursor is preferable over TiCl$_4$. To conclude this part, the optimal solution that is used for the next optimizing step contains TiCl$_3$:Ti(OBu)$_4$ as a precursor and 1 g of F-108 as a surfactant.

2.5.2. Optimizing the ratio between TiCl$_3$ and Ti(OBu)$_4$

Since the TiCl$_3$-based precursor was the crucial factor positively affecting the hydrogen evolution as shown previously, the molar ratio between TiCl$_3$ and Ti(OBu)$_4$ was further optimized to reach the highest rate of hydrogen. This optimization was excluded from the previous DoE study because changing the molar ratio could affect several variables such as TiO$_2$ phases, the optical absorbance and the crystalline size [26]. These changes could affect in turn the photocatalytic activity; therefore, the responses could not be directly related to the studied factor. The experiments with different molar ratios of TiCl$_3$/Ti(OBu)$_4$ were conducted while fixing the total amount of titanium to (11.4×10^{-3} mol) and utilizing 1 g of F-108 as a surfactant.

Table 2-3 shows photocatalytic activities of the obtained samples compared to the commercial photocatalyst UV100 and P25 photocatalysts. Interestingly, all the self-prepared materials were able to generate molecular hydrogen from ethanolic-aqueous solutions even in the absence of any co-catalyst. Table 2-3 highlights the strong dependence of the photocatalytic evolution of hydrogen on the quantity of TiCl$_3$ in the precursor. The photonic efficiencies (ξ) for the hydrogen evolution reaction have been calculated according to Eqs. (2-3 and 2-4) [37], and the results are presented in Table 2-3.

$$\xi\,(\%) = \frac{\text{formation rate (mol.}\,s^{-1})}{\text{photon flux (mol.}\,m^2.\,s^{-1})}\;x\;100 \;=\; \frac{V.\Delta c}{I_0.\,A.\,\Delta t}\;x\;100 \qquad (2-3)$$

$$I_0 = \frac{I.\lambda}{N_A.\,h.\,c} \qquad\qquad\qquad\qquad (2-4)$$

where V is the suspension volume (0.006 l), $\Delta c/\Delta t$ is the formation rate (mol.s^{-1}), A is the illuminated area (4.2 x 10^{-4} m^2), I is the light intensity (W.m^{-2}), λ is the corresponding wavelength (m), N_A is the Avogadro's constant (6.02 x 10^{23} mol^{-1}), h is the Planck constant (6.63 x 10^{-34} W.s^2) and c is the velocity of light (3 x 10^8 m.s^{-1}). According to the results presented in Table 2-3, TiCl$_3$ as a single precursor provides positive advantages for the EISA method to synthesize active TiO$_2$ material in powder form. TiCl$_3$ seems to be the ideal precursor among the other tested precursors as it is an easily handled solution that leads to the formation of bare TiO$_2$ with approximately 1.5-fold higher photonic efficiency in comparison to other prepared materials. The use of TiCl$_3$ as a precursor provides as well the simplicity and the reliability of the EISA method because it eliminates the employing of alkoxides, which could negatively affect the final product.

Table 2-3 Synthesis parameters with the photocatalytic activities of the different self-prepared materials in comparison with the commercially available photocatalysts.

#	$TiCl_3$:$Ti(OBu)_4$	H_2 μmol h^{-1} g^{-1}	ξ ^{a} %
S1	0.2:0.8	796.8 $\pm$ 38.1	1.5
S2	0.4:0.6	953.4 $\pm$ 46.8	1.9
S3	0.6:0.4	574.2 $\pm$ 37.2	1.1
S4	0.8:0.2	669.9 $\pm$ 40.4	1.3
S5	1:0	1221.6 $\pm$ 58.1	2.4
UV100		ND ^{b}	-
P25		ND ^{b}	-

^{a} Photonic efficiency (ξ) calculated for the mean H_2 rate, and ^{b} Not detected (ND) after 2 hours of illumination according to the limits of detection (0.4 μmol for H_2) of the GC analysis.

2.5.3. The photocatalytic application over the optimized (S5) material

The photocatalytic activity was followed-up by the determination of molecular hydrogen and acetaldehyde formed in the gas phase in addition to the carboxylic acids formed in the liquid phase. The data were collected after two hours of irradiating an ethanolic aqueous suspension. Table 2-4 illustrates the huge differences in photocatalytic activities between the optimized photocatalyst (S5) and the UV100. Molecular hydrogen is only detected over S5, which is possessing much higher photocatalytic activity towards the conversion of ethanol. According to the literature, the surface defects serve additionally as adsorption sites to transfer the charge carriers to the adsorbed species, thus promoting the photocatalytic reaction [38, 39]. Around 7.1 mmol of ethanol (28% of the initial concentration) were decreased over S5 compared to 5.9 mmol (23.3%) over UV100. It is worth mentioning that these values include both, the amount converted of ethanol as well as the amount adsorbed on TiO_2. This indicates the higher photocatalytic activity of the prepared material because it exhibits around 2.4-fold lower surface area than UV100. The conversion of ethanol was accompanied by the formation of acetaldehyde and molecular hydrogen following the Eqs. (2-5 and 2-6), respectively [40].

$$CH_3CH_2OH + 2h_{VB}^+ \rightarrow CH_3CHO + 2H^+ \tag{2-5}$$

$$2H^+ + 2e_{CB}^- \rightarrow H_2 \tag{2-6}$$

Where h_{VB}^+ and e_{CB}^- represent the holes and electrons, respectively, generated on the photocatalysts by light absorption.

It is well known that hydroxyl radicals ($^{\bullet}OH$) can react with ethanol, mainly through the abstraction of a hydrogen atom from the C–H bond (Eq. 2-7). This step is followed by the formation of acetaldehyde (Eq. 2-8) that is the principal stable product through the electron injection into the conduction band of TiO_2, a process called "current doubling" [41]. The current doubling mechanism occurs when using any alcohol carrying a hydrogen atom at the carbon atom in the α-position to its hydroxyl group [42]. Ethanol was transferred over S5 to produce 0.43 mmol of acetaldehyde as the major by-product after 2 hours of illumination. The quantity of acetaldehyde was 10-folds higher over S5 than in the case of UV100. Simultaneously, 0.023 mmol of molecular hydrogen and traces of acetic acid (Eq. 2-9) were formed over S5 compared to undetectable amounts of these products over Hombikat UV100.

$$CH_3CH_2OH + {}^{\bullet}OH \rightarrow CH_3{}^{\bullet}CHOH + H_2O \qquad (2\text{-}7)$$

$$CH_3{}^{\bullet}CHOH + h_{VB}^+ \rightarrow CH_3CHO + H^+ \qquad (2\text{-}8)$$

$$CH_3CHO + H_2O + 2h_{VB}^+ \rightarrow CH_3COOH + 2H^+ \qquad (2\text{-}9)$$
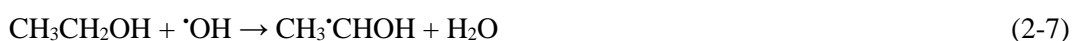
Using Eqs. 2-3 and 2-4, the photonic efficiencies of the formed products were calculated and listed in Table 2-4. The superior band structure of S5 has definitely a positive impact. This includes the more negative potential of its flat band edge beside the higher charge carrier density. The improvement of TiO_2 conductivity enhances the charge carrier transport from the bulk to the surface and the charge-transfer reaction [43]. Furthermore, the broad distribution of trapped states at different energetic depths, besides the better separation between the charge carriers could be the main reason for such higher photocatalytic activity. Although the conversion of ethanol to acetaldehyde and molecular hydrogen was more efficient over our sample (S5), however, the amount of molecular hydrogen evolved over S5 was 18-folds lower than the amount formed of acetaldehyde.

Table 2-4 The photocatalytic activities of S5 and UV100 after 120 min of irradiation under simulated solar light.

#	Ethanol mmol	C_2H_4O mmol	ξ acetaldehyde %	Acetic acid mmol	ξ acetic acid %	H_2 mmol	ξH_2 %
Initial	25.32	-	-	-	-	-	-
Photolysis	25.09	ND [a]	NA [b]	ND [a]	NA [b]	ND [a]	NA [b]
UV100	19.40	0.04.2	4.10	ND [a]	NA [b]	ND [a]	NA [b]
S5	18.24	0.430	42.1	4.9×10^{-6}	4.8×10^{-4}	0.023	2.20

[a] Not detected (ND), [b] Not applicable (NA)

In order to investigate in more detail, the enhancement in the photocatalytic activity over the S5 sample, long-term experiments were conducted either under the full solar spectrum or in the presence of a cut-off filter $\geq$ 420 nm. Using the same photocatalytic system, the hydrogen evolution was followed-up in 60 min intervals. S5 showed again much better photocatalytic activity even under visible light conditions. Figure 2-5 illustrates the photocatalytic behavior of S5 against the time. Molecular hydrogen was produced during the first 60 min under simulated solar irradiation and possessed linear increasing until 360 min, then the evolution followed a second linear increase but at a lower rate. However, the evolution of hydrogen was detected after 120 min under visible light and reached a 10-fold lower amount at the end of the 600 min irradiation comparing the full solar light experiment. Several conversion products have been previously reported upon the photoreforming of ethanol over Au/TiO$_2$ including acetaldehyde, acetic acid, acetone, ethene, ethylene and methane [40, 44, 45]. Our GC-MS analysis detected traces of methane, ethylene and carbon monoxide in the gas phase; hence, the formation of such compounds could negatively affect the evolution of molecular hydrogen, as some of them are undesirable and or could not involve in the current doubling effect. UV100, on the other hand, showed inactivity during the first 460 min before the evolution of a relatively neglected amount of hydrogen gas over the rest period.

These results from the photocatalytic experiments suggested that detailed structural and optical characterizations for the prepared samples are needed.
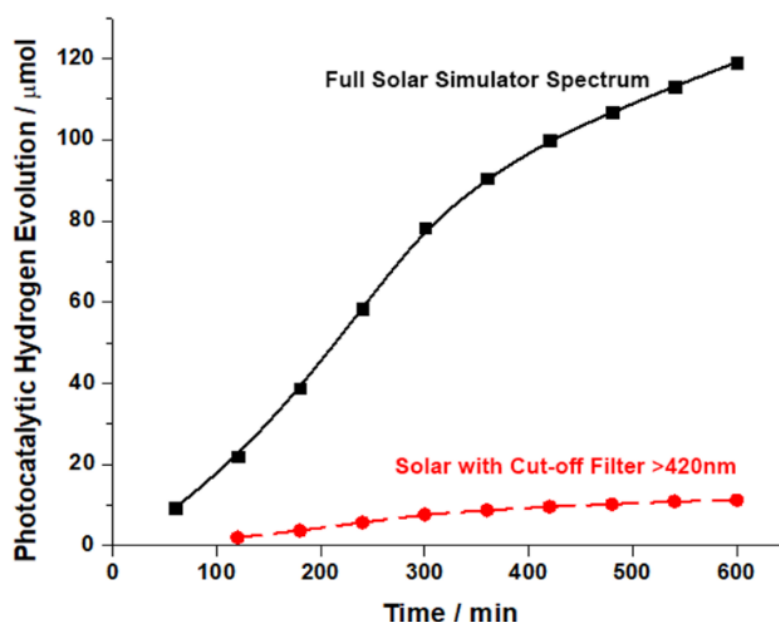
Figure 2-5 long-term photocatalytic hydrogen evolution from ethanoic solution over S5 under the full solar spectrum, and in the presence of a cut-off filter of 420 nm.

2.5.4. Physical and chemical characterization of the synthesized materials:

XRD measurements along with the standard pattern of both, pure anatase (Natl. Bur. Stand. # 00-021-1272) and pure rutile (Natl. Bur. Stand. # 00-021-1276) are demonstrated in Figure 2-6. By comparing the XRD patterns of pure anatase and rutile to those of samples synthesized using TiCl$_3$ with mole fractions of 0.6 and 0.8, one can clearly see the formation of mixed phases with different ratios of anatase and rutile. All the other samples exhibit only the XRD pattern of pure anatase. Data in Table 2-5 clearly confirm the crucial role of the crystalline phase, since materials having a pure anatase phase exhibited better photocatalytic activities. The photocatalytic hydrogen evolution was dramatically dropped down in in the mixed-phase samples. This correlates with other reported results showing a higher hydrogen production for anatase-based TiO$_2$ photocatalysts due to the more negative potential of the conduction band edge and the presence of trapped states lying below its Fermi level [46]. On the other hand, many other researchers found a huge benefit of mixed-phase TiO$_2$ due to the synergistic effect of anatase and rutile [47, 48].
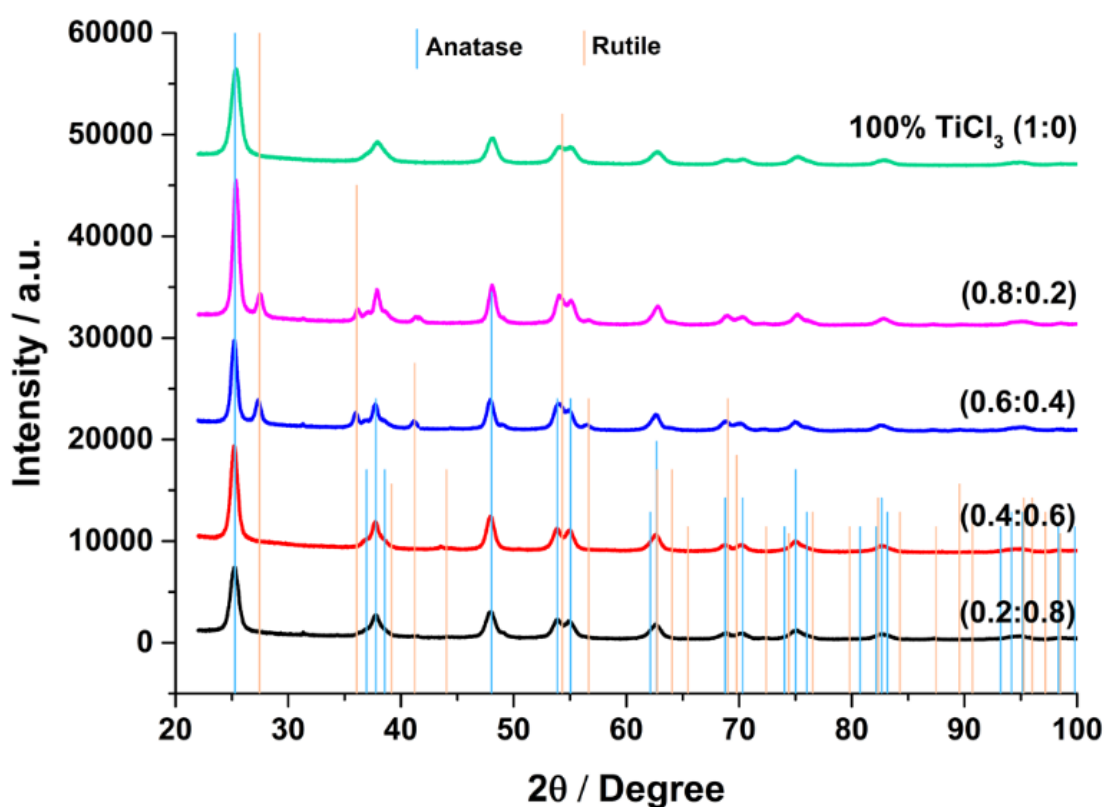
Figure 2-6 XRD patterns of the self-prepared photocatalysts compared to the standard patterns of anatase and rutile.

Table 2-5 Synthesis parameters with the physiochemical and optical properties of the different prepared materials.

#	$TiCl_3$:$Ti(OBu)_4$	S_{BET} [a] $m^2\,g^{-1}$	A:R [b] %	D [c] (anatase) nm	E_g [d] eV
S1	0.2:0.8	116.1 ± 0.9	100	9.6	3.10
S2	0.4:0.6	117.7 ± 0.6	100	11.4	3.08
S3	0.6:0.4	104.7 ± 0.6	78	13.6	2.97
S4	0.8:0.2	107.3 ± 0.7	86	13.2	2.98
S5	1:0	121.3 ± 0.9	100	9.1	2.99
UV100		289.5 ± 1.4	100	7.4	3.20
P25		49.1 ± 0.4	72	21.5	3.05

[a] BET surface area (S_{BET}), [b] Anatase to rutile ratio (A:R) according to XRD measurements, [c] Crystalline size (D) calculated from the XRD data, [d] Energy band gap (E_g) calculated from UV-VIS data and the Tauc plots.

SEM images presented in Figure 2-S1 for the material prepared from (100% $TiCl_3$) show nanocrystalline spherical morphology for agglomerated nano-sized particles with a diameter of about 500 nm and wide distribution of non-ordered pores throughout the aggregated particles. On the other hand, a grain size ranging from 9 to 15 nm for nanoscale powder with many crystal lattice planes and a good crystallinity is estimated from TEM and high-resolution TEM images presented in Figure 2-S2 (a) and (b), respectively. An apparent correlation between the hydrogen evolution and the surface area is clearly noticed among the prepared materials as illustrated in Figure 2-7. The increase in the surface area from 105 to 121 $m^2\,g^{-1}$ leads to a 2.5-fold enhancement of the molecular hydrogen evolution rate. In contrast, the high surface area in case of UV100 does not reflect any activity towards the photocatalytic hydrogen evolution. These observations, therefore, point out to the dominant role of precursor type on the photocatalytic activity.

Figure 2-S3 (a) demonstrates the N_2 adsorption–desorption isotherms recorded for the nanostructured S5 photocatalyst. According to BET method, these isotherms revealed a type IV characteristic of mesoporous materials [49]. This result is in good agreement with predictions, as EISA soft-templating method is reported to increase the surface area through mesoporous structures [50]. The distribution of pore size shown in Figure 2-S3 (b) is calculated by BJH method, where the average pore diameter for S5 was 5.1 nm. Although the structure contained mesopores with a pore diameter range between 2 and 8 nm, however, these pores characterized as non-ordered and showed a wide distribution range. In Soft-templating methods including EISA, the mesostructures could collapse upon removing the surfactant by calcination [51] leading sometimes to non-ordered mesopore structures. This is a drawback of the soft-templating technique.
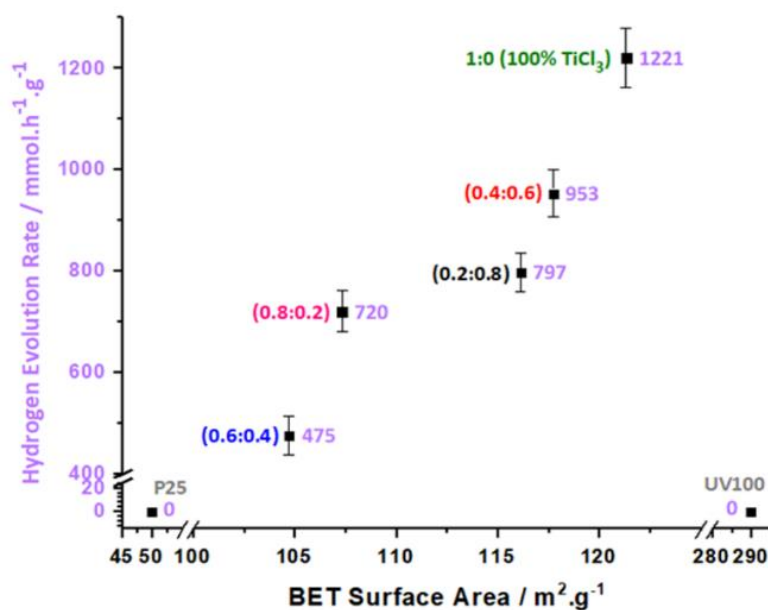
Figure 2-7 relationships between the photocatalytic activity (after 120 min irradiation) and BET surface area for the self-prepared photocatalysts.

The optical properties of the prepared materials were measured by means of UV-VIS spectroscopy and the obtained reflectance data are presented in Figure 2-8 (a and b). A clear optical response in the visible range until around 600 nm can be noticed in $TiCl_3$-based materials compared to UV100 that manly absorbs in the UV range. This visible response is not due to doping with foreign atoms since the EDX analysis of all the self-prepared nanoparticles showed peaks for titanium and oxygen elements without any trace of other impurities within the detection limit of the EDX. Such visible light response was noticed by other researchers and has been attributed to defects in TiO_2 [8, 48]. The energy band gaps were also affected throughout the prepared materials. A clear relationship between the quantity of $TiCl_3$ in the precursor and the bandgap energies of the anatase samples is proven since a narrowing of the band gaps upon increasing the $TiCl_3$ ratio was noticed as demonstrated in Figure 2-7(b) and Table 2-3. Because doping is unlikely to happen as stated before, the presence of defect states has been reported to drastically alter the electronic structure of the semiconductor. Such defects introduce additional energy levels in the middle of the bandgap and could, therefore, narrow its bandgap energy and improves the visible light absorption [52]. Oxygen vacancies represent the most common defects in TiO_2, which have been related to the unpaired electrons that were located initially in an O 2p orbital of the valence band. These electrons can then be transferred, by the removal of the corresponding oxygen atom, into the conduction band to interact with Ti^{4+} giving the corresponding Ti^{3+} defects, creating shallow and deep sub-bandgap Ti^{3+} states below the conduction band [53-55].
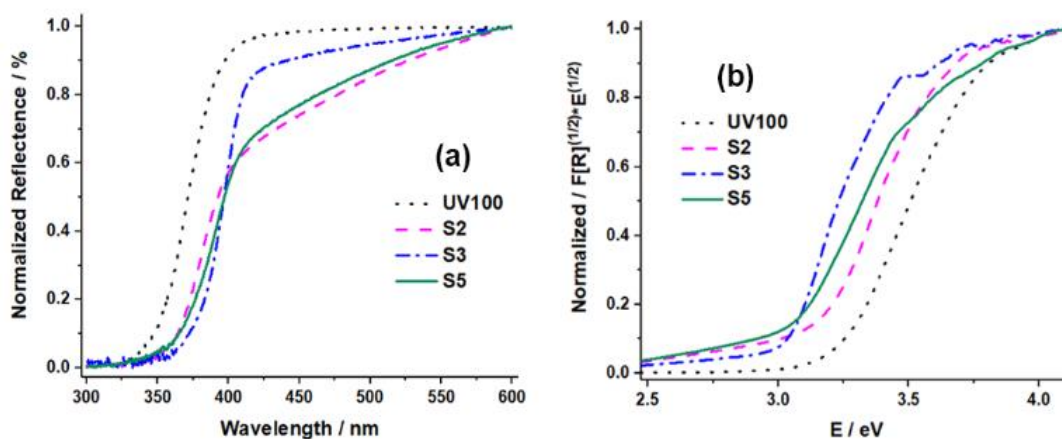
Figure 2-8 UV–Visible light reflectance spectra (a), and Tauc plots (b) of the tested photocatalysts.

The flat-band potentials were derived from the Mott−Schottky plots for electrodes of TiO₂ thin film on FTO. The flat-band potential for the film prepared from TiCl₃ through the same EISA method possessed a value of (-0.24 V *vs.* NHE at pH =0). This result clearly proves that the narrowing in the bandgap energy is accompanied with a shifting of the flat-band potential towards more negative potential compared to the E_{fb} for pure anatase TiO₂ (-0.19 V *vs.* NHE) [56, 57] and the E_{fb} for a self-prepared electrode prepared from TiCl₄ in the same conditions (-0.17 V *vs.* NHE). The more negative the potential of the flat band is, the higher the reduction potential of the photogenerated electrons is. This leads to a more favorable reduction reaction of H⁺ to produce molecular hydrogen (H^+/H_2 = 0 V *vs.* NHE). Consequently, the valence band edges were calculated from the values of the band-gap energy and the flat-band potential. S5 material underwent a corresponding widening in its valence band edge to a less positive potential (2.74 V *vs.* NHE at pH =0) comparing to both, the pure anatase TiO₂ (3.00 V *vs.* NHE) and the electrode prepared from TiCl₄ (2.98 V *vs.* NHE). Such effect was noticed by Wang *et al.* [58] who produced highly defective TiO₂ with a widening in the valence band top edge leading to remarkably a higher photocatalytic activity compared with normal TiO₂. They explained this observation by the efficient charge transfer in bulk and at the semiconductor/electrolyte interface. The shifting of the flat-band potential, together with the widening of the valance band edge point out once more to the presence of defects in the structure of TiO₂, especially, due to the absence of foreign dopants. The introduction of such defects has been usually accompanied by an increase in the charge carrier densities (ND) of the studied materials. A charge carrier density value of $9.3 \times 10^{+20}$ cm⁻³ in S5 sample was recorded upon the analysis of its M-S plots. This value is noticeably higher than that of pure anatase TiO₂ ($0.4 - 0.8 \times 10^{+19}$ cm⁻³) [56] and of the electrode prepared from TiCl₄ ($8.1 \times 10^{+19}$). The density of the charge carriers affects the depletion layer and the recombination rate of the semiconductor [59]. Kang *et al.* [60] noticed a negative shift of E_{fb} upon NaBH₄ reduction due to the formation of defects, which serve as electron donors [13]. In addition, they found that NaBH₄ treatment increases the donor density of reduced TiO₂,

thus resulting in a higher electrical conductivity as well as in the faster charge carriers transport. Higher donor densities are expected to shift the Fermi level of TiO$_2$ toward the conduction band and to facilitate the charge separation at the semiconductor–electrolyte interface, by increasing the degree of band bending [13]. The same observations were reported by Mehta et *al.* [61], who found that treating TiO$_2$ with hydrogen under partial pressure conditions enhanced the photocatalytic response due to surface defects, which induced a higher charge carrier concentration and a more negative flat band potential.

The 1.5-fold higher photonic efficiency of S5 in comparison to other prepared materials can be explained therefore by its higher optical absorption, as well as by the improved charge carrier creation and utilization. Therefore, the synthesis of TiO$_2$ starting from TiCl$_3$ (sample S5) not only provides the simplicity of the synthesis method, but it enhances additionally the optical and the electronic properties of TiO$_2$, leading to increase both, the photocatalytic hydrogen evolution and the photonic efficiency, even in the absence of any co-catalyst.

2.5.5. Transient Reflectance Spectroscopy

The transient absorption spectra obtained for UV100 and S5 0.1 µs after the laser pulse are presented in Figure 2-9 (a). While the powders being kept under an inert nitrogen atmosphere, the two materials showed broad spectra, which is in good agreement with the literature as the trapped charge carrier species absorb light over a broad wavelength range [33]. It has been reported that the transient absorption signals observed for TiO$_2$ above 600 nm are attributed to trapped electrons [62], whereas the transient absorption observed between 400 nm and 530 nm is attributed to the trapped holes [62, 63]. Because the experiments were performed in the absence of an electron donor or acceptor the transient reflectance signals represent a sum of trapped electron and trapped hole states. Both measurements were identically repeated in N$_2$–methanol vapor environment to follow-up the changes in the transient absorption spectra and to link the transient signals to the possible trapped charge carriers. After the introduction of the methanol vapor, no changes of the transient absorption signals have been observed for UV100 in the wavelength range from 650 to 710 nm, while the transient absorption intensity in the wavelengths ranges from 410 to 625 nm deteriorate (see Figure 2-9a). Accordingly, the latter wavelengths range can be attributed to trapped holes reacting rapidly with methanol within 1 ns [64].
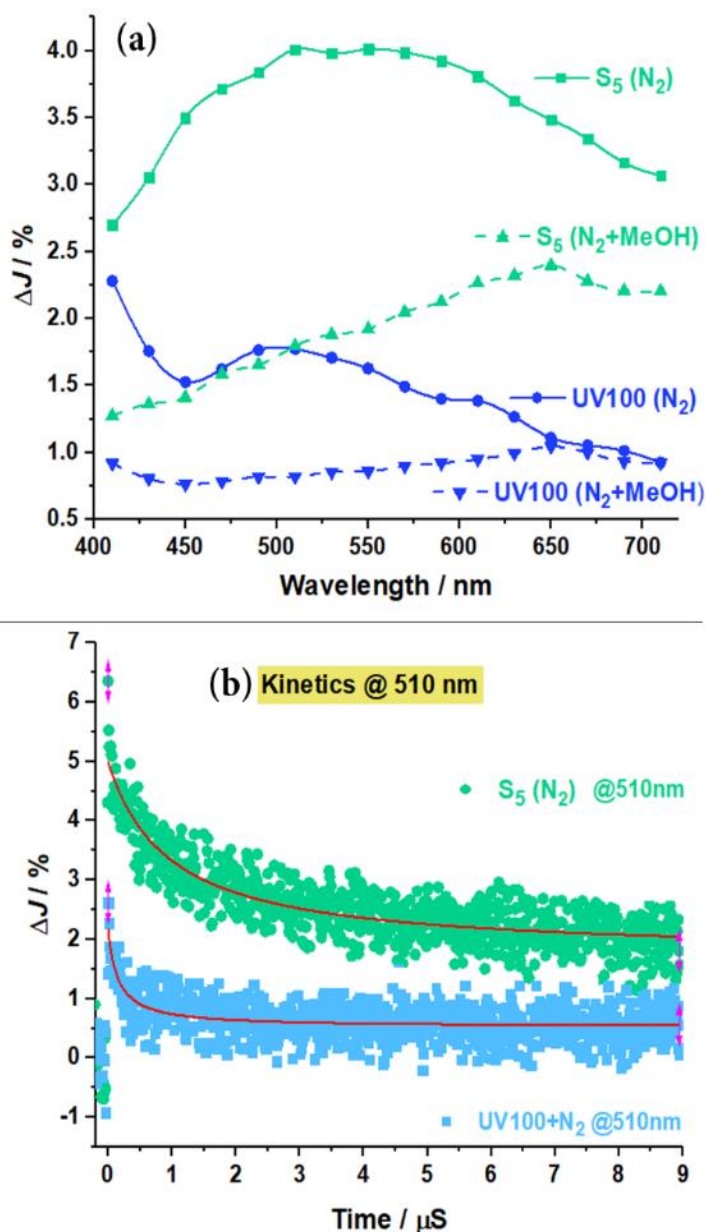
Figure 2-9 Transient absorption spectra (a) measured at 0.1 µs after laser excitation in a N$_2$ and a N$_2$–methanol vapour atmosphere, transient absorption signals (b) observed at 510 nm in a N$_2$ and N$_2$–methanol vapour atmosphere. λ$_{ex}$ = 355 nm with a cut-off filter of 400 nm for detection.

On the other hand, the transient absorption spectrum of S5 exhibits a maximum at 650 nm that can be correlated to the d-d transition of the Ti^{3+} blue centers. However, the whole transient absorption spectrum in the methanol environment has remarkably lower absorptions comparing to the N$_2$ atmosphere. This clearly indicates the very broad distribution of trapped holes over the whole studied spectral range of wavelengths, which indicates that the holes are delocalized over different trapping sites, with the holes being trapped at different energetic depths resulting in such broad transient absorption spectra. Bahnemann et *al.* [65] confirmed that at least two different types of holes have to be considered, namely, the deeply poor-reactive trapped holes (at 450 nm) besides the

free holes that possess a higher oxidation potential. It is well reported that the valence band holes can be rapidly transported to the surface, where a surface hole trap sites are formed on Ti-O$_s$H and/or Ti-O$_s$-Ti. These surface trapped holes (Ti-O$_s$H$^{\bullet+}$ and/or Ti-Os$^{\bullet+}$-Ti) are the main oxidants for any adsorbed electron donor. The different trapped states for holes in addition to the higher reactivity with methanol in our self-prepared material point out the better migration of the charge carriers, as methanol can only react with the surface trapped holes, while the bulk carriers remain in the system [32]. The investigations delivered from the transient reflectance spectroscopy revealed a delocalization of holes over different surface trapping sites with a higher oxidation potential than other deeply trapped sites. Kong et *al*. [39] found that increasing the ratio of the concentration of surface defects to bulk defects improves the separation between the photogenerated carriers, thereby enhancing the photocatalytic activity. This conclusion has also been proposed by Ohtani [66], who claimed the necessity to control precisely the structural properties to develop high active photocatalysts. In this context, the density of surface shallow traps should be maximized and the density of deep traps minimized. It has been reported that defects in TiO₂ could perform as a co-catalyst, which enhance the usage of the photogenerated electrons in the reduction process [52]. Hole trapping sites participate in such surface defects that play a decisive role in adsorption and surface reactivity. They can serve as charge carrier traps as well as adsorption sites where the charge carrier transfer to adsorbed species can reduce the charge carrier recombination [39].

The transient absorption kinetics for both materials at 510 nm in an N₂ atmosphere are presented in Figure 2-9(b). Both signals showed an increase in absorption immediately after the laser pulse, however, the self-prepared photocatalyst exhibited around 3-fold higher signal intensity of the initial absorption J_0. This result confirms the higher charge densities of the prepared material. A rapid decrease in the absorption signal is occurred followed by reaching a long-lasting, nearly constant absorption. The characteristic times after which J_0 at 510 nm decays to J_0/e (~37%) are around 0.5 μs and 4 μs for UV100 and S5, respectively. Comparing the transient absorption kinetics at 510 nm, the self-prepared sample showed decay with a longer lifetime than for UV100. The decay kinetics of the photogenerated charge carriers could be fitted by second-order reaction kinetics according to Eq. (2-10).

$$\Delta J(t) = \frac{J_0}{K_r.J_0.t + 1} \tag{2-10}$$

A rate constant K_r values of $10.9 \times 10^{+7}$ and $1.74 \times 10^{+7}$ (s%)$^{-1}$ for UV100 and S5, respectively have been obtained evincing improved charge carrier separation in the prepared material even in the absence of an electron donor. Thus, in the presence of suitable electron donors, the electrons are available for an extended period to induce reduction reactions. Such phenomena have been assigned to the surface defects that enable the capture of the electrons and suppress the recombination of

electrons and holes [38], and could, in turn, facilitate the migration of charge carriers to the surface due to the slower charge carrier recombination. To sum up the observations of this section, a higher concentration and a longer lifetime of the photogenerated charge carriers in the prepared samples have been obtained, as well as a broad distribution of trapped states, acting most likely as surface defect sites.

2.6. Conclusion

We successfully applied the design of experiment approach combined with full factorial design to investigate the most influential variable affecting the preparation of TiO_2 through EISA method. $TiCl_3$ is the decisive factor that maximizes the photocatalytic hydrogen evolution. Combining $TiCl_3$ as a precursor with F-108 as a surfactant leads to the formation of pure anatase TiO_2 characterized by its response to the visible light in addition to its unexpected photocatalytic activity towards the hydrogen evolution in absence of any co-catalyst. The higher photocatalytic activity could be related to the band edge positions and the higher charge carrier density that facilitates the transport of charge carriers. The wider distribution of energetically different trapping sites for the holes increases the adsorption sites and accelerates their reactions with adsorbates; hence the synthesized material could be used as a photocatalyst in a promising environmental-friendly technique aiming to the generation of renewable energy source. Future studies will be done to explain the photocatalytic activity of the prepared material towards the evolution of hydrogen gas. Finally, in order to demonstrate the viability of semiconductor photocatalysis to be scaled-up for environmental remediation and energy conversion, several technical and economic factors, which are related to reactor design, should be considered. These factors include the uniform distribution of illumination and photocatalytic particulates as well as reaction kinetics. The issue of providing a sufficient specific surface area of catalyst and effective photocatalyst illumination is particularly important in this area. The simplicity of the preparation method and the possibility to produce molecular hydrogen without using a co-catalyst are an opportunity to scale-up the manufacturing such photocatalysts for large scale reactors towards an economic commercial distribution. Scaling up of the photocatalyst synthesis developed herein should be feasible, both technically and economically. It will, however, require appropriate technical equipment, which currently are not available in the authors´ laboratory.

2.7. Supporting information

Table 2-S1 The proposed order of experiments built by DoE including the studied factors besides the results of the conducted experiments.

PT	ST	SQ	H$_2$ rate	S$_{BET}$
		g	µmol h^{-1} g^{-1}	m^2 g^{-1}
TiCl$_4$:Ti(OBu)$_4$	F-108	1	623.5	120.0
TiCl$_4$:Ti(OBu)$_4$	F-108	2	575.9	123.1
TiCl$_3$:Ti(OBu)$_4$	F-108	2	936.4	120.4
TiCl$_3$:Ti(OBu)$_4$	P123	1	774.7	105.2
TiCl$_3$:Ti(OBu)$_4$	P123	2	733.9	108.9
TiCl$_3$:Ti(OBu)$_4$	F-108	1	999.8	118.3
TiCl$_3$:Ti(OBu)$_4$	P123	2	757.3	109.9
TiCl$_4$:Ti(OBu)$_4$	F-108	2	553.3	122.0
TiCl$_3$:Ti(OBu)$_4$	F-108	1	980.2	117.1
TiCl$_4$:Ti(OBu)$_4$	P123	1	452.5	107.2
TiCl$_4$:Ti(OBu)$_4$	F-108	1	587.4	118.9
TiCl$_4$:Ti(OBu)$_4$	P123	2	442.2	110.0
TiCl$_4$:Ti(OBu)$_4$	P123	1	469.0	108.1
TiCl$_4$:Ti(OBu)$_4$	P123	2	425.1	109.1
TiCl$_3$:Ti(OBu)$_4$	F-108	2	957.2	121.2
TiCl$_3$:Ti(OBu)$_4$	P123	1	804.8	106.0

Table 2-S2 The factors and their interaction effects on the surface area (ANOVA results) in FFD.

Source of Variation	D.F.	Sum of Squares	Mean Squares	F Ratio	*P* Value [a]
Model	7	6.29E+02	8.99E+01	1.85E+02	3.27E-08
PT	1	8.12E+00	8.12E+00	1.67E+01	3.47E-03
ST	1	5.83E+02	5.83E+02	1.20E+03	5.23E-10
SQ	1	3.54E+01	3.54E+01	7.30E+01	2.70E-05
PT • ST	1	4.23E-01	4.23E-01	8.71E-01	3.78E-01
PT • SQ	1	9.03E-01	9.03E-01	1.86E+00	2.10E-01
ST • SQ	1	6.25E-02	6.25E-02	1.29E-01	7.29E-01
PT • ST • SQ	1	9.03E-01	9.03E-01	1.86E+00	2.10E-01
Residual	8	3.88E+00	4.85E-01		
Pure Error	8	3.88E+00	4.85E-01		
Total	15	6.33E+02			

[a] $\alpha = 0.05$, S $= 0.6964$, $R^2 = 99.39\%$, R^2(adj) $= 98.85\%$.
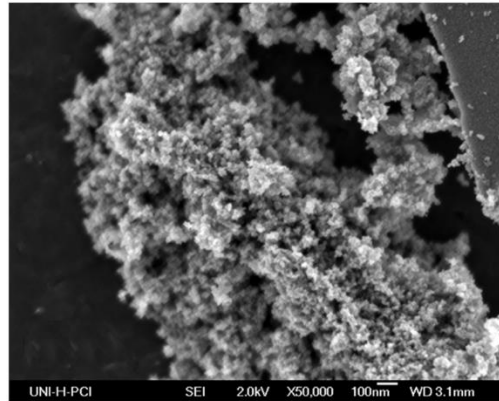
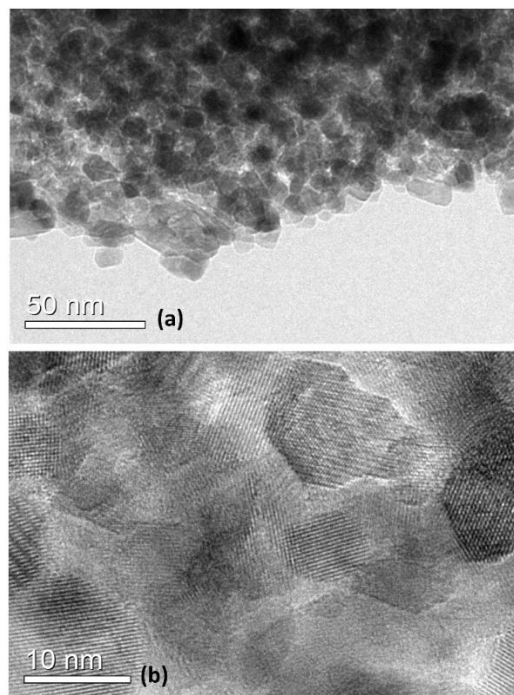**Figure 2-S1 SEM image in 100 nm scale (X50,000) for S5 powder.**

Figure 2-S2 TEM image in 50 nm scale (a), and HRTEM image in 10 nm scale (b) for S5 powder.
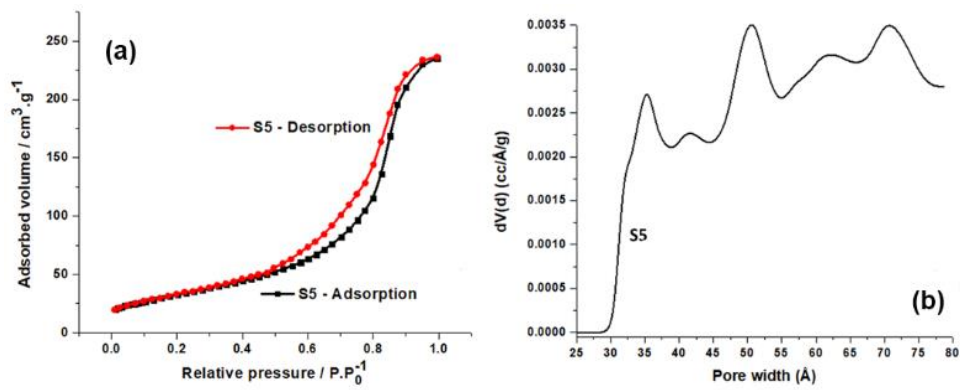
Figure 3-S Nitrogen adsorption–desorption isotherms (a) and pore size distribution (b) of S5 powder.

2.8. Acknowledgments

2.9. References

1. AlSalka, Y., et al., *Co-catalyst-free photocatalytic hydrogen evolution on TiO₂: Synthesis of optimized photocatalyst through statistical material science.* Applied Catalysis B: Environmental, 2018. **238**: p. 422-433.
2. AlSalka, Y., et al., *Understanding the degradation pathways of oxalic acid in different photocatalytic systems: Towards simultaneous photocatalytic hydrogen evolution.* Journal of Photochemistry and Photobiology A: Chemistry, 2018.
3. Friehs, E., et al., *Toxicity, phototoxicity and biocidal activity of nanoparticles employed in photocatalysis.* Journal of Photochemistry and Photobiology C: Photochemistry Reviews, 2016. **29**: p. 1-28.
4. Fujishima, A. and K. Honda, *Electrochemical photolysis of water at a semiconductor electrode.* Nature, 1972. **238**(5358): p. 37 - 38.
5. Masolo, E., et al., *Mesoporous Titania Powders: The Role of Precursors, Ligand Addition and Calcination Rate on Their Morphology, Crystalline Structure and Photocatalytic Activity.* Nanomaterials, 2014. **4**(3): p. 583.
6. Wan, Y. and Zhao, *On the Controllable Soft-Templating Approach to Mesoporous Silicates.* Chemical Reviews, 2007. **107**(7): p. 2821-2860.
7. Etacheri, V., et al., *Visible-light activation of TiO₂ photocatalysts: Advances in theory and experiments.* Journal of Photochemistry and Photobiology C: Photochemistry Reviews, 2015. **25**: p. 1-29.
8. Pan, X., et al., *Defective TiO₂ with oxygen vacancies: synthesis, properties and photocatalytic applications.* Nanoscale, 2013. **5**(9): p. 3601-3614.
9. Yang, H., et al., *Free-standing and oriented mesoporous silica films grown at the air-water interface.* Nature, 1996. **381**(6583): p. 589-592.
10. Brinker, C.J., et al., *Evaporation-Induced Self-Assembly: Nanostructures Made Easy.* Advanced Materials, 1999. **11**(7): p. 579-585.
11. Mahoney, L. and R.T. Koodali, *Versatility of Evaporation-Induced Self-Assembly (EISA) Method for Preparation of Mesoporous TiO₂ for Energy and Environmental Applications.* Materials, 2014. **7**(4): p. 2697-2746.
12. Pan, J.H., X.S. Zhao, and W.I. Lee, *Block copolymer-templated synthesis of highly organized mesoporous TiO₂-based films and their photoelectrochemical applications.* Chemical Engineering Journal, 2011. **170**(2): p. 363-380.
13. Zhang, J., et al., *Ligand-Assisted Assembly Approach to Synthesize Large-Pore Ordered Mesoporous Titania with Thermally Stable and Crystalline Framework.* Advanced Energy Materials, 2011. **1**(2): p. 241-248.
14. Grosso, D., et al., *Fundamentals of Mesostructuring Through Evaporation-Induced Self-Assembly.* Advanced Functional Materials, 2004. **14**(4): p. 309-322.
15. Crepaldi, E.L., et al., *Controlled Formation of Highly Organized Mesoporous Titania Thin Films: From Mesostructured Hybrids to Mesoporous Nanoanatase TiO₂.* Journal of the American Chemical Society, 2003. **125**(32): p. 9770-9786.

16.   Soler-Illia, G.J.d.A.A. and C. Sanchez, *Interactions between poly(ethylene oxide)-based surfactants and transition metal alkoxides: their role in the templated construction of mesostructured hybrid organic-inorganic composites.* New Journal of Chemistry, 2000. **24**(7): p. 493-499.

17.   Yang, P., et al., *Block Copolymer Templating Syntheses of Mesoporous Metal Oxides with Large Ordering Lengths and Semicrystalline Framework.* Chemistry of Materials, 1999. **11**(10): p. 2813-2826.

18.   Luo, H., C. Wang, and Y. Yan, *Synthesis of Mesostructured Titania with Controlled Crystalline Framework.* Chemistry of Materials, 2003. **15**(20): p. 3841-3846.

19.   Sung, C.-C., et al., *Synthesis of highly ordered and worm-like mesoporous TiO₂ assisted by tri-block copolymer.* Solid State Ionics, 2008. **179**(27): p. 1300-1304.

20.   Bosc, F., et al., *Mesostructure of Anatase Thin Films Prepared by Mesophase Templating.* Chemistry of Materials, 2004. **16**(11): p. 2208-2214.

21.   Soler-Illia, G.J.d.A.A., et al., *Chemical Strategies To Design Textured Materials:â€‰from Microporous and Mesoporous Oxides to Nanonetworks and Hierarchical Structures.* Chemical Reviews, 2002. **102**(11): p. 4093-4138.

22.   Cassiers, K., et al., *Surfactant-Directed Synthesis of Mesoporous Titania with Nanocrystalline Anatase Walls and Remarkable Thermal Stability.* The Journal of Physical Chemistry B, 2004. **108**(12): p. 3713-3721.

23.   Stanley, N.D. and L.M. Stephen, *Chapter 10 An Example of Regression Analysis on Existing Data*, in *Data Handling in Science and Technology*. 1993, Elsevier. p. 177-197.

24.   AlSalka, Y., F. Karabet, and S. Hashem, *Development and optimisation of quantitative analytical method to determine BTEX in environmental water samples using HPLC-DAD.* Analytical Methods, 2010. **2**(8): p. 1026-1035.

25.   AlSalka, Y., F. Karabet, and S. Hashem, *Evaluation of electrochemical processes for the removal of several target aromatic hydrocarbons from petroleum contaminated water.* Journal of Environmental Monitoring, 2011. **13**(3): p. 605-613.

26.   Chen, L., et al., *Synthesis of Well-Ordered Mesoporous Titania with Tunable Phase Content and High Photoactivity.* The Journal of Physical Chemistry C, 2007. **111**(32): p. 11849-11853.

27.   Hakki, A., et al., *Hydrogen Production by Heterogeneous Photocatalysis A2 - Wandelt, Klaus*, in *Encyclopedia of Interfacial Chemistry*. 2018, Elsevier: Oxford. p. 413-419.

28.   Mee, R.W., *Analysis of Full Factorial Experiments*, in *A Comprehensive Guide to Factorial Two-Level Experimentation*. 2009, Springer New York: New York, NY. p. 27-74.

29.   Brandani, P. and P. Stroeve, *Kinetics and Equilibria of Adsorption of PEO-PPO-PEO Triblock Copolymers on a Hydrophilic Self-Assembled Monolayer on Gold.* Macromolecules, 2004. **37**(17): p. 6640-6643.

30.   Shah, V., et al., *Correlation of Dynamic Surface Tension with Sedimentation of PTFE Particles and Water Penetration in Powders.* Langmuir, 2015. **31**(51): p. 13725-13733.

31.   López, R. and R. Gómez, *Band-gap energy estimation from diffuse reflectance measurements on sol–gel and commercial TiO₂: a comparative study.* Journal of Sol-Gel Science and Technology, 2012. **61**(1): p. 1-7.

32.   Schneider, J., et al., *Improved charge carrier separation in barium tantalate composites investigated by laser flash photolysis.* Physical Chemistry Chemical Physics, 2016. **18**(16): p. 10719-10726.

33.   Sieland, F., J. Schneider, and D.W. Bahnemann, *Fractal Charge Carrier Kinetics in TiO₂.* The Journal of Physical Chemistry C, 2017. **121**(43): p. 24282-24291.

34.   Cordell, R.L., et al., *GC-MS analysis of ethanol and other volatile compounds in micro-volume blood samplesâ€"quantifying neonatal exposure.* Analytical and Bioanalytical Chemistry, 2013. **405**(12): p. 4139-4147.

35.   Ab Rahman, J., *Analysing Research Data*, in *Brief Guidelines for Methods and Statistics in Medical Research*. 2015, Springer Singapore: Singapore. p. 35-101.

36.   Cheng, V.A. and L.M. Walker, *Transport of nanoparticulate material in self-assembled block copolymer micelle solutions and crystals.* Faraday Discussions, 2016. **186**(0): p. 435-454.

37.   Braslavsky, S.E., et al., *Glossary of terms used in photocatalysis and radiation catalysis (IUPAC Recommendations 2011).* Pure and Applied Chemistry, 2011. **83**(4): p. 931 - 1014.

38.   Zhijiao, W., et al., *Effects of bulk and surface defects on the photocatalytic performance of size-controlled TiO$_2$ nanoparticles.* Nanotechnology, 2017. **28**(27): p. 275706.

39.   Kong, M., et al., *Tuning the Relative Concentration Ratio of Bulk Defects to Surface Defects in TiO$_2$ Nanocrystals Leads to High Photocatalytic Efficiency.* Journal of the American Chemical Society, 2011. **133**(41): p. 16414-16417.

40.   Puga, A.V., et al., *Production of H$_2$ by Ethanol Photoreforming on Au/TiO$_2$.* Advanced Functional Materials, 2014. **24**(2): p. 241-248.

41.   Schneider, J. and D.W. Bahnemann, *Undesired Role of Sacrificial Reagents in Photocatalysis.* The Journal of Physical Chemistry Letters, 2013. **4**(20): p. 3479-3483.

42.   Gao, R., A. Safrany, and J. Rabani, *Fundamental reactions in TiO$_2$ nanocrystallite aqueous solutions studied by pulse radiolysis.* Radiation Physics and Chemistry, 2002. **65**(6): p. 599-609.

43.   Amano, F., et al., *Effect of Ti^{3+} Ions and Conduction Band Electrons on Photocatalytic and Photoelectrochemical Activity of Rutile Titania for Water Oxidation.* The Journal of Physical Chemistry C, 2016. **120**(12): p. 6467-6474.

44.   Sanchez-Sanchez, M.C., et al., *Mechanistic Aspects of the Ethanol Steam Reforming Reaction for Hydrogen Production on Pt, Ni, and PtNi Catalysts Supported on γ-Al$_2$O$_3$.* The Journal of Physical Chemistry A, 2010. **114**(11): p. 3873-3882.

45.   Mattos, L.V., et al., *Production of Hydrogen from Ethanol: Review of Reaction Mechanism and Catalyst Deactivation.* Chemical Reviews, 2012. **112**(7): p. 4094-4123.

46.   Li, R., et al., *Achieving overall water splitting using titanium dioxide-based photocatalysts of different phases.* Energy & Environmental Science, 2015. **8**(8): p. 2377-2382.

47.   Kho, Y.K., et al., *Photocatalytic H$_2$ Evolution over TiO$_2$ Nanoparticles. The Synergistic Effect of Anatase and Rutile.* The Journal of Physical Chemistry C, 2010. **114**(6): p. 2821-2829.

48.   Liu, N., et al., *Hydrogenated Anatase: Strong Photocatalytic Dihydrogen Evolution without the Use of a Co-Catalyst.* Angewandte Chemie International Edition, 2014. **53**(51): p. 14201-14205.

49.   Sing, K.S.S., *Reporting Physisorption Data for Gas/Solid Systems with Special Reference to the Determination of Surface Area and Porosity.* 1982, Brunel University: UK. p. 2201—2218.

50.   Li, W., et al., *A Perspective on Mesoporous TiO$_2$ Materials.* Chemistry of Materials, 2014. **26**(1): p. 287-298.

51.   Ren, Y., Z. Ma, and P.G. Bruce, *Ordered mesoporous metal oxides: synthesis and applications.* Chemical Society Reviews, 2012. **41**(14): p. 4909-4927.

52.   Xiong, L.-B., et al., *in the Surface of Titanium Dioxide: Generation, Properties and Photocatalytic Application.* Journal of Nanomaterials, 2012. **2012**: p. 13.

53.   Wen, M., et al., *In situ synthesis of Ti^{3+} self-doped mesoporous TiO$_2$ as a durable photocatalyst for environmental remediation.* Chinese Journal of Catalysis, 2015. **36**(12): p. 2095-2102.

54.   Zhang, X., et al., *Facile synthesis and enhanced visible-light photocatalytic activity of Ti^{3+}-doped TiO$_2$ sheets with tunable phase composition.* Frontiers of Chemical Science and Engineering, 2015. **9**(3): p. 349-358.

55.   Cushing, S.K., et al., *Effects of Defects on Photocatalytic Activity of Hydrogen-Treated Titanium Oxide Nanobelts.* ACS Catalysis, 2017. **7**(3): p. 1742-1748.

56.   Kavan, L., et al., *Electrochemical and Photoelectrochemical Investigation of Single-Crystal Anatase.* Journal of the American Chemical Society, 1996. **118**(28): p. 6716-6723.

57.   Beranek, R., *(Photo)electrochemical Methods for the Determination of the Band Edge Positions of TiO₂-Based Nanomaterials.* Advances in Physical Chemistry, 2011. **2011**: p. 20.

58.   Wang, S., et al., *Titanium-Defected Undoped Anatase TiO₂ with p-Type Conductivity, Room-Temperature Ferromagnetism, and Remarkable Photocatalytic Performance.* Journal of the American Chemical Society, 2015. **137**(8): p. 2975-2983.

59.   Chen, Z., H. Dinh, and E. Miller, *Photoelectrochemical Water Splitting. Standards, Experimental Methods, and Protocols*. 1 ed. SpringerBriefs in Energy. 2013: Springer-Verlag New York. 126.

60.   Kang, Q., et al., *Reduced TiO₂ nanotube arrays for photoelectrochemical water splitting.* Journal of Materials Chemistry A, 2013. **1**(18): p. 5766-5774.

61.   Mehta, M., et al., *Hydrogen treated anatase TiO₂: a new experimental approach and further insights from theory.* Journal of Materials Chemistry A, 2016. **4**(7): p. 2670-2681.

62.   Murakami, Y., et al., *Femtosecond Diffuse-Reflectance Spectroscopy of Various Commercially Available TiO₂ Powders.* Spectroscopy Letters, 2011. **44**(2): p. 88-94.

63.   Wang, X., et al., *Transient Absorption Spectroscopy of Anatase and Rutile: The Impact of Morphology and Phase on Photocatalytic Activity.* The Journal of Physical Chemistry C, 2015. **119**(19): p. 10439-10447.

64.   Tamaki, Y., et al., *Direct Observation of Reactive Trapped Holes in TiO₂ Undergoing Photocatalytic Oxidation of Adsorbed Alcohols: Evaluation of the Reaction Rates and Yields.* Journal of the American Chemical Society, 2006. **128**(2): p. 416-417.

65.   Bahnemann, D.W., M. Hilgendorff, and R. Memming, *Charge Carrier Dynamics at TiO₂ Particles: Reactivity of Free and Trapped Holes.* The Journal of Physical Chemistry B, 1997. **101**(21): p. 4265-4275.

66.   Ohtani, B., *Titania Photocatalysis beyond Recombination: A Critical Review.* Catalysts, 2013. **3**(4): p. 942-953.

Chapter Three: Understanding the Degradation Pathways of Oxalic Acid in Different Photocatalytic Systems: Towards Simultaneous Photocatalytic Hydrogen Evolution

3.1. Foreword

3.2. Abstract

The photocatalytic degradation of aqueous oxalic acid has been investigated employing different photocatalytic systems under constant pH conditions. A self-prepared TiO_2 was utilized during the photocatalytic investigations in a bare and a platinized form. The synthesized pure anatase phase TiO_2 had a 10 nm grain size and a BET surface area of ca. 121 m^2 g^{-1} with relatively higher photocatalytic activity compared to the commercially available TiO_2 photocatalyst UV100. Complete photocatalytic degradation of oxalic acid was observed within 60 min of illumination under aerobic conditions with no by-product been detected. In the absence of molecular oxygen, a perceptible amount of formic acid was formed in the liquid phase, as determined quantitatively by means of ion chromatography. The formation of formic acid suggests that a photo-Kolbe reaction tacks place under oxygen-free conditions. The formation of formic acid was also noticed when platinized TiO_2 (0.25 wt.%) was employed, together with an enhancement of the reactions photonic efficiency to the quadruple. A hydrogen evolution could only observe under an oxygen-free condition with, again, a higher formation rate over the platinized material. However, upon complete photoreforming of oxalic acid, the overall amount of the photocatalytically evolved hydrogen using $Pt_{0.25\%}/TiO_2$ represented only 60% of the theoretical amount. Therefore, it is suggested that the source of H atoms could be the $HC_2O_4^-$ species rather than molecular oxalic acid. A detailed mechanism for the photocatalytic degradation of aqueous oxalic acid at different photocatalytic conditions is proposed and discussed.

Keywords Photocatalysis; TiO_2; Hydrogen evolution; Photocatalytic reforming; Oxalic acid; Solar fuel.

3.3. Introduction

With the increasing water pollution and the stringent environmental regulations concerning water and wastewater contaminant content, efficient water treatment technologies have gained importance worldwide in the last two decades. Among those techniques, heterogeneous photocatalysis, particularly the TiO_2-based one [1-3], has attained great interest due to its promising efficiency in mineralizing organic pollutants in water [4]. In parallel, finding clean alternative sources of energy becomes a persistent need to overcome the environmental problems created by the modern consumption-based lifestyle.

Molecular hydrogen seems to be a potential ideal environmental-friendly fuel for the future due to its high energy content of 122 $kJ.g^{-1}$ compared to other fuels such as gasoline (40 $kJ.g^{-1}$) [5]. Recently, nanoparticulate photocatalytic systems have attracted tremendous attention as a clean technology for the generation of hydrogen [6, 7]. A photocatalytic process involves a light-induced generation of an electron-hole pair in the conduction and valence band of a semiconductor material, respectively. Consequently, TiO_2 could act as an electron donor and an electron acceptor for other molecules adsorbed on its surface [2]. Unfortunately, the lack of light absorption within the visible wavelength regime, as well as the fast recombination of photogenerated charge carriers limits its practical usage. Electron donors, e.g, organic contaminants, have been used as sacrificial reagents to improve this process because they can react irreversibly with the photogenerated holes suppressing their recombination with electrons [8]. Noble metals, in particular, platinum, play an essential role in photocatalytic hydrogen formation systems [4, 9]. The loading of platinum nanoparticles on the surface of TiO_2 promotes the transfer of the photogenerated holes to the surface (according to the Schottky barrier model) [10], which allows, in turn, the trapped electrons and the free bulk electrons to migrate and accumulate in the platinum nanoparticles. This phenomenon enhances the formation of molecular hydrogen by reducing the reduction potential of protons [2, 11].

Achieving the dual-functionality, i.e., the photocatalytic degradation of pollutants and the simultaneous generation of hydrogen gas is a great added value of this technique. Unfortunately, different operational conditions need to be applied for each process to achieve their optimal reaction yield. [12]. Since molecular oxygen competes with protons as electrons acceptors, the absence of oxygen is a prerequisite for the photocatalytic reduction of protons to molecular hydrogen. Contrary, the degradation of organic compounds could be negatively affected by a lack of molecular oxygen. Combining both photocatalytic processes has already been reported [12-14], however, the mechanism and the extent by which the sacrificial reagent contributes to the hydrogen formation still need to be clarified.

To the best of our knowledge, also the usage of oxalic acid as an electron donor has rarely been reported in the literature so far. Moreover, during the photocatalytic degradation of organic carboxylic acids, a deep comprehension of the final reaction step by which these compounds release carbon dioxide remains unclear [15]. The decomposition of oxalic acid should generally evolve hydrogen and carbon dioxide in a 1:2 molar ratio. The fate of oxalic acid is found to follow the main features of the photoreforming process, and the presence of the metal co-catalyst plays an inevitable role in the pathway of the reaction [16]. Li et *al.* [17] investigated the effects of variation of the pH, the amount of deposited platinum and the addition of inorganic anions on the rate of the photocatalytic hydrogen evolution over platinized TiO_2 using oxalic acid as an electron donor. They omitted to follow the formation of any by-product and found that kinetics follow a Langmuir-type behavior. Draganic et *al.* [18] reported that the reactivity of the reaction between $\cdot$OH radicals and oxalic acid decreases in the order of $HC_2O_4^- > C_2O_4^{2-} \gg H_2C_2O_4$, which could explain the higher rate of hydrogen evolution between pH 3 and 4. Generally, the photo-Kolbe reaction mediated by the photogenerated carriers in TiO_2 is completely changed by the presence of molecular oxygen; the photogenerated electrons participate in $n-1$ RH alkylation, while the presence of molecular oxygen favors the formation of $n-1$ acid instead.

Herein, the photocatalytic degradation of oxalic acid with simultaneous hydrogen evolution under different conditions was investigated. Oxalic acid was chosen as a model compound due to its high adsorption and strong reductive electron donor properties [19, 20]. In this work, a systematic study of the mechanism(s) of oxalic acid degradation was investigated at a constant pH value during the experiments. The degradation efficiencies were calculated for both, oxygen-free and oxygen-rich systems and the formation of conversion products released in oxygen-free conditions was investigated additionally. Finally, the impact of platinum on the photocatalytic hydrogen evolution and the contribution of oxalic acid as a sacrificial reagent were discussed.

3.4. Experimental

3.4.1. Materials

All chemicals were used as received without any further purification, while the deionized water was supplied by a Millipore Mill-Q system at a resistivity of 18.2 MΩ cm at 25 ºC. Triblock copolymers pluronic F-108, chloroplatinic acid hydrate $H_2PtCl_6 \cdot xH_2O$ ($\geq$99.9%), acetylacetone ($\geq$99%), perchloric acid (70%) and oxalic acid ($\geq$99%) were purchased from Sigma-Aldrich. Titanium(III) chloride (15%) in HCl (10%) was purchased from Merck. Ethanol ($\geq$99.8%) and sodium carbonate anhydrous ($\geq$99%) were purchased from Carl-Roth.

3.4.2. Preparation Methods

The Evaporation-Induced Self-Assembly (EISA) method was employed to synthesize TiO_2 in its pure anatase phase. In a typical synthesis [21], 1 g of F-108 triblock copolymer surfactant was dissolved in 20 mL of ethanol under vigorous stirring followed by the addition of 1.1 mL of acetylacetone and 9.94 mL of $TiCl_3$ solution. After 2 h of continuous stirring at room temperature, the mixture was transferred to a petri dish and heat-treated at 40ºC for 24 h followed by calcination at 400ºC for 12 h (at a heating rate of 4ºC min^{-1}).

TiO_2 loaded with 0.25 wt.% platinum nanoparticles ($Pt_{0.25\%}/TiO_2$) was prepared by following the photodeposition method according to Melvin et *al.* [22]. In a typical experiment; 100 mg of the prepared TiO_2 photocatalyst was added to a mixture of water:methanol (9:1). After purging of the suspension with argon for 30 min, a calculated amount of $H_2PtCl_6 \cdot xH_2O$ was added to the solution. Afterward, the obtained suspension was illuminated with UV(A) light employing a Philips CLEO lamp for 6 h inside a climatic chamber with an adjusted temperature of 15°C. The solid was then collected by centrifugation, followed by repeated washing with distilled water for three times before final drying at 100 °C for 24 h.

3.4.3. Characterization

The X-ray powder diffraction measurements were performed using a Bruker DB Advance diffractometer (Bruker AXS GmbH) with a Bragg-Brentano geometry using Cu Kα radiation. The XRD patterns were used to determine the formed phases as well as to calculate the average crystallite sizes (D) according to Scherrer's formula [23] with $K = 0.94$ as the crystal lattice constant, $\lambda = 0.154$ nm as the x-ray wavelength of CuKα, β as the full width of the peak measured at half maximum intensity, and θ as the Bragg's angle of the peak. BET surface area was measured by the single-point standard Micromeritics FlowSorb II 2300 instrument equipped with a Micromeritics AutoMate 23. TEM measurements were carried out on a Tecnai G2 F20 TMP (FEI) with an acceleration voltage of 200 kV field emission gun (FEG).

3.4.4. Photocatalytic experiments

The photocatalytic experiments were carried out in a closed glass reactor equipped with a cooling jacket. A suspension of (18.7 mmol l^{-1}) bare TiO_2 or (6.2 mmol l^{-1}) $Pt_{0.25\%}/TiO_2$ as a photocatalyst in 215 ml of oxalic acid solution (1.11 mmol l^{-1}) as a model organic compound was illuminated under vigorous stirring. The irradiation unit was placed at a distance of 15 cm from the reactor and it consisted of a Xe arc lamp CSX 450 W (Phillips) and a lamp house LAX 1450 with a power supply SVX 1450 from Müller Elektronik-Optik. The glass reactor was connected to a pH-stat system, which contains a pH electrode combined with an Ag/AgCl reference electrode as shown in

Figure 3-1. The temperature was kept constant at 20 °C during the entire experiment by means of a
thermostatic bath from Julabo. The suspension was continuously purged with pure argon (>
99.999%) or pure oxygen (> 99.999%) during the whole experiment, including adsorption and
irradiation periods. All used gases were supplied by Linde. An adsorption period of 12 hours was
employed to ensure reaching the dark adsorption equilibrium prior to the start of the irradiation.
The pH-stat technique was employed to perform the kinetic measurements at pH 3. The automatic
titration unit consisted of a Titrino 794 from Metrohm equipped with perchloric acid (0.1 mol l^{-1}).
All changes in volume that occurred due to the adding and withdrawing of the liquid were taken
into account when calculating the concentrations at each time step.
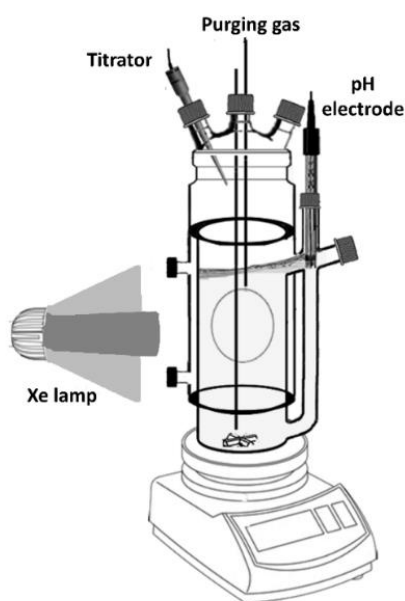
Figure 3-1 schematic diagram of the photocatalytic system.

The photocatalytic degradation of oxalic acid was periodically monitored by High-Performance Ion
Chromatography (HPIC), in which the dissolved amount of oxalic acid was quantified by
withdrawing 1 ml of filtered suspension. The analyses were performed using a Dionex ICS-1000
with a temperature-controlled conductivity detector (constant at 35 °C) and an electro-regenerator
suppressor. Sodium carbonate solution (9×10^{-3} mol l^{-1}) was used as the eluent which was pressed
through an Ion Pac AS9-HC 2×250 mm column equipped with a guard column of Ion Pac AG9-
HC 2×50 mm from Dionex. To quantify the hydrogen gas, which was evolved during the
photocatalytic reforming experiments, a 50 µL gas sample was periodically taken from the reactor
gas headspace over the suspension using a Valco gas-tight sampling syringe equipped with a push-
button valve. The sample was then injected into the injection port of a Shimadzu GC-8A, equipped
with a TCD detector and a stainless-steel GC column (3 m x 2.1 mm) packed with 60/80 molecular
sieve 5A (Sigma-Aldrich). The column temperature was fixed at 80 °C, while the temperature of

both, the injector and the TCD detector were maintained at 120 °C. The photonic efficiencies ξ for both, the oxalic acid degradation and the hydrogen gas formation, have been calculated according to Eqs. (3-1 and 3-2) [24].

$$\xi = \frac{\text{degradation or formation rate } (mol.\,s^{-1})}{\text{photon flux } (mol.\,m^2.\,s^{-1})} = \frac{V.\,\Delta c}{I_0.\,A.\,\Delta t} \qquad (3-1)$$

$$I_0 = \frac{I.\,\lambda}{N_A.\,h.\,c} \qquad (3-2)$$

where V is the suspension volume (0.215 l), $\Delta c/\Delta t$ is the degradation or the formation rate (mol.s^{-1}), A is the illuminated area (8.04 x 10^{-4} m^2), I is the light intensity (W m^{-2}), λ is the corresponding wavelength (m), N_A is the Avogadro's constant (6.02 x 10^{23} mol^{-1}), h is the Planck constant (6.63 x 10^{-34} W s^2) and c is the velocity of light (3 x 10^8 m s^{-1}). From the measurement of the spectral irradiance in the wavelength range from 320 nm to 380 nm at the irradiated window of the photoreactor, the photon flux was found to be I_0= 94 x 10^{-6} mol m^{-2} s^{-1}. Ignoring loss of light due to reflecting and scattering out of the photoreactor, 75.6 x 10^{-9} mole of photons are entering the photoreactor per second.

3.5. Results

3.5.1. Characterization and evaluation of the self-prepared photocatalyst:

Figure 3-2(a) shows the XRD patterns of the prepared TiO$_2$ powders in comparison to the patterns of pure anatase, which confirm the formation of the pure anatase phase with crystallite sizes in the range of 10 nm (according to Scherrer's equation using the average value corresponding to the 101 and 200 reflexes in the calculation). The activity of the prepared TiO$_2$ was compared with that of the commercially available UV100 because both materials possess the pure anatase phase and similar crystallite sizes. Batch photocatalytic measurements were performed in 10 ml crimp glass vials containing 10 mg of TiO$_2$ suspended in 8 ml aqueous oxalic acid (1.11 mmol l^{-1}). The vials were purged with pure argon for 15 min and then irradiated for 120 min by a 1000 W xenon lamp (Hönle UV Technology, Sol 1200). The amount of molecular hydrogen in the gas phase along with the remaining amount of oxalic acid in the liquid phase were quantified. The performances of both photocatalysts are summarized in Table 3-1. There it is presented, that the self-prepared TiO$_2$ photocatalyst shows an around 5% higher photocatalytic degradation activity than the commercial photocatalyst. This enhanced activity was also reflected by the higher performance for the photocatalytic hydrogen evolution since small quantities of hydrogen were detected compared to zero activity of UV100. Due to these facts, the self-prepared photocatalyst was used in further mechanistic studies.

Table 3-1 The performance of self-prepared TiO₂ and UV-100 towards photocatalytic oxalic acid degradation and simultaneous hydrogen evolution.

Photocatalyst	Photocatalytic hydrogen evolution / μmol h^{-1}	Degradation rate of oxalic acid / %
Self-prepared	1.01	96.55
UV100	N/D [a]	91.48

[a] Not detected (N/D)

Figure 3-2(b) presents the TEM image of the prepared Pt/TiO₂, which confirms a good crystallinity of the nanoscaled powder by clearly showing the crystals lattice planes. The grain size ranged around 10 - 12 nm, which is in good agreement with the XRD results. The loaded small platinum nanoparticles (ca. 1-5 nm) can also be clearly seen in Figure 2 (b). Both bare and platinized TiO₂ have a relatively high BET surface area of 121.3 m^2 g^{-1} and 120.4 m^2 g^{-1}, respectively.
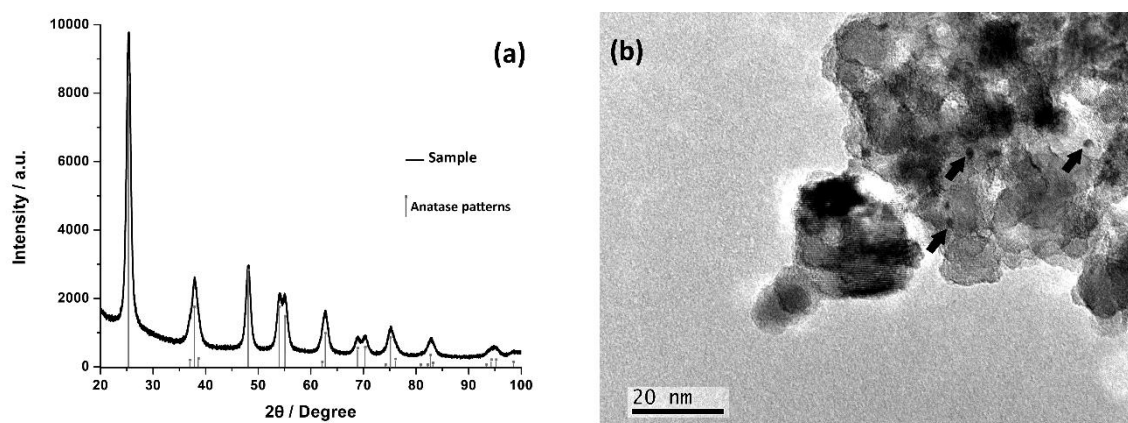
Figure 3-2 XRD patterns of the prepared bare TiO₂ (a), and TEM image for Pt/TiO₂ (b).

3.5.2. The photocatalytic oxidation of oxalic acid in the presence of molecular oxygen

The photocatalytic oxidation of oxalic acid was investigated over bare TiO₂ in an oxygen-rich system using a continuous flow of pure oxygen gas during the adsorption and the photocatalytic periods. Figure 3-3 illustrates the changes in the amounts of oxalic acid (in moles) during the illumination time. As expected, the concentration of oxalic acid was dramatically decreased during the first 30 min of irradiation and complete degradation was achieved in less than 60 min. Perchloric acid was automatically added by the titrator unit to neutralize any produced hydroxyl anions maintaining the pH stable at 3 during the whole experiment. Interestingly, the added amounts of perchloric acid showed a mirror profile of that of the degraded oxalic acid, indicating that the ratio of the produced OH$^-$ to the removed oxalic acid was equal to unity.
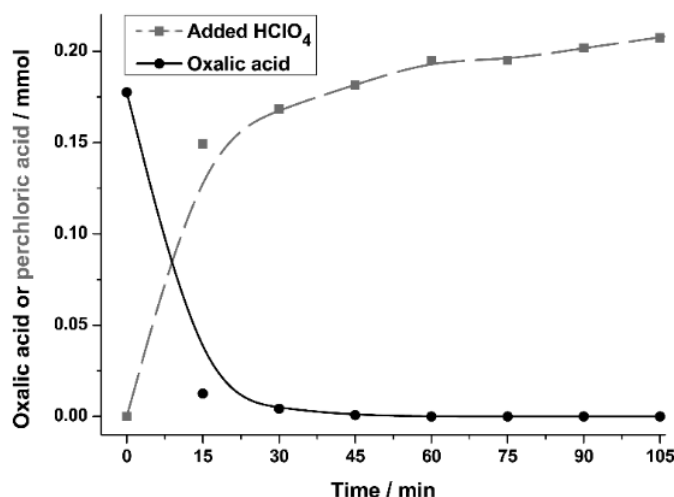
Figure 3-3 the photocatalytic oxidation of oxalic acid using bare TiO$_2$ in the presence of oxygen. The initial oxalic acid concentration was 1.11 mmol l^{-1} at pH 3.

3.5.3. The photocatalytic degradation/reforming of oxalic acid in the absence of molecular oxygen

The photocatalytic degradation of the oxalic acid solution was investigated employing either bare TiO$_2$ or Pt$_{0.25\%}$/TiO$_2$ in an argon atmosphere. Gradual degradation of oxalic acid over bare TiO$_2$ was noticed as shown in Figure 4. Comparing the results illustrated in Figure 3-4 with that in Figure 3-3, it can be clearly noticed that the degradation of oxalic acid was accomplished at a much lower rate under oxygen-free conditions. Only 50% of the initial oxalic acid concentration was converted after 360 min illumination time. In parallel, a gradual continuous formation of formic acid was recorded as shown in Figure 3-4; however formic acid was only formed in a very small amount (molar ratio of 0.14 for formic acid:oxalic acid) compared to the total amount of degraded oxalic acid.
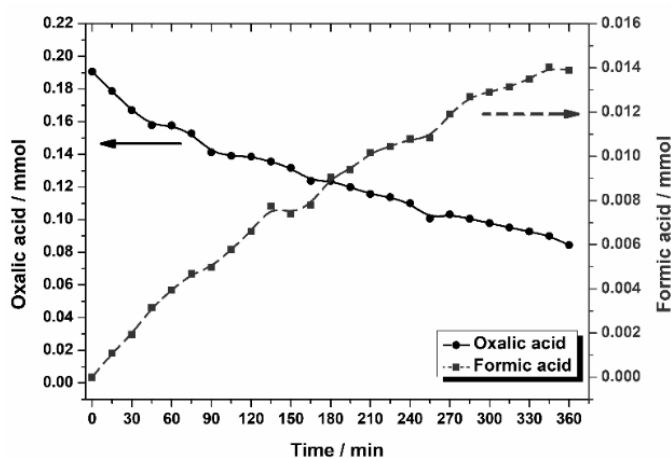
Figure 3-4 the photocatalytic degradation of oxalic acid with the formation of formic acid using bare TiO$_2$ under a continuous flow of argon. The initial oxalic acid concentration was 1.11 mmol l^{-1} at pH 3.

On the other hand, faster conversion of oxalic acid was recorded over the platinized TiO_2 as shown in Figure 3-5. There, 50% of the employed oxalic acid was decomposed within only 60 min, which is ca. 5-fold faster than its degradation over bare TiO_2. Formic acid as a by-product from the conversion of oxalic acid was also formed but in lower concentration in comparison to the case of bare TiO_2. The formation kinetics of formic acid shown in Figure 5 depends highly on the degradation kinetics of oxalic acid. Moreover, the presence of platinum as a co-catalyst facilitates the formation of hydrogen gas during the photocatalytic test. The evolution of hydrogen gas had an induction period during the first 45 min of illumination. The induction period was followed by a constant formation of hydrogen until the complete degradation of oxalic acid was obtained and the further generation of hydrogen gas was unquantifiable.
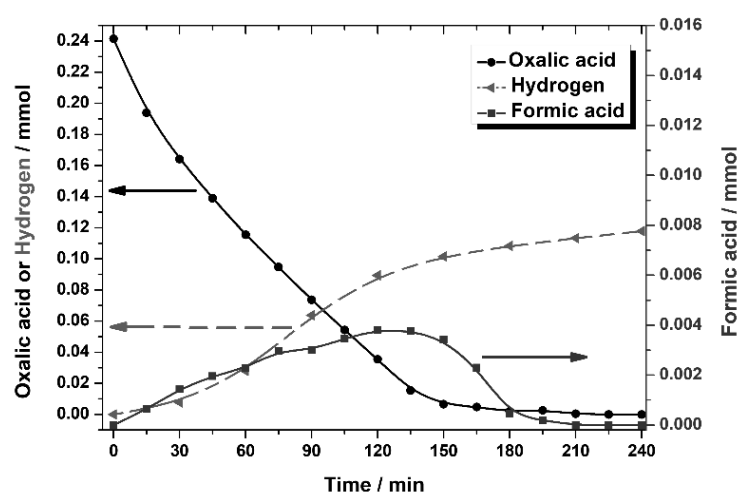
Figure 3-5 the photocatalytic reforming of oxalic acid with the formation of formic acid and hydrogen gas by Pt/TiO₂ under a continuous flow of argon. The initial oxalic acid concentration was 1.11 mmol l⁻¹ at pH 3.

3.6. Discussion

3.6.1. Distribution of the dissolved species at pH 3

The pH of 3 was carefully chosen according to Li et *al.* [17], who reported a maximized photocatalytic hydrogen evolution at about pH 2.9, where oxalic acid is almost exclusively present in the form of $HC_2O_4^-$. It is important to mention that at the applied pH value, i.e., pH 3, $HC_2O_4^-$ is with a fraction exceeding 90% the dominated species in the solution because of its dissociation that occurs at $pK_{a1} = 1.25$ and $pK_{a2} = 4.28$ [18]. Therefore a comparable small concentration of $H_2C_2O_4$ and $C_2O_4^{2-}$ remains in the solution, as shown in Figure 3-6 (a) [25]. On the other hand, when formic acid was released as a by-product, it would present in the form of HCOOH, which is the most dominant species at the employed pH as Figure 6(b) shows [26].
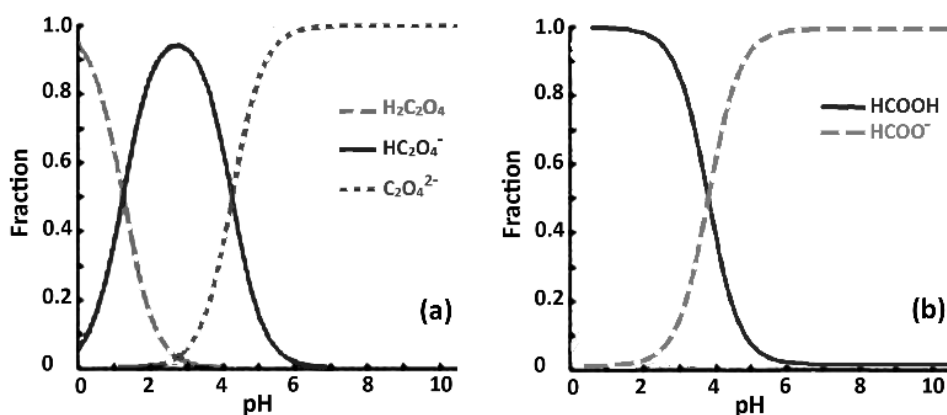
Figure 3-6 distribution of oxalic acid species (a) and formic acid species (b) in the pH regime from 0 to 10. Adapted from ref. [25] and [26].

3.6.2. Photocatalytic oxidation of oxalic acid in the presence of molecular oxygen

The overall photocatalytic oxidation of oxalic acid over illuminated TiO_2 can be summarized by Eqs. (3-3 to 3-5).

$$HC_2O_4^- + \tfrac{1}{2}\,O_2 \xrightarrow{h\nu,\ TiO_2} 2CO_2 + OH^- \tag{3-3}$$

$$H_2C_2O_4 + \tfrac{1}{2}\,O_2 \xrightarrow{h\nu,\ TiO_2} 2CO_2 + H_2O \tag{3-4}$$

$$C_2O_4^{2-} + \tfrac{1}{2}\,O_2 + H_2O \xrightarrow{h\nu,\ TiO_2} 2CO_2 + 2OH^- \tag{3-5}$$
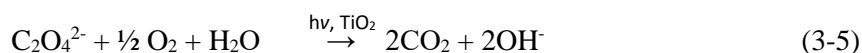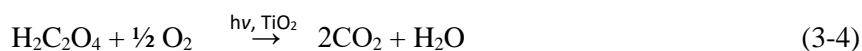
A rise in the pH value is expected, resulting from the generation of OH^- during the photocatalytic oxidation of oxalic acid as described by Eqs. 3-3 and 3-5. This assumption was exactly fulfilled since continuous dosing of perchloric acid was accomplished. There was a direct link between the degradation of oxalic acid and the addition of perchloric acid to stabilize the pH at 3 (see Figure 3-3). As $HC_2O_4^-$ is the dominant species at the working pH, Eq. 3-3 would be the main mechanism contributing to the mineralization of mono-protonated oxalic acid into carbon dioxide and equivalent amounts of OH^-. At 45 min of irradiation, around 0.181 mmol of H^+ was added to neutralize the generation of OH^-, whereas the initial amount of oxalic acid (0.237 mmol) was completely removed from the solution. These calculations show that 76% of the neutralization was achieved during the first 45 min. However, OH^- was continuously formed at a much lower rate after this period. The amount of OH^- reached ca. 0.23 mmol at 105 min, which is equal to the initial amount of oxalic acid. This difference can be attributed to the adsorbed oxalic acid which cannot be directly detected by the HPIC but its ongoing oxidation still forms OH^-. This is in good agreement with the behavior noticed by Ivanova et *al.* [24]. In the presence of molecular oxygen, the formation of $^\bullet OH$ radicals and the reduction of molecular oxygen are thermodynamically favored as proven by Kosanić [27]. The importance of molecular oxygen for the mineralization of oxalic acid is based on its efficient reaction with the photogenerated electrons upon the formation

of superoxide or hydroperoxide radicals. Such a reaction inhibits the electron-hole recombination and leaves the photogenerated holes fully available to react with adsorbed water or organic molecules [28]. Consequently, the formed $^\bullet OH$ radicals could react with $HC_2O_4^-$ forming $^\bullet COOH$ which is consumed by reacting with molecular oxygen to form hydroperoxide radicals (Eq. 3-6). The later radicals could, in turn, transfer to hydrogen peroxide generating molecular oxygen in addition to $^\bullet OH$ radicals (Eqs 7-8). Our HPIC analysis indicates the lack of any intermediates or by-products in solution upon the photocatalytic oxidation of oxalic acid. This result is in agreement with the work of Kosanić [27], who found that the photocatalytic decomposition of oxalic acid at pH 3.5 gave only carbon dioxide.

$$HC_2O_4^- + {}^\bullet OH \quad \rightarrow \quad CO_2 + {}^\bullet COOH + OH^- \qquad (6)$$

$$2HO_2^\bullet \quad \rightarrow \quad H_2O_2 + O_2 \qquad (7)$$

$$H_2O_2 + TiO_2(e^-) \quad \rightarrow \quad {}^\bullet OH + OH^- + TiO_2 \qquad (8)$$
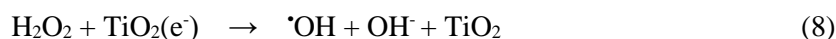
3.6.3. The photocatalytic degradation/reforming of oxalic acid under oxygen-free conditions

A lower decomposition rate of oxalic acid was recorded in the absence of molecular oxygen (see Figure 4). The simultaneous formation of intermediates and the evolution of hydrogen gas indicate different mechanism (s) for the photocatalytic degradation of oxalic acid in oxygen-free conditions. Reactions (Eqs. 3-9 to 3-21), or parts of them, are the potential reactions which accompany the degradation of oxalic acid under oxygen-free conditions, taking into account that some of the mentioned intermediates are just an assumption based on literature references. Oxalic acid, formic acid and OH^- have been traced in-situ during the experiments to prove the mechanism.

$$H_2C_2O_4 \quad \leftrightarrow \quad HC_2O_4^- + H^+ \qquad (3\text{-}9)$$

$$OH^-_{(ads)} + TiO_2(h^+) \rightarrow {}^\bullet OH + TiO_2 \qquad (3\text{-}10)$$

$$HC_2O_4^- + {}^\bullet OH \rightarrow HC_2O_4^\bullet + OH^- \qquad (3\text{-}11)$$

$$HC_2O_4^- + TiO_2(h^+) \rightarrow HC_2O_4^\bullet + TiO_2 \qquad (3\text{-}12)$$

$$HC_2O_4^\bullet \rightarrow HCO_2^\bullet + CO_2 \qquad (3\text{-}13)$$

$$HCO_2^\bullet \leftrightarrow {}^\bullet CO_2^- + H^+ \qquad (3\text{-}14)$$

$${}^\bullet CO_2^- + TiO_2 \rightarrow CO_2 + TiO_2(e^-) \qquad (3\text{-}15)$$

$$H^+ + TiO_2(e^-) \rightarrow H^\bullet + TiO_2 \qquad (3\text{-}16)$$

$${}^\bullet CO_2^- + H^\bullet \rightarrow HCOO^- \qquad (3\text{-}17)$$

$$HCOO^\bullet + TiO_2(e^-) \rightarrow HCOO^- + TiO_2 \qquad (3\text{-}18)$$

$$\cdot CO_2^- + \cdot CO_2^- \rightarrow CO_2 + CO_2^{2-} \tag{3-19}$$
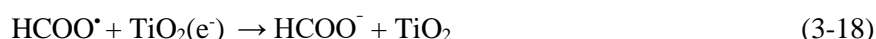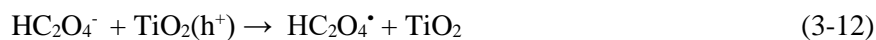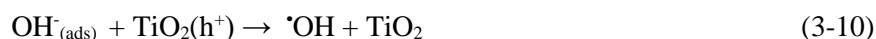
The photogenerated holes in the valance band of TiO_2 are able to react with the adsorbed species including both, the organic compounds and the water molecules or hydroxyl ions (Eqs 3-12 and 3-10, respectively) [2]. Following the deprotonation of one proton at pH 3 (Eq. 3-9), the degradation of $HC_2O_4^-$ could be initiated by two possible routes; either indirectly by $\cdot OH$ radicals which were formed by the oxidation of OH^- (Eqs 3-10 and 3-11), or directly by the photogenerated holes (Eq. 3-12). Once the $HC_2O_4^\cdot$ radical is formed it will rapidly undergo further degradation to form carbon dioxide while simultaneously injecting electrons in the conduction band of TiO_2 according to the so-called current doubling effect (Eqs 3-13 to 3-15). The lower photocatalytic efficiency of bare TiO_2 towards the degradation of oxalic acid in an oxygen-free system can be attributed to the absence of molecular oxygen, which plays a crucial role in scavenging the photogenerated electrons. Molecular oxygen can further enhance the process by generating highly oxidative $\cdot OH$ radicals. The same behavior has been proven for other organic compounds by many researchers, such as Sakagushi et al., who recorded a more facile photocatalytic degradation of 2-propanol under aerobic conditions in comparison with oxygen-free systems. They explained this effect by the contribution of molecular oxygen in the decomposition pathways, as well as by the role of molecular oxygen initiating the photogeneration of $\cdot OH$ radicals themselves [29].

Abstracting one electron from $HC_2O_4^-$ by an $\cdot OH$ radical results in the formation of $HC_2O_4^\cdot$, according to Eq. 3-11. The formation of such radicals has been observed by Yamada et al. using nanosecond laser flash photolysis [30]. $HC_2O_4^\cdot$ radical is known to decompose to carbon dioxide and carbon dioxide radical anion $\cdot CO_2^-$ (Eqs. 3-13, 3-14). The formation of $\cdot CO_2^-$ has been detected by Mulazzani et al. who conducted continuous and pulse radiolysis experiments using methylviologen as a mechanistic probe [31] and by Kaoufi and Bard through cyclic voltammetry experiments [32]. Because $\cdot CO_2^-$ is a strong reductive agent ($E^0 = -1.9$ V) [31], an electron transfer from $\cdot CO_2^-$ to TiO_2 (Eq. 3-15) can easily occur. This mechanism is in agreement with the work of Yamada et al., who reported that two equivalents of $QuPh^\cdot–NA$ were formed by the photoreduction of 2-phenyl-4-(1-naphthyl)-quinolinium ion ($QuPh^+–NA$) by oxalate due to an electron transfer from $\cdot CO_2^-$ to $QuPh^+–NA$ [33].

Compared to the bare TiO_2 the enhancement of the oxalic acid degradation over platinized TiO_2, shown in Figure 3-5, is related to the presence of platinum as a co-catalyst, which acts as an antenna, by collecting the photogenerated electrons. This improves the separation between the charge carriers and prevents their recombination, which increases the available amount and lifetime of photogenerated holes. However, even in the presence of platinum nanoparticles on the surface of TiO_2, the oxygen-free system is still much less effective in degrading oxalic acid in comparison to

the oxygen-rich system. A similar result was reported by Kim and Choi for the photocatalytic degradation of trichloroacetate on TiO_2, where the presence of molecular oxygen had a strong positive effect (more than 6-fold) on the activity of bare anatase phase TiO_2 compared to the same test carried in the presence of N_2 [34]. They found also that platinization significantly enhanced the reactivity by reducing the electron-hole pair recombination rate through the formation of a Schottky-barrier. The pH_{zpc} of TiO_2 is ~ 5.5, hence one expects a strong interaction between the positively-charged TiO_2 surface and $HC_2O_4^-$ molecules at pH = 3, which is used in this work [17]. Therefore, direct photocatalytic oxidation of oxalic acid on the surface of TiO_2 is expected.

The formation of formic acid as a by-product is most likely happening either by the reaction of hydrogen radicals with $^\bullet CO_2^-$ (Eqs. 3-16 and 3-17), or by releasing carbon dioxide from oxalic acid radicals while simultaneously generating formic acid radicals (Eqs. 3-13 and 3-18). However, the amount of released formic acid was very small compared to the corresponding converted amount of oxalic acid. This low conversion yield is expected because $CO_2^{\bullet -}$ can easily inject their electrons in the conduction band of TiO_2; hence they transform to their thermodynamically most stable form, which is carbon dioxide (Eq. 3-15). After a total degradation of 10% and 50% over bare TiO_2, the ratios between the degraded oxalic acid to the formed formic acid were 8.4% and 15.8%, respectively. It is obvious that the formation of formic acid had a close dependency on the degradation of oxalic acid since its quantity was continuously raised with the ongoing decomposition of oxalic acid. Monocarboxylic acids have previously been reported to be formed upon the anaerobic degradation of elementary dicarboxylic acids, such as oxalic acid [15]. Yamada et al. detected the formation of formic acid by ^1H NMR during the photocatalytic hydrogen evolution from deaerated mixed solutions of QuPh$^+$–NA, oxalate and platinum nanoparticles [30]. They reported that some portion of the oxalate acts as a one-electron donor to provide formic acid and suggested that $^\bullet CO_2^-$ derived from $HC_2O_4^\bullet$ radicals may be further reduced by hydrogen adsorbed on platinum nanoparticles to provide formate. Lower quantities of formic acid were formed when platinum was employed as a co-catalyst. Interestingly, a simultaneous degradation of formic acid was accomplished once the complete decomposition of oxalic acid in solution was achieved (see Figure 3-5). This subsequent fast oxidation of formic acid could be explained by the presence of platinum acting as a co-catalyst. After a total degradation of 10% and 50% in the presence of platinum, the ratio between the degraded quantity of oxalic acid and the formed quantity of formic acid were 39.6% and 53.1%, respectively. Eqs. 3-18 and 3-19 describe the dominating reactions that contribute to the formation of formic acid in the presence of a co-catalyst. In both cases in the course of the formic acid formation, the simultaneous consumption of a very small amount of protons in the solution is expected.

The importance of $^\bullet$OH radicals in the photocatalytic degradation of oxalic acid was then evaluated by conducting a homogeneous photodegradation under the same oxygen-free conditions and without the use of any photocatalyst. Instead of TiO_2, a solution of potassium nitrate (0.3 mmol.l^{-1}) was added and the experiment was conducted as described above. It is well reported [35, 36] that nitrate solutions undergo a photolysis reaction upon illumination and generate atomic oxygen radical anions, which in turn could react within nanoseconds with protons producing $^\bullet$OH radicals as presented in Eqs. 3-20 and 3-21, respectively. Table 3-2 presents the changes in both, oxalic and formic acid concentrations under oxygen-free conditions in heterogeneous and homogeneous systems, respectively. In direct comparison, 36.8% of the oxalic acid was degraded homogeneously by photolytically generated $^\bullet$OH radicals in contrast to 51.8% upon photocatalytic degradation. This result confirms the crucial role of $^\bullet$OH radicals in the degradation of oxalic acid in our photocatalytic system. On the other hand, formic acid was also formed during the homogeneous photodegradation of oxalic acid. Interestingly, both reaction systems released a similar amount of formic acid.

Table 3-2 Comparison between the heterogeneous and homogeneous photodegradation of oxalic acid.

System	Remaining oxalic acid / mmol	Degradation of oxali acid / %	Maximum amount of formic acid / mmol
TiO_2	0.092	51.83	0.0135
Pt/TiO_2	0	100.00	0.0055
NO_3^-	0.150	36.84	0.0121

$$NO_3^- + h\nu \rightarrow NO_2^\bullet + O^{\bullet -} \qquad (3\text{-}20)$$

$$O^{\bullet -} + H^+ \rightarrow {}^\bullet OH \qquad (3\text{-}21)$$

The photocatalytic reforming of oxalic acid is generally accompanied by the formation of both, carbon dioxide and molecular hydrogen according to Eq. 3-22. Although the photocatalytic experiment was performed under oxygen-free conditions, the absence of a suitable co-catalyst diminishes the capability for the protons to be reduced. The relatively high overpotential of the hydrogen evolution reaction almost completely suppresses the formation of molecular hydrogen on the unmodified surface of TiO_2; hence the detection of such trace amounts of hydrogen gas, if formed, was difficult. The presence of platinum as a co-catalyst promoted the photocatalytic generation of hydrogen gas over Pt/TiO_2, as shown in Figure (5) for our experiments. A constant formation of hydrogen until the complete degradation of oxalic acid followed an induction period of 45 min. We think that during this induction period, the little generated amount of molecular hydrogen diffused in the gas headspace, which represents around a quarter of the total reactor volume. The detection of such small quantities was difficult as their values were close to the

hydrogen detection limit of the employed GC system (DL $\geq$ 0.009 mmol calculated from the signal to noise ratio). This assumption could be further verified by employing a smaller glass vessel with less headspace. In this case, close to no induction period of the hydrogen evolution could be observed.

The contribution of oxalic acid in the photocatalytic formation of hydrogen gas was calculated based on the ratio between the total moles of formed hydrogen gas to those of consumed oxalic acid. Upon complete degradation, the molar ratio of hydrogen/oxalic acid was found to be 0.6 instead of a theoretical ratio of 1 according to Eq. (3-22). The formation of formic acid that could in principle consume the protons from the solution may participate in this unexpected low ratio, but for sure it is not the only reason. Yamada et *al.* obtained a similar effect, where the hydrogen yields of the photocatalytic reactions have not reached 100% using oxalate as a sacrificial electron donor, even after optimization of the reaction conditions. They ascribed this result to the formation of formate as a by-product during the photocatalytic reaction, which was unable to act as an electron donor at low concentrations [30]. Li et *al.* [17] noticed also that the amount of hydrogen formed was consistent with the amount of reacted oxalate during the first steps of the reaction, however, the hydrogen evolution rate became lower than the degradation rate of oxalate with increasing reaction time. Oxalic acid has been proven to form hydrogen at faster rates than formic acid and formaldehyde on Pt/TiO$_2$ under UV illumination [37]. However, the negative influences of formic acid on the generation of molecular hydrogen would be relatively negligent, because formic acid was only formed as a minor product in our study. Another possibility for such low hydrogen yield could be the direct reaction of oxalic acid to carbon dioxide either with hydrogen peroxide or with molecular oxygen, which resulted from the decomposition of hydrogen peroxide. These kinds of reactions prevent the contribution of oxalic acid in the hydrogen formation. However, further investigations should be done to explain this unexpected low yield.

$$H_2C_2O_4 \rightarrow H_2 + 2CO_2 \hspace{4cm} (3\text{-}22)$$

3.6.4. Observations relating to the photocatalytic degradation of oxalic acid:

Table 3-3 presents the photonic efficiencies and several kinetic parameters regarding the different investigated reactions. The rate of photocatalytic degradation decreased in the order of TiO$_2$(O$_2$) $\succ$ Pt/TiO$_2$(Ar) > TiO$_2$(Ar). Here, the important role of molecular oxygen for the complete mineralization of organic pollutants in water is clearly shown, although it prevents the generation of hydrogen. On the contrary, working with bare TiO$_2$ in the absence of molecular oxygen does not only negatively affect the degradation rate but also produces only a negligible amount of hydrogen. The presence of platinum as a co-catalyst was an added value to accelerate both sides, the

degradation of oxalic acid and the simultaneous generation of hydrogen gas. The presence of such co-catalyst decreases the recombination of charge carriers [8] by accumulating the photogenerated electrons on its surface for the reduction of protons to molecular hydrogen and leaving the holes behind for the oxidation reactions. Based on the obtained results and on the assumptions from previous works regarding the photogenerated radicals, the photoreforming of oxalic acid over TiO_2 in oxygen-free conditions can follow the main mechanism suggested in Scheme 3-1.

Table 3-3 kinetic parameters and photonic efficiencies delivered from the studied photocatalytic system.

#	Kinetics of degradation	$K_{degradation}$ min^{-1}	$t_{1/2\ degradation}$ min	OA/FA ^{c} molar ratio	OA/H$_2$ ^{d} molar ratio	ξ^e oxalic %	ξ^e H$_2$ %
Oxygen+ bare TiO_2	1st order	93.1 x10^{-3}	7.45	N/A^a	N/A	0.522	N/A
O$_2$-free+ bare TiO_2	1st order	1.6 x10^{-3}	435.9	15.8	N/D^b	0.057	N/D
O$_2$-free+ Pt/TiO_2	1st order	13.5 x10^{-3}	51.2	53.2	0.6	0.246	0.126

^{a} Not applicable (N/A), ^{b} Not detected (N/D), ^{c} the molar ratio of oxalic acid (OA)/formic acid (FA) calculated at 50% degradation, ^{d} the molar ratio of oxalic acid (OA)/H$_2$ calculated at 50% degradation, ^{e} the photonic efficiency (ξ).
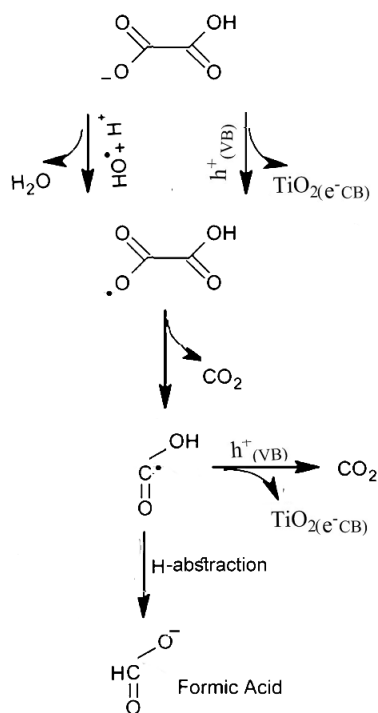
Scheme 3-1 the suggested reaction sequence of the oxalic acid photoreforming reaction, based on the results employing bare TiO_2.

Bare TiO_2 was found to be significantly less active than Pt/TiO_2. For this reason, a higher concentration of bare TiO_2 has been employed in the experiments in order to obtain a quantifiable concentration of the product in a reasonable period of time. Since the photocatalytic process highly depends on the interaction of light and TiO_2, the activity could be significantly reduced as a result of shading and scattering of light in high concentrated TiO_2 suspensions [38]. To investigate the possible shading effect by using such a relatively higher concentration of TiO_2, a similar experiment in a lower concentration of bare TiO_2 (6.2 mmol l^{-1}) was conducted. The same trend of oxalic acid degradation was observed but at a much lower rate than in the case of the higher TiO_2 concentration. In addition, the formation of formic acid also possessed the same trend but with a lower formation rate. Furthermore, the obtained product concentrations were below the detection limits during the first 30 min. Based on these observations, the negative effect of shading by using a higher concentration of TiO_2 can be considered as negligible.

The distinction between a semiconductor-assisted photoreaction (turnover number TON < 1) and a catalyzed photoreaction (TON $\geqslant$ 1) seems difficult in the case of heterogeneous photocatalysis because TiO_2 fulfills the dual role of a light harvester and a catalytic surface [39]. As an example, the photocatalyzed reduction by Pt/TiO_2 in the presence of some electron donors, which have been claimed to be photocatalytic, may be described more appropriately as semiconductor-assisted photoreactions [39, 40]. In the heterogeneous photocatalytic systems, the reactions are accomplished over the active sites on the surface of TiO_2. Unfortunately, the difficulties in determining the exact number of active sites make the calculation of TON rather challenging. The surfaces of the anatase nanoparticles have been well characterized by Mendive et *al.* [41] in terms of adsorption sites available for oxalic acid molecules. They found that at pH 3.7, the adsorption on hydrated anatase surfaces was through mono and bidentate complexes and the repulsion forces limited the maximum surface coverage. A number of 3 was found to be a maximum number of adsorbed oxalic acid molecules per nm^2 on nanoparticulate anatase [41], indicating that in case oxalic acid is adsorbed in a monodentate manner. The other available sites at the (100) surface remain occupied by water molecules and can be ceded to form bidentate structures. Taking into consideration the value of BET surface area, and a maximum of 3 active sites per nm^2 (equivalent to the proposed number of the adsorbed oxalic acid molecules), the concentration of active sites in the suspension was found to be 0.9 mmol.l^{-1} for bare TiO_2 and 0.3 mmol.l^{-1} for Pt/TiO_2. Assuming a complete degradation of the probe molecule to carbon dioxide, TON of 1.23 and 3.68 can be calculated for bare and platinized TiO_2, respectively. Based on these calculated values and taking into account the above-mentioned assumptions, the studied processes could be considered as photocatalytic.

3.7. Conclusion

In this study, TiO_2 with the relatively high surface area was successfully synthesized in its pure anatase phase through the EISA method and its photocatalytic activity was found to be higher than that of the commercially available photocatalyst UV100. The prepared TiO_2 was modified by platinum nanoparticles in order to enhance the hydrogen evolution from an aqueous solution of oxalic acid. The results suggest that platinum nanoparticles loaded on TiO_2 turn oxalic acid into an efficient electron donor, allowing the photocatalytic formation of hydrogen over the platinum nanoparticles. It was shown that the oxygen-free conversion of oxalic acid proceeds through a photocatalytic light-induced Kolbe reaction, generating formic acid as a minor product. Within the studied pH regime, the photocatalytic reforming was carried out on both, direct and indirect pathways. The direct one is initiated by the photogenerated holes that oxidize the adsorbed $HC_2O_4^-$ to $HC_2O_4^{\bullet}$ radicals followed by the formation of the photo-Kolbe products. The indirect pathway could be in turn initiated by the oxidation of adsorbed H_2O/OH^- *via* the photogenerated holes resulting in the formation of $^{\bullet}OH$ radicals. The amount of molecular hydrogen obtained during the degradation reaction was found to be lower than the theoretically calculated value. This may be due to the formation of formic acid and/or the reaction of oxalic acid with the formed hydrogen peroxide. However, this point needs to be clarified further in future investigations. Our study confirms the potential use of photocatalyst-metal systems to efficiently convert organic pollutants to valuable alternative fuels. However, further engineering aspects need to be optimized.

3.8. Acknowledgments

3.9. References

1.   Freitag, J. and D.W. Bahnemann, *Influence of the Metal Work Function on the Photocatalytic Properties of TiO₂ Layers on Metals.* ChemPhysChem, 2015. **16**(12): p. 2670-2679.
2.   Schneider, J., et al., *Understanding TiO2 Photocatalysis: Mechanisms and Materials.* Chemical Reviews, 2014. **114**(19): p. 9919-9986.
3.   Irawaty, W., F.E. Soetaredjo, and A. Ayucitra, *Understanding the Relationship between Organic Structure and Mineralization Rate of TiO₂-mediated Photocatalysis.* Procedia Chemistry, 2014. **9**(Supplement C): p. 131-138.
4.   Friehs, E., et al., *Toxicity, phototoxicity and biocidal activity of nanoparticles employed in photocatalysis.* Journal of Photochemistry and Photobiology C: Photochemistry Reviews, 2016. **29**(Supplement C): p. 1-28.

5.   Singh, A., et al., *Biohydrogen Production from Lignocellulosic Biomass: Technology and Sustainability.* Energies, 2015. **8**(11): p. 12357.

6.   Ismail, A.A. and D.W. Bahnemann, *Photochemical splitting of water for hydrogen production by photocatalysis: A review.* Solar Energy Materials and Solar Cells, 2014. **128**(Supplement C): p. 85-101.

7.   Hakki, A., et al., *Hydrogen Production by Heterogeneous Photocatalysis*, in *Reference Module in Chemistry, Molecular Sciences and Chemical Engineering*. 2017, Elsevier.

8.   Schneider, J. and D.W. Bahnemann, *Undesired Role of Sacrificial Reagents in Photocatalysis.* The Journal of Physical Chemistry Letters, 2013. **4**(20): p. 3479-3483.

9.   Ahmed, L.M., et al., *Role of Platinum Deposited on TiO₂ in Photocatalytic Methanol Oxidation and Dehydrogenation Reactions.* International Journal of Photoenergy, 2014. **2014**: p. 9.

10.   Zhang, H., G. Chen, and D.W. Bahnemann, *Photoelectrocatalytic materials for environmental applications.* Journal of Materials Chemistry, 2009. **19**(29): p. 5089-5121.

11.   Pichat, P., *Index*, in *Photocatalysis and Water Purification*. 2013, Wiley-VCH Verlag GmbH & Co. KGaA. p. 399-406.

12.   Kim, J., D. Monllor-Satoca, and W. Choi, *Simultaneous production of hydrogen with the degradation of organic pollutants using TiO₂ photocatalyst modified with dual surface components.* Energy & Environmental Science, 2012. **5**(6): p. 7647-7656.

13.   Romão, J., et al., *Photocatalytic methanol assisted production of hydrogen with simultaneous degradation of methyl orange.* Applied Catalysis A: General, 2016. **518**(Supplement C): p. 206-212.

14.   Peterson, A., et al., *Simultaneous Photodegradation and Hydrogen Production with TiO₂/Pt/CdS Using UV–Visible Light in the Presence of a Sacrificial Agent and a Pollutant*, in *Materials and Processes for Solar Fuel Production*, B. Viswanathan, V. Subramanian, and J.S. Lee, Editors. 2014, Springer New York: New York, NY. p. 153-171.

15.   Sun, Y., et al., *An Unexpected Fluctuating Reactivity for Odd and Even Carbon Numbers in the TiO₂-Based Photocatalytic Decarboxylation of C₂-C₆ Dicarboxylic Acids.* Chemistry – A European Journal, 2014. **20**(7): p. 1861-1870.

16.   Puga, A.V., *Photocatalytic production of hydrogen from biomass-derived feedstocks.* Coordination Chemistry Reviews, 2016. **315**(Supplement C): p. 1-66.

17.   Li, Y., G. Lu, and S. Li, *Photocatalytic hydrogen generation and decomposition of oxalic acid over platinized TiO₂.* Applied Catalysis A: General, 2001. **214**(2): p. 179-185.

18.   Draganic, Z.D., M.M. Kosanic, and M.T. Nenadovic, *Competition studies of the hydroxyl radical reactions in some .gamma.-ray irradiated aqueous solutions at different pH values.* The Journal of Physical Chemistry, 1967. **71**(8): p. 2390-2395.

19.   Pellegrin, Y. and F. Odobel, *Sacrificial electron donor reagents for solar fuel production.* Comptes Rendus Chimie, 2017. **20**(3): p. 283-295.

20.   Mogyorósi, K., et al., *Comparison of the substrate dependent performance of Pt-, Au- and Ag-doped TiO₂ photocatalysts in H₂-production and in decomposition of various organics.* Reaction Kinetics and Catalysis Letters, 2009. **98**(2): p. 215.

21.   Chen, L., et al., *Synthesis of Well-Ordered Mesoporous Titania with Tunable Phase Content and High Photoactivity.* The Journal of Physical Chemistry C, 2007. **111**(32): p. 11849-11853.

22.   Melvin, A.A., et al., *M-Au/TiO₂ (M = Ag, Pd, and Pt) nanophotocatalyst for overall solar water splitting: role of interfaces.* Nanoscale, 2015. **7**(32): p. 13477-13488.

23.   Patterson, A.L., *The Scherrer Formula for X-Ray Particle Size Determination.* Physical Review, 1939. **56**(10): p. 978-982.

24.   Ivanova, I., et al., *Photocatalytic degradation of oxalic and dichloroacetic acid on TiO₂ coated metal substrates.* Catalysis Today, 2013. **209**(Supplement C): p. 84-90.

25.   Wenger, M. and J. Bernstein, *Designing a Cocrystal of γ-Amino Butyric Acid.* Angewandte Chemie International Edition, 2006. **45**(47): p. 7966-7969.

26.   Li, Q., et al., *One step recovery of succinic acid from fermentation broths by crystallization.* Separation and Purification Technology, 2010. **72**(3): p. 294-300.

27. Kosanić, M.M., *Photocatalytic degradation of oxalic acid over TiO₂ power.* Journal of Photochemistry and Photobiology A: Chemistry, 1998. **119**(2): p. 119-122.

28. Turchi, C.S. and D.F. Ollis, *Photocatalytic degradation of organic water contaminants: Mechanisms involving hydroxyl radical attack.* Journal of Catalysis, 1990. **122**(1): p. 178-192.

29. Sakaguchi, N., et al., *Effect of dissolved oxygen and lanthanide ions in solution on TiO₂ photocatalytic oxidation of 2-propanol.* Research on Chemical Intermediates, 2006. **32**(2): p. 95-101.

30. Yamada, Y., et al., *Photocatalytic hydrogen evolution from carbon-neutral oxalate with 2-phenyl-4-(1-naphthyl)quinolinium ion and metal nanoparticles.* Physical Chemistry Chemical Physics, 2012. **14**(30): p. 10564-10571.

31. Mulazzani, Q.G., et al., *Interaction of formate and oxalate ions with radiation-generated radicals in aqueous solution. Methylviologen as a mechanistic probe.* The Journal of Physical Chemistry, 1986. **90**(21): p. 5347-5352.

32. Kanoufi, F. and A.J. Bard, *Electrogenerated Chemiluminescence. 65. An Investigation of the Oxidation of Oxalate by Tris(polypyridine) Ruthenium Complexes and the Effect of the Electrochemical Steps on the Emission Intensity.* The Journal of Physical Chemistry B, 1999. **103**(47): p. 10469-10480.

33. Yamada, Y., et al., *A composite photocatalyst of an organic electron donor-acceptor dyad and a Pt catalyst supported on semiconductor nanosheets for efficient hydrogen evolution from oxalic acid.* Catalysis Science & Technology, 2015. **5**(1): p. 428-437.

34. Kim, S. and W. Choi, *Dual Photocatalytic Pathways of Trichloroacetate Degradation on TiO₂: Effects of Nanosized Platinum Deposits on Kinetics and Mechanism.* The Journal of Physical Chemistry B, 2002. **106**(51): p. 13311-13317.

35. Zafiriou, O.C., *Sources and reactions of OH and daughter radicals in seawater.* Journal of Geophysical Research, 1974. **79**(30): p. 4491-4497.

36. Brezonik, P.L. and J. Fulkerson-Brekken, *Nitrate-Induced Photolysis in Natural Waters: Controls on Concentrations of Hydroxyl Radical Photo-Intermediates by Natural Scavenging Agents.* Environmental Science & Technology, 1998. **32**(19): p. 3004-3010.

37. Li, Y., G. Lu, and S. Li, *Photocatalytic production of hydrogen in single component and mixture systems of electron donors and monitoring adsorption of donors by in situ infrared spectroscopy.* Chemosphere, 2003. **52**(5): p. 843-850.

38. Dalrymple, O.K. and D.Y. Goswami, *Mechanistic Modeling of Photocatalytic Water Disinfection*, in *Advances in Photocatalytic Disinfection*, T. An, H. Zhao, and P.K. Wong, Editors. 2017, Springer Berlin Heidelberg: Berlin, Heidelberg. p. 273-315.

39. Serpone, N., et al., *Turnovers and photocatalysis: A mathematical description.* Journal of Photochemistry and Photobiology A: Chemistry, 2000. **130**(2): p. 83-94.

40. Childs, L.P. and D.F. Ollis, *Is photocatalysis catalytic?* Journal of Catalysis, 1980. **66**(2): p. 383-390.

41. Mendive, C.B., et al., *Adsorption of oxalate on anatase (100) and rutile (110) surfaces in aqueous systems: experimental results vs. theoretical predictions.* Physical Chemistry Chemical Physics, 2009. **11**(11): p. 1794-1808.

Chapter Four: Photocatalytic H$_2$ Evolution from Oxalic Acid: Effect of Co-catalysts and Carbon Dioxide Radical Anion on the Surface Charge Transfer Mechanisms

4.1. Foreword

This chapter contains the article "Photocatalytic H$_2$ Evolution from Oxalic Acid: Effect of Co-catalysts and Carbon Dioxide Radical Anion on the Surface Charge Transfer Mechanisms" by Yamen AlSalka, Osama Al-Madanat, Mariano Curti, Amer Hakki, and Detlef W. Bahnemann. Reproduced with permission from ACS Applied Energy Materials (Just Accepted Manuscript, DOI: 10.1021/acsaem.0c00826). Copyright 2020 American Chemical Society.

4.2. Abstract

Photocatalytic reforming of carboxylic acids on co-catalyst-loaded semiconductors, e.g., of oxalic acid on Pt/TiO$_2$, is an attractive process for H$_2$ generation that has been studied for many years. Experimental support for the surface reaction mechanisms, nevertheless, is still insufficient. Herein, the mechanism of the photocatalytic conversion of oxalic acid in anaerobic conditions together with the total yields have been deeply investigated employing self-prepared TiO$_2$ photocatalysts loaded with different noble metals (Pt and/or Au). While the photocatalytic H$_2$ evolution remarkably occurs over bare TiO$_2$, the loading with a co-catalyst significantly boosts the activity. Pt/TiO$_2$ shows higher photonic efficiencies than Au/TiO$_2$, whereas bimetallic Au-Pt/TiO$_2$ has no additional advantage. The turnover numbers (TONs) of complete degradation have been calculated as 4.86 and 12.14 over bare TiO$_2$ and noble-metals/TiO$_2$, respectively, confirming true photocatalytic processes. The degradation of oxalic acid has been experimentally confirmed to proceed *via* the photo-Kolbe reaction forming $^\bullet CO_2^-$ radicals. The contribution of the current doubling mechanism and the effect of the disproportionation reaction of radicals on the total yield is discussed, showing a loss of efficiency due to secondary reactions. A remarkable diversion of H$_2$ evolution was recorded in all cases with Pt/TiO$_2$ showing ca. 30% decrease in the evolved amounts of H$_2$ with respect to the theoretically expected amount. This diversion can be attributed to (i) the increase in charge carriers recombination due to oxalic acid consumption, (ii) the incomplete scavenging of the photogenerated electrons by Pt nanoparticles as proved by solid-phase EPR spectroscopy, (iii) the formation of by-products, which depends on the nature of the co-catalyst, and (iv) the disproportionation of $^\bullet CO_2^-$ radicals, which reduces the contribution of the current doubling. Formate and formaldehyde have

been experimentally detected and EPR spin-trap experiments confirm a surface charge transfer mechanism through the TiO$_2$/oxalic acid interface.

Keywords Photocatalysis, photoreforming, oxalic acid, H$_2$ production, carbon dioxide radical anion, TiO$_2$.

4.3. Introduction

Conventional energy sources are in progressive depletion, and they are related in one way or another to the environmental problems. The growing world energy consumption and the global trend towards sustainability highlight our biggest challenge, i.e., the development of environmentally friendly energy based on renewable sources. Due to its high enthalpy of combustion and the possibility to produce it from renewable sources, molecular hydrogen is considered the most promising alternative fuel to satisfy energy demands [1]. However, H$_2$ production by a sustainable process is still a challenging task. The photocatalytic reforming of organic substrates has emerged as a clean candidate. The key component in such a system is the photocatalyst that generates, with the help of sufficient light energy, holes to oxidize the organic molecules and electrons to drive proton reduction and thus H$_2$ evolution. Titanium dioxide is an inexpensive and stable photocatalyst with well-positioned band edges that give sufficient driving force for many photocatalytic reactions [2]. Bare TiO$_2$, however, shows low photocatalytic activity for H$_2$ evolution due to the fast recombination of the photogenerated charge carriers and the kinetics of proton reduction by its conduction band electrons [3]. It is well known that the activity of TiO$_2$ is improved by loading co-catalysts on its surface, such as noble metals, to hinder recombination and enhance the interfacial charge transfer to the adsorbed molecules. Among various noble metals, Pt and Au are reported to be appropriate co-catalysts to promote the H$_2$ evolution reaction (HER). Nevertheless, noble metals can also catalyze the back-reaction of H$_2$ and O$_2$, yielding H$_2$O [4, 5].

The reaction mechanism on the surface of TiO$_2$ is the core of the photocatalytic reforming [6], which is determined by the structural and electronic properties of both the photocatalyst and the HER co-catalyst. Identification of reaction pathways and intermediates while changing the photocatalyst and/or the co-catalyst is the key to understand and thus improve the overall photocatalytic reforming process. Significant progress in this direction has come from computational simulations. For example, Mendive et *al.* have done comprehensive studies concerning the adsorption of oxalic acid on TiO$_2$ surfaces including possible surface reaction mechanisms [7, 8]. Although their model predicted the formation of several by-products upon irradiation, the formation of such products has not been experimentally confirmed yet [9].

Oxalic acid is considered as a water pollutant resulting from sources such as the textile and metallurgical industries [10]. Oxalic acid is also formed as an intermediate during the mineralization of a variety of organic compounds [11]. Although H$_2$ production rates employing oxalic acid as an electron donor have been reported to be higher than those employing formic acid or formaldehyde over Pt/TiO$_2$ under UV irradiation [12], most of the previous reports in which oxalic acid was used have shown the evolution of non-stoichiometric H$_2$ amounts [10, 13, 14]. Nevertheless, most of the researchers consider only the reaction rates, but not the total yields of photocatalytic reactions because the complete conversion of the substrate usually requires very long times.

Furthermore, only a few reports have been published discussing the effect of co-catalysts on the TiO$_2$-mediated photocatalytic reforming of oxalic acid in aqueous suspension. Moreover, little is known about the surface reaction mechanism and the lack of stoichiometry of H$_2$ production from oxalic acid. The determination of the total yields of photocatalytic reactions is usually ignored but it can be a large source of efficiency loss. Most authors, additionally, showed only relative changes in concentrations; hence, only a few reports could unambiguously show the catalytic action of photocatalysts based on turnover numbers [15]. Herein, the photocatalytic degradation of oxalic acid with the simultaneous H$_2$ evolution over different photocatalysts is investigated, closing the gap of knowledge between the theoretical and experimental aspects. The reaction mechanism for the photocatalytic decomposition of aqueous oxalic acid is proposed. We discuss, as well, the contribution of the current doubling mechanism and the disproportionation reaction of radicals on the total yield, showing that even while oxalic acid disappears completely, some efficiency is lost due to secondary reactions. We investigate this problem in detail trying to find the cause and to solve it by testing different co-catalysts on the surface of TiO$_2$. Furthermore, the turnover numbers of the reactions have been calculated, discussing the photocatalytic actions of different photocatalysts.

4.4. Experimental

4.4.1. Materials synthesis and characterization

All chemicals were used as received without any further purification. Deionized water with a resistivity of 18.2 MΩ.cm at 25 °C was produced by a Millipore Mill-Q system. Oxalic acid ($\geq$99%), chloroplatinic acid hydrate H$_2$PtCl$_6\cdot$xH$_2$O ($\geq$99.9%), Tetrachloroauric(III) acid trihydrate HAuCl$_4\cdot$3H$_2$O (99%) and the spin trap 5,5-dimethyl-1-pyrroline-N-oxide (DMPO) were purchased from Sigma-Aldrich. Methanol ($\geq$99.5%) and anhydrous sodium carbonate ($\geq$99%) were purchased from Carl-Roth.

We reported recently [1] the photocatalytic H$_2$ evolution over self-prepared noble metal-free anatase TiO$_2$ in the presence of ethanol as an electron donor. Here, the same material was synthesized by the EISA (evaporation induced self-assembly) method from TiCl$_3$ as a precursor. Briefly, the triblock copolymer surfactant F-108 was dissolved in ethanol followed by the addition of acetylacetone and TiCl$_3$ as the only titanium source. The mixture was then heat-treated at 40 ºC for 24 h followed by calcination at 400 ºC for 12 h. In parallel, a frequently-studied anatase TiO$_2$ sample was prepared from TiCl$_4$:Ti(OBu)$_4$ in a molar ratio of 0.4:0.6 as precursors. X-ray diffraction analysis in Figure 4-S1 showed the patterns of pure anatase, with crystallite sizes in the range of 10-15 nm for the sample prepared from TiCl$_3$ and 10-20 nm for the sample prepared from TiCl$_4$:Ti(OBu)$_4$ according to Scherrer's equation applied to 101 reflexes. These values are in agreement with those obtained from transmission electron microscopy (TEM) images (Figure 4-S2). Both samples have also relatively high Brunauer – Emmett – Teller (BET) specific surface areas of 121.3 m^2 g^{-1} and 117.4 m^2 g^{-1}, respectively. TiO$_2$ prepared from TiCl$_3$ showed, as well, a higher density of charge carriers and a more negative conduction band potential as determined by Mott–Schottky measurements (shown elsewhere) [1].

Different noble-metal loaded TiO$_2$ photocatalyst powders (Pt$_{0.25\%}$/TiO$_2$, Au$_{1\%}$/TiO$_2$, and Au$_{1\%}$-Pt$_{0.25\%}$/TiO$_2$) were prepared following a photodeposition method [13]. In a typical preparation, the prepared TiO$_2$ was suspended in a 10% (v/v) aqueous methanol solution and purged with argon. H$_2$PtCl$_6$·xH$_2$O and/or HAuCl$_4$·3H$_2$O were then added to the suspension, followed by the illumination with a Philips CLEO UV(A) lamp at 15 °C. The solids were then collected by centrifugation, washed repeatedly with deionized water and dried at 100 °C for 24 h. TEM images for the sample prepared from TiCl$_3$ (Figure 4-S2) showed good crystallinity of the nanoscaled powders and distribution of small metal nanoparticles having diameters of 1 - 5 nm and 5 - 10 nm for Pt and Au, respectively.

Having established the synthesis protocols and the characterization we subsequently studied the photocatalytic activity of the samples *via* batch experiments in 10 ml crimp glass vials together with 8 mg of photocatalyst suspended in 8 ml aqueous oxalic acid (100 mmol l^{-1}) at pH ~3. The vials were closed and purged with argon for 15 min and then irradiated with a 1000 W xenon lamp (Hönle UV Technology, Sol 1200). The amounts of molecular hydrogen were quantified using a GC-TCD chromatograph and showed in Figure 4-S3. The sample prepared from TiCl$_3$ showed a significantly higher photocatalytic activity than the conventional photocatalyst prepared from TiCl$_4$:Ti(OBu)$_4$ in both the bare and platinized forms. We noticed the same behavior when using ethanol as an electron donor and explained it by a high density of charge carriers exhibiting a longer lifetime and higher activity as revealed from transient absorption spectroscopy (TAS) measurements (shown

elsewhere) [1]. We, therefore, applied the photocatalyst prepared from $TiCl_3$ in our mechanistic studies.

4.4.2. Photocatalytic experiments and analytical procedures

A continuous-flow setup connected to a quadrupole mass spectrometer (QMS) was used to follow the evolved gases from the photocatalytically reformed oxalic acid in its aqueous solutions. The use of this setup enables long term tests to be carried out without the difficulties that occur in a closed photocatalytic system, i.e., the overpressure inside the reactor [13, 16].

The photocatalytic experiments were performed at 20 °C in a 65 ml double-jacket glass photoreactor attached to a quadrupole mass spectrometer (Hiden HPR-20) for gas analysis, as shown in Figure 4-S4. Argon was continuously flowed over the reaction mixture at 5.0 cm^3 min^{-1} as a carrier gas by using a precise mass flow controller. In a typical experiment, 62.5 mg of bare TiO_2 or 25 mg of TiO_2 loaded with noble metal was added to 50 ml of 1.11 mmol l^{-1} oxalic acid at pH ~3. All solutions were prepared in 1 mmol l^{-1} KNO_3 to preserve their ionic strengths and adjust their pH [17]. The presence of nitrate had a negligible effect on the production of H_2. A xenon arc lamp (Osram XBO 1000 W Xenon Arc Lamp in a Müller LAX 1000 lamp housing) was used as the light source. Before starting the illumination, the photocatalytic system was stabilized in the dark for 2 h to reach the adsorption equilibrium and a steady baseline. The suspension was then continuously irradiated with an irradiance of 31 mW cm^{-2} in the wavelength range of 320 – 380 nm. An optical filter of 310 nm was placed in the front of the xenon lamp to prevent the photolysis of oxalic acid [18]. The use of the 310 nm optical filter also avoids the photolysis of nitrate, hence preventing any homogeneous photolysis of oxalic acid. The photon flux at the irradiated window of the photoreactor was found to be I_0= 9.83 x 10^{-5} mol m^{-2} s^{-1} in the wavelength range from 320 nm to 380 nm. Approximately 49.4 x 10^{-9} mole of photons entered the suspension per second when ignoring the loss of light due to reflection and scattering out of the photoreactor. The photonic efficiencies were calculated based on the Eqs. S1 and S2.

All photocatalytic experiments were performed twice, with an estimated error of ±5%. The quantitative determination of gases was done by calibrating the QMS with standard argon-diluted H_2 and CO_2 (Linde Gas, Germany). The amounts of oxalic acid, as well as dissolved by-products, were periodically quantified by high-performance ion chromatography (HPIC, Dionex ICS-1000) equipped with a temperature-controlled conductivity detector (35 °C) and an electro-regenerator suppressor. Aliquots of 0.5 ml samples were withdrawn and filtered prior to their injection into the chromatograph. A sodium carbonate solution (9 mmol l^{-1}) was pressed through an Ion Pac AS9-HC 2 × 250 mm column equipped with a guard column of Ion Pac AG9-HC 2 × 50 mm from Dionex.

4.4.3. EPR experiments

Electron Paramagnetic Resonance (EPR) investigations were performed with an X-band MiniScope MS400 spectrometer (Magnettech GmbH, Germany) with a microwave frequency of 9.42 GHz. A UV spot-light (LC8, Hamamatsu, 200 W super-quiet mercury-xenon lamp) was used to irradiate the samples. For powder samples, EPR spectra were recorded using sample tubes at liquid nitrogen temperature after purging with argon. The employed microwave power was 5 mW and the modulation frequency and amplitude were adjusted at 100 kHz and 0.15 mT, respectively. The nature of the photogenerated species during the irradiation of TiO$_2$/oxalic acid suspensions was detected employing the spin-trap technique with DMPO as a spin-trapping agent. The experiments were conducted in sealed capillaries for suspensions containing 1 g l^{-1} of photocatalyst, 5.5 mmol l^{-1} of oxalic acid adjusted at pH ~ 3 and 0.8 mmol l^{-1} of DMPO in the absence of O$_2$. The acquisition was done using a center field of 335.4086 mT, sweep time of 15 s, 4096 data points, modulation amplitude of 0.2 mT, microwave power of 10 mW and gain of 5. The spectra for the spin-trap experiments were fitted using the Easy Spin simulator package [19].

4.5. Results and discussion

4.5.1. Tracing oxalic acid photocatalytic degradation: the total yields of gas-phase products

Figure 4-1 shows the time course of the photocatalytic H$_2$ and CO$_2$ evolution from 1.11 mmol l^{-1} aqueous oxalic acid over TiO$_2$ loaded with different co-catalysts. The curves in Figure 4-1 are the integrated signals of the photocatalytic gas evolution rates in Figure 4-S5. In all cases, both H$_2$ and CO$_2$ gases are immediately produced upon illumination, reaching a maximum production rate followed by a gradual decrease in the rates until none of the gases are detected. We relate such a decrease to the consumption of oxalic acid, a behavior similar to that noticed by Kandiel et *al.* during the reforming of methanol [16]. Different amounts of gases are obviously produced depending on the material used. Interestingly, the use of a self-prepared bare TiO$_2$ results in H$_2$ evolution, even without any HER co-catalyst, as previously reported for alcohols reforming [1]. We consider such a performance as a notable step forward because negligible H$_2$ evolution over bare TiO$_2$ has been previously reported [5, 10].

Modifying bare TiO$_2$ with noble metals does, indeed, boost the photocatalytic activity. As displayed in Figure 4-S5 gold and platinum nanoparticles increase the evolution rate of both H$_2$ and CO$_2$ gases, with Pt being more effective than Au. The co-deposition of both noble metals does not result in an additive effect, with the bimetallic co-catalyst reaching lower evolution rates than Pt/TiO$_2$. Noteworthy, no molecular oxygen was detected during the photocatalytic experiments, even when only a very low concentration of oxalic acid remained in suspension. The photocatalytic splitting of water into H$_2$ and O$_2$ both in the presence and absence of oxalic acid appears thus to be negligible.
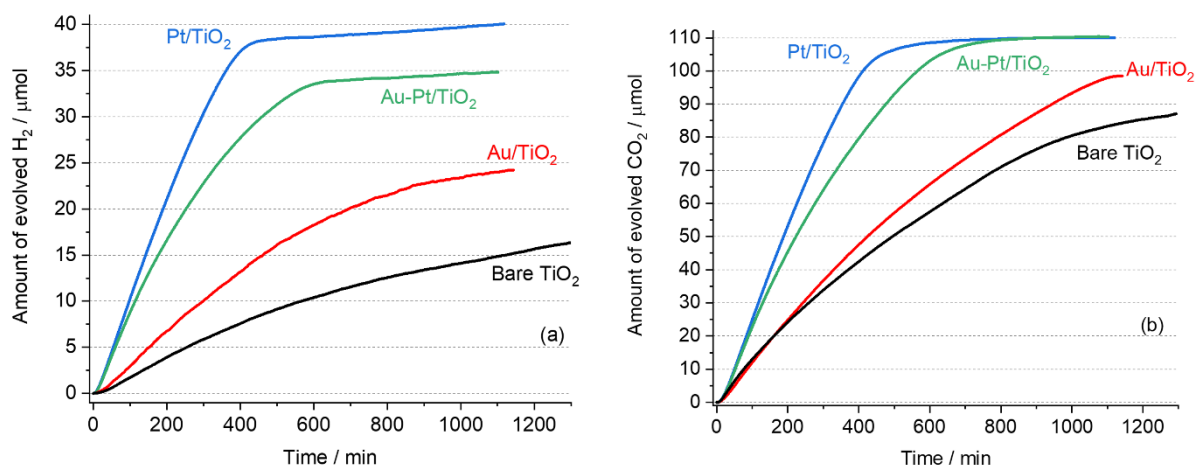
Figure 4-1 Photocatalytically evolved amounts of H_2 (a) and CO_2 (b) from 50 ml aqueous suspensions of 1.11 mmol l^{-1} oxalic acid at pH ~3 over the different photocatalysts. The experiments were conducted until no gases were detected.

Table 4-1 presents the total produced amounts of H_2 and CO_2 gases. Taking the amounts of evolved CO_2 as a measure of oxalic acid oxidation, the activity is found to increase in the sequence bare $TiO_2 < Au/TiO_2 < Pt/TiO_2 \approx Au-Pt/TiO_2$. Looking at the evolved H_2, the formed amounts increases in the order bare $TiO_2 < Au/TiO_2 < Au-Pt/TiO_2 < Pt/TiO_2$. The type of co-catalyst affects the photonic efficiency of H_2 evolution to a larger extent as compared with that of the CO_2 formation. For example, Pt NPs increase the photonic efficiency of H_2 evolution by 5-fold, 2.5-fold and 1.2-fold compared to bare TiO_2, Au/TiO_2, and $Au-Pt/TiO_2$, respectively. On the other hand, they only rise the photonic efficiency of CO_2 production by 2.5-fold, 1.9-fold, and 1.1-fold, respectively. This means the oxidation of oxalic acid on bare TiO_2 is feasible, but it is to a much larger extent upon the modification with noble metals. Our results are in good agreement with the work of Bamwenda et *al.* [20] showing a 30% lower overall activity of Au/TiO_2 than that of Pt/TiO_2. They attributed this to the more effective trapping and pooling of photogenerated electrons by Pt.

We also examined the possible contribution of a visible light activity from Au-containing materials, which is related to the plasmonic effect of Au NPs [21]. The experiment was repeated employing $Au_{1\%}$-$Pt_{0.25\%}/TiO_2$ and using a long-pass filter with a cut-on wavelength of 410 nm. The time course of the photocatalytic gas evolution is represented in Figure 4-S6. A severe decline in the photocatalytic activity was recorded, especially for the H_2 evolution. Only 3.35 and 7.04 µmol of H_2 and CO_2, respectively, were detected after 20 hours of visible light irradiation. Au NPs loaded on TiO_2 prepared in this work thus exhibit poor activity in the visible light region, in addition to their negative roles hindering the activity of Pt when the full light spectrum is used, as shown in Figure 4-1. Our results thus contradict the reports showing that Au−Pt bimetallic system on the surface of TiO_2 may have better catalytic properties compared to pure Au and pure Pt [22].

Table 4-1 Total amounts of H$_2$ and CO$_2$ gases evolved from 1.11 mmol l^{-1} oxalic acid (OA) at pH ~3 over the different materials.

	H$_2$ μmol	CO$_2$ μmol	CO$_2$:H$_2$ ratio	CO$_2$:OA$_{(total)}$ ratio	H$_2$:OA$_{(total)}$ ratio	ζ^a of H$_2$/%	ζ^a of CO$_2$/%
Bare TiO$_2^b$	16.3 ± 0.7	86.6 ± 3.2	5.30	1.60	0.29	0.66	3.80
Au$_{1\%}$/TiO$_2$	24.2 ± 1.5	98.5 ± 3.9	4.07	1.77	0.44	1.13	4.12
Pt$_{0.25\%}$/TiO$_2$	40.1 ± 1.4	110.0 ± 3.2	2.74	1.98	0.72	3.41	8.78
Au$_{1\%}$-Pt$_{0.25\%}$/TiO$_2$	34.8 ± 1.4	110.3 ± 3.1	3.17	1.99	0.63	2.56	7.19

^{a} The photonic efficiencies are based on the amounts evolved during 300 min of irradiation. ^{b} The amount of bare TiO$_2$ used is 2.5-fold more than that of loaded TiO$_2$ materials.

Noble-metal-loaded TiO$_2$ photocatalysts provide a significantly higher photocatalytic activity than bare TiO$_2$. We relate such an enhancement, on the one hand, to the charge carriers rectification, i.e. directing the flow of the photogenerated charge carriers in opposite directions [23] minimizing both the recombination of e$^-$/h$^+$ and the trapping of e$^-$ as Ti^{3+} ions. However, the affinity of metal NPs to capture the electrons significantly depends on the type of metal. This can be assigned to the formation of a Schottky barrier at the noble metal−TiO$_2$ interface because the work functions of noble metals are larger than that of TiO$_2$ [24]. The larger the work function of the noble metal is, the higher is the Schottky barrier and, consequently, the better is the photocatalytic activity of the composite [25]. We believe, hence, that noble metals act as a sink for electrons, with platinum being more efficient than gold (work functions of 5.65 eV for Pt and 5.10 eV for Au) [26]. When such a Schottky barrier is created, the photocatalytic activity is enhanced due to a lower probability for the recombination of photogenerated charge carriers [27].

We assume, on the other hand, that noble metals facilitate the electron transfer process to the respective acceptor species, e.g. H$^+$, lowering the overpotential of reduction [28]. In fact, density functional theory (DFT) calculations regarding the hydrogen binding energy showed that binding to Pt results in a smaller Gibbs free-energy change (- 0.09 eV) compared to gold (0.45 eV). This, indeed, explains our results because Pt has the best electrocatalytic activity for HER from the viewpoint of thermodynamics [29, 30]. A difference in the discharge of electrons into the electrolyte has been reported by Subramanian et al. [31], who studied luminescent ZnO colloids and proved a complete discharge of electrons into the solution in the case of Pt but not Au, because only a partial recovery of the emission was recorded when Au NPs were added to pre-UV-irradiated ZnO colloids, while Pt NPs caused almost complete recovery of the quenched emission.

Assuming that the oxalic acid photocatalytic reforming occurs according to Eq. 4-1, the expected molar ratio of the evolved gases should be $CO_2:H_2 = 2$.

$$H_2C_2O_4 \quad\quad\quad \rightarrow \quad H_2 \; + \; 2CO_2 \quad\quad\quad\quad\quad\quad (4\text{-}1)$$
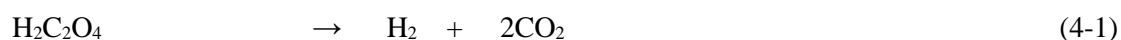
However, as shown in Table 4-1, the obtained $CO_2:H_2$ ratios for all the tested samples are higher than 2, while the calculated $H_2:OA$ ratios are lower than 1. For example, using the most-efficient material, Pt/TiO_2, both $CO_2:H_2$ and $H_2:OA$ of 2.7 and 0.72, respectively, are non-stoichiometric ratios. We also reported such a lower stoichiometric $H_2:OA$ ratio in our previous work ($H_2:OA$ molar ratio ≈ 0.6) [13]. A possible reason is the progressive blockage of active sites on the noble metal co-catalysts by the adsorption of molecular hydrogen [32]. Noble metals have been shown to act as active sites for hydrogen dissociation and adsorption [33]. However, DFT calculations [33] have predicted an increase in hydrogen dissociation when small amounts of Pt are added to Au, while a stronger H-Pt interaction was predicted when the number of Au atoms nearby Pt atoms increased. Another possible reason is the increase in the charge carrier recombination rate as the concentration of oxalic acid decreases. The formation of by-products should also be considered as a source of non-stoichiometry and it is discussed in detail in section "3.5". Deviations from the stoichiometry have also been previously reported for the reforming of oxalic acid by other authors. For example, Kmetykó et al. [34] showed a ratio of about 0.64 when they performed long term irradiation of $Pt\text{-}TiO_2$ in the presence of 0.05 mol l^{-1} oxalic acid. On the other hand, Yamada et al. [14] have reported 80 % of the stoichiometric amount based on the irradiation of a 3 mmol l^{-1} oxalate solution in the presence of Pt NPs and 2-phenyl-4-(1-naphthyl)quinolinium ion ($QuPh^+$-NA) as a photocatalyst. They have related this lower value to the formation of by-products such as formic acid and formaldehyde.

4.5.2. Tracing oxalic acid photocatalytic degradation: water-soluble reaction products

4.5.2.1. Effect of co-catalysts

The concentration of oxalic acid in the solution was followed by means of HPIC. As can be seen in Figure 4-2, a gradual consumption of oxalic acid was recorded during 500 min of irradiation, with complete degradation only achieved over platinized TiO_2. These results correlate with the gas evolution behaviors: the sharp decline in gas production after 400 min matches the almost complete consumption of oxalic acid. Table 4-2 shows the data of oxalic acid degradation, in which the initial degradation rate of oxalic acid increases in the order of bare $TiO_2 < Au/TiO_2 < Au\text{-}Pt/TiO_2 < Pt/TiO_2$. The degradation over bare TiO_2, indeed, obeys the lowest rate due to a higher recombination rate of the photogenerated charge carriers. However, with an initial degradation rate of 3.63 μmol l^{-1} min^{-1}, Pt/TiO_2 shows better performance than $Au\text{-}Pt/TiO_2$, which can be due to the formation of by-products. By comparing the photonic efficiencies of oxalic acid degradation (Table 4-2) with those of CO_2 production (Table 4-1),

ζ_{CO2}/ζ_{OA} are almost 2 for Pt/TiO_2 on the surface of TiO_2. This indicates that the pathway of the reaction might be different when Au NPs as mono-co-cocatalysts are loaded since almost direct oxidation of oxalic acid to CO_2 over Pt/TiO_2 is expected.
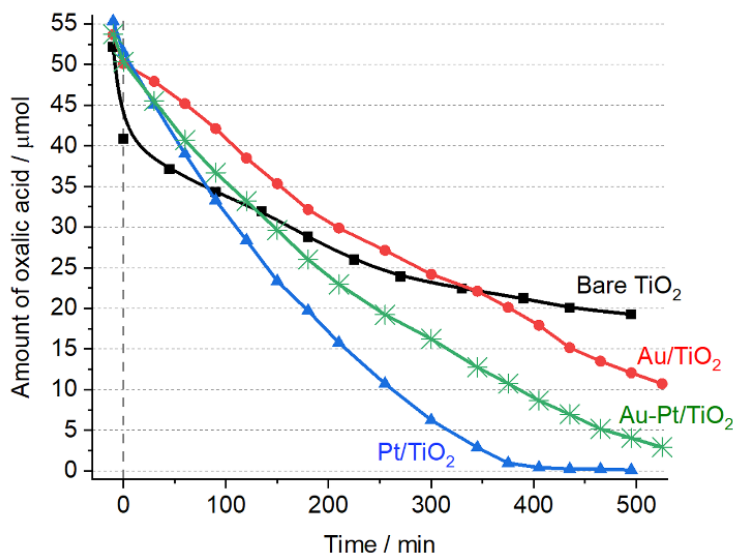

Figure 4-2 *Profiles of oxalic acid disappearance in suspension, detected by HPIC during the irradiation in the presence of different photocatalysts. Initial oxalic acid concentration: 1.11 mmol l^{-1}, reaction volume: 50 ml, photocatalyst loading: 1.25 g l^{-1} (bare TiO_2) and 0.5 g l^{-1} (noble-metal/TiO_2).*

Table 4-2 Kinetic parameters for the degradation of 1.11 mmol l^{-1} oxalic acid at pH ~3 over the different materials used.

	$r_{d,0}{}^a$ / μmol l^{-1} min^{-1}	ζ^b of degradation / %
Bare $TiO_2{}^c$	1.05	1.56
$Au_{1\%}/TiO_2$	1.01	2.23
$Pt_{0.25\%}/TiO_2$	3.63	4.91
$Au_{1\%}$-$Pt_{0.25\%}/TiO_2$	2.64	3.37

[a] The initial degradation rates are calculated for the first 60 min of irradiation. [b] The photonic efficiencies are based on the amounts consumed during 300 min of irradiation. [c] The amount of bare TiO_2 used is 2.5-fold that of loaded TiO_2 materials.

4.5.2.2. Adsorption capacity and turnover numbers

The adsorption of oxalic acid (1.11 mmol l^{-1}) onto bare TiO_2 (1.25 g l^{-1}) decreased when increasing the solution pH, as shown in Figure 4-S7. The surface area normalized uptake of oxalic acid at saturation conditions (SANU, see Eq. 2) decreases in the order of 9.1×10^{13}, 6.3×10^{13}, 3.6×10^{12} and 2.2×10^{11} molecules cm^{-2} at pH values of 3, 5, 7, and 10, respectively. This strong decrease in surface coverage is expected since both the surface of TiO_2 and oxalic acid shift towards their conjugated

bases (of anionic character) as the pH increases. Our zeta potential measurement showed an isoelectric point (pH_{zpc}) of TiO_2 nanoparticles close to 5.5 [13]; therefore, their surface charge is mostly positive for pH < 5.5 and negative for pH > 5.5. On the other hand, $HC_2O_4^-$ and $HC_2O_4^{2-}$ are the major fractions of oxalate species in the solution in pH range from 1.25 to 4.28 and at pH > 4.28, respectively [13]. Therefore, at pH ~3, we expect a strong interaction between $HC_2O_4^-$ molecules and the positively-charged TiO_2 surface. As the solution pH increases, the repulsive forces between the negatively-charged TiO_2 nanoparticles and the negatively-charged oxalate increase, resulting in the observed decline in the uptake.

$$SANU = \frac{\text{Number of adsorbed molecules (molecules)}}{\text{Surface area of the catalyst in the suspension } (cm^2)} \qquad (4-2)$$

Giving thought to the BET surface area values along with the amounts adsorbed after saturation, we calculated the adsorption of 0.91 molecules per nm^2. Hence, the concentration of active sites in the suspension was calculated as 0.23 x10^{-3} and 0.09 x10^{-3} mol l^{-1} for bare TiO_2 and noble-metals/TiO_2, respectively. These results are comparable with other reports showing that the adsorption of oxalic acid on hydrated anatase surfaces at pH 3.7 occurs most likely through monodentate complexes [8]. Based on the concentration of active sites, turnover numbers (TONs) for complete oxidation have values of 4.86 and 12.14 over bare TiO_2 and noble-metals/TiO_2, respectively. Owing to the fact of a catalyzed photoreaction has a TON $\geqslant$ 1 [35], we consider all the conversion processes studied as truly photocatalytic.

4.5.2.3. Detected by-products in the liquid phase

The HPIC method was used to detect the by-products in the liquid phase, where a well-resolved peak was eluted at a retention time identical to that of formate. This confirms formate as the main by-product in the liquid phase, in accordance with our recent work [13]. The time-profiles of formate release over the studied materials are shown in Figure 4-3(a and b). A continuous increase in the amounts of formate was noticed, especially over bare and Au/TiO_2. In the case of Pt/TiO_2 and Au-Pt/TiO_2, the production reached a maximum amount in 300 min, after which a fast decrease was observed. Nevertheless, very small amounts of formate were produced compared to the converted amount of oxalic acid. This is in agreement with previous reports showing that the anaerobic degradation of elementary di-carboxylic acids, e.g., oxalic acid, resulted in the formation of the corresponding monocarboxylic acid [36]. For example, the ^1H NMR detection of formic acid and formaldehyde was possible during the photocatalytic H_2 evolution using oxalate, QuPh$^+$–NA as a photocatalyst and Pt NPs as an HER catalyst. The proposed mechanism postulated that oxalate acts as a one-electron donor, while $^\cdot CO_2^-$ radicals can be reduced to formate by hydrogen adsorbed on Pt NPs [14].
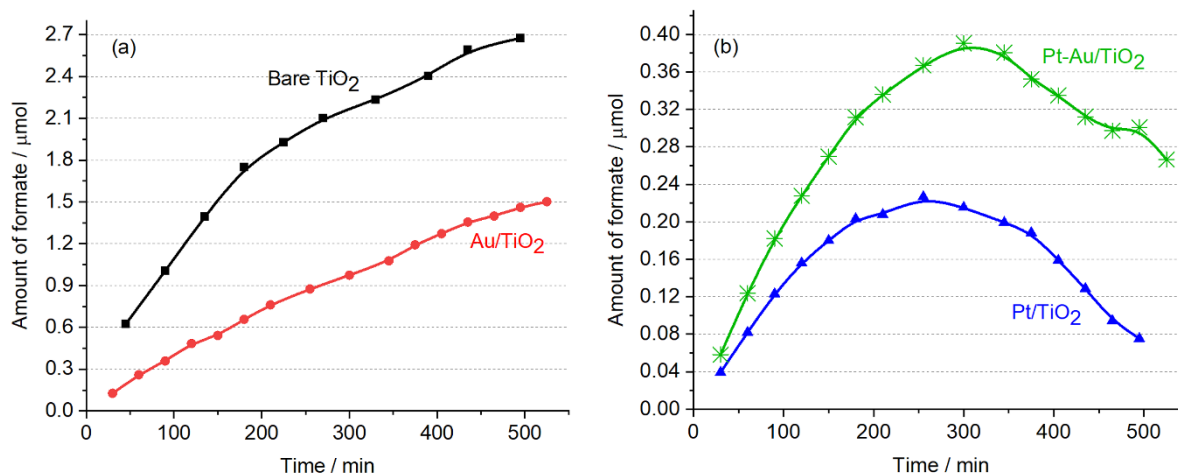
Figure 4-3 Produced amounts of formate in the suspension during the irradiation detected by HPIC over bare TiO$_2$ and Au/TiO$_2$ (a), and over Pt/TiO$_2$ and Au-Pt/TiO$_2$ (b).

4.5.3. Effect of initial oxalic acid concentration on gas production

The influence of the initial concentration of oxalic acid was additionally investigated *via* the study of the long-term gas evolution from a 100 mmol l^{-1} oxalic acid solution adjusted to pH ~3. As shown in Figure 4-4 and Figure 4-S8, the gases are immediately produced after starting the illumination to reach a saturation level within 100 min, keeping a stable evolution rate until switching off the light source. The obtained results confirm the stability of the catalysts over long term irradiation. This confirms, as well, that the gradual decrease in the gas evolution when a lower oxalic acid concentration was used is mainly due to the consumption of the acid from the solution, which increases the recombination of charge carriers. The rise in the gas evolution rate by a factor of 1.5 when the oxalate concentration was increased by a factor of 100 is expected since most photocatalytic processes follow Langmuir-type dependences. For example, Li et *al.* have similarly reported an increase in the rate of H$_2$ production while increasing the initial concentration of oxalic acid, while the independence of the rate on the concentration was observed for $C_0 > 5$ mmol l^{-1} [10].
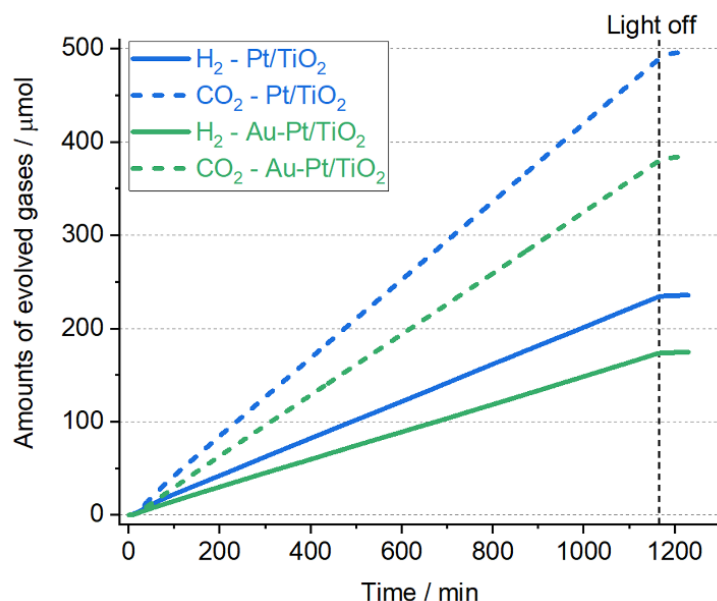
Figure 4-4 Photocatalytically evolved amounts of H₂ and CO₂ from 50 ml aqueous suspensions of 100 mmol l⁻¹ oxalic acid at pH ~3 over Pt/TiO₂ and Au-Pt/TiO₂.

Pt/TiO₂ again shows the best performance with total H_2 and CO_2 amounts of 235.4 and 496.8 µmol, respectively, compared to 174.2 and 384.9 µmol produced over Au-Pt/TiO₂. The molar ratios CO_2:H_2 after 20 h of irradiation are found to be 2.11 and 2.21 over Pt/TiO₂ and Au-Pt/TiO₂, respectively. Although these ratios are still higher than 2, they are closer to the theoretical value than those for the lower concentrations of oxalic acid (see Table 4-1). Proton adsorption, as well as H_2 desorption on Pt, seems to be unaffected by such higher oxalic acid concentrations. This was also reported by Orts et al. [37], who did not observe any blocking effect on hydrogen adsorption over Pt (111) and Pt (110) electrodes in the presence of oxalic acid in acidic medium.

4.5.4. EPR investigations

4.5.4.1. EPR in solid phase

The paramagnetic centers produced on the irradiated TiO₂ powders were observed *via* in situ EPR spectroscopy under an argon atmosphere at 77 K. The EPR spectra of irradiated Pt/TiO₂ in the presence of oxalic acid after 1 and 5 min of UV irradiation were recorded and plotted after subtracting the dark spectrum. As shown in Figure 4-5, very weak signals of both trapped holes ($g > 2$, signal H) and trapped electrons ($g < 2$, signal E_T) were observed during the irradiation. Signal H ($g_x = 2.004$, $g_y = 2.014$, $g_z = 2.018$) has been attributed to the photogenerated holes trapped at the oxygen atoms as Ti⁴⁺-O˙⁻-Ti⁴⁺-OH⁻ near the hydrated anatase surface [38, 39]. On the other hand, the signal E_T ($g_{\parallel} = 1.962$ and $g_{\perp} = 1.992$) has been attributed to the photogenerated electrons trapped in the bulk as Ti³⁺ ions [38, 40, 41]. The observation of this signal (E_T) in the EPR spectra even when Pt (an electron scavenger) is loaded on the TiO₂ surface means that not all the photogenerated electrons are scavenged by the loaded Pt NPs, but instead, some of them can be trapped in the bulk as Ti³⁺ centers. These trapped electrons can negatively

97

affect H$_2$ production due to their low reactivity, which can clarify the non-stoichiometric CO$_2$:H$_2$ ratio observed in this material (see table 4-1).

Interestingly, another broad and unfeatured signal (signal E$_S$) was detected, which became more intense with the irradiation time. This broad signal E$_S$ is most likely related to the injection of electrons from $^{\cdot}$CO$_2^-$ radicals, which then spread on the surface of the photocatalyst. Such a broad signal was also observed by Chiesa et *al.* [41] when they injected electrons in the solid in different ways. They assigned this signal to the excess electrons near the surface of anatase TiO$_2$. A similar signal was reported by Howe and Grätzel [42], who have shown that the photogenerated electrons can be trapped as surface Ti^{3+} species in the presence of polyvinyl alcohol as a hole scavenger. Micic et *al.* [43] found a broad asymmetric EPR signal at g= 1.981, indicating the formation of Ti^{3+} from electron trapping on the surface due to electron injection from methanol radicals into TiO$_2$ particles. They reported the disappearance of this signal when Hg^{2+} was present in the solution due to its reduction to Hg by the $^{\cdot}$CH$_2$OH radical, E^0(CH$_2$0/$^{\cdot}$CH$_2$0H) = -0.97 V.
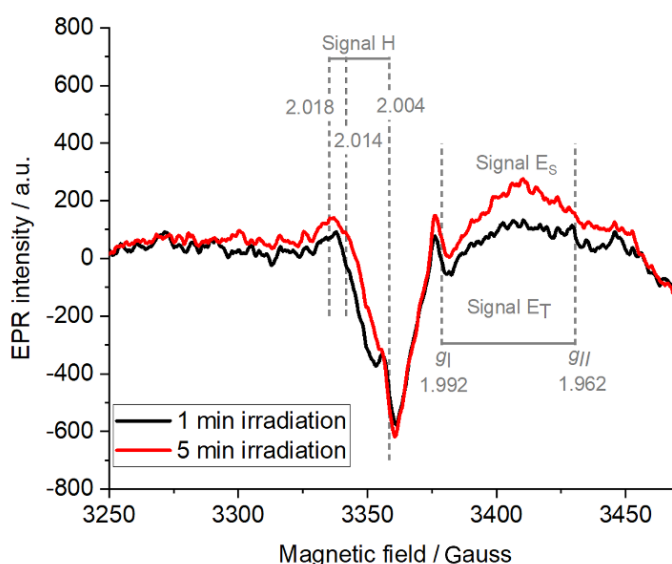

Figure 4-5 EPR spectra recorded when Pt/TiO$_2$ was irradiated for 1 min (black) and 5 min (red) in the absence of molecular oxygen at 77 K in the presence of oxalic acid. Data are shown after the subtraction of the dark spectra.

4.5.4.2. EPR in aqueous suspension

The nature of the photogenerated species during the degradation of oxalic acid in the absence of molecular oxygen has been traced employing the EPR spin-trap technique with DMPO as a spin-trapping agent. Figure 4-6(a-d) shows the time course of EPR spectra for the different materials, where no EPR signals were observed under dark conditions. While the EPR signals started to appear after 1 min of irradiation in the case of Pt/TiO$_2$ and Au-Pt/TiO$_2$, the signals production for Au/TiO$_2$ and bare TiO$_2$ required more time, i.e. 4 min and 7 min, respectively. Under UV irradiation, complex EPR signals belong to overlapping DMPO adducts were recorded. Interestingly, for all the herein

investigated materials, no DMPO$^•$-OH adducts were produced as a four-line (1:2:2:1) EPR signal with hyperfine parameters of a_N = a$_H$ = 14.9 G and g = 2.0057 [44]. Thus, oxalic acid can either inhibit the formation of hydroxyl radicals because of its direct oxidation with photogenerated holes or can react faster than DMPO with any $^•$OH radical produced upon irradiation. An identical result has been reported where the DMPO$^•$–OH spin adduct completely disappeared when oxalic acid was added to a perfluorooctanoic acid/TiO$_2$ dispersion [45]. In this context, the rate constants of the reaction of $^•$OH radical with DMPO and HC$_2$O$_4^-$ were found to be 2.0 x 10^9 and 1.9 x 10^8 M^{-1} s^{-1} [46, 47], respectively. However, the higher concentration of oxalic acid besides its adsorption strength on TiO$_2$ would facilitate its reaction with $^•$OH radicals, if any, even though the 10-fold lower kinetics. Hence, it is not completely clear from the EPR data whether the direct oxidation with photogenerated holes is the dominant mechanism.
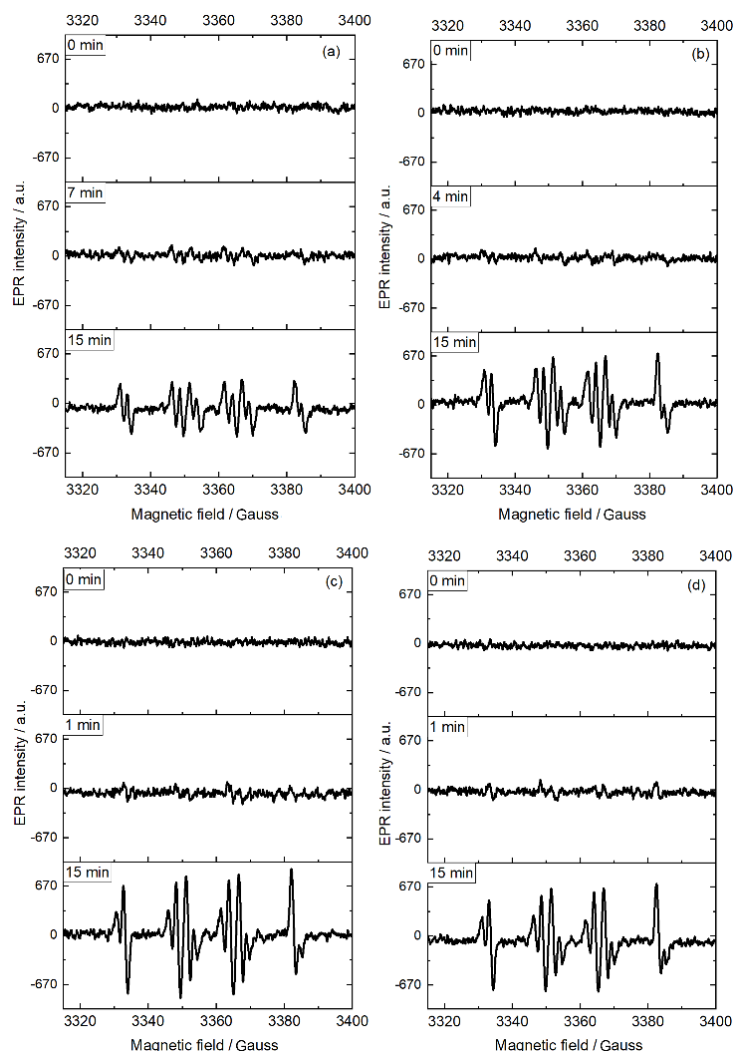

Figure 4-6 EPR spectra observed in the absence of O$_2$ after UV irradiation of aqueous suspensions of oxalic acid (5.5 mmol l^{-1} at pH ~3) and DMPO (0.8 mmol l^{-1}) in the presence of (1 g l^{-1}) bare TiO$_2$ (a), Au/TiO$_2$ (b), Pt/TiO$_2$ (c), and Au-Pt/TiO$_2$ (d).

As a result of $\cdot CO_2^-$ formation, we expect a DMPO$^\cdot$-CO$_2^-$ spin adduct to be produced. In order to detect this signal, an EPR experiment with an irradiated suspension of 1 g l^{-1} of Pt/TiO$_2$ and 3 mmol l^{-1} formate at pH ~3 was conducted. As shown in Figure 4-S9, a six-line EPR signal of approximately the same intensities was produced with hyperfine parameters of $a^N = 15.46$ G, $a_\beta^H = 18.34$ G and $g = 2.005$, which are similar to the parameters for the DMPO$^\cdot$-CO$_2^-$ spin adduct mentioned in the literature.[48] The simulation of the complex EPR spectra from the oxalic acid suspension of Figure 4-6 can be seen in Figure 4-7(a), which is fitted by overlapping of three spin adducts, DMPO$^\cdot$-CO$_2^-$ ($a^N = 15.40$ G, $a_\beta^H = 18.28$ G) and two other six-line signals, which are typical for carbon-centered DMPO spin-adducts [48] (see Figure 4-7(b)). The first signal fits well the DMPO$^\cdot$-CHO resulting from formyl radicals with hyperfine parameters of ($a^N = 15.51$ G, $a_\beta^H = 21.09$ G) [49]. The third signal has hyperfine parameters of ($a^N = 15.67$ G, $a_\beta^H = 23.33$ G), which most likely belong to the DMPO$^\cdot$-(CO-CO$_2^-$) because of their similar values to hydroxyalkyl-radical spin-adducts [48]. This means that other organic radicals are formed simultaneously with the production of carbon dioxide anion radicals.
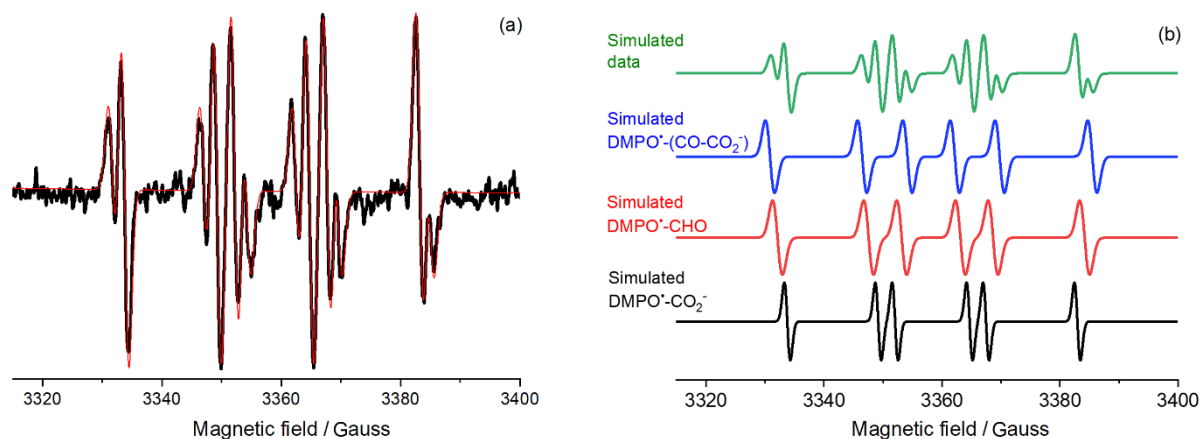

Figure 4-7 EPR spin trap experiment in the absence of O$_2$ for a UV-irradiated oxalic acid suspension; (a) experimental spectrum (black) with its simulation (red); and (b) simulated spectrum of the mixed radicals and of each DMPO$^\bullet$-radical spin adduct. The suspension contained oxalic acid (5.5 mmol l^{-1}), DMPO (0.8 mmol l^{-1}), and Pt/TiO$_2$ (1 g l^{-1}). The extracted signals in Figure 4-7(b) were normalized to evince the overlap of the different species.

The intensities of the EPR spectra in Figure 4-6 increase with the irradiation time in the order of Pt/TiO$_2$ > Au-Pt/TiO$_2$ > Au-TiO$_2$ > bare TiO$_2$ confirming the enhancement in the formation of radicals by the noble metals. Depending on the materials used, the relative intensities of the adduct signals varied. Lower production of the DMPO$^\cdot$-CO$_2^-$ spin adduct compared to the other spin adducts was noticed over bare and gold loaded TiO$_2$. In contrast, Pt NPs accelerate the production rate of $\cdot CO_2^-$, which was slightly hindered when gold is concurrently introduced.
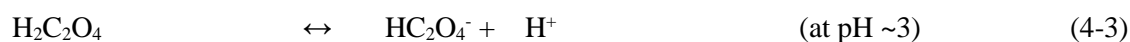
Our EPR results are in good agreement with the theoretical calculations done by Mendive et al. [9], who have predicted a direct transfer of e$^-$ and h$^+$ to the adsorbed oxalic acid at the TiO$_2$ surface.

They have also predicted the production of aldehyde molecules accounting for the reduction of the carboxylic group (see Scheme 4-1).

4.5.5. The proposed mechanism of the oxalic acid photocatalytic reforming

One could assume that the chemistry of the photocatalytic reforming of oxalic acid is rather simple and follows Eq. 1 with molar ratios of $CO_2:H_2$ and $H_2:OA$ equal to 2 and 1, respectively. However, to obtain such ratios the mechanism should occur according to the current doubling effect. Such a reaction mechanism illustrates that at least half of the detected H_2 is formed through the action of holes and not of electrons. Nevertheless, the detection of a photocatalytic H_2 yield of 200%, i.e., direct evidence for "current doubling", in the photocatalytic hydrogen generation has not been previously shown.

At pH ~3, $HC_2O_4^-$ are the dominant oxalic acid species in the solution (Eq. 4-3), as revealed from the adsorption data and due to its first dissociation constant $pK_{a1}(H_2C_2O_4) = 1.25$ [13]. The photogenerated holes in the valence band of TiO_2 react either with the adsorbed water to form hydroxyl radicals (Eq. 4-4) or directly with the adsorbed $HC_2O_4^-$ to produce $HC_2O_4^{\bullet}$ radicals (Eq. 4-6) that can be also generated through the reaction between $HC_2O_4^-$ and hydroxyl radicals on the surface of TiO_2 (Eq. 4-5). We believe that the direct reaction with the photogenerated holes might be dominant in our experimental conditions because oxalic acid adsorbs strongly at the photocatalyst surface. The direct photocatalysis mechanism has been associated with systems where the substrate adsorbs strongly at the photocatalyst surface, establishing a good electronic contact [50]. Some previous reports have shown that oxalate can be oxidized *via* an indirect hole transfer, i.e., hydroxyl radical oxidation [51, 52]. However, these studies have been performed either photoelectrochemically or photocatalytically in strongly acidic conditions (pH < 2). On the other hand, Mendive et *al.* have concluded from their ATR-FTIR experiments the direct oxidation of oxalic acid at the TiO_2 surface by the hole formed upon UV(A) light absorption [9]. They have theoretically predicted that $^{\bullet}OH$ radicals, if involved in the reactions, only arise from the cleavage of chemical bonds of the adsorbed oxalic acid and not from adsorbed water.

$$H_2C_2O_4 \quad\quad \leftrightarrow \quad\quad HC_2O_4^- + H^+ \quad\quad (\text{at pH ~3}) \quad\quad (4\text{-}3)$$

$$OH^-_{(ads)} + h^+_{(VB)} \quad\quad \rightarrow \quad\quad ^{\bullet}OH_{(ads)} \quad\quad\quad\quad\quad\quad\quad\quad\quad\quad (4\text{-}4)$$

$$HC_2O_4^- + {}^{\bullet}OH_{(ads)} \quad\quad \rightarrow \quad\quad HC_2O_4^{\bullet} + OH^- \quad\quad\quad\quad\quad\quad (4\text{-}5)$$

$$HC_2O_4^- + h^+_{(VB)} \quad\quad \rightarrow \quad\quad HC_2O_4^{\bullet} \quad\quad\quad\quad\quad\quad\quad\quad\quad\quad (4\text{-}6)$$
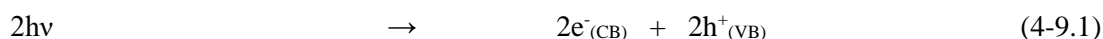
The one-electron oxidation process of oxalic acid through the C-C cleavage *via* the photo-Kolbe mechanism (Eqs. 4-7 and 4-8) results in the formation of a strongly reducing radical as an

intermediate, i.e., the carbon dioxide radical anion $^{\bullet}CO_2^-$ [$E^0(CO_2/^{\bullet}CO_2^-) = -1.9$ V] [53]. This radical is an excellent reducing agent and can consequently participate in many redox reactions. The formation of $^{\bullet}CO_2^-$ is confirmed from our EPR spin-trap results, while the injection of their electrons is detected in our solid-phase EPR data. The formation of $^{\bullet}CO_2^-$ has been, as well, detected through radiolysis experiments using methylviologen as a mechanistic probe [54] and through cyclic voltammetry experiments [55]. The carbon dioxide radical anion has a $pK_a(^{\bullet}CO_2H)$ of about 2.3 [56], hence, in our experimental conditions (pH > 3), $^{\bullet}CO_2^-$ is the dominant generated species (Eqs. 4-7 and 4-8).
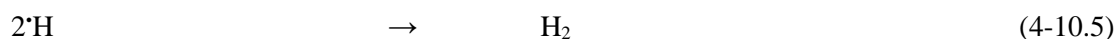
$$HC_2O_4^{\bullet} \qquad\qquad \rightarrow \quad CO_2 \;+\; H^{\bullet}CO_2 \tag{4-7}$$

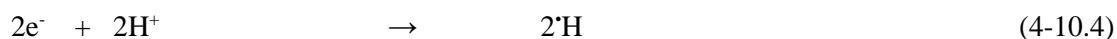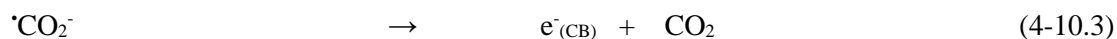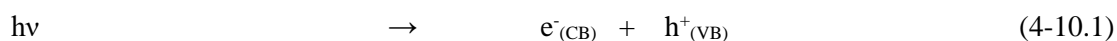$$H^{\bullet}CO_2 \qquad\qquad \leftrightarrow \quad {}^{\bullet}CO_2^- \;+\; H^+ \tag{4-8}$$

However, $^{\bullet}CO_2^-$ radicals might render the photoreforming reaction rather complicated. Since the formation of a hydrogen molecule requires two electrons and $^{\bullet}CO_2^-$ radicals can inject their electrons in TiO₂ (current-doubling), we can suggest three different mechanisms for the H₂ production from oxalic acid: (1) the "no current doubling" mechanism, in which two-photons are required to produce molecular hydrogen (Figure 4-8(a) and Eqs. 4-9.1 to 4-9.6) and the molar ratio H₂:OA is 0.5; (2) the "current doubling" mechanism, in which one electron is photoproduced while the second electron originates from the $^{\bullet}CO_2^-$ radical (Figure 4-8(b) and Eqs. 4-10.1 to 4-10.6), with a molar ratio of H₂:OA equal to 1; and (3) the "radical recombination" mechanism, in which one photon produces a formate anion without the production of a H₂ molecule (Scheme 4-1 and Eqs. 4-11.1 to 4-11.5). The latter mechanism has been proposed by Yamada et al. [14] and has been also theoretically predicted by Mendive et al. [9] due to the cleavage of the C-C bond followed by the addition of $^{\bullet}H$ atoms to the adsorbed $^{\bullet}CO_2^-$ radicals.

Mechanism (1) NO current doubling:

$$2h\nu \qquad\qquad \rightarrow \qquad 2e^-_{(CB)} \;+\; 2h^+_{(VB)} \tag{4-9.1}$$

$$2h^+ \;+\; 2HC_2O_4^- \qquad \rightarrow \qquad 2CO_2 \;+\; 2^{\bullet}CO_2^- + 2H^+ \tag{4-9.2}$$

$$2^{\bullet}CO_2^- + H^+ \qquad\qquad \rightarrow \qquad CO_2 \;+\; HCO_2^- \tag{4-9.3}$$

$$2e^- \;+\; 2H^+ \qquad\qquad \rightarrow \qquad 2^{\bullet}H \tag{4-9.4}$$

$$2^{\bullet}H \qquad\qquad\qquad \rightarrow \qquad H_2 \tag{4-9.5}$$

$$2h\nu \;+\; H^+ + 2HC_2O_4^- \qquad \rightarrow \qquad 3CO_2 \;+\; H_2 \;+\; HCO_2^- \tag{4-9.6}$$

Mechanism (2) with current doubling:

$h\nu$	$\rightarrow$	$e^-_{(CB)}$ + $h^+_{(VB)}$	(4-10.1)
h^+ + $HC_2O_4^-$	$\rightarrow$	CO_2 + $\cdot CO_2^-$ + H^+	(4-10.2)
$\cdot CO_2^-$	$\rightarrow$	$e^-_{(CB)}$ + CO_2	(4-10.3)
$2e^-$ + $2H^+$	$\rightarrow$	$2\cdot H$	(4-10.4)
$2\cdot H$	$\rightarrow$	H_2	(4-10.5)
$h\nu$ + H^+ + $HC_2O_4^-$	$\rightarrow$	$2CO_2$ + H_2	(4-10.6)

Mechanism (3) radical recombination:

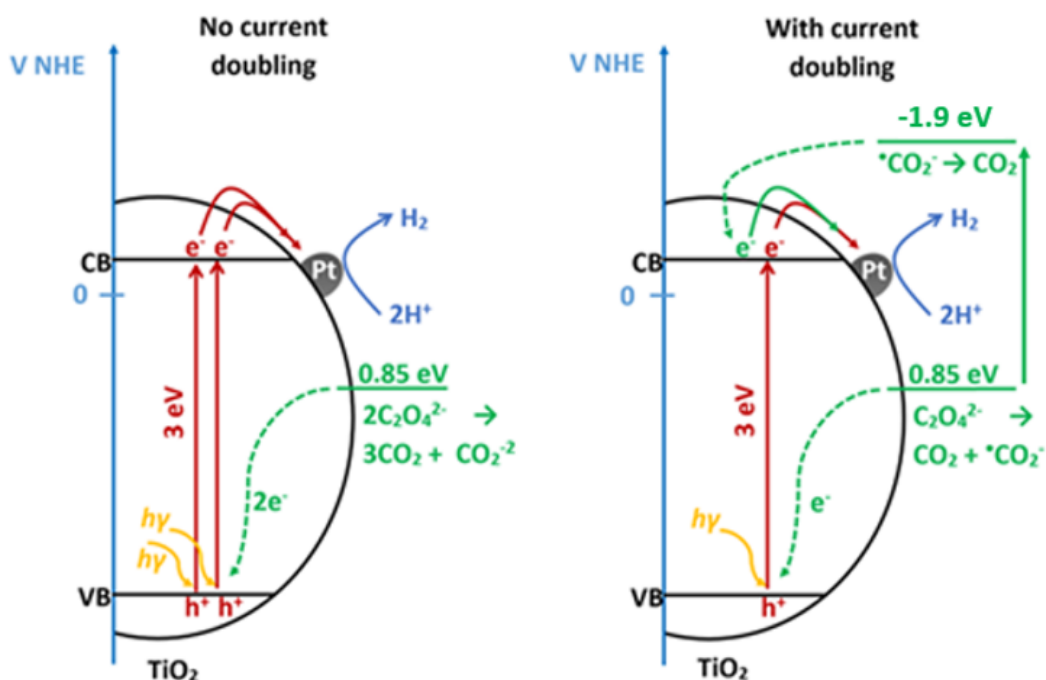|			
$h\nu$	$\rightarrow$	$e^-_{(CB)}$ + $h^+_{(VB)}$	(4-11.1)
h^+ + $HC_2O_4^-$	$\rightarrow$	CO_2 + $\cdot CO_2^-$ + H^+	(4-11.2)
e^- + H^+	$\rightarrow$	$\cdot H$	(4-11.3)
$\cdot CO_2^-$ + $\cdot H$	$\rightarrow$	HCO_2^-	(4-11.4)
$h\nu$ + $HC_2O_4^-$	$\rightarrow$	CO_2 + HCO_2^-	(4-11.5)

Figure 4-8 *Schematic representation of the two-hole mechanism (no current doubling) and the one-hole mechanisms (with current doubling). The standard reduction potential of oxalic acid is taken from Ref. [57].*

We note that the disproportionation of $^{\bullet}CO_2^-$ radicals can compete with the electron injection to TiO$_2$. Carbon dioxide radical anions show a bimolecular decay rate constant between 7.5 x 10^8 and 1.4 x 10^9 l mol^{-1} s^{-1} [56]. However, the injection of electrons from $(CH_3)_2^{\bullet}COH$ radicals [E^0= -1.8 V] into the conduction band of TiO$_2$ has a rate constant between 1.6 x 10^8 and 4 x 10^8 l mol^{-1} s^{-1} [58, 59]. Importantly, Safrany et al. [60] showed that the disproportionation of the $(CH_3)_2^{\bullet}COH$ radicals compete with the electron injection in TiO$_2$. Hence, the disproportionation of $^{\bullet}CO_2^-$ radicals might interfere with the current doubling.

The disproportionation of two $^{\bullet}CO_2^-$ radicals leads to the formation of CO$_2$ and formate anion and/or formic acid [pK_a(HCOOH) = 3.75] [13] as per Eq. 9.3 and Scheme 4-1. The generation of formate is mainly due to the head-to-tail recombination of two $^{\bullet}CO_2^-$ radicals. Flyunt et al. [56] have demonstrated using radiolysis experiments that more than 90% of $^{\bullet}CO_2^-$ radicals recombined to produce formate and carbon dioxide instead of recombination at the carbon to generate oxalate.

Our experimental results using Pt/TiO$_2$ show that the molar ratio of H$_2$:OA is 0.72. We assume, hence, that the photocatalytic reforming of oxalic acid mostly occurs via the combination of mechanisms (1) and (2). Of interest here is the fact that current doubling is not perfect, i.e., the H$_2$:OA is significantly lower than 1. Owing to the previous discussion, we suggest that the total reforming of oxalic acid over Pt/TiO$_2$ follows mechanisms (1) and (2) with a similar probability, leading to a maximum yield of H$_2$ between 0.5 and 1. The by-products, e.g., formate, may not act as hole scavengers at low concentrations especially in the presence of oxalic acid on the surface of the photocatalyst. It has been demonstrated that oxalic acid adsorbs more strongly on TiO$_2$ than formate, which favors the photocatalytic reforming of oxalic acid even in the presence of an excess amount of formate [5].

The lower contribution of the current doubling can be due to the incomplete transfer of the injected electrons to platinum NPs as shown by our solid-phase EPR results. Moreover, $^{\bullet}CO_2^-$ radicals can react with other species in suspension, taking into account the nature of the species and the lifetime of the radical. It was previously noted that current doubling for methanol never reaches the same extent as the hole-induced current and that its extent depends on many factors such as concentration, pH and light intensity [61]. Such a lower contribution has been also observed by Nogami and Kennedy [62], who investigated the photo-oxidation mechanisms of methanol, formaldehyde, and formic acid using the rotating ring disk electrode technique with n-TiO$_2$ as a disk electrode. They found upon illumination that, although true current-doubling (100% increase) was not achieved, photocurrent increases of ~50% were observed.

When other photocatalysts are employed (i.e. bare TiO$_2$, Au/TiO$_2$, and Au-Pt/TiO$_2$), the H$_2$:OA molar ratios are lower (Table 4-1). In the case of bare TiO$_2$, the ratio is even lower than 0.5, i.e. the

expected value from mechanism 1. From these considerations, we expect in these cases a stronger contribution of mechanism (3). Indeed, the recombination of ˙H atoms on platinum is higher than on gold (recombination factor γ = 0.06 and 0.03 at 293 K for Pt and Au, respectively) [63], decreasing, in this case, the probability of mechanism (3). Moreover, it has been reported that ˙H atoms are produced on TiO_2 surfaces before their recombination on the metal co-catalysts [64, 65], and that ˙H atoms can spillover from the metal co-catalyst to the titanium dioxide surface [66]. Thus, in bare TiO_2 the absence of a co-catalyst means that a large fraction of ˙H will end up producing formate (Eq. 4-11.4), decreasing the yield of H_2. This argument is supported by the distinct amounts of produced formate over the different materials (Figure 4-3). Another possible pathway for the production of formate can proceed *via* the cleavage of the C-O bond as predicted previously [9], forming the adsorbed ˙CO-CO_2^- radicals. The formed radicals can react with ˙H atoms producing adsorbed glyoxylate. The later might undergo cleavage of its C-C bond, producing formaldehyde through the reaction between ˙H atoms and formyl radicals. In addition to the detection of formyl radicals by means of the EPR spin-trap experiments, the production of formaldehyde was also detected by following the color developed upon its derivatization with Nash's reagent [67]; however, the quantitation of these trace amounts was difficult.

4.6. Conclusion

This work demonstrates the H_2 evolution from oxalic acid photoreforming using self-prepared TiO_2 photocatalysts. The conversion of oxalic acid to H_2 and CO_2 is feasible even on bare TiO_2; however, the loading of different mono-metallic (Pt or Au) and bi-metallic (Au-Pt) co-catalysts reflects in higher photocatalytic conversions. The surface coverage relates strongly to the pH and is found to be maximized at pH 3 through the adsorption of 0.91 oxalic acid molecules per nm^2 of TiO_2 surface.

During the photocatalytic reforming, CO_2:H_2 molar ratios are found to be higher than the stoichiometric ratio. The complete consumption of oxalate on Pt/TiO_2 results in about 30 % lower amounts of H_2 than expected. Several explanations have been discussed: (i) the dissociation of hydrogen on Pt NPs followed by its adsorption on the metal surface can block the active sites and deteriorate the evolution; (ii) the incomplete scavenging of photogenerated electrons by Pt NPs, as shown by solid-phase EPR spectroscopy, can negatively affect the H_2 evolution because of the low reactivity of the trapped electrons; (iii) the disproportionation of ˙CO_2^- radicals, which lowers the contribution of the current doubling in the total reforming mechanism, and (iv) a simultaneous formation of by-products on the irradiated TiO_2 surface as revealed from the EPR spin-trap experiments, e.g., formate and formaldehyde, that can compete with H_2 production.

A better understanding of the oxalic acid surface reaction mechanism on irradiated-TiO_2 surfaces is vital in creating efficient systems for the production of molecular hydrogen. Therefore,

eliminating the inconvenient side-reactions as well as the adsorption of hydrogen on Pt might
enhance the production of H$_2$ to reach a 100% contribution of the current doubling effect in the
photoreforming process.
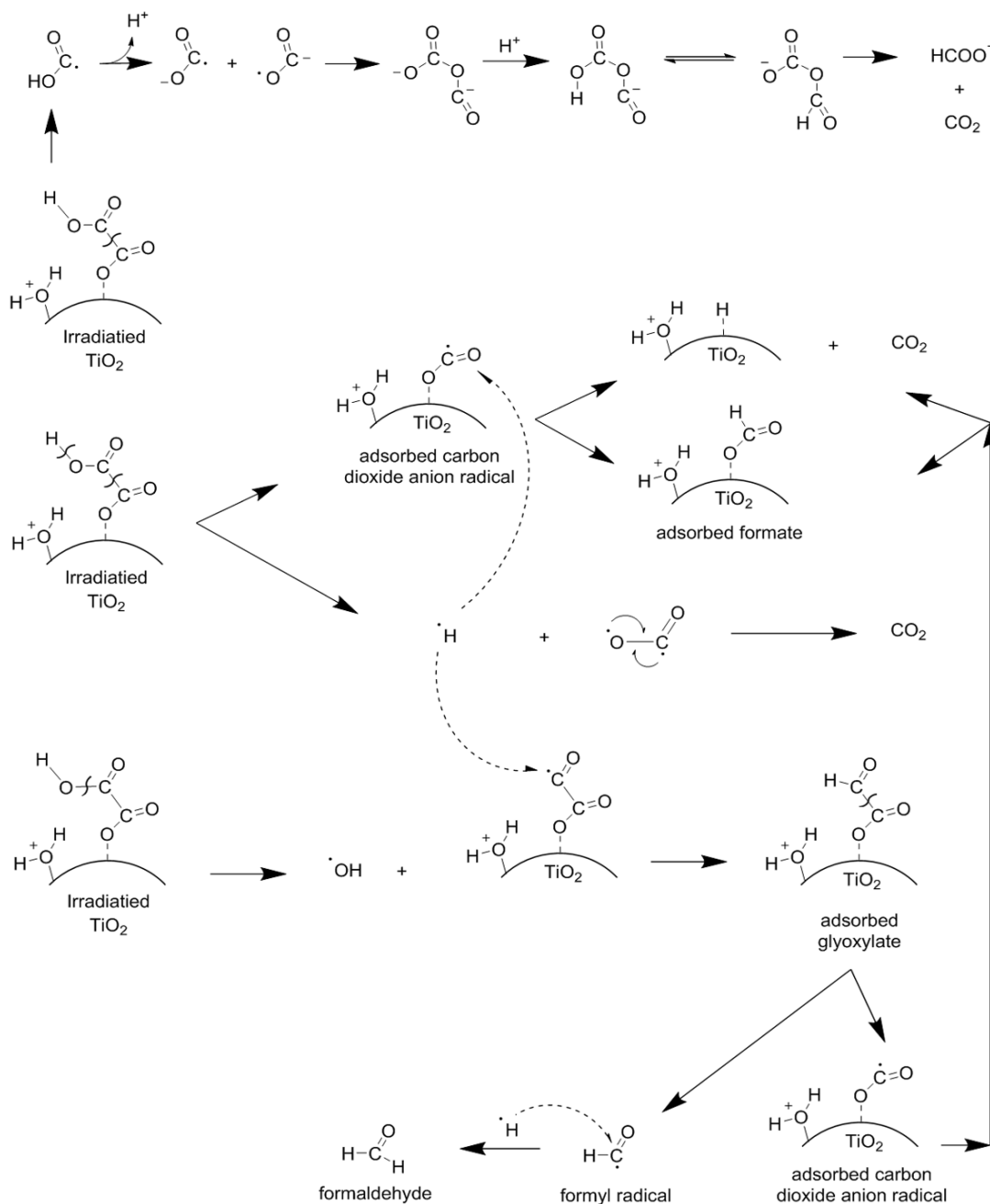
Scheme 4- 1. The proposed surface reaction mechanism of the photocatalytic oxalic acid conversion on TiO$_2$.

4.7. Supporting information
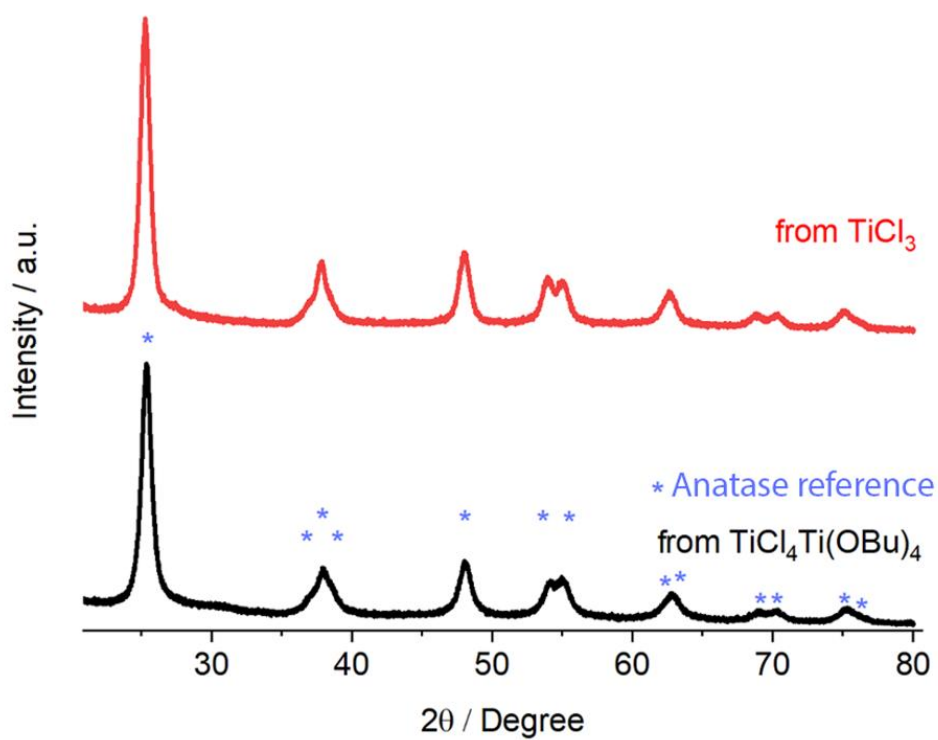
XRD patterns

Figure 4-S1. X-ray diffraction (XRD) patterns of the self-prepared photocatalysts: (black) from TiCl$_4$(TiOBu)$_4$; (red) from TiCl$_3$. The stars show the reference values for anatase TiO$_2$ from ICDD entry 03-065-5714.
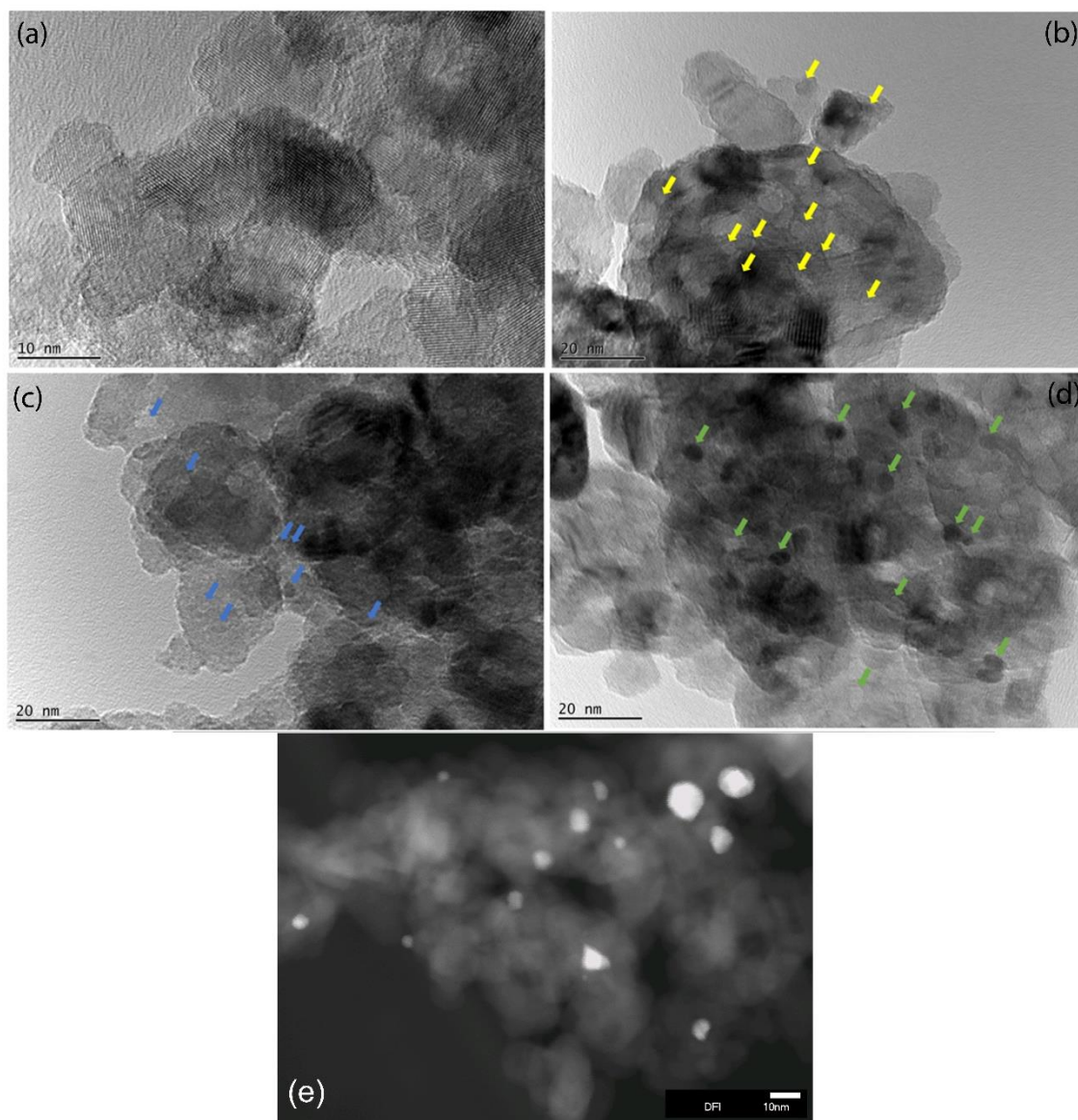
TEM images

Figure 4-S2. Transmission electron microscopy (TEM) images for bare TiO₂ (a), Au/TiO₂ (b), Pt/TiO₂ (c), and Au-Pt/TiO₂ (d). TEM dark-field image for Au-Pt/TiO₂ (e). The arrows indicate the presence of the metallic nanoparticles.
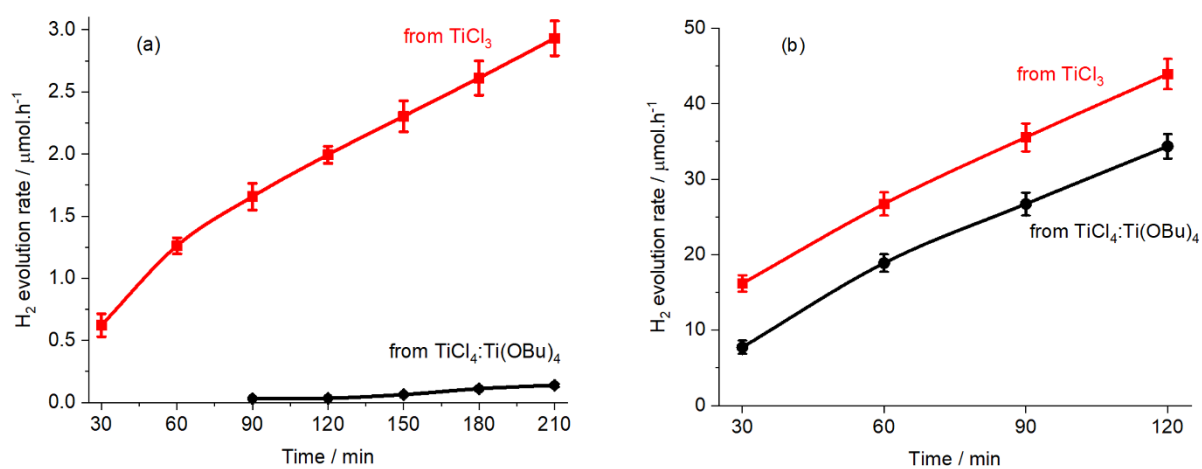
Batch photocatalytic screening experiments

Figure 4-S3. Batch photocatalytic hydrogen evolution experiments from 100 mmol l⁻¹ oxalic acid at pH ~3 using simulated solar light and GC-TCD for H₂ quantification; (a) over 1 g l⁻¹ bare TiO₂; (b) over 0.5 g l⁻¹ Pt₀.₂₅%/TiO₂.

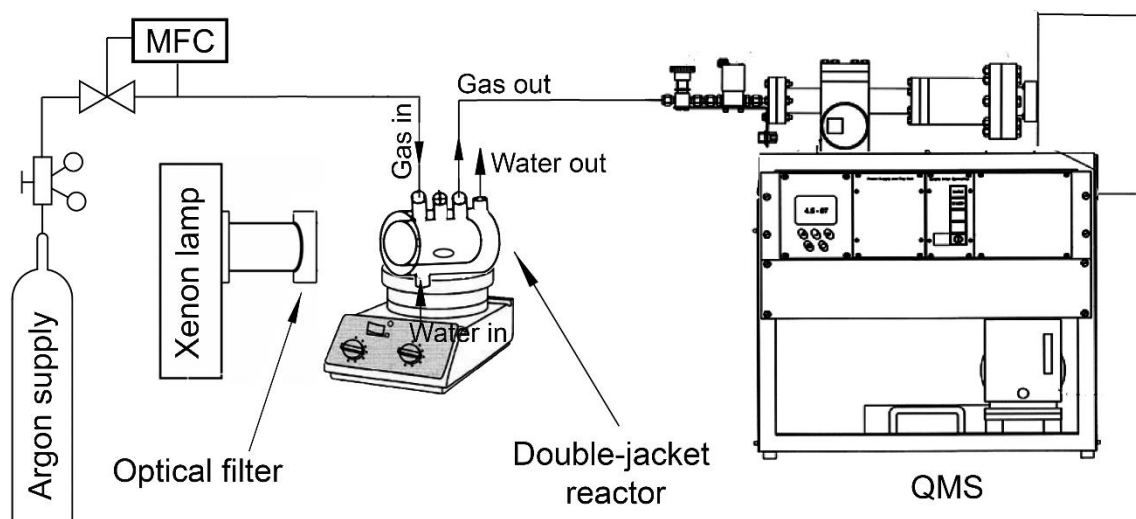## Contionous-flow photocatalytic setup

Figure 4-S4. Experimental setup for the continuous measurement of the photocatalytic gas evolution.
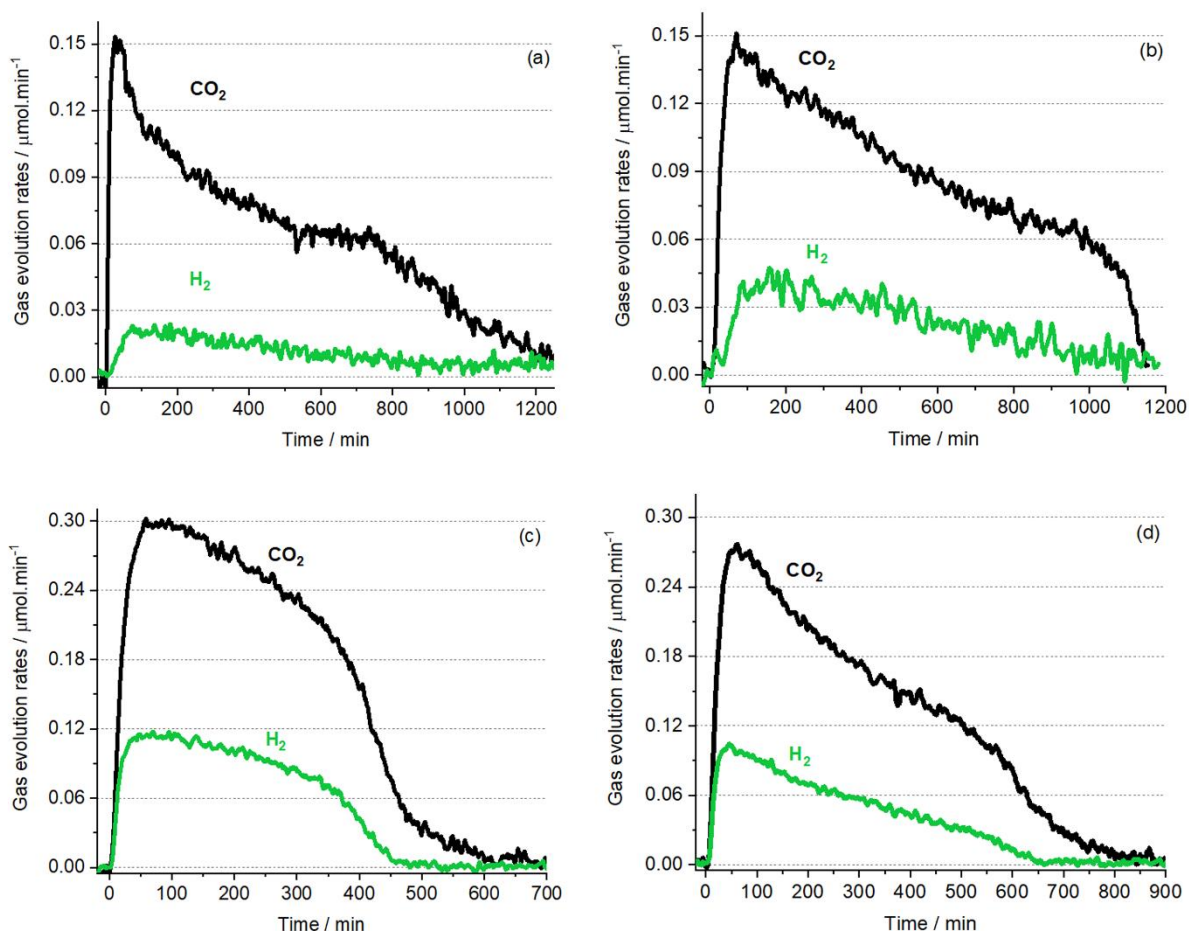
Photocatalytic gas formation rates

Figure 4-S5. Formation rates of the main gases i.e., CO$_2$, H$_2$, evolved from 50 ml aqueous suspensions of 1.11 mmol l^{-1} oxalic acid at pH ~3 over bare TiO$_2$ (a), Au$_{1\%}$/TiO$_2$ (b), Pt$_{0.25\%}$/TiO$_2$ (c) and Au$_{1\%}$-Pt$_{0.25\%}$/TiO$_2$ (d), respectively.

Photonic efficiency calculation

The photonic efficiency ξ of the photocatalytic conversion has been calculated according to Eqs. S1 and S2 [1].

$$\xi = \frac{\text{degradation or formation rate (mol.}\,s^{-1})}{\text{photon flux (mol.}\,m^2.s^{-1})} = \frac{V.\Delta c}{I_0.A.\Delta t} \tag{S1}$$

$$I_0 = \frac{I.\lambda}{N_A.h.c} \tag{S2}$$

where V is the suspension volume (0.05 l), $\Delta c/\Delta t$ is the degradation or the formation rate (mol s^{-1}), A is the illuminated area (5.03 x 10^{-4} m^2), I is the light intensity (W m^{-2}), λ is the corresponding wavelength (m), N_A is the Avogadro's constant (6.02 x 10^{23} mol^{-1}), h is the Planck constant (6.63 x 10^{-34} W s^2) and c is the velocity of light (3 x 10^8 m s^{-1}).

Time course of the visible-light photocatalytic H_2 and CO_2 evolution
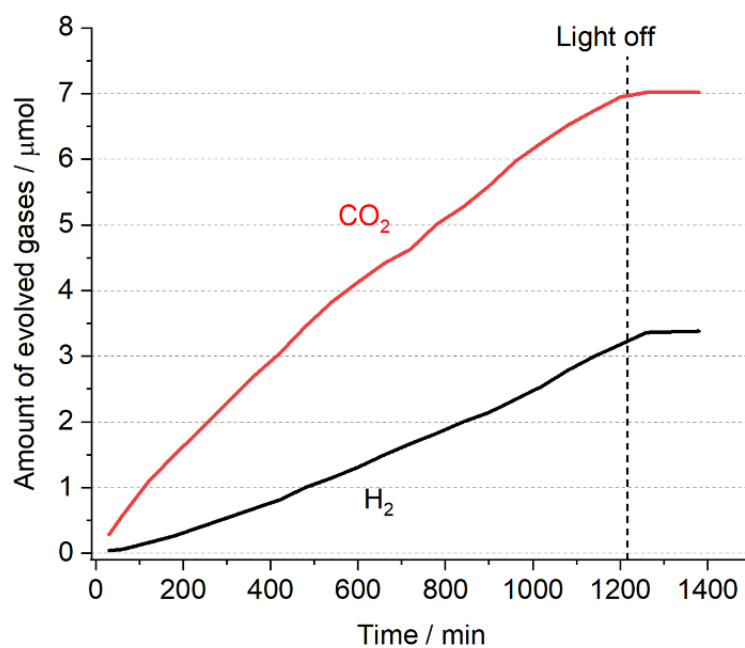
Figure 4-S6. Photocatalytically evolved amounts of H_2 and CO_2 from 50 ml aqueous suspensions of 1.11 mmol l^{-1} oxalic acid at pH ~3 over bare $Au_{1\%}$-$Pt_{-0.25\%}$/TiO_2 using a longpass filter with a cut-on wavelength of 410 nm.

The effect of pH on the adsorption of oxalic acid

Figure S7. Adsorbed amounts of oxalic acid on the surface of bare TiO_2 in dark conditions starting from 1.11 mmol l^{-1} oxalic acid adjusted at different pH values.

Photocatalytic gas formation rates from 100 mmol l^{-1} oxalic acid
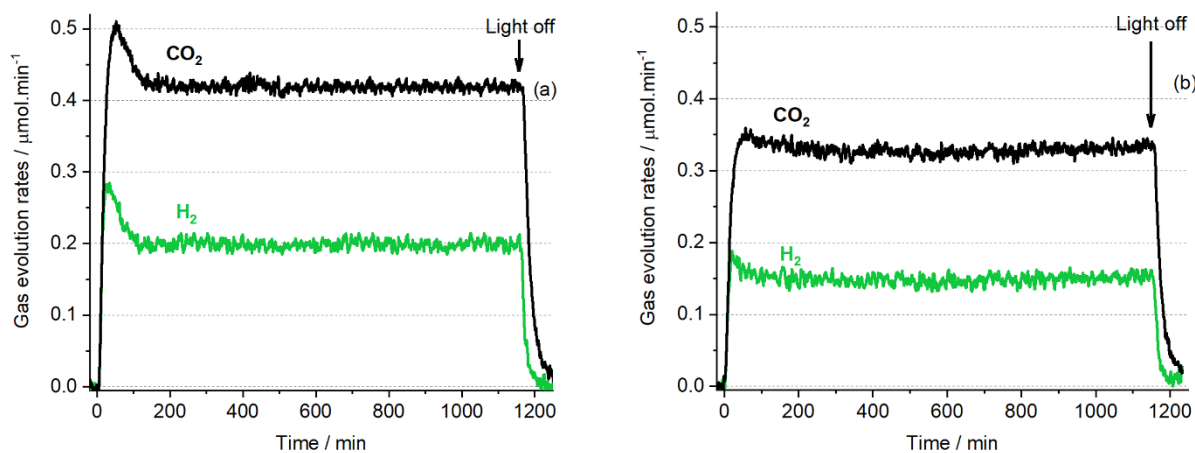
Figure S8. Formation rates of the main gases i.e., CO$_2$, H$_2$, evolved from 50 ml aqueous suspensions of 100 mmol l^{-1} oxalic acid at pH ~3 over Pt$_{0.25\%}$/TiO$_2$ (a) and Au$_{1\%}$-Pt$_{-0.25\%}$/TiO$_2$ (b), respectively.
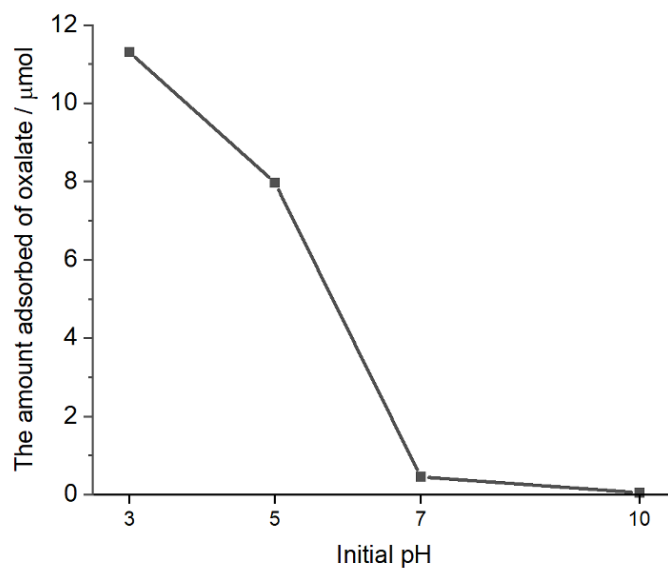
EPR spectrum of carbon dioxide radical anion
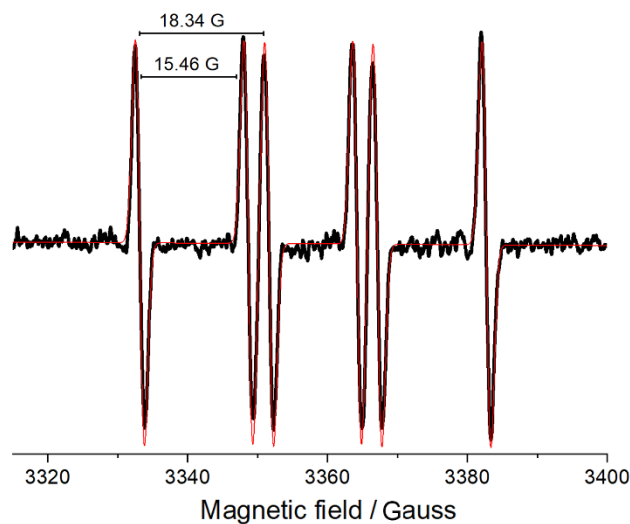
Figure S9. The simulation of an EPR experimental spectrum observed in the absence of O$_2$ upon the UV irradiation of aqueous suspension of formate. The test suspension contained (3.5 mmol l^{-1} at pH ~3), DMPO (0.8 mmol l^{-1}) in the presence of (1 g l^{-1}) of Pt/TiO$_2$.

4.8. Acknowledgments

4.9. References

1.   AlSalka, Y., et al., *Co-catalyst-free photocatalytic hydrogen evolution on TiO$_2$: Synthesis of optimized photocatalyst through statistical material science.* Applied Catalysis B: Environmental, 2018. **238**: p. 422-433.
2.   Friehs, E., et al., *Toxicity, phototoxicity and biocidal activity of nanoparticles employed in photocatalysis.* Journal of Photochemistry and Photobiology C: Photochemistry Reviews, 2016. **29**: p. 1-28.
3.   Schneider, J., et al., *Understanding TiO$_2$ photocatalysis: mechanisms and materials.* Chemical reviews, 2014. **114**(19): p. 9919-9986.
4.   Takanabe, K., *Photocatalytic water splitting: quantitative approaches toward photocatalyst by design.* ACS Catalysis, 2017. **7**(11): p. 8006-8022.
5.   Puga, A.V., *Photocatalytic production of hydrogen from biomass-derived feedstocks.* Coordination Chemistry Reviews, 2016. **315**: p. 1-66.
6.   Guo, Q., et al., *Elementary photocatalytic chemistry on TiO$_2$ surfaces.* Chemical Society Reviews, 2016. **45**(13): p. 3701-3730.
7.   Mendive, C.B., et al., *ATR-FTIR measurements and quantum chemical calculations concerning the adsorption and photoreaction of oxalic acid on TiO$_2$.* Physical chemistry chemical physics, 2006. **8**(27): p. 3232-3247.
8.   Mendive, C.B., et al., *Adsorption of oxalate on anatase (100) and rutile (110) surfaces in aqueous systems: experimental results vs. theoretical predictions.* Physical Chemistry Chemical Physics, 2009. **11**(11): p. 1794-1808.
9.   Mendive, C.B., et al., *Oxalic acid at the TiO$_2$/water interface under UV (A) illumination: Surface reaction mechanisms.* Journal of catalysis, 2015. **322**: p. 60-72.
10.   Li, Y., G. Lu, and S. Li, *Photocatalytic hydrogen generation and decomposition of oxalic acid over platinized TiO$_2$.* Applied Catalysis A: General, 2001. **214**(2): p. 179-185.
11.   Franch, M.I., et al., *Photocatalytic degradation of short-chain organic diacids.* Catalysis today, 2002. **76**(2-4): p. 221-233.
12.   Li, Y., G. Lu, and S. Li, *Photocatalytic production of hydrogen in single component and mixture systems of electron donors and monitoring adsorption of donors by in situ infrared spectroscopy.* Chemosphere, 2003. **52**(5): p. 843-850.
13.   AlSalka, Y., et al., *Understanding the degradation pathways of oxalic acid in different photocatalytic systems: Towards simultaneous photocatalytic hydrogen evolution.* Journal of Photochemistry and Photobiology A: Chemistry, 2018. **366**: p. 81-90.
14.   Yamada, Y., et al., *Photocatalytic hydrogen evolution from carbon-neutral oxalate with 2-phenyl-4-(1-naphthyl) quinolinium ion and metal nanoparticles.* Physical Chemistry Chemical Physics, 2012. **14**(30): p. 10564-10571.
15.   Ohtani, B., *Photocatalysis A to Z—What we know and what we do not know in a scientific sense.* Journal of Photochemistry and Photobiology C: Photochemistry Reviews, 2010. **11**(4): p. 157-178.

16. Kandiel, T.A., I. Ivanova, and D.W. Bahnemann, *Long-term investigation of the photocatalytic hydrogen production on platinized TiO$_2$: an isotopic study.* Energy & Environmental Science, 2014. **7**(4): p. 1420-1425.

17. Ivanova, I., et al., *Photocatalytic degradation of oxalic and dichloroacetic acid on TiO$_2$ coated metal substrates.* Catalysis Today, 2013. **209**: p. 84-90.

18. Yamamoto, S. and R.A. Back, *The gas-phase photochemistry of oxalic acid.* The Journal of Physical Chemistry, 1985. **89**(4): p. 622-625.

19. Stoll, S. and A. Schweiger, *EasySpin, a comprehensive software package for spectral simulation and analysis in EPR.* Journal of Magnetic Resonance, 2006. **178**(1): p. 42-55.

20. Bamwenda, G.R., et al., *Photoassisted hydrogen production from a water-ethanol solution: a comparison of activities of Au-TiO$_2$ and Pt-TiO$_2$.* Journal of Photochemistry and Photobiology A: Chemistry, 1995. **89**(2): p. 177-189.

21. Tanaka, A., et al., *Preparation of Au/TiO$_2$ with Metal Cocatalysts Exhibiting Strong Surface Plasmon Resonance Effective for Photoinduced Hydrogen Formation under Irradiation of Visible Light.* ACS Catalysis, 2013. **3**(1): p. 79-85.

22. Gallo, A., et al., *Bimetallic Au–Pt/TiO$_2$ photocatalysts active under UV-A and simulated sunlight for H$_2$ production from ethanol.* Green Chemistry, 2012. **14**(2): p. 330-333.

23. Kamat, P.V., *Photophysical, Photochemical and Photocatalytic Aspects of Metal Nanoparticles.* The Journal of Physical Chemistry B, 2002. **106**(32): p. 7729-7744.

24. Fu, X., et al., *Photocatalytic reforming of biomass: A systematic study of hydrogen evolution from glucose solution.* International Journal of Hydrogen Energy, 2008. **33**(22): p. 6484-6491.

25. Khan, M.R., et al., *Schottky barrier and surface plasmonic resonance phenomena towards the photocatalytic reaction: study of their mechanisms to enhance photocatalytic activity.* Catalysis Science & Technology, 2015. **5**(5): p. 2522-2531.

26. Michaelson, H.B., *The work function of the elements and its periodicity.* Journal of Applied Physics, 1977. **48**(11): p. 4729-4733.

27. Schneider, J., T.A. Kandiel, and D.W. Bahnemann, *Solar Photocatalytic Hydrogen Production: Current Status and Future Challenges*, in *Materials and Processes for Solar Fuel Production*, B. Viswanathan, V. Subramanian, and J.S. Lee, Editors. 2014, Springer New York: New York, NY. p. 41-74.

28. Kamat, P.V., *Manipulation of Charge Transfer Across Semiconductor Interface. A Criterion That Cannot Be Ignored in Photocatalyst Design.* The Journal of Physical Chemistry Letters, 2012. **3**(5): p. 663-672.

29. Nørskov, J.K., et al., *Trends in the exchange current for hydrogen evolution.* Journal of The Electrochemical Society, 2005. **152**(3): p. J23-J26.

30. Dong, H., et al., *Three-dimensional nitrogen-doped graphene supported molybdenum disulfide nanoparticles as an advanced catalyst for hydrogen evolution reaction.* Scientific reports, 2015. **5**: p. 17542.

31. Subramanian, V., E.E. Wolf, and P.V. Kamat, *Green Emission to Probe Photoinduced Charging Events in ZnO−Au Nanoparticles. Charge Distribution and Fermi-Level Equilibration.* The Journal of Physical Chemistry B, 2003. **107**(30): p. 7479-7485.

32. Huber, G.W., et al., *Aqueous-phase reforming of ethylene glycol over supported Pt and Pd bimetallic catalysts.* Applied Catalysis B: Environmental, 2006. **62**(3-4): p. 226-235.

33. Hu, M., et al., *Hydrogen adsorption on platinum–gold bimetallic nanoparticles: A density functional theory study.* The Journal of Physical Chemistry C, 2013. **117**(29): p. 15050-15060.

34. Kmetykó, Á., et al., *Photocatalytic H$_2$ production using Pt-TiO$_2$ in the presence of oxalic acid: Influence of the noble metal size and the carrier gas flow rate.* Materials, 2014. **7**(10): p. 7022-7038.

35. Serpone, N., et al., *Turnovers and photocatalysis: A mathematical description.* Journal of Photochemistry and Photobiology A: Chemistry, 2000. **130**(2-3): p. 83-94.

36. Sun, Y., et al., *An Unexpected Fluctuating Reactivity for Odd and Even Carbon Numbers in the TiO$_2$-Based Photocatalytic Decarboxylation of C$_2$-C$_6$ Dicarboxylic Acids.* Chemistry–A European Journal, 2014. **20**(7): p. 1861-1870.

37. Orts, J., et al., *Electrochemical behaviour of oxalic acid on platinum electrodes in acidic medium: Pt (100), Pt (111), Pt (110) and stepped surfaces.* Journal of electroanalytical chemistry and interfacial electrochemistry, 1990. **281**(1-2): p. 199-219.

38. Nakaoka, Y. and Y. Nosaka, *ESR investigation into the effects of heat treatment and crystal structure on radicals produced over irradiated TiO$_2$ powder.* Journal of Photochemistry and Photobiology A: Chemistry, 1997. **110**(3): p. 299-305.

39. Howe, R.F. and M. Gratzel, *EPR study of hydrated anatase under UV irradiation.* Journal of Physical Chemistry, 1987. **91**(14): p. 3906-3909.

40. Livraghi, S., et al., *On the nature of reduced states in titanium dioxide as monitored by electron paramagnetic resonance. I: the anatase case.* The Journal of Physical Chemistry C, 2011. **115**(51): p. 25413-25421.

41. Chiesa, M., et al., *Charge trapping in TiO$_2$ polymorphs as seen by Electron Paramagnetic Resonance spectroscopy.* Physical Chemistry Chemical Physics, 2013. **15**(24): p. 9435-9447.

42. Howe, R.F. and M. Gratzel, *EPR observation of trapped electrons in colloidal titanium dioxide.* The Journal of Physical Chemistry, 1985. **89**(21): p. 4495-4499.

43. Micic, O., et al., *Photoinduced hole transfer from titanium dioxide to methanol molecules in aqueous solution studied by electron paramagnetic resonance.* The Journal of Physical Chemistry, 1993. **97**(50): p. 13284-13288.

44. Roberts, J.G., et al., *The hydroxyl radical is a critical intermediate in the voltammetric detection of hydrogen peroxide.* Journal of the American Chemical Society, 2016. **138**(8): p. 2516-2519.

45. Wang, Y. and P. Zhang, *Photocatalytic decomposition of perfluorooctanoic acid (PFOA) by TiO$_2$ in the presence of oxalic acid.* Journal of hazardous materials, 2011. **192**(3): p. 1869-1875.

46. Marriott, P.R., M.J. Perkins, and D. Griller, *Spin trapping for hydroxyl in water: a kinetic evaluation of two popular traps.* Canadian Journal of Chemistry, 1980. **58**(8): p. 803-807.

47. Ervens, B., S. Gligorovski, and H. Herrmann, *Temperature-dependent rate constants for hydroxyl radical reactions with organic compounds in aqueous solutions.* Physical Chemistry Chemical Physics, 2003. **5**(9): p. 1811-1824.

48. Buettner, G.R., *Spin Trapping: ESR parameters of spin adducts 1474 1528V.* Free Radical Biology and Medicine, 1987. **3**(4): p. 259-303.

49. Bauer, N.A., et al., *Detection of the formyl radical by EPR spin-trapping and mass spectrometry.* Free Radical Biology and Medicine, 2018. **116**: p. 129-133.

50. Mendive, C.B., M. Curti, and D. Bahnemann, *CHAPTER 3 Current Issues Concerning the Mechanism of Pristine TiO$_2$ Photocatalysis and the Effects on Photonic Crystal Nanostructures*, in *Photocatalysis: Fundamentals and Perspectives.* 2016, The Royal Society of Chemistry. p. 51-79.

51. Doudrick, K., et al., *Nitrate reduction in water using commercial titanium dioxide photocatalysts (P25, P90, and Hombikat UV100).* Journal of Environmental Engineering, 2011. **138**(8): p. 852-861.

52. Mora-Sero, I., et al., *Photoelectrochemical behavior of nanostructured TiO$_2$ thin-film electrodes in contact with aqueous electrolytes containing dissolved pollutants: A model for distinguishing between direct and indirect interfacial hole transfer from photocurrent measurements.* The Journal of Physical Chemistry B, 2005. **109**(8): p. 3371-3380.

53. Hakki, A., J. Schneider, and D. Bahnemann, *CHAPTER 2 Understanding the Chemistry of Photocatalytic Processes*, in *Photocatalysis: Fundamentals and Perspectives.* 2016, The Royal Society of Chemistry. p. 29-50.

54. Mulazzani, Q.G., et al., *Interaction of formate and oxalate ions with radiation-generated radicals in aqueous solution. Methylviologen as a mechanistic probe.* The Journal of Physical Chemistry, 1986. **90**(21): p. 5347-5352.

55. Kanoufi, F. and A.J. Bard, *Electrogenerated chemiluminescence. 65. An investigation of the oxidation of oxalate by tris (polypyridine) ruthenium complexes and the effect of the electrochemical steps on the emission intensity.* The Journal of Physical Chemistry B, 1999. **103**(47): p. 10469-10480.

56. Flyunt, R., M.N. Schuchmann, and C. von Sonntag, *A Common Carbanion Intermediate in the Recombination and Proton-Catalysed Disproportionation of the Carboxyl Radical Anion, CO$_2^{\cdot-}$, in Aqueous Solution.* Chemistry–A European Journal, 2001. **7**(4): p. 796-799.

57. Chen, C., J.F. Khosrowabadi Kotyk, and S.W. Sheehan, *Progress toward Commercial Application of Electrochemical Carbon Dioxide Reduction.* Chem, 2018. **4**(11): p. 2571-2586.

58. Gao, R., A. Safrany, and J. Rabani, *Fundamental reactions in TiO$_2$ nanocrystallite aqueous solutions studied by pulse radiolysis.* Radiation Physics and Chemistry, 2002. **65**(6): p. 599-609.

59. Dimitrijevic, N.M., et al., *Revealing the Nature of Trapping Sites in Nanocrystalline Titanium Dioxide by Selective Surface Modification.* The Journal of Physical Chemistry B, 2003. **107**(30): p. 7368-7375.

60. Safrany, A., R. Gao, and J. Rabani, *Optical Properties and Reactions of Radiation Induced TiO$_2$ Electrons in Aqueous Colloid Solutions.* The Journal of Physical Chemistry B, 2000. **104**(24): p. 5848-5853.

61. Hykaway, N., et al., *Current-doubling reactions on titanium dioxide photoanodes.* The Journal of Physical Chemistry, 1986. **90**(25): p. 6663-6667.

62. Nogami, G., *Investigation of "Current Doubling" Mechanism of Organic Compounds by the Rotating Ring Disk Electrode Technique.* Journal of The Electrochemical Society, 1989. **136**(9): p. 2583.

63. Melin, G.A. and R.J. Madix, *Energy accommodation during hydrogen atom recombination on metal surfaces.* Transactions of the Faraday Society, 1971. **67**(0): p. 2711-2719.

64. Joo, J.B., et al., *Promotion of atomic hydrogen recombination as an alternative to electron trapping for the role of metals in the photocatalytic production of H$_2$.* Proceedings of the National Academy of Sciences, 2014. **111**(22): p. 7942-7947.

65. Walenta, C.A., et al., *Why co-catalyst-loaded rutile facilitates photocatalytic hydrogen evolution.* Physical Chemistry Chemical Physics, 2019. **21**(3): p. 1491-1496.

66. Karim, W., et al., *Catalyst support effects on hydrogen spillover.* Nature, 2017. **541**(7635): p. 68-71.

67. Nash, T., *The colorimetric estimation of formaldehyde by means of the Hantzsch reaction.* Biochemical Journal, 1953. **55**(3): p. 416.

Chapter Five: Concluding Discussion and Related Supportive Experiments

5.1. Foreword

Oxygen-free heterogeneous photocatalysis is a sustainable solution to convert photon energy into the storable fuel H_2. On a (metal modified) semiconductor, the adsorbed organic molecules are oxidized to CO_2, meanwhile, protons are reduced to H_2. Most efforts have so far been focused on the development of efficient photocatalysts for the photoreforming of just a few specific compounds, e.g., methanol, acetic acid, and glycerol. TiO_2 is known to be the most studied semiconductor photocatalyst. The scientific community is working, to date, hard to overcome the limitations mentioned in Chapter 1, which still prevent that TiO_2 can be considered as a real promising photocatalyst. Moreover, the synthesis and the modification of TiO_2 photocatalysts are still proceeding in a non-methodological way. Besides, the interfacial surface reactions of organic substrates leading to their transformation to other valuable products, i.e., H_2, have rarely been mechanistically investigated. Moreover, most researchers pay attention to the H_2 evolution reaction rates but not to the total yields of all photocatalytic reactions involving in the overall process. Based on these critical points, photocatalysis is still waiting to be turned into practical applications with regard to solar fuel synthesis.

The Evaporation-induced self-assembly (EISA) method is a soft-templating method characterized by its simplicity to produce mesoporous TiO_2 powders and thin-films [1]. Many studies have been conducted to elucidate the effect of the EISA process parameters on the final products. It has been found that a small change in one of the parameters, i.e., of the precursor type and ratio, the surfactant quantity and type, the solvent, the RH, and/or the calcination temperature, will affect significantly the properties of the thus prepared TiO_2, i.e., the phase content, the mesoporous structure, the optical properties, and hence the photocatalytic activity. However, several parameters affecting the EISA process have been previously changed while ignoring other factors or neglecting real optimization procedures. Furthermore, the use of a rather limited spectrum of titanium precursors, i.e., the most studied precursor $TiCl_4$ is rather difficult to handle, is a common characteristic amongst most previous studies.

In this thesis, a statistical tool, i.e., the Design of Experiment (DoE), has been used to systematically investigate how the simultaneous change of several parameters can affect the properties of the newly synthesized TiO_2 photocatalyst employing the EISA method. The output of such a statistical framework forms a reliable base for an optimized synthesis method for a TiO_2 with improved photocatalytic properties.

The TiO$_2$ produced *via* optimized parameters was then used to investigate the degradation of oxalic acid in different photocatalytic systems, i.e., in aerobic and anaerobic systems, which can be regarded as the "cornerstone" for the understanding of the photocatalytic reforming pathways. Finally, the thus prepared TiO$_2$, bare and loaded with noble metals, has been employed for the production of H$_2$ from aqueous solutions of oxalic acid elucidating the role of the co-catalyst used and the surface reaction mechanisms of the anodic half-reaction of photocatalytic oxalic acid reforming. Fundamental research regarding these issues is rare. Oxalic acid was chosen as a model compound since even though it is a rather "simple" organic molecule, the mechanism of its degradation is still not understood in detail. Moreover, the few existing studies on this topic contain some contradicting data, especially related to the stoichiometric calculations as mentioned in Section 1-8. Finally, oxalic acid can be considered as a potential water pollutant and is found in some industrial effluents (seen section 1-8).

5.2. Synthesizing a TiO$_2$ photocatalyst for water-splitting without a noble metal

The work described in Chapter 2 was done to synthesize a TiO$_2$ photocatalyst having the properties needed to photocatalytically evolve H$_2$ *via* photoreforming processes without any additional noble metal co-catalyst. This can be generally summarized in Figure 5-1.
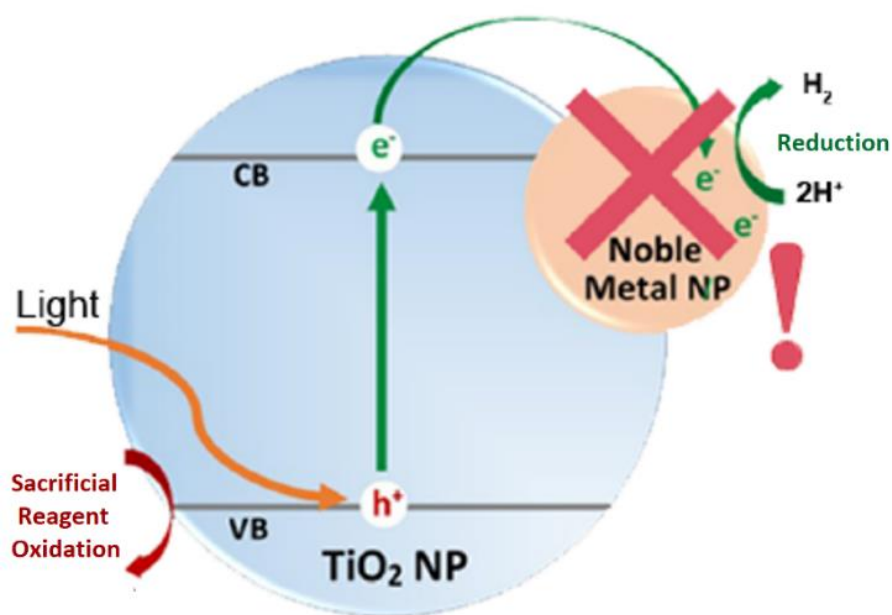

Figure 5-1 Schematic diagram summarizing the main results of Chapter 2

Aiming to reduce both, the time and the costs of consuming chemicals required to establish an optimized process, the DoE approach was employed to optimize the synthesis of TiO$_2$ *via* the EISA method. DoE is a statistical tool allowing to change all levels of the factors studied simultaneously,

in order to achieve a process optimization using the smallest number of experimental runs [2]. Two titanium-precursor combinations, that is, (TiCl$_4$:Ti(OBu)$_4$, and TiCl$_3$:Ti(OBu)$_4$), and two different surfactants (pluronics F-108 and P-123) were employed in this a methodological statistical tool to determine the significant factors, as well as their optimum parameters. TiCl$_3$, which is very easy to handle compared to TiCl$_4$, has rarely been employed before for the synthesis of TiO$_2$. As shown in Figure 5-2, a general Full Factorial Design (FFD) of 16 experimental runs was built to investigate the effects of three factors on the prepared materials: the titanium-precursor type, the surfactant type, and the surfactant quantity. After their synthesis, the prepared materials were evaluated regarding their photocatalytic activity for the hydrogen evolution in the presence of ethanol as a sacrificial reagent. Combining the FFD with the Analysis of Variance (ANOVA) has clearly simplified the investigation of the most influential variables affecting the preparation of TiO$_2$ through the EISA method.
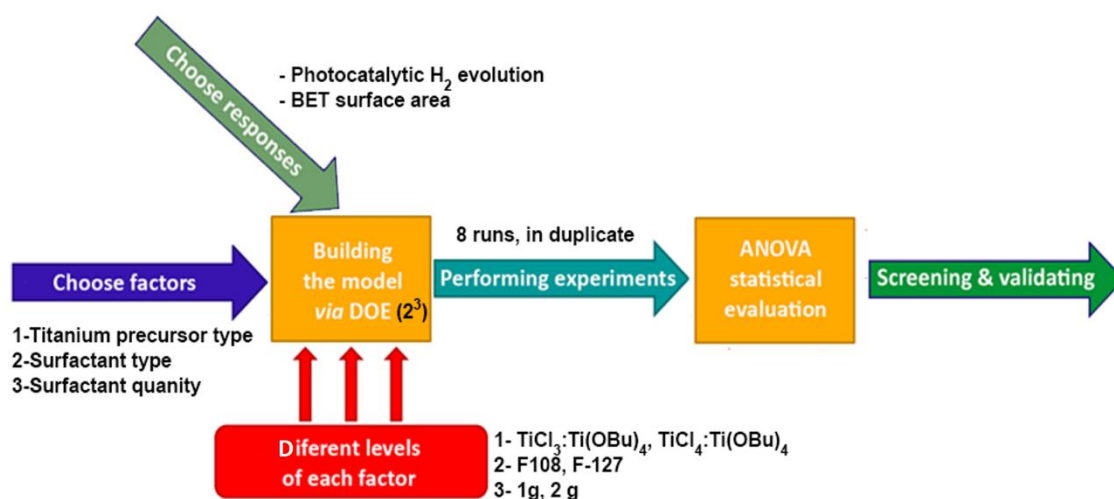
Figure 5-2 Schematic diagram explaining the DoE approach

The ANOVA results revealed that all the studied factors were statistically significant on both, the photocatalytic H$_2$ production and the BET surface area of the TiO$_2$ powder but in different magnitudes. The Pareto chart that is shown in Figure 5-3(a) can be used to determine the magnitude and the importance of the effects, evincing that the titanium-precursor type has the highest statistical impact on the H$_2$ evolution.
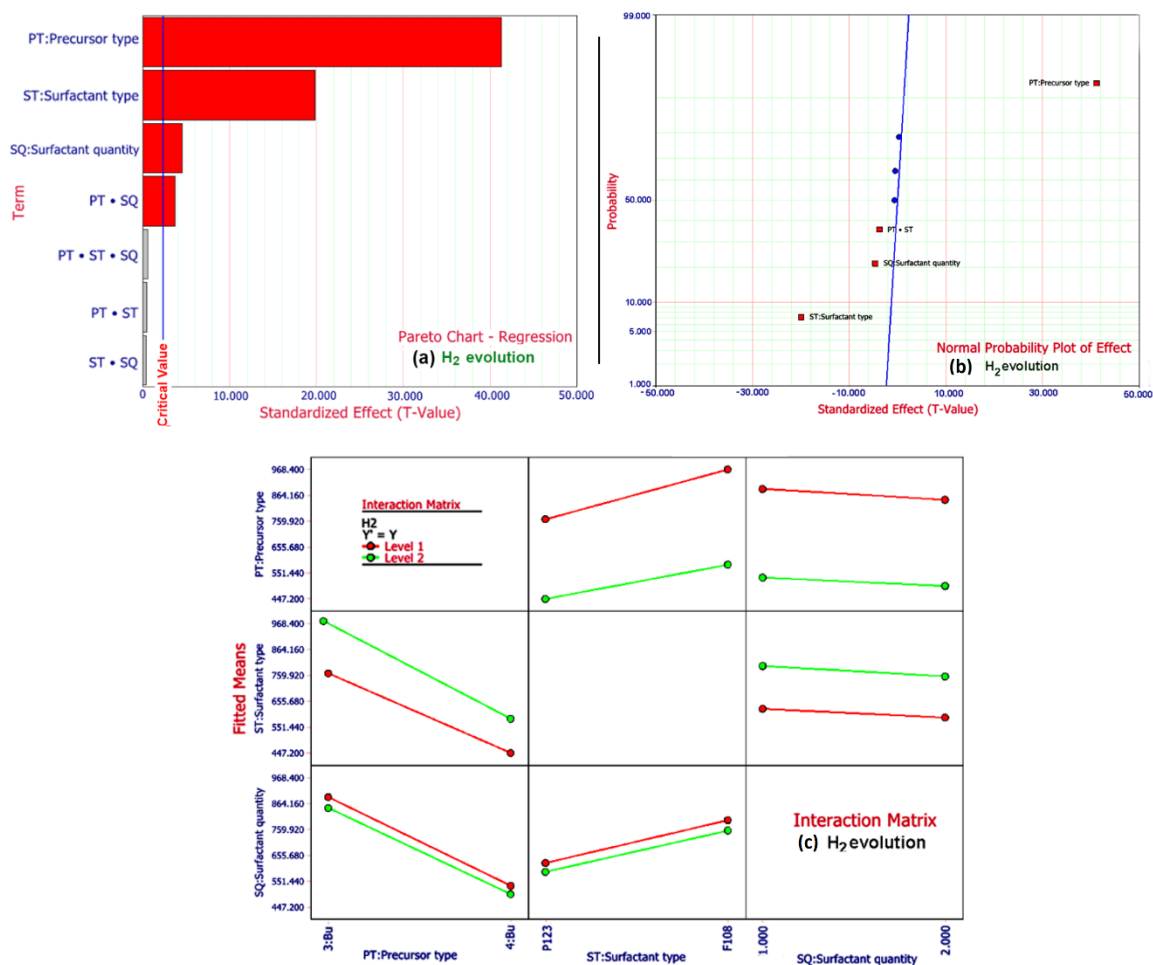
Figure 5-3 Pareto Charts delivered from Full Factorial Design and ANOVA test for photocatalytic hydrogen evolution from aqueous ethanolic suspension (a); the normal probability plots delivered from ANOVA analysis (b); the interaction matrix delivered from ANOVA analysis related to the hydrogen evolution response (b).

The normal probability plot of the standardized effects (Figure 5-3(b)) is used to examine the magnitude, the direction and the importance of the effects. In the agreement with the previous discussion, all the studied factors are statistically significant at the 0.05 level. In addition, the precursor type has a positive standardized effect, hence, the high level of this factor, that is, the $TiCl_3$-based precursor, increases the hydrogen evolution. The surfactant type and the surfactant quantity have, in contrast, negative standardized effects. Consequently, the low levels of these factors, which are F-108 and 1 g, leading to an increase in the hydrogen evolution. The interaction plots in Figure 5-3(c) can be used to show how the relationship between one factor and the respective response, i.e., the H_2 evolution, depends on the value of a second factor. From these interaction plots, it is obvious that with $TiCl_3$:$Ti(OBu)_4$ being the precursor the H_2 evolution can be maximized. On the other hand, the surfactant type is the predominant factor affecting the surface area with F-108 yielding the maximal BET values. The optimization features of the DoE are, hence, successfully utilized to identify the factors that optimize the synthesis method, i.e., the use of $TiCl_3$:$Ti(OBu)_4$ as a precursor and of 1 g F-108 as a surfactant.

DoE outputs form a reliable base for starting the next step of optimization, which is finding the best precursor combination. In this context, different TiO_2 samples were prepared from different ratios between $TiCl_3$ and $Ti(OBu)_4$ as precursors while using 1 g of F-108 as the surfactant. Increasing the $TiCl_3$ ratio in the precursor-mixture resulted in a correlated enhancement in both, the H_2 evolution and the BET surface area for the anatase samples (see Figure 5-4). Based on the photocatalytic batch experiments, TiO_2 prepared from $TiCl_3$ exhibited a 1.5-fold higher photonic efficiency in comparison to other prepared materials. The material prepared from $TiCl_3$ as the only precursor revealed a pure anatase phase having a BET surface area of 121.3 ± 0.9 m^2 g^{-1} and a photocatalytic H_2 evolution of 1221.6 ± 58.1 µmol h^{-1} g^{-1} in the absence of any noble metal co-catalyst. This relatively higher specific surface area offers more active-sites for the adsorbates, hence, allowing more susceptible interfacial charge transfer reactions. This sample showed, as well, a better photocatalytic activity of the ethanol conversion to acetaldehyde compared to the commercially available photocatalysts, i.e., Hombikat UV100 and P25.
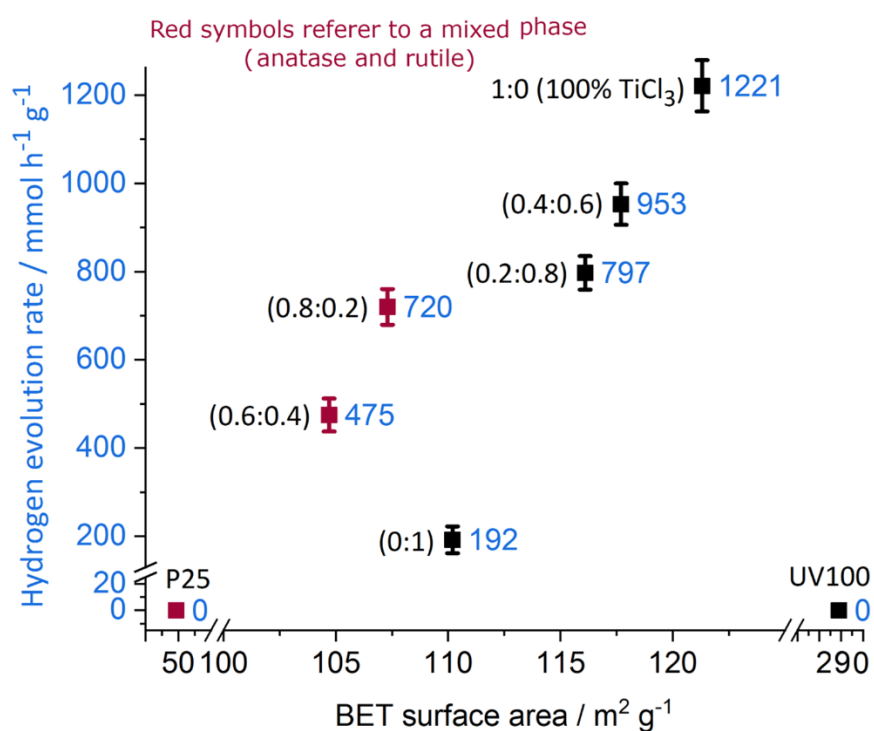
Figure 5-4 Relationship between the photocatalytic activity (after 120 min irradiation) and the BET surface area for the self-prepared photocatalysts.

While changing the ratio between the titanium precursors, the phase ratio between anatase and rutile TiO_2 is altered, thus, the photocatalytic performance is consequently affected. While two TiO_2 samples exhibit mixed anatase/rutile phases, the others have a pure anatase phase. The presence of the rutile phase drastically reduces the BET surface area, resulting in a lower H_2 evolution efficiency. This correlates with previous reports showing a higher hydrogen production yield for anatase-based TiO_2 photocatalysts due to their more negative potential of the conduction band edge

and the lower rates of charge recombination due to the presence of trap states locating below the Fermi level [3-5].

SEM and TEM images reveal a spherical morphology and a grain size ranging from 9 to 15 nm of crystalline structures in random orientation. The lattice arrangement of the crystalline structure is resolved and the Debye-Scherrer rings are completely enclosed, indicating the nanocrystalline structure of the TiO_2 material. The N_2 adsorption-desorption isotherms reveal a type IV characteristic of mesoporous materials according to the BET method [6]. However, these pores are characterized as non-ordered and show a wide distribution range. Hence, the presence of an ordered-mesoporous structure is not clearly confirmed, that is, the enhanced efficiency is most likely independent from such a mesoporous structure.

It is of importance to study the electronic structure of TiO_2, which delivers useful information regarding the efficiency of the material. Since oxygen has a much higher electronegativity than titanium, the valence electrons are transferred from the oxygen to the titanium ion. The main features of the TiO_2 molecular orbital (MO) diagram correlate with the calculated band structure, in which the valence band is mainly composed of O-2p orbitals, whereas the conduction band is primarily Ti-3d in character [7] as shown in Figure 5-5. One of the important insights that can be obtained from the electronic band structure is the mobility of the charge carriers, which is related to the width of the conduction and valence bands. The higher the overlap between the atomic wavefunctions is, the broader are the bands and the easier is the transport of free charge carriers through the material [7].
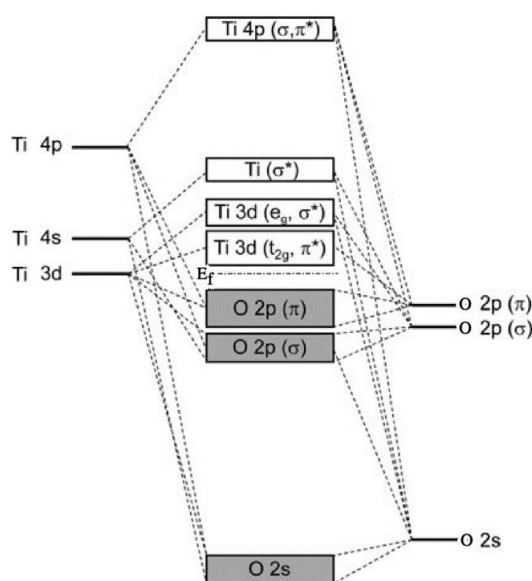

Figure 5-5 Molecular orbital diagram of TiO_2 [7, 8], adapted with permission from Ref. [7].

The electronic band structure of the optimized TiO_2 was experimentally studied using UV-Vis spectroscopy and Mott−Schottky measurements. The prepared material is characterized by its response to a wider range of light, i.e., had an energy band gap of 2.99 eV. As shown in Figure 5-6(a), a clear optical response in the visible range until around 1200 nm can be noticed in the prepared material compared to the commercially available Hombikot UV100 that mainly absorbs in the UV range. This visible response is most likely not due to doping with foreign atoms because of the lack of any foreign atom in the precursors used during the synthesis procedure. Furthermore, the EDX did not detect other impurities within its detection limit. Such visible light response was noticed by other researchers and has been attributed to oxygen vacancies or Ti^{3+} defect states in TiO_2 [9, 10]. Such defects introduce additional energy levels in the bandgap, hence, narrowing the effective bandgap energy and improving the visible light absorption [11]. Figure 5-6(b) represents long-term experiments conducted either under full solar illumination or in the presence of cut-off filter ≥ 420 nm. Obviously, the evolution of molecular hydrogen is detected after 120 min upon the irradiation with the visible light reaching a 10-fold lower amount compared to the full solar light experiment after 600 min of irradiation. This confirms the visible light-activity of the prepared material.
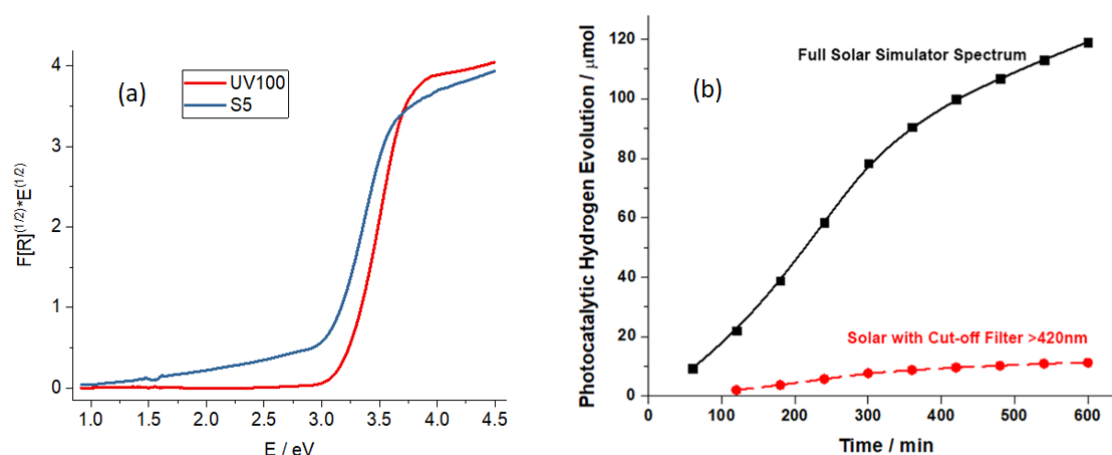
Figure 5-6 Tauc plots of the prepared sample compared to Hombikat UV100 (a), and long-term photocatalytic hydrogen evolution from ethanoic solution under the full solar illumination and in the presence of a 420 nm cut-off filter (b).

The flat-band potential of the optimized TiO_2 material, derived from the Mott−Schottky plots, yields a value of (-0.24 V *vs.* NHE at pH =0), thus a more negative potential compared to the E_{fb} for the electrode prepared from $TiCl_4$ in the same conditions (-0.17 V *vs.* NHE). This, indeed, results in better conditions for the HER reaction to proceed because the more negative the potential of the flat band is, the higher is the reduction potential of the photogenerated electrons. However, a widening in the valence band to a less positive potential (2.74 V *vs.* NHE at pH =0) has been calculated. Such observations were noticed by Wang et *al.* [12] who produced highly defective TiO_2 exhibiting a widening in the valence band, leading to a remarkably higher photocatalytic activity

compared with normal TiO_2. They explained this observation by a more efficient charge transfer both in the bulk and at the semiconductor/electrolyte interface.

While the previous discussion dealt with the holes in the valance band, the majority charge carrier, i.e., the electrons, should be also discussed. In this context, the electrode prepared using $TiCl_3$ as the only precursor exhibits a charge carrier density of $9.3 \times 10^{+20}$ cm^{-3}; i.e., around 11-fold higher compared to that of the electrode prepared from $TiCl_4$ as a precursor ($8.1 \times 10^{+19}$ cm^{-3}). It is widely accepted that the introduction of defects in TiO_2 is usually accompanied by an increase in the charge carrier densities, which might be the case in the prepared sample. Hence, the optimized material is characterized by its improved electronic structure resulting in unexpected photocatalytic efficiency. Owing to the schematic band structure shown in Figure 5-7, the presence of defects might be the reason for such observations.
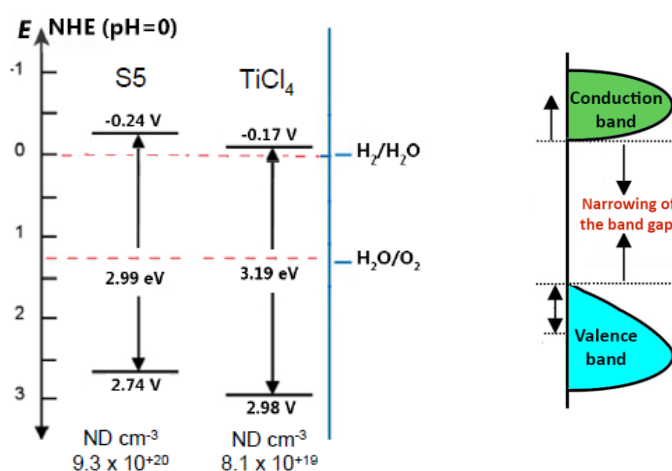
Figure 5-7 Schematic diagram of the enhanced band structure obtained.

The dynamics of the trapped charge carriers were studied by the TAS technique, which reveals that upon laser excitation at 355 nm, the concentration of the trapped charge carriers is much higher in the case of the prepared material compared to Hombikat UV 100 (see Figure 5-8(a)). It is generally accepted that the transient absorption signals observed for TiO_2 above 600 nm are attributed to trapped electrons [13], whereas the transient absorption observed between 400 nm and 530 nm is attributed to the trapped holes [13, 14]. Hence, a very broad distribution of trapped holes over the whole studied spectral range of wavelengths is confirmed in the prepared material. This is because the transient absorption spectra, especially in the range from 400 until 600 nm, are reduced upon introducing ethanol vapors as hole scavengers. The shapes of the transient absorption spectra observed immediately after the laser pulse, therefore, are in good agreement with other studies published previously [15]. Thus, the holes are delocalized over different trapping sites, most likely near the surface being, thus, ready for participating in the reactions with the adsorbates. The presence of methanol reduces both transient absorption spectra but to a much higher extent the

spectrum related to the self-prepared TiO_2. The higher reactivity with methanol confirming that the holes are trapped in different trapping sites located at the surface because methanol react with the surface trapped holes, while the bulk carriers remain in the system [16]. The transient absorption kinetics in a nitrogen atmosphere (Figure 5-8(b)) show that the self-prepared photocatalyst exhibit around 3-fold higher signal intensity of the initial absorption J_0. This result confirms that an increase number of charges will remain to be eventually trapped in their respective traps on the semiconductor particles.
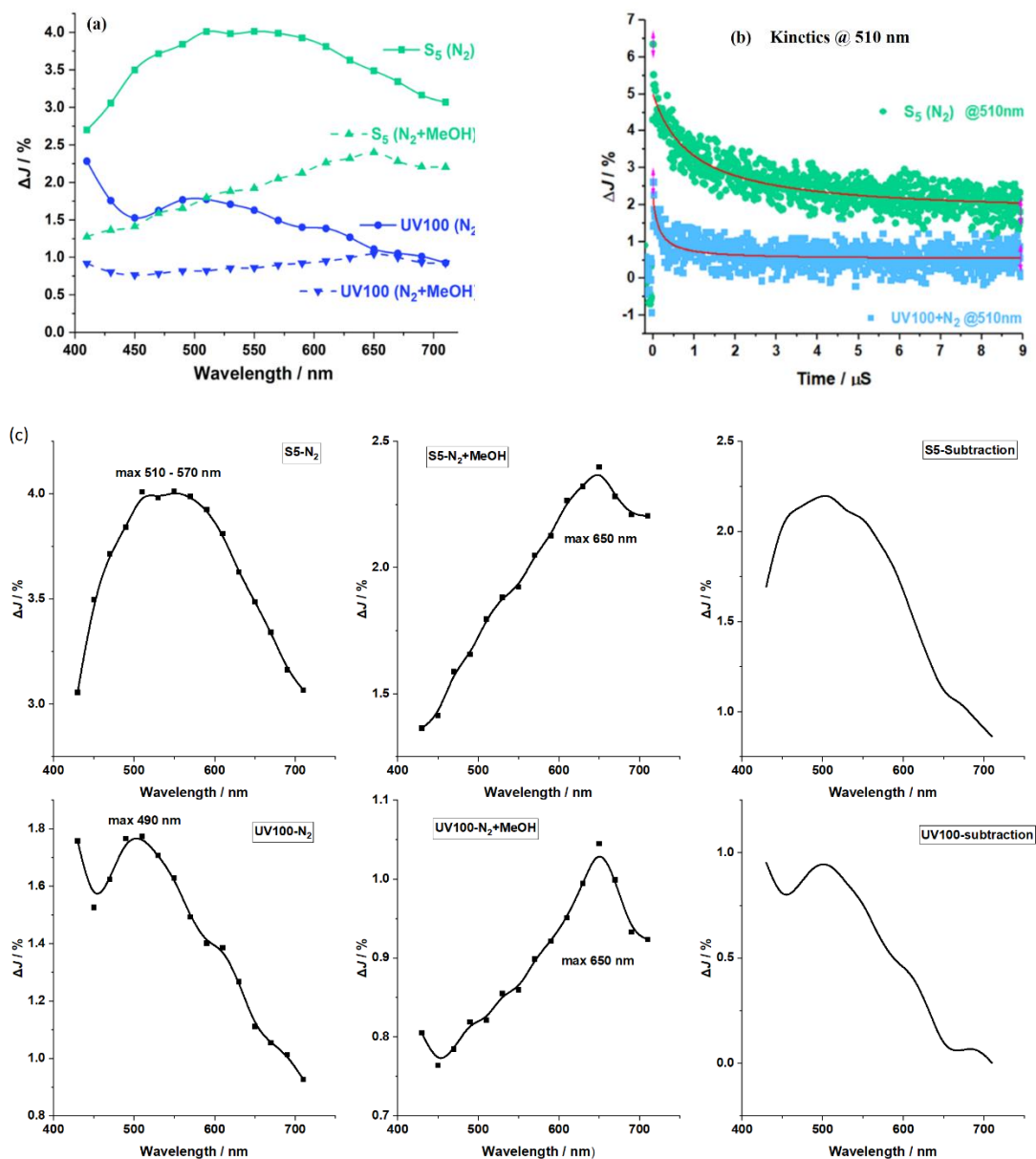
Figure 5-8 Transient absorption spectra (a) measured at 0.1 µs after laser excitation in an N_2 and an N_2–methanol vapor atmosphere; transient absorption signals (c) observed at 510 nm in an N_2 and N_2–methanol vapor atmosphere; detailed transient absorption spectra (c) including the spectra resulting from subtracting the spectrum in N_2–methanol conditions from the spectrum in N_2. λex = 355 nm, 2 mJ laser energy, cut-off filter of 400 nm for detection.

Bahnemann et *al.* [15] confirmed that at least two different types of holes have to be considered, namely, the deeply poor-reactive trapped holes (at 450 nm) besides the free holes that possess a higher oxidation potential and cannot be detected spectroscopically. It is well reported that the valence band holes can be rapidly transported to the surface, where a surface hole trap sites are formed on $Ti-O_sH$ and/or $Ti-O_s-Ti$. These surface trapped holes ($Ti-O_sH^{\bullet+}$ and/or $Ti-Os^{\bullet+}-Ti$) are the main oxidants for any adsorbed electron donor. The investigations performed by the transient reflectance spectroscopy revealed a delocalization of holes over different surface trapping sites with a higher oxidation potential than other deeply trapped sites. Kong et *al.* [17] found that increasing the ratio of the concentration of surface defects to bulk defects improves the separation between the photogenerated carriers, thereby enhancing the photocatalytic activity. This conclusion has also been proposed by Ohtani [18], who claimed the necessity to maximize the density of surface shallow traps while minimizing the density of deep traps to develop highly active photocatalysts. It has been reported that defects in TiO_2 could perform as a co-catalyst, which enhance the usage of the photogenerated electrons in the reduction process [11]. Hole trapping sites participate in such surface defects that play a decisive role in adsorption and surface reactivity. They can serve, hence, as adsorption sites where the charge carrier transfer to adsorbed species can reduce the charge carrier recombination [17].

The detailed transient absorption spectra are shown in Figure 5-8(c) and revealed in spectral change between the prepared material and Hombikat UV100. While the TA spectrum of UV100 exhibits maximum absorption at 490 nm, the spectrum related to the prepared TiO_2 has broad-maximum absorption range between 510 and 570 nm. Such a spectral change has been noticed by Katoh et *al.* in their TAS spectra of nanocrystalline TiO_2 films [19], which are presented in Figure 5-9. TA spectra are consisted by three spectral components of trapped electrons, holes and conducting electrons. They noticed that the excitation with lower laser energy produces lower concentration of trapped electron, whereas the higher excitation energy results in higher concentration of trapped electron. Thus, the spectral contribution of the trapped electrons is notably pronounced at high excitation energy. The authors have explained the change in the trapped electrons' spectrum under high-density conditions by the effect of positive charges of holes residing near the electrons, i.e., due to the Coulomb interaction of the electron with a positive charge [19, 20]. Therefore, the TA spectral change between the prepared TiO_2 and Hombikat UV100 might be due to a change in the trapped electrons' spectrum resulting from the higher density of the holes, increasing the Coulomb interaction with the electrons.
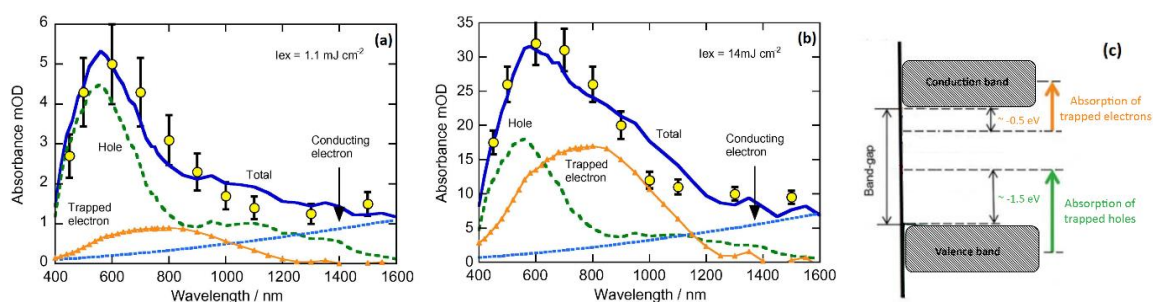
Figure 5-9 TA spectra of TiO$_2$ films recorded just after excitation by 355-nm laser pulses at (a) low (I_{ex} = 1.1 mJ cm^{-2}) and (b) high (I_{ex} = 14 mJ cm^{-2}) excitation energies. The solid lines are the spectra obtained from summing the spectra of three components: holes (broken lines), trapped electrons (triangles), and conducting electrons (dotted lines). Schematic illustration (c) showing energy levels of the trapped carriers. Reprinted with permission from Ref. [19].

An 11-fold higher concentration of charge carriers as revealed from the electrochemical experiments, should, on the other hand, lead to a much higher density of recombination centers. In this context, the transient absorption kinetics at 510 nm for the prepared TiO$_2$ and Hombikat UV100 have been investigated (Figure 5-8(c)). The self-prepared sample shows decay with a longer lifetime than the decay time for UV100. The decay kinetics of the photogenerated charge carriers could be fitted by second-order reaction kinetics with rate constant K_r values of $10.9 \times 10^{+7}$ and $1.74 \times 10^{+7}$ (s%)$^{-1}$ for UV100 and S5, respectively. It should, however, be noted that a portion of these decays takes already place during the length of the laser pulse resulting in uncertainty for the determination of absolute rate constants. This 6-fold lower decay of the transient absorption signal in the prepared TiO$_2$ evincing a longer lifetime for the charge carriers and an improved charge carrier separation. Such phenomena have been assigned to the surface defects that enable the capture of the excited electrons, suppressing the recombination of electrons and holes [21]. Bahnemann et al. [15] observed a fast initial decay of the transient absorption signals in pure colloidal TiO$_2$ suspensions obeys first-order kinetics with a rate constant of $k_1 = 1.3 \times 10^{+7}$ s^{-1}. However, many reports described the transient absorption decay of the trapped charge carriers by second-order reaction kinetics according to the bimolecular recombination of the electron-hole pairs coupled by Coulombic forces. Rothenberger et al. showed by a stochastic kinetic model that when the particle contains a high number of electron-hole pairs, their recombination follows second order kinetics, while at very low occupancy of the semiconductor particle by charge carriers their recombination obeys first-order kinetics, respectively [22].

Hence, the higher concentration of charge carriers does not reflect in a corresponding higher recombination rate, in contrast, the material shows 10-fold lower decay kinetics compared to Hombikat UV100. Based on the previous discussion, the optimal parameters for the EISA method resulted in the synthesis of bare TiO$_2$, which drives the H$_2$ evolution reaction and improves the oxidation of the organic substrates. This was related, indeed, to its higher surface area, better absorption of light

energy, the longer lifetime of charge carriers, and the broad distribution of trap states acting most likely as surface-defect sites.

Such observations have, as well, been reported for the self-doped TiO_2, i.e., gray and black TiO_2. These types of materials own many surface defects as Ti^{3+} ions and oxygen vacancies, turning the color darker [23]. Chen et *al.* [24] reported for the first time the synthesis of black TiO_2 nanomaterial having high visible light absorption for photocatalysis. They showed a narrowing of the bandgap to 1.54 eV by introducing electronic states forming significant VB tailing. Recently, co-catalyst-free gray TiO_2 nanomaterials showed high photocatalytic H_2 production in the presence of hole scavengers [25-27]. The researchers explained this activity by the concentration and nature of defects compared to commercial anatase. These anatase materials have shown shallow electronic levels that might account for superior electron transport and electron diffusion to the surface [28, 29] and reduce also electron-hole recombination. Furthermore, the high-pressure hydrogenation of commercially available anatase TiO_2 powder under high-temperature can activate it for photocatalytic H_2 evolution [9]. This treatment assists the formation of voids and of a stable defect structure that appears to be key for the observed co-catalytic effect on TiO_2 nanoparticles. The character of the self-induced catalytic centers is similar to the phenomenology of noble-metal co-catalytic effects on TiO_2.

However, the synthesis of gray/black TiO_2 usually requires a high-temperature treatment of TiO_2 in various reducing atmospheres (e.g., vacuum, Ar, H_2 /Ar, and pure H_2) [23, 30], which is not the case in EISA preparation method used. Hence, extended investigations might be done to understand the origin of the enhanced properties of the self-prepared TiO_2 sample.

5.3. Additional investigations on the nature of defects

XPS measurements were carried out using a Leybold Heraeus hemispherical analyzer (100mm radius) with non-monochromatic Mg & Al Anode as an X-ray source and by-pass energy of 50 eV. For data correction, the energy of the C1s-line was set to 284.6 eV and used as the reference. The fitting of data was performed using XPSPEAK 4.1 software. Figure 5-10 represents the XPS spectrum for a sample synthesized *via* the EISA method using $TiCl_4$ and $Ti(OBu)_4$ as precursors (a) and the XPS spectrum for the optimized sample synthesized using $TiCl_3$ (b). The Ti 2p1/2 and Ti 2p3/2 spin-orbital splitting photoelectrons in Figure 5-10(a) are located at binding energies of 464.32 and 458.62 eV, respectively. These binding energies and the peak separation of 5.7 eV between the Ti 2p1/2 and Ti 2p3/2 are in good agreement with the characteristic peaks of Ti^{4+} in anatase TiO_2 [31]. Unexpectedly, the XPS spectrum of the optimized sample in Figure 5-10(b) does not show any characteristic peak related to Ti^{3+} at 457.9 eV or an apparent peak broadening in this range of binding energies. This, indeed, denies the existence of surface Ti^{3+} defects. Interestingly,

the other two peaks of Ti $2p_{3/2}$ and $2p_{1/2}$ are centered at the binding energies of 460.12 eV and 454.52 eV, respectively, with a peak separation of 5.6 eV. These values are in good agreement with the characteristic peaks of Ti^{2+} in TiO_2 [32, 33].
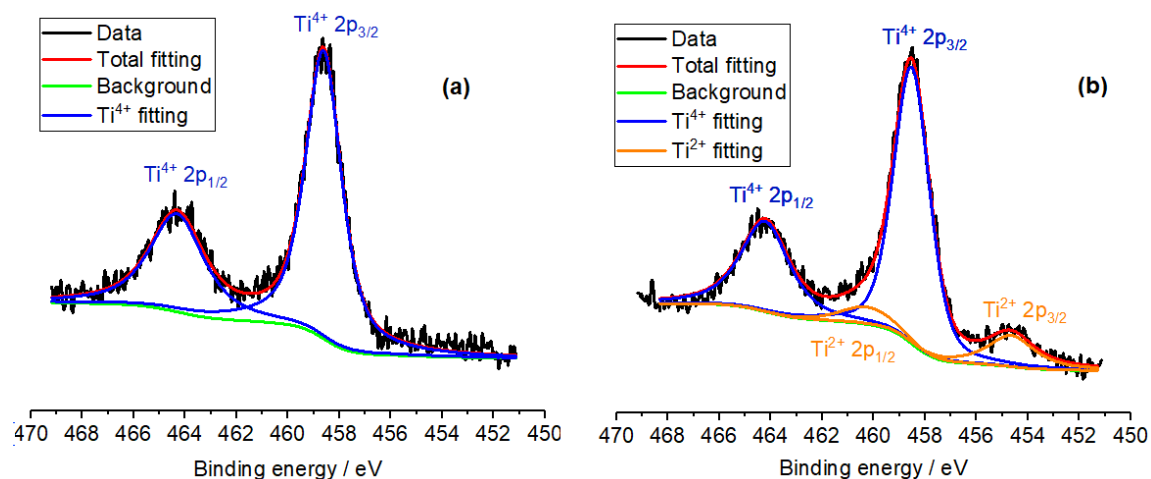

Figure 5-10 XPS analysis of a normal TiO₂ (a), and for the optimized TiO₂ sample (b). The fitting was done using XPSPeak41 software.

Owing to the XPS measurements, the presence of Ti^{2+} species on the surface of TiO_2 is confirmed. In this context, we prepared several TiO_2 samples based on different ratios between the precursors $TiCl_3$: $Ti(OBu)_4$. The photocatalytic activity of H_2 evolution depends strongly on the amount of $TiCl_3$ in the precursor mixture, i.e., the higher the $TiCl_3$ ratio is, the higher is the H_2 evolution. However, the XPS measurements of these samples show almost similar spectra, i.e., the area of Ti^{2+} peak at 454.52 eV is not remarkably affected. Thus, the optimized TiO_2 sample contains most likely Ti^{2+} in interstitial sites in addition to the surface Ti^{2+}. However, the presence of interstitial Ti^{2+} was not experimentally confirmed. Because of its 2 electrons in the 3d orbitals, the conductive properties of Ti^{2+} can enhance the activity of the prepared TiO_2. Nevertheless, this is the first report regarding Ti^{2+} modified-TiO_2 in such a method, in which Ti^{2+} and Ti^{4+} are formed simultaneously. The formation of Ti^{2+} most likely proceed as a result of the thermal disproportionation of $TiCl_3$ as described in Eq. 5-1 [34].

$$TiCl_3 \xrightarrow{\Delta} TiCl_4 + TiCl_2 \qquad\qquad (5\text{-}1)$$

Few reports showed that TiO_2 can be reduced under harsh conditions, e.g., Ar ion bombardment [35] or electrochemical reduction [33], to produce Ti^{3+} and Ti^{2+} as defect states. However, the use of these techniques involves the synthesis of TiO_2 followed by its severe modification which is not the case in our preparation method. For example, Swaminathan et *al.* used the electrochemical cathodization to produce a highly active catalyst ($TiO_{1.23}$) for the hydrogen evolution reaction, which showed low onset potential (75 mV vs. RHE) and Tafel slope (88 mV.dec^{-1}). Their XPS

analysis revealed in a broad peak at lower binding energy (455.9 eV) assigned to Ti^{2+}, apart from the major peak of Ti^{4+} at 458.5 eV. They explained the HER activity of the $TiO_{1.23}$ by the presence of Ti^{2+}, which ensures effective electron transport and helps to hop of electrons due to the delocalization of the electron density *via* d-orbitals overlapping. Zhou et. al. [36] reported Ti^{2+} defects in their modified TiO_2 nanotubes. They showed that the Ar^+-ion bombardment of TiO_2 nanotubes resulted in a high content of sub-oxide (Ti^{3+}, Ti^{2+} states). These sub-oxide states beneficially affect the photocatalytic hydrogen evolution rate under open-circuit conditions. They claimed that Ti-sub-oxide states can act as co-catalytic centers, allowing an enhanced photocatalytic hydrogen evolution from TiO_2 nanotubes.

Two main characteristics are delivered from the optical properties of the prepared sample shown in Figure 5-6(a): i) the spectrum is shifted to lower energies, indicating a decrease in the optical bandgap; ii) the absorption coefficient is increased in the visible range up to 1200 nm. These facts are consistent with the presence of an electronic band close to the conduction band for the defected material [29]. While oxygen vacancies are the predominant defect species, titanium interstitials influence also the properties of TiO_2 and cannot be ignored. The formation of oxygen vacancies and titanium interstitials is favored in reducing conditions. Nowotny et *al.* [37, 38] showed that applying a reducing environment results in the reduction of the optical band gap of TiO_2, which is related to structural relaxations induced by oxygen vacancies and the associated formation of larger defects as it is represented in Figure 5-11. As shown in this figure, both titanium interstitials and oxygen vacancies form donor-type centers, in which the lower the positive charge of a titanium interstitial ion is, the closer is the defect state from the CB. The existence of the band of defect states just below the conduction band minimum can cause an overlapping between them, allowing for an enhanced absorption for sub-bandgap light. The high concentration of vacancies can break the selection rules for indirect transitions, thus enhancing the absorption for photon frequencies below the direct bandgap [29]. Hence, the optical gap of the prepared TiO_2 is narrowed by intraband transitions as shown in black hydrogenated titanium dioxide nanocrystals [24]. These observations have been also reported by Pei et *al.* [39] in their reduced non-stoichiometric TiO_{2-x} single crystals containing Ti^{3+} and oxygen vacancies, by Anpo et *al.* [40] in their self-doped Ti^{3+}-TiO_2 nanoparticles prepared by a solvothermal method with $NaBH_4$ added as a reductant, by Zuo et *al.* [41] in their reduced-self-doped Ti^{3+}-TiO_2 prepared by a combustion method, and by Swaminathan et *al.* [42] in their reduced-TiO_2 prepared *via* electrochemical cathodization method.
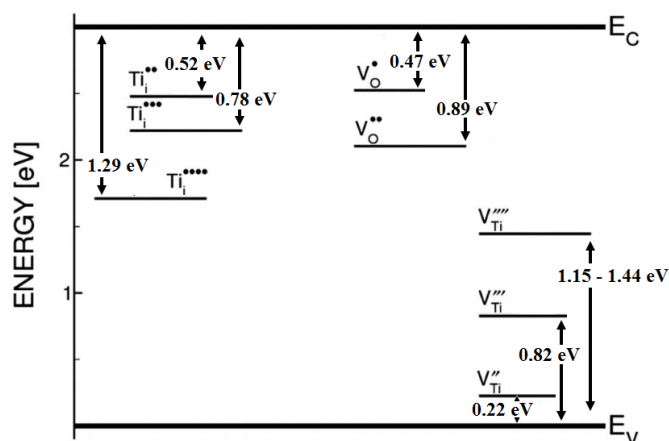
Figure 5-11 The energy levels of intrinsic defects of different ionization degree in TiO_2 semiconductor [37, 38]. V_O is an oxygen vacancy, Ti_i is a titanium ion in an interstitial site, and V_{Ti} is a titanium vacancy. Adapted with permission from Ref. [38]. The used notation of defects in nonstoichiometric compounds is Kröger and Vink notation [43].

The overlap of defect states with the conduction band minimum can create a high density of electrons in the conduction band, as well as a high density of holes in the valence band. This would, according to Kamat et *al.*, generate a Burstein-Moss shift, in which the energy levels near the bottom of the band fill up, and optical transitions, thus, have to involve higher empty band states, resulting in a blue shift of the fundamental absorption edge [44]. The upshift of the conduction band edge results in a higher electric potential than that of non-defective TiO_2 with respect to $\varphi(H^+/H_2)$, and thus easier H_2 production [45]. This shift can be illustrated in Figure 5-12(a), in which the possible molecular orbital diagram in the presence of Ti^{2+} defects is presented.

It is also possible, in the prepared sample, that islands of TiO are distributed on the surface of TiO_2. It should be noted that the detection of TiO patterns by XRD was not possible, maybe because the content, if any, is lower than the detection limit. Moreover, with TEM measurements, the detection of an amorphous phase was not possible. Figures 5-12(b) and 5-12(c) show the calculated band structure for both anatase TiO_2 and TiO, in which it is clearly demonstrated that TiO exhibits a higher Fermi energy than TiO_2. Ern and Switendick applied the augmented-plane-wave (APW) method to study the electronic band structure of TiO. They reported that the density of states of the 3d bands in TiO rises at the Fermi level, reaching a maximum at about 2 eV above the Fermi energy [46]. Chen et al. showed in their UPS calculations that the work function of TiO (3.01 eV) is higher than that of TiO_2 [47]. In this case, TiO can act as a noble metal, collecting the photogenerated electrons from the CB of TiO_2 and reducing the recombination of the photogenerated charge carriers. However, Greiner et al. [48] found in their UPS calculations a general trend in which the lower cation oxidation states of transition metal oxides have the effect of decreasing an oxide's work function. They reported work function values around 4.5 eV and 5.3 eV for TiO and TiO_2 thin polycrystalline films, respectively. In this case, electron injection from TiO to TiO_2 is expected, where no depletion layer can be formed, and the junction would be ohmic.
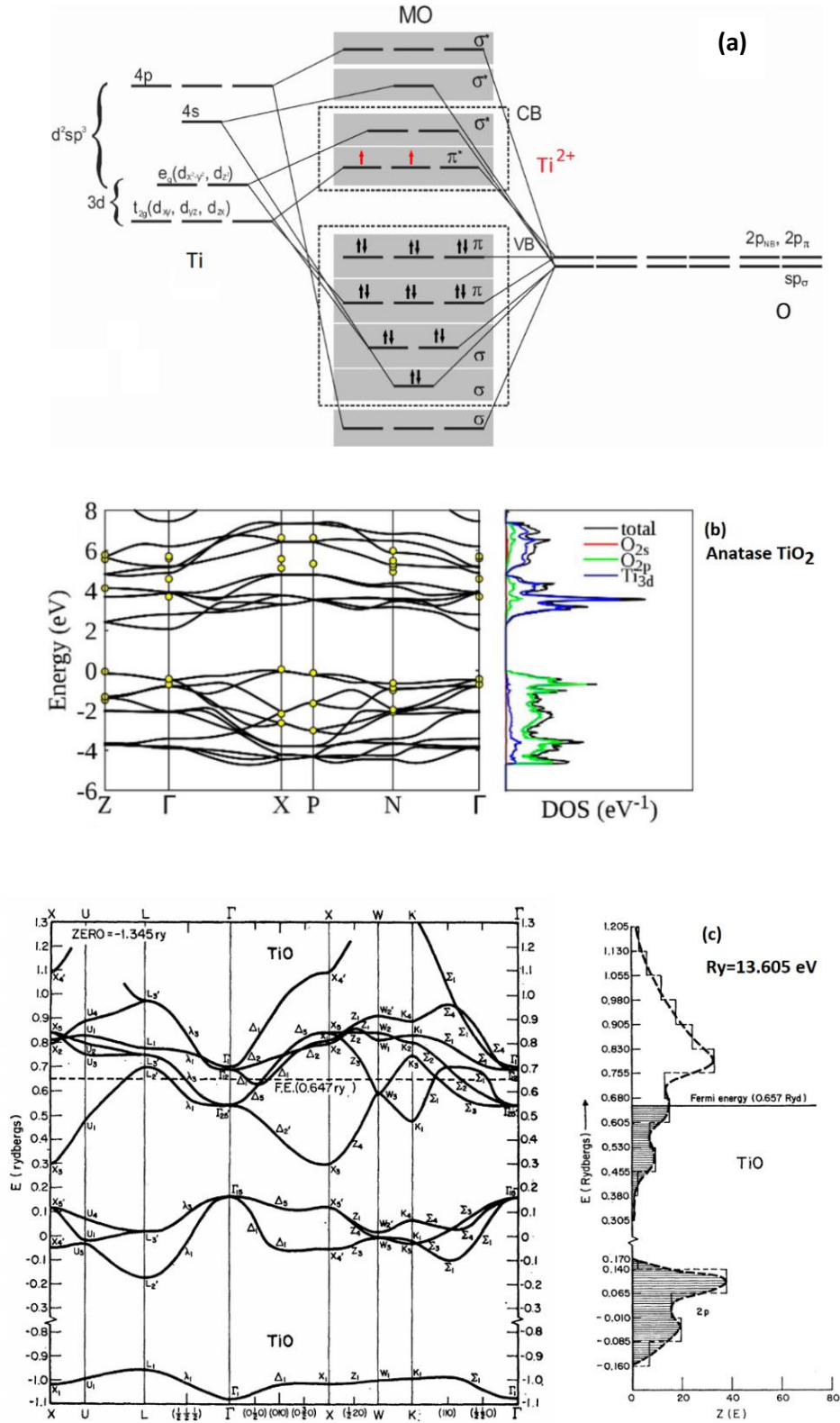
Figure 5-12 The possible TiO$_6$ octahedral MO (molecular orbitals) diagram for defected TiO$_2$ [49, 50], adapted with permission from Ref. [49] (a); band structure and the corresponding DOS of anatase calculated by DFT-GGA while setting the VB maximum to 0 eV, adapted with permission from Ref. [51] (b); energy bands with the density of states for TiO calculated by the augmented-plane-wave (APW) method, adapted with permission from Ref. [46] (c).

The transient absorption spectroscopy of Figure 5-8(b) shows a slower decay of the transient absorption signal for the prepared TiO_2 confirming a longer lifetime for the charge carriers. This observation has also been reported by Wheeler et *al.* [52], who investigated the ultrafast charge carrier relaxation dynamics of hydrogen-treated TiO_2 ($H:TiO_2$) nanowire arrays using time-resolved fluorescence (TRF) and femtosecond transient absorption (TA) pump−probe spectroscopies. They showed an overall 2-fold slower decay of the TA of the $H:TiO_2$ sample with UV excitation as compared to the untreated sample, which is indicative of long-lived electron-hole pairs. They concluded that hydrogen treatment lengthens the lifetime of the charge carriers, most likely in trap states or the V_O states.

To confirm that the photocatalytic activity is related to the presence of Ti^{2+} in the prepared TiO_2, the conductive oxide, TiO, was physically mixed with the commercially available anatase TiO_2, Hombikat UV100, in a 1:99 w/w ratio, respectively. Each of TiO and UV100 does not show any photocatalytic H_2 formation from the photocatalytic reforming of ethanol. However, as shown from GC chromatograms presented in Figure 5-13, H_2 is produced from the composite material and increased with the irradiation time. This clearly indicates the pivot role of Ti^{2+} in improving the photocatalytic properties of anatase TiO_2, especially the HER.
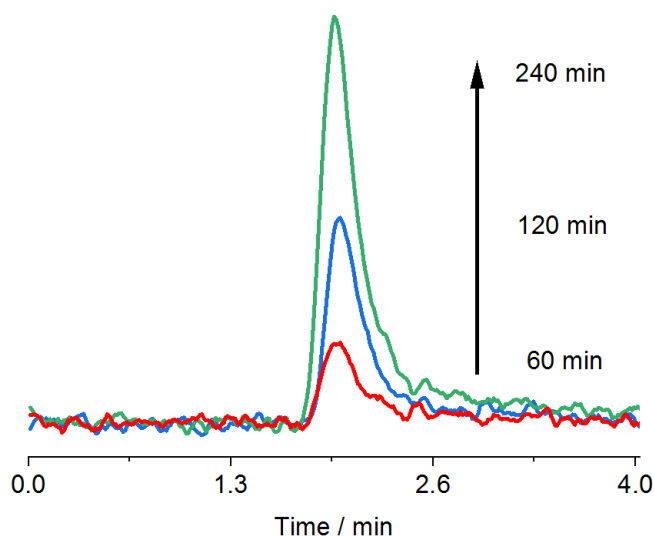
Figure 5-13 GC chromatograms of the H$_2$ detection during the irradiation time.

In this context, Swaminathan and Ravichandran [50] concluded that the severe cathodization of TiO_2 results in the presence of metallic Ti^{2+} ion, instead of Ti^{3+}, which turns the reduced TiO_2 as an HER catalyst (least HER overpotential - $\eta_{10\,mA/cm^2} \approx 198$ mV). They demonstrated that the Ti^{2+} governs catalytic performance because of their electron density that can be easily delocalized *via* d orbitals overlapping, which is essential for good catalytic performance. Furthermore, due to d-electron filling in their reduced titania, dense packing of d-band occurs and makes its electronic structure similar to that of metals. Consequently, the corresponding Ti^{2+} can exhibit metallic behavior, which supports the active behavior of reduced titania [50].

5.4. Insights into the photocatalytic oxidation of oxalic acid

The work described in Chapter 3 addresses oxalic acid oxidation behaviors in different photocatalytic systems. Understanding the photocatalytic oxidation of oxalic acid on the surface of TiO_2, indeed, forms a reliable base in investigating the photoreforming process. For this purpose, the self-prepared TiO_2 was used in its bare form and after modification with Pt NPs as co-catalysts. The photocatalytic experiments were conducted in different systems while maintaining the pH stable at 3 during the whole period of the reaction by means of a pH-stat technique. The pH of 3 was carefully chosen according to Li et *al.*, who reported a maximized photocatalytic hydrogen evolution at about pH 2.9 [53]. Interestingly, the batch photocatalytic experiments reveal that the self-prepared TiO_2 photocatalyst has around 5% higher photocatalytic degradation activity than the commercial Hombikat UV100. The detection of H_2 is also possible over the prepared material, which is not the case over Hombikat UV100.

The photo-oxidation of oxalic acid on bare TiO_2 in O_2-saturated conditions is found to proceed very fast without the detection of by-products. This is related to the use of a powerful oxidative system, in which different spices, e.g., the photogenerated holes, the $^\bullet OH$ radicals, and the superoxide radicals $O_2^{-\bullet}$ can participate in the total mineralization of oxalic acid to CO_2. In the presence of molecular oxygen, the formation of $^\bullet OH$ radicals and the reduction of molecular oxygen are thermodynamically favored as proven by Kosanić [54]. The overall photocatalytic oxidation of oxalic acid over illuminated TiO_2 in the O_2-reach system can be summarized by Eq. 5-2. Unfortunately, in such a system, H_2 production is inhibited due to the fast scavenging of the photogenerated electron by molecular oxygen forming superoxide radicals. It has been reported that O_2 has a stronger ability to trap electrons compared to H^+. Besides, the presence of O_2 favorites the back reaction to water [55].

$$HC_2O_4^- + \tfrac{1}{2}\,O_2 \xrightarrow{\ h\nu,\ TiO_2\ } 2CO_2 + OH^- \tag{5-2}$$

The use of the O_2-free photocatalytic system results in a dramatic decrease in the rate of photocatalytic oxalic acid oxidation. Around 60-fold and 7-fold lower rates have been noticed on bare TiO_2 and Pt/TiO_2, respectively, compared with the case of O_2-reach conditions (see Figure 5-14). This is related to the photogenerated holes being the main oxidative spices in the absence of oxygen, rather than the highly oxidative ROS. The lower photocatalytic efficiency of bare TiO_2 towards the degradation of oxalic acid in an O_2-free system can be also attributed to the role of O_2 in scavenging the photogenerated electrons, thus decreasing the recombination of charge carriers. The overall oxalic acid transformation in the O_2-free system can be described by the Eq. 5-3.

$$H_2C_2O_4 \rightarrow H_2 + 2CO_2 \tag{5-3}$$

The same behavior has been proven for other organic compounds. For example, photocatalytic degradation of 2-propanol under aerobic conditions has been reported to be faster in comparison with O_2-free systems. This effect was explained by the contribution of molecular oxygen in the decomposition pathways, as well as by the role of molecular oxygen initiating the photogeneration of $^\bullet OH$ radicals themselves [56] as can be seen in Eqs. 5-4 to 5-7. Shibata et. al. reported about 80 - 90% decrease in the amount of $^\bullet OH$ radicals generated on irradiated TiO_2 under anaerobic conditions comparing to those in the air-saturated reaction [57].

$$O_2 + e^-_{CB} \rightarrow O_2^{-\bullet} \tag{5-4}$$

$$2O_2^{-\bullet} + 2H^+ \rightarrow H_2O_2 + O_2 \tag{5-6}$$

$$H_2O_2 + e^-_{CB} \rightarrow {}^\bullet OH + OH^- \tag{5-6}$$

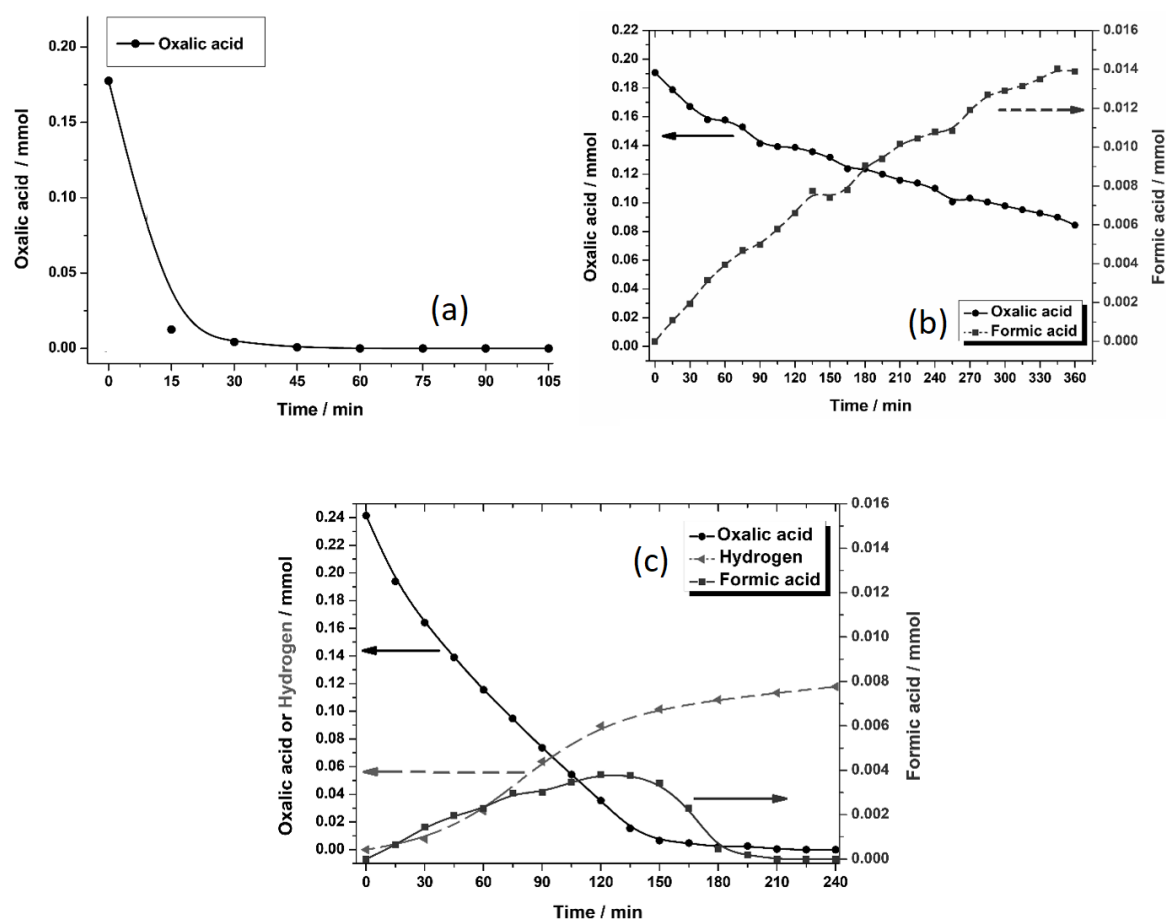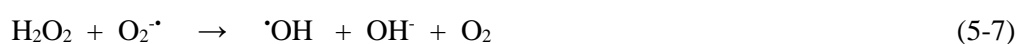$$H_2O_2 + O_2^{-\bullet} \rightarrow {}^\bullet OH + OH^- + O_2 \tag{5-7}$$

Figure 5-14 The degradation behaviors of oxalic acid in different systems including O_2-reach on bare TiO_2 (a), O_2-free on bare TiO_2 (b), and O_2-free on Pt/TiO_2 (c). OA concentration is 1.11 mmol.l^{-1}, pH =3.

The importance of $^{\bullet}OH$ radicals in the photocatalytic degradation of oxalic acid was then evaluated by conducting a homogeneous photodegradation under the same oxygen-free conditions, in which a solution of 0.3 mmol l^{-1} potassium nitrate was used instead of TiO_2. It is well reported [58] that nitrate solutions undergo a photolysis reaction upon illumination by UV light, generating $NO_2^{\bullet}$ radicals and atomic oxygen radical anions ($^{\bullet}O^-$), respectively. The later radicals react, in turn, within nanoseconds with protons producing $^{\bullet}OH$ radicals. Thus, nitrate photosystem is used as a source for the homogenous production of $^{\bullet}OH$ radicals. In the same conditions and illumination time, the use of such a system results in a 36.8% degradation of oxalic acid compared to 51.8% upon the photocatalytic degradation over TiO_2. Thus, $^{\bullet}OH$ radicals, if produced in the TiO_2 photocatalytic system, contribute effectively to the degradation of oxalic acid.

Compared to the bare TiO_2, the enhancement of the oxalic acid degradation over platinized TiO_2, shown in Figure 5-14(c), is related to the presence of platinum as a co-catalyst, which acts as an antenna that collects the photogenerated electrons. This improves the separation between the charge carriers and prevents their recombination. However, even in the presence of platinum nanoparticles on the surface of TiO_2, the oxygen-free system is still much less effective in degrading oxalic acid in comparison to the oxygen-saturated system.

In such an anaerobic system, H_2 is produced especially over Pt/TiO_2. After an induction period during the first 45 min of irradiation, a constant formation of H_2 until the complete degradation of oxalic acid is detected as shown in Figure 5-14(c). During such an induction period, the little generated amount of molecular hydrogen diffuses in the gas headspace of the reactor. The detection of such small quantities is difficult because of the hydrogen detection limit of the employed GC system (DL $\geq$ 0.009 mmol calculated from the signal to noise ratio). Nevertheless, around 40% less H_2 is formed than stoichiometrically expected. The production of by-product, i.e. fromate, is detected, however, very low quantities of formate have been produced over Pt/TiO_2. Interestingly, the degradation of formate is noticed to efficiently proceed on Pt/TiO_2 when the concentration of oxalic acid becomes very low, which is not the case on bare TiO_2. This can be explained by the fact of the higher adsorption capacity of oxalic acid on the surface of titanium dioxide, which hinders any other oxidation of the co-existence molecules [59, 60]. Monocarboxylic acids have previously been reported to be formed upon the anaerobic degradation of elementary dicarboxylic acids [61]. Yamada et al. detected the formation of formic acid by ^1H NMR during the photocatalytic hydrogen evolution from de-aerated mixed solutions of QuPh$^+$–NA, oxalate and platinum nanoparticles [62].

Such observations clearly confirm the need to design a potential photocatalytic system, if any, in which the oxidation and the reduction can separately proceed; i.e. O_2-reach and O_2-free systems, to achieve the goal of fast mineralization with simultaneous production of H_2.

5.5. Mechanistic insights into the photocatalytic reforming of oxalic acid

The work described in Chapter 4 discusses the effect of the co-catalyst on the photocatalytic reforming of oxalic acid. It also discovers the interfacial charge transfer mechanism, through it the photoreforming of oxalic acid on the surface of TiO_2 can proceed. The main findings in this chapter can be summarized in Figure 5-15.
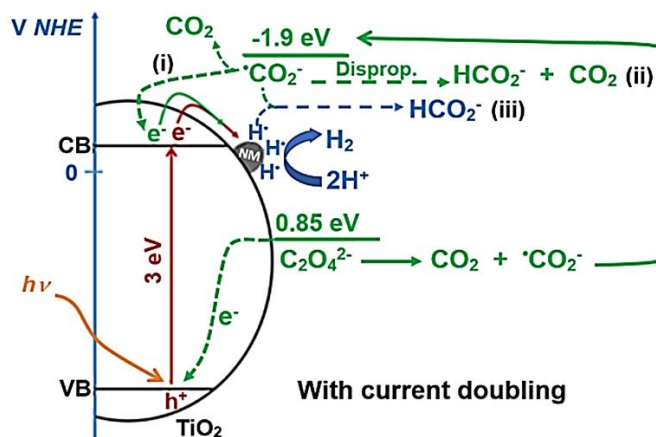

Figure 5-15 Schematic diagram summarizing the main results of Chapter 4.

For this purpose, the self-prepared TiO_2 was used in its bare form and after the modification by several noble metal-co-catalysts. The photocatalytic experiments were conducted at an initial pH of 3 and were followed until no gas evolution was detected. A continuous-flow setup connected to a quadrupole mass spectrometer (QMS) was used to follow the evolved gases from the photocatalytically reformed oxalic acid in its aqueous solutions. The use of this setup enables long term tests to be carried out without the difficulties that occur in a closed photocatalytic system, i.e., the overpressure inside the reactor [63, 64].

Interestingly, bare TiO_2 offers a photocatalytic activity for H_2 evolution even without any HER co-catalyst due to its outstanding properties previously discussed. The sample prepared from $TiCl_3$ showed significantly higher photocatalytic activity than the conventional photocatalyst prepared from $TiCl_4$:$Ti(OBu)_4$ in both, the bare and the platinized forms. This is due to the presence of Ti^{2+} defects that turn TiO_2 as an active material for photocatalytic hydrogen production and enhance its activity of organic substrates oxidation. As discussed previously, these defects improve the optical properties, decrease the recombination of charge carriers, increase the density and the transportation of charge carriers, and can induce the HER.

Noteworthy, no molecular oxygen was detected during the photocatalytic experiments using all the materials, even when only a very low concentration of oxalic acid remained in suspension. The photocatalytic splitting of water into H_2 and O_2 both in the presence and absence of oxalic acid

appears thus to be negligible. Pt/TiO_2 is obviously the most active photocatalyst among bare TiO_2, Au/TiO_2, and $Au-Pt/TiO_2$. This was in terms of H_2 production, CO_2 evolution, and oxalic acid consumption as can be seen in Figure 5-16. For example, Pt NPs increase the photonic efficiency of H_2 evolution by 5-fold, 2.5-fold, and 1.2-fold compared to bare TiO_2, Au/TiO_2, and $Au-Pt/TiO_2$, respectively. On the other hand, Pt/TiO_2 enhanced the photonic efficiency of CO_2 production by 2.5-fold, 1.9-fold and 1.1-fold, respectively. The ranking of CO_2 evolution fits well with the kinetics of oxalic acid consumption from the solution shown in Figure 5-16(c). Owing to these results, Pt turns TiO_2 as an active material for both half-reactions of the photocatalytic reforming of oxalic acid. This means the oxidation of oxalic acid on bare TiO_2 is feasible, but it is to a much larger extent upon the modification with noble metals. This observation in good agreement with the work of Bamwenda et *al.* [65] showing a 30% lower overall activity of Au/TiO_2 than that of Pt/TiO_2. They attributed this to the more effective trapping and pooling of photogenerated electrons by Pt.

However, the co-deposition of both noble metals does not result in an additive effect, with the bimetallic co-catalyst reaching lower evolution rates than Pt/TiO_2. The possible contribution of a visible light activity from Au-containing materials, which is related to the plasmonic effect of Au NPs [66] was also examined by employing $Au_{1\%}-Pt_{0.25\%}/TiO_2$ and using a long-pass filter with a cut-on wavelength of 410 nm. A severe decline in the photocatalytic activity was recorded, especially for the H_2 evolution. Au NPs loaded on TiO_2 prepared in this work thus exhibit poor activity in the visible light region, in addition to their negative roles hindering the activity of Pt when the full light spectrum is used. Our results thus contradict the reports showing that Au−Pt bimetallic system on the surface of TiO_2 may have better catalytic properties compared to pure Au and pure Pt [67].

Hence, the modification of TiO_2 with a suitable co-catalyst is needed, with the Pt NPs being definitely the right choice. Pt NPs would inhibit the charge carriers' recombination by sinking the photogenerated electrons due to their higher work functions than Au NPs (5.65 eV of Pt > 5.10 eV of Au [68]). The inhibition of charge carriers recombination, when such a Schottky barrier is created, is the bottleneck to enhance the photocatalytic activity even when a sacrificial reagent is used [69]. Pt NPs also can catalyze efficiently the HER at a relatively lower overpotential of reduction [70]. The density functional theory (DFT) calculations regarding the hydrogen binding energy showed that binding to Pt results in a smaller Gibbs free-energy change (- 0.09 eV) compared to gold (0.45 eV), indicating that Pt has the best electrocatalytic activity for HER from the viewpoint of thermodynamics [71, 72]. In addition, Pt facilitates the quick discharge of electrons from semiconductor nanoparticles into the electrolyte [73] faster than that of Au NPs [70]. This has been reported by Subramanian et *al.* [74], who studied luminescent ZnO colloids and proved a complete discharge of electrons into the solution in the case of Pt but not Au.
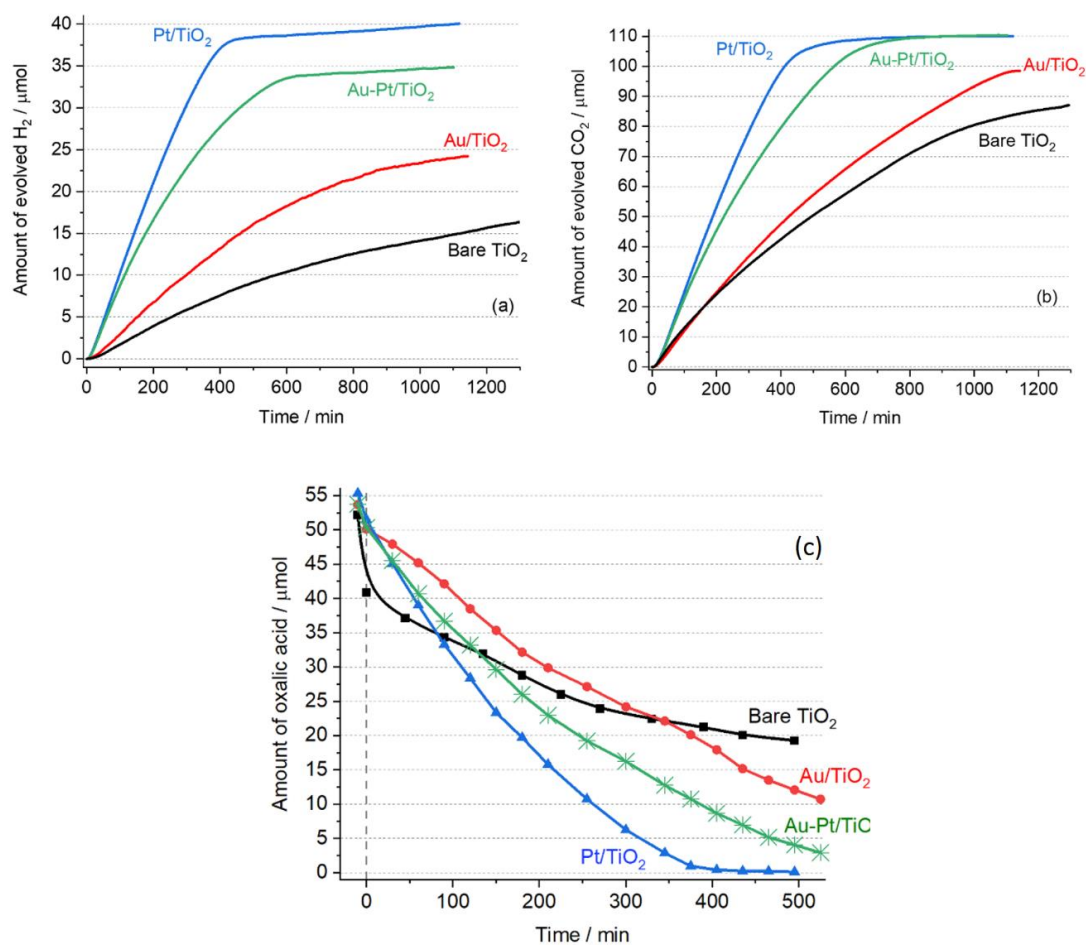
Figure 5-16 The time course of amounts of H$_2$ (a) and CO$_2$ (b) formed over the different materials; The kinetics behaviors of oxalic acid consumption in the liquid phase (c).

However, using the most-efficient material, Pt/TiO$_2$, results in around 30% less H$_2$ evolution than theoretically expected. Such a lower stoichiometric H$_2$:OA ratio has been also reported in our previous work (H$_2$:OA molar ratio ≈ 0.6) [64]. A possible reason is the progressive blockage of active sites on the noble metal co-catalysts by the adsorption of molecular hydrogen [75]. Noble metals have been shown to act as active sites for hydrogen dissociation and adsorption [76], hence, the adsorption of the hydrogen on the surface of metal nanoparticles, should not be neglected as a reason for such a non-stoichiometric H$_2$ amount. Another possible reason is the increase in the charge carrier recombination rate as the concentration of oxalic acid decreases. The formation of by-products should also be considered as a source of non-stoichiometry. Deviations from the stoichiometry have also been previously reported for the reforming of oxalic acid. For example, Kmetykó et al. [77] showed a ratio of about 0.64 when they performed long term irradiation of Pt-TiO$_2$ in the presence of 0.05 mol l^{-1} oxalic acid. On the other hand, Yamada et al. [78] have reported 80 % of the stoichiometric amount based on the irradiation of a 3 mmol l^{-1} oxalate solution in the presence of Pt NPs and 2-phenyl-4-(1-naphthyl)quinolinium ion (QuPh$^+$-NA) as a photocatalyst.

They have related this lower value to the formation of by-products such as formic acid and formaldehyde.

EPR spectroscopy in an argon atmosphere at 77 K was used to identify the paramagnetic centers produced on the irradiated TiO_2 powders (Figure 5-17). In these spectra, signal H (g_x = 2.004, g_y= 2.014, g_z= 2.018) is attributed to the photogenerated holes. This signal was reported previously as the holes trapped at the oxygen atoms as Ti^{4+}-$O^{\cdot-}$-Ti^{4+}-OH^- near the hydrated anatase surface [79, 80]. On the other hand, the signal E_T (g_{II} = 1.962 and $g_\perp$= 1.992) belongs to the photogenerated electrons and has been reported to be trapped in the bulk as Ti^{3+} ions [79, 81, 82]. The production of (E_T) signal in the EPR spectra even when Pt (an electron scavenger) is loaded on the TiO_2 surface confirms that not all the photogenerated electrons are scavenged, but instead, some of them are trapped in the bulk as Ti^{3+} centers. These trapped electrons can negatively affect H_2 production due to their low reactivity.

Another broad and unfeatured signal (signal E_S) was also detected and became more intense with the irradiation time. This broad signal E_S is most likely related to the injection of electrons from $^\cdot CO_2^-$ radicals, which then spread on the surface of the photocatalyst. Such a broad signal was observed by Chiesa et al. [82] when they injected electrons in the solid in different ways. They assigned this signal to the excess electrons near the surface of anatase TiO_2. A similar signal was reported by Howe and Grätzel [83], who have shown that the photogenerated electrons can be trapped as surface Ti^{3+} species in the presence of polyvinyl alcohol as a hole scavenger. Micic et al. [84] found a broad asymmetric EPR signal at g= 1.981, indicating the formation of Ti^{3+} from electron trapping on the surface due to electron injection from methanol radicals into TiO_2 particles. They reported the disappearance of this signal when Hg^{2+} was present in the solution due to its reduction to Hg by the $^\cdot CH_2OH$ radical, $E^0(CH_2O/^\cdot CH_2OH)$ = -0.97 V.
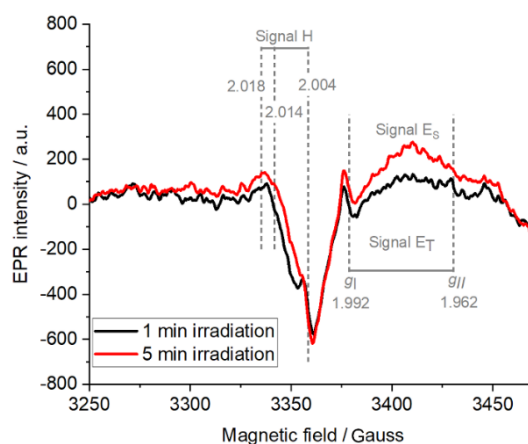

Figure 5-17 EPR spectra recorded when Pt/TiO₂ was irradiated for 1 min (black) and 5 min (red) in the absence of molecular oxygen at 77 K in the presence of oxalic acid.

The adsorption of oxalic acid onto bare TiO_2 decreases when increasing the solution pH, where the surface area normalized uptake decreases from 9.1×10^{13} to 2.2×10^{11} molecules cm^{-2} when the pH increases from 3 to 10. This strong decrease in the adsorption capacity is related to the catalyst surface properties (pH_{zpc} around 5.5 [64]) and the oxalic acid species present in the solution (pK_{a1} and pK_{a2} are 1.25 and 4.28, respectively [64]). Therefore, at pH ~3, a strong interaction between $HC_2O_4^-$ molecules and the positively-charged TiO_2 surface is expected.

It is very important to distinguish between a semiconductor-assisted photoreaction (turnover number TON < 1) and a catalyzed photoreaction, that is photocatalytic, (TON $\geqslant$ 1). This is a general problem, nowadays, in the photocatalytic investigations as revealed from the review of Prof. Ohtani [85] because TON is ignored when discussing the data. In this context and giving thought to the BET surface area values along with the amounts adsorbed after saturation, the adsorption of 0.91 oxalic acid molecules per nm^2 was calculated. Hence, the concentration of active sites in the suspension is 0.23 x10^{-3} and 0.09 x10^{-3} mol l^{-1} for bare TiO_2 and Pt/TiO_2, respectively. TONs, calculated as the complete consumption of oxalic acid have values of 4.86 and 12.14 over bare TiO_2 and Pt/TiO_2, respectively. Owing to the fact of a catalyzed photoreaction has a TON $\geqslant$ 1 [86], confirming that all the conversion processes studied are photocatalytic.

The formation of formate as the main by-product in the liquid phase is confirmed. The amounts of formate are dependent on the material used (Figure 5-18). Nevertheless, very small amounts of formate are produced compared to the amount of oxalic acid converted. As can be seen, formate starts to oxidize on Pt/TiO_2 after around 300 min of irradiation, i.e., once oxalic acid is consumed from the solution, which can be explained by the higher adsorption properties of oxalic acid. This is in agreement with previous reports showing that the anaerobic degradation of elementary dicarboxylic acids, e.g., oxalic acid, resulted in the formation of the corresponding monocarboxylic acid [87]. For example, the ^1H NMR detection of formic acid and formaldehyde was possible during the photocatalytic H_2 evolution using oxalate, QuPh$^+$–NA as a photocatalyst and Pt NPs as an HER catalyst. The proposed mechanism postulated that oxalate acts as a one-electron donor, while $^{\bullet}CO_2^-$ radicals can be reduced to formate by hydrogen adsorbed on Pt NPs [78].
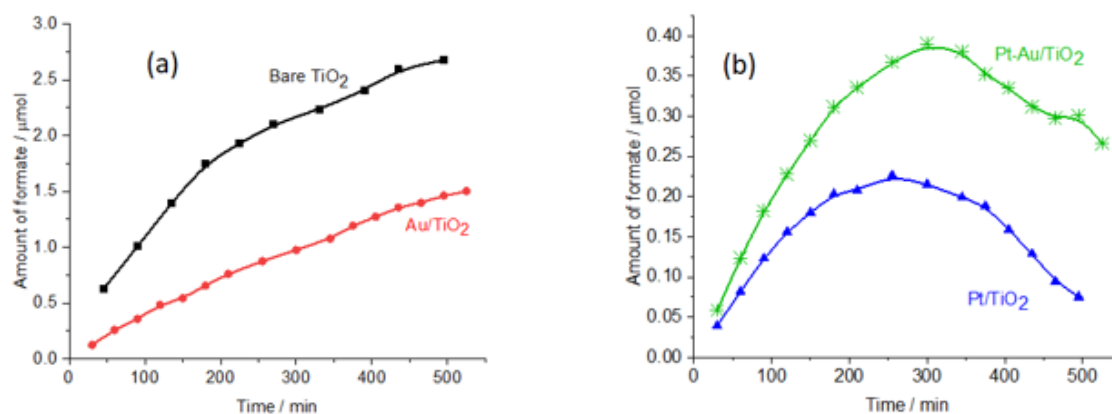
Figure 5-18 The amounts of formate produced in the suspension during the irradiation detected by HPIC over bare TiO$_2$ and Au$_{1\%}$/TiO$_2$ (a) and over Pt$_{0.25\%}$/TiO$_2$ and Au$_{1\%}$-Pt$_{0.25\%}$/TiO$_2$ (b).

EPR spin-trap technique with DMPO as a spin-trapping agent was used to determine the photogenerated species in the absence of molecular oxygen. No DMPO$^\bullet$-OH adducts were produced as shown in Figure 5-19(a). An identical result has been reported where DMPO$^\bullet$–OH spin adduct completely disappeared when oxalic acid has been added to perfluorooctanoic acid/TiO$_2$ dispersion [88]. Thus, oxalic acid can either inhibit the formation of hydroxyl radicals because of the direct oxidation with photogenerated holes or can react faster with any $^\bullet$OH radical produced upon the irradiation. In this context, the rate constants of the reaction of $^\bullet$OH radical with DMPO and HC$_2$O$_4^-$ were found to be 2.0 x 10^9 and 1.9 x 10^8 M^{-1} s^{-1} [89, 90], respectively. However, the higher concentration of oxalic acid besides its adsorption strength on TiO$_2$ would facilitate its reaction with $^\bullet$OH radicals, if any, even though the 10-fold lower kinetics. Hence, it is not completely clear from the EPR data whether the direct oxidation with photogenerated holes is the dominant mechanism.

Nevertheless, The simulation of the complex EPR spectra from the oxalic acid suspension can be seen in Figure 5-19(a), which is fitted by overlapping of three spin adducts, DMPO$^\bullet$-CO$_2^-$ (a^N = 15.40 G, a_β^H = 18.28 G) [91] and two other six-line signals, which are typical for carbon-centered DMPO spin-adducts [91] (see Figure 19(b)). The first signal fits well the DMPO$^\bullet$-CHO resulting from formyl radicals with hyperfine parameters of (a^N = 15.51 G, a_β^H = 21.09 G) [92]. The third signal has hyperfine parameters of (a^N = 15.67 G, a_β^H = 23.33 G), which most likely belong to the DMPO$^\bullet$-(CO-CO$_2^-$) because of their similar values to hydroxyalkyl-radical spin-adducts [91]. This means that other organic radicals are formed simultaneously with the production of carbon dioxide anion radicals. The intensities of the EPR spectra in Figure 5-19 increase with the irradiation time in the order of Pt/TiO$_2$ > Au-Pt/TiO$_2$ > Au-TiO$_2$ > bare TiO$_2$ confirming the enhancement in the formation of radicals by the noble metals. The EPR results are in good agreement with the theoretical calculations done by Mendive et al. [93], who have predicted a direct transfer of e$^-$ and h$^+$ to the adsorbed oxalic acid at the TiO$_2$ surface as shown in Figure 5-20. They have also predicted the production of aldehyde molecules accounting for the reduction of the carboxylic group.
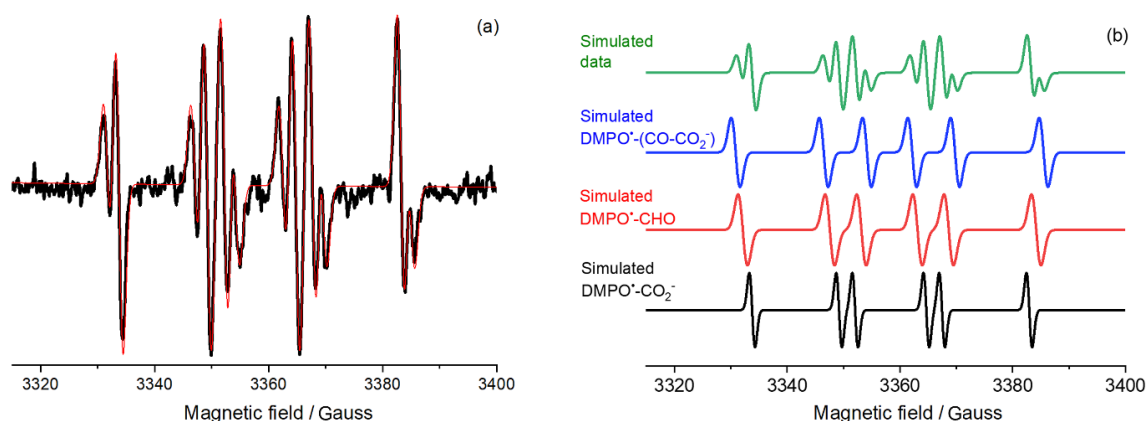
Figure 5-19 EPR spin trap experiment in the absence of O_2 for a UV-irradiated oxalic acid suspension; (a) experimental spectrum with its simulation; and (b) simulated spectrum of the mixed radicals and of each DMPO•-radical spin adduct. The test suspension contained oxalic acid (5.5 mmol l^{-1}), DMPO (0.8 mmol l^{-1}) in the presence of (1 g l^{-1}) of Pt/TiO$_2$.
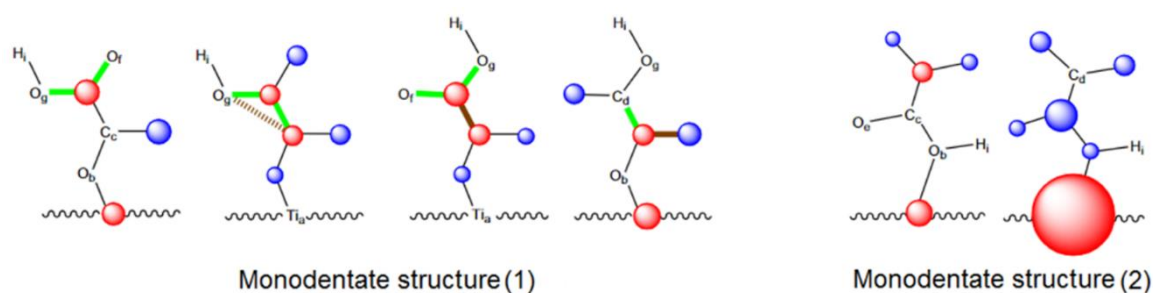
Figure 5-20 A scheme of oxalic acid molecules with red and blue circles where the atom becomes more negative and more positive, respectively; dash bonds belong to the bonds that are weakened due to the irradiation. Adapted with permission from Ref. [93].

One could assume that the chemistry of the photocatalytic reforming of oxalic acid is rather simple and follows Eq. 1 with molar ratios of CO_2:H_2 and H_2:OA equal to 2 and 1, respectively. However, to obtain such ratios the mechanism should occur according to the current doubling effect. Such a reaction mechanism illustrates that at least half of the detected H_2 is formed through the action of holes and not of electrons. Nevertheless, the detection of a photocatalytic H_2 yield of 200%, i.e., direct evidence for "current doubling", in the photocatalytic hydrogen generation has not been previously shown.

At pH ~3, $HC_2O_4^-$ are the dominant oxalic acid species in the solution (Eq. 5-8), as revealed from the adsorption data and due to its first dissociation constant $pK_{a1}(H_2C_2O_4) = 1.25$ [64]. The photogenerated holes in the valence band of TiO_2 react either with the adsorbed water to form hydroxyl radicals (Eq. 5-9) or directly with the adsorbed $HC_2O_4^-$ to produce $HC_2O_4^•$ radicals (Eq. 5-11) that can be also generated through the reaction between $HC_2O_4^-$ and hydroxyl radicals on the surface of TiO_2 (Eq. 5-10). We believe that the direct reaction with the photogenerated holes might be dominant in our experimental conditions because oxalic acid adsorbs strongly at the photocatalyst surface. The

direct photocatalysis mechanism has been associated with systems where the substrate adsorbs strongly at the photocatalyst surface, establishing a good electronic contact.[94] Some previous reports have shown that oxalate can be oxidized *via* an indirect hole transfer, i.e., hydroxyl radical oxidation [95, 96]. However, these studies have been performed either photoelectrochemically or photocatalytically in strongly acidic conditions (pH < 2). On the other hand, Mendive et *al.* have concluded from their ATR-FTIR experiments the direct oxidation of oxalic acid at the TiO_2 surface by the hole formed upon UV(A) light absorption [93]. They have theoretically predicted that $^{\bullet}OH$ radicals, if involved in the reactions, only arise from the cleavage of chemical bonds of the adsorbed oxalic acid and not from adsorbed water.

$$H_2C_2O_4 \quad\quad \leftrightarrow \quad HC_2O_4^- + \; H^+ \quad\quad\quad (\text{at pH} \sim 3) \quad\quad (5\text{-}8)$$

$$OH^-_{(ads)} \; + \; h^+_{(VB)} \quad \rightarrow \quad {}^{\bullet}OH_{(ads)} \quad\quad\quad\quad\quad\quad (5\text{-}9)$$

$$HC_2O_4^- \; + \; {}^{\bullet}OH_{(ads)} \quad \rightarrow \quad HC_2O_4^{\bullet} \; + \; OH^- \quad\quad\quad\quad (5\text{-}10)$$

$$HC_2O_4^- \; + \; h^+_{(VB)} \quad \rightarrow \quad HC_2O_4^{\bullet} \quad\quad\quad\quad\quad\quad\quad (5\text{-}11)$$
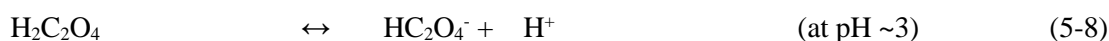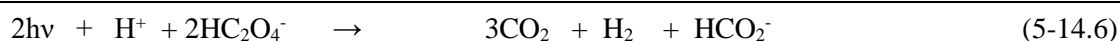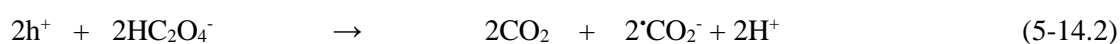
The one-electron oxidation process of oxalic acid through the C-C cleavage *via* the photo-Kolbe mechanism (Eqs. 5-12 and 5-13) results in the formation of a strongly reducing radical as an intermediate, i.e., the carbon dioxide radical anion $^{\bullet}CO_2^-$ $[E^0(CO_2/^{\bullet}CO_2^-) = -1.9 \text{ V}]$ [97]. This radical is an excellent reducing agent and can consequently participate in many redox reactions. The formation of $^{\bullet}CO_2^-$ is confirmed from our EPR spin-trap results, while the injection of their electrons is detected in our solid-phase EPR data. The formation of $^{\bullet}CO_2^-$ has been, as well, detected through radiolysis experiments using methylviologen as a mechanistic probe [98] and through cyclic voltammetry experiments [99]. Carbon dioxide radical anion has a $pK_a(^{\bullet}CO_2H)$ ~ 2.3 [100], hence, in our experimental conditions (pH > 3), $^{\bullet}CO_2^-$ is the dominant generated species (Eqs. 5-12 and 5-13).
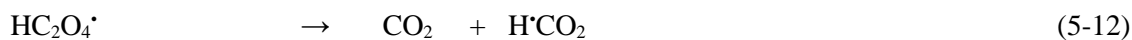
$$HC_2O_4^{\bullet} \quad\quad\quad \rightarrow \quad CO_2 \; + \; H^{\bullet}CO_2 \quad\quad\quad\quad\quad (5\text{-}12)$$

$$H^{\bullet}CO_2 \quad\quad\quad \leftrightarrow \quad {}^{\bullet}CO_2^- \; + \; H^+ \quad\quad\quad\quad\quad (5\text{-}13)$$

However, $^{\bullet}CO_2^-$ radicals might render the photoreforming reaction rather complicated. Since the formation of a hydrogen molecule requires two electrons and $^{\bullet}CO_2^-$ radicals can inject their electrons in TiO_2 (current-doubling), we can suggest three different mechanisms for the H_2 production from oxalic acid. (1) Upon two-photon absorption and generation of two e^-/h^+ pair, two oxalic acid molecules inject two electrons into the valence band to be trapped by the photogenerated holes, while both electrons in the conduction band are then used to reduce two protons to molecular hydrogen. This mechanism is the "no current doubling" mechanism (Figure 5-21(a) and Eqs. 5-14.1 to 5-14.6), which leads to a molar ratio H_2:OA of 0.5. (2) Upon one-photon absorption and generation of one e^-/h^+ pair, oxalic acid injects one electron into the valence band to be trapped by

the photogenerated hole. The $^\bullet CO_2^-$ radical formed has enough energy to transfer another electron into the conduction band of TiO_2. It is thus clear that the second electron originates directly from $^\bullet CO_2^-$ radicals. Both electrons in the conduction band are then used to reduce two protons to molecular hydrogen. This mechanism is the "current doubling" mechanism (Figure 5-21(b) and Eqs. 5-15.1 to 5-15.6), which leads to a molar ratio of H_2:OA of 1. (3) The "radical recombination" mechanism, in which one photon produces a formate anion without the production of a H_2 molecule (Scheme 5-1 and Eqs. 5-16.1 to 5-16.5). The latter mechanism has been proposed by Yamada et *al.* [78] and has been also theoretically predicted by Mendive et *al.* [93] due to the cleavage of the C-C bond followed by the addition of $^\bullet H$ atoms to the adsorbed $^\bullet CO_2^-$ radicals.

Mechanism (1) NO current doubling:

$2h\nu$	$\rightarrow$	$2e^-_{(CB)} + 2h^+_{(VB)}$	(5-14.1)
$2h^+ + 2HC_2O_4^-$	$\rightarrow$	$2CO_2 + 2^\bullet CO_2^- + 2H^+$	(5-14.2)
$2^\bullet CO_2^- + H^+$	$\rightarrow$	$CO_2 + HCO_2^-$	(5-14.3)
$2e^- + 2H^+$	$\rightarrow$	$2^\bullet H$	(5-14.4)
$2^\bullet H$	$\rightarrow$	H_2	(5-14.5)
$2h\nu + H^+ + 2HC_2O_4^-$	$\rightarrow$	$3CO_2 + H_2 + HCO_2^-$	(5-14.6)

Mechanism (2) with current doubling:

$h\nu$	$\rightarrow$	$e^-_{(CB)} + h^+_{(VB)}$	(5-15.1)
$h^+ + HC_2O_4^-$	$\rightarrow$	$CO_2 + ^\bullet CO_2^- + H^+$	(5-15.2)
$^\bullet CO_2^-$	$\rightarrow$	$e^-_{(CB)} + CO_2$	(5-15.3)
$2e^- + 2H^+$	$\rightarrow$	$2^\bullet H$	(5-15.4)
$2^\bullet H$	$\rightarrow$	H_2	(5-15.5)
$h\nu + H^+ + HC_2O_4^-$	$\rightarrow$	$2CO_2 + H_2$	(5-15.6)

Mechanism (3) radical recombination:

$h\nu$	$\rightarrow$	$e^-_{(CB)} + h^+_{(VB)}$	(5-16.1)
$h^+ + HC_2O_4^-$	$\rightarrow$	$CO_2 + ^\bullet CO_2^- + H^+$	(5-16.2)
$e^- + H^+$	$\rightarrow$	$^\bullet H$	(5-16.3)
$^\bullet CO_2^- + ^\bullet H$	$\rightarrow$	HCO_2^-	(5-16.4)
$h\nu + HC_2O_4^-$	$\rightarrow$	$CO_2 + HCO_2^-$	(5-16.5)
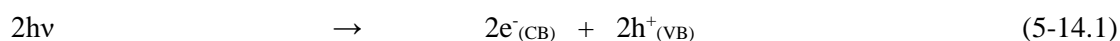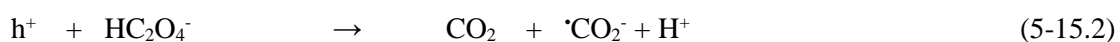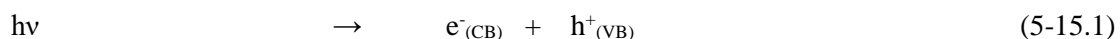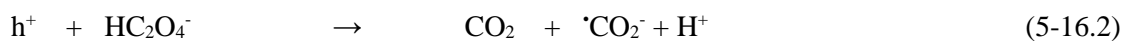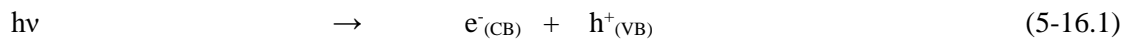
Figure 5-21 Schematic representation of the two-hole mechanism (no current doubling) and the one-hole mechanisms (with current doubling). The standard reduction potential of oxalic acid is taken from ref. [101].

The disproportionation of $^{\bullet}CO_2^-$ radicals can compete with the electron injection to TiO_2. Carbon dioxide radical anions show a bimolecular decay rate constant between 7.5×10^8 and 1.4×10^9 l mol^{-1} s^{-1} [100]. However, the injection of electrons from $(CH_3)_2^{\bullet}COH$ radicals [$E^0 = -1.8$ V] into the conduction band of TiO_2 has a rate constant between 1.6×10^8 and 4×10^8 l mol^{-1} s^{-1} [102, 103]. Importantly, Safrany et al. [104] showed that the disproportionation of the $(CH_3)_2^{\bullet}COH$ radicals competes with the electron injection in TiO_2. Hence, the disproportionation of $^{\bullet}CO_2^-$ radicals might interfere with the current doubling.

The disproportionation of two $^{\bullet}CO_2^-$ radicals leads to the formation of CO_2 and formate anion and/or formic acid [pK_a(HCOOH) = 3.75] [64] as per Eq. 9.3 and Scheme 5-1. The generation of formate is mainly due to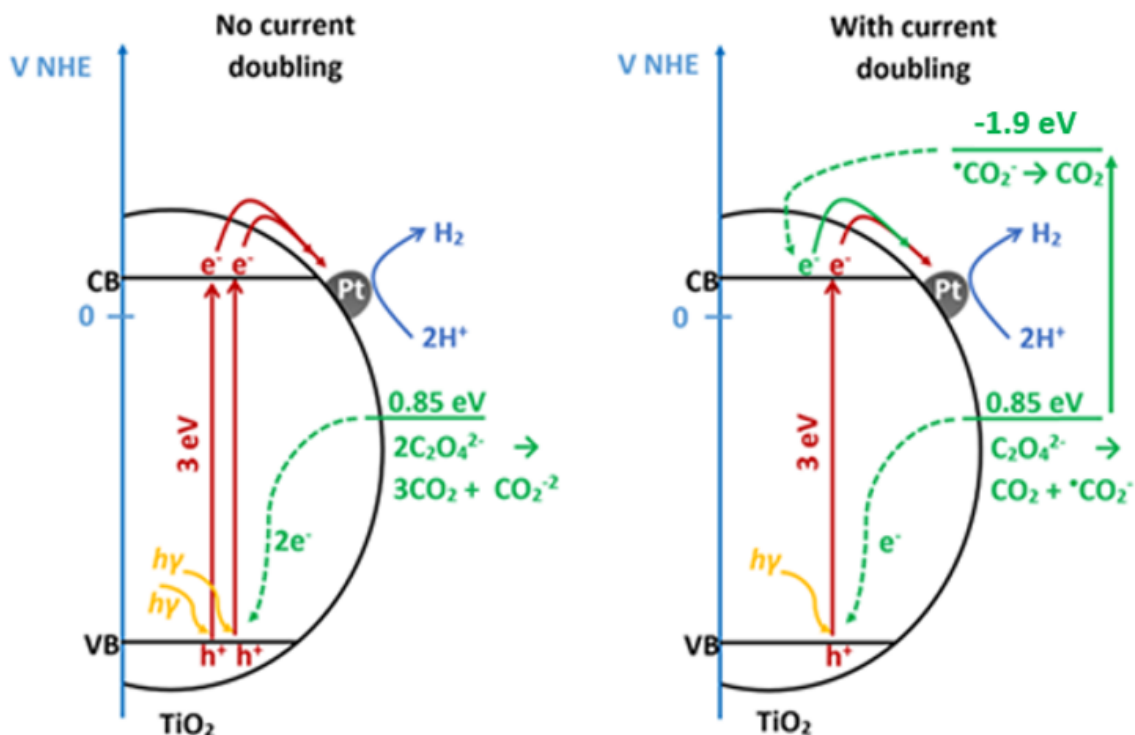 the head-to-tail recombination of two $^{\bullet}CO_2^-$ radicals. Flyunt et al. [100] have demonstrated using radiolysis experiments that more than 90% of $^{\bullet}CO_2^-$ radicals recombined to produce formate and carbon dioxide instead of recombination at the carbon to generate oxalate.

Our experimental results using Pt/TiO_2 show that the molar ratio of H_2:OA is 0.72. We assume, hence, that the photocatalytic reforming of oxalic acid mostly occurs via the combination of mechanisms (1) and (2). Of interest here is the fact that current doubling is not perfect, i.e., the H_2:OA is significantly lower than 1. Owing to the previous discussion, we suggest that the total reforming of oxalic acid over Pt/TiO_2 follows mechanisms (1) and (2) with a similar probability,

leading to a maximum yield of H_2 between 0.5 and 1. The by-products, e.g., formate, may not act as hole scavengers at low concentrations especially in the presence of oxalic acid on the surface of the photocatalyst. It has been demonstrated that oxalic acid adsorbs more strongly on TiO_2 than formate, which favors the photocatalytic reforming of oxalic acid even in the presence of an excess amount of formate [59].

The lower contribution of the current doubling can be due to the incomplete transfer of the injected electrons to platinum NPs as shown by our solid-phase EPR results. Moreover, $^{\bullet}CO_2^{-}$ radicals can react with other species in suspension, taking into account the nature of the species and the lifetime of the radical. It was previously noted that current doubling for methanol never reaches the same extent as the hole-induced current and that its extent depends on many factors such as concentration, pH and light intensity [105]. Such a lower contribution has been also observed by Nogami and Kennedy [106], who investigated the photo-oxidation mechanisms of methanol, formaldehyde, and formic acid using the rotating ring disk electrode technique with n-TiO_2 as a disk electrode. They found upon illumination that, although true current-doubling (100% increase) was not achieved, photocurrent increases of ~50% were observed.

When other photocatalysts are employed (i.e. bare TiO_2, Au/TiO_2, and Au-Pt/TiO_2), the H_2:OA molar ratios are lower. In the case of bare TiO_2, the ratio is even lower than 0.5, i.e. the expected value from mechanism 1. From these considerations, we expect in these cases a stronger contribution of mechanism (3). Indeed, the recombination of $^{\bullet}H$ atoms on platinum is higher than on gold (recombination factor $\gamma = 0.06$ and 0.03 at 293 K for Pt and Au, respectively) [107], decreasing, in this case, the probability of mechanism (3). Moreover, it has been reported that $^{\bullet}H$ atoms are produced on TiO_2 surfaces before their recombination on the metal co-catalysts [108, 109], and that $^{\bullet}H$ atoms can spillover from the metal co-catalyst to the titanium dioxide surface [110]. Thus, in bare TiO_2 the absence of a co-catalyst means that a large fraction of $^{\bullet}H$ will end up producing formate (Eq. 5-16.4), decreasing the yield of H_2. This argument is supported by the distinct amounts of produced formate over the different materials (Figure 5-17). Another possible pathway for the production of formate can proceed *via* the cleavage of the C-O bond as predicted previously [93], forming the adsorbed $^{\bullet}CO$-CO_2^{-} radicals. The formed radicals can react with $^{\bullet}H$ atoms producing adsorbed glyoxylate. The later might undergo cleavage of its C-C bond, producing formaldehyde through the reaction between $^{\bullet}H$ atoms and formyl radicals. In addition to the detection of formyl radicals by means of the EPR spin-trap experiments, the production of formaldehyde was also detected by following the color developed upon its derivatization with Nash's reagent [111]; however, the quantitation of these trace amounts was difficult.
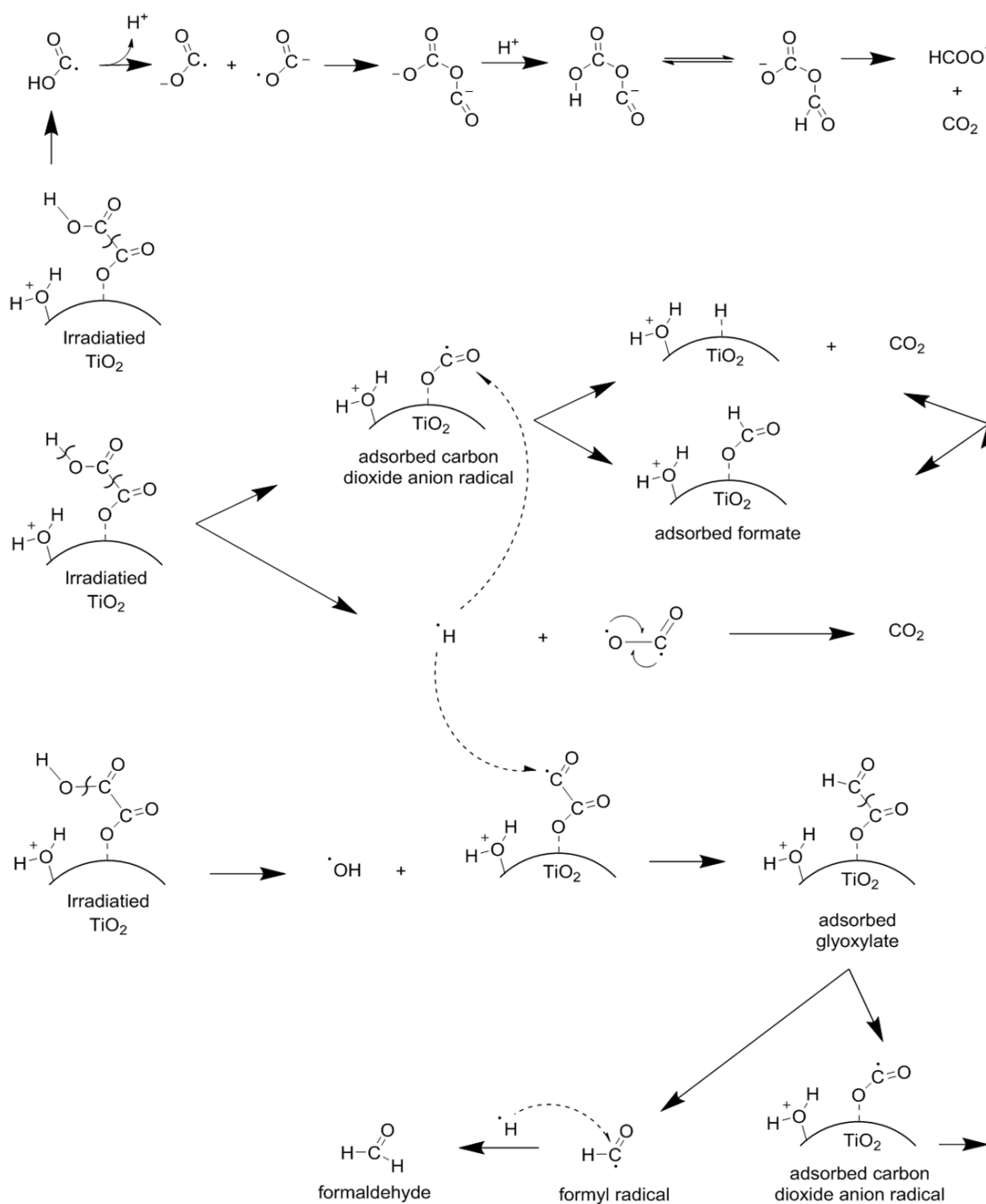
Scheme 5-1. The proposed surface reaction mechanism of the photocatalytic oxalic acid conversion on TiO₂.

5.6. Additional investigations into H_2 production from oxalic acid on Pt/TiO₂

The photocatalytic experiments, in which QMS was used as the gas detector, were repeated after the addition of 20 mmol l⁻¹ KI to the suspension. Interestingly, higher amounts of gases, especially H_2, are evolved when using KI until 800 min of irradiation, after which no-detection of gases is possible as shown in Figure 5-22. Hence, when the concentration of oxalic acid getting lower with the irradiation time, KI act as an effective hole scavenger ensuring the good separation between the charge carriers over the whole range, producing H_2 more efficiently.

The total amounts of H_2 and CO_2 gases were found to be 55.14 ± 1.410 and 112.1 ± 3.141 µmol, respectively. Here, $CO_2:H_2$, $H_2:OA_{(total)}$ and $CO_2:OA_{(total)}$ ratios are 2.033, 0.993 and 2.020, respectively. Interestingly, the calculated ratios are in accordance with the theoretical expected ratios. These numbers confirm a total conversion of oxalic acid with a stoichiometric amount evolved of molecular hydrogen, which was not the case in the absence of KI. Noteworthy, even in the presence of KI, H_2 is not detected when oxalic acid is totally consumed from the suspension. This observation confirms that KI enhance the activity, while oxalic acid is the responsible of H_2 production.
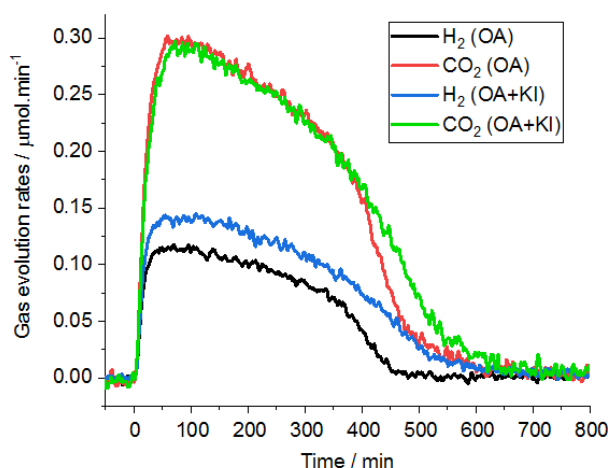

Figure 5-22 Time course of the gas evolution rates over Pt/TiO$_2$ in the absence and in the presence of 20 mmol l^{-1} KI in addition to 1.11 mmol l^{-1} oxalic acid.

Unfortunately, it was impossible to track the concentration of oxalic acid in suspension due to the interference of KI in the HPIC analysis. However, the formation of formate as a by-product was inhibited upon the presence of KI in the suspension, indicating the fast transformation of $^\bullet CO_2^-$ radical to CO_2 instead of their reactions with $^\bullet H$ atoms. Besides, EPR spin-trap spectra showed the formation of only one DMPO-spin adduct related to $^\bullet CO_2^-$ radicals, hence, KI inhibits the formation of the other radicals.

In conclusion, HPIC and EPR spin-trap results confirm the inhibition of by-products formation when KI is used, where $^\bullet CO_2^-$ radicals are the only species detected upon the irradiation. This can be assigned to the fast reaction between I_2 formed upon the oxidation of KI and $^\bullet CO_2^-$ radicals, transferring the latter to CO_2. This mechanism is proposed in Eqs. 5-16 to 5-21, respectively.

The presence of KI can, additionally, affect the Hydrogen adsorption on platinum, disturbing the H-Pt bonding. Chemisorbed iodide ions have been found to cause a decrease in the amount of adsorbed hydrogen on Pt surfaces [112]. It has been also reported a repulsive interaction between adsorbed hydrogen and halogen atoms. Thus, it has been found that H-I co-adsorption is of a competitive character [113].

$$2I^- + h^+_{VB} \rightarrow I_2^{-\bullet} \qquad\qquad K= 3.2 \times 10^9 \text{ [114]} \qquad\qquad (5\text{-}16)$$

$$2\,I_2^{-\bullet} \rightarrow I_3^- + I^- \qquad\qquad\qquad\qquad\qquad\qquad (5\text{-}17)$$

$$I_3^- \leftrightarrow I^- + I_2 \qquad\qquad\qquad\qquad\qquad\qquad\qquad (5\text{-}18)$$

$$I_3^- + e^- \rightarrow I_2^{-\bullet} + I^- \qquad\qquad\qquad\qquad\qquad\qquad (5\text{-}19)$$

$$I_2 + e^- \rightarrow I_2^{-\bullet} \qquad\qquad\qquad\qquad\qquad\qquad\qquad (5\text{-}20)$$

$$^\bullet CO_2^- + I_2 \rightarrow I_2^{-\bullet} + CO_2 \qquad\qquad K= 7 \times 10^9 \text{ [115]} \qquad\qquad (5\text{-}21)$$
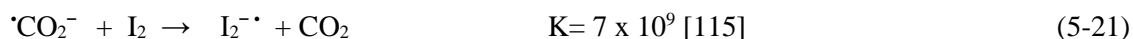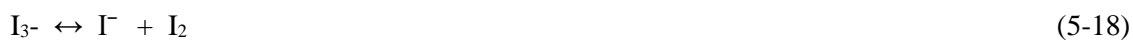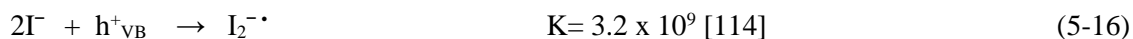
5.7. Concluding remarks and future outlooks

The first aim of this study was to systematically develop TiO_2 photocatalysts that can photocatalytically produce molecular hydrogen from reforming reactions without the use of expensive noble-metal co-catalysts. The "Design of Experiments" approach combined with the "Full Factorial Design" has successfully been applied to investigate the most influential factors and to optimize, in few experimental runs, the synthesis of TiO_2 through the EISA method. Although the bare photocatalysts produced may not have photonic efficiencies being high enough for the practical applications, this work has advanced the understanding of new types of interstitial defects and/or surface defects, which apparently have a great impact on the optical, physical, and electronic properties of TiO_2. These are, indeed, the main properties that should be improved to positively promote the photocatalytic activity accordingly. Future investigations regarding the procedure, by which the Ti(II) contents can be increased are highly recommended. Moreover, producing this type of defected material exhibiting higher surface area and an ordered mesoporous structure will definitely raise the performance. Deeper and theoretical calculations should also be conducted to further understanding the catalytic mechanism by which Ti(II) drives the HER reaction.

The investigations carried out in the second part of this research have provided many opportunities for future research. The most important outcomes can be summarized as follows: (1) oxalic acid is an efficient material to produce H_2 *via* the photoreforming in Pt/TiO_2 suspension, (2) the photocatalytic activity is found to be strongly correlated with the work function of the respective metal, (3) the interfacial charge reaction mechanism through which oxalic acid is converted to CO_2, formate, and formaldehyde has been established, (4) the distribution of the main and of the by-products depends largely on the employed co-catalyst, (5) the apparently lower yield of H_2 as stoichiometrically expected can be explained by the formation of by-products, and (6) the presence of KI inhibits the formation of by-products, thus promoting the H_2 evolution yielding the theoretical expected amounts. The mechanism, by which KI affects the photocatalytic efficiency is most certainly an interesting research aspect for future investigations.

5.8. References

1.   Mahoney, L. and R.T. Koodali, *Versatility of Evaporation-Induced Self-Assembly (EISA) Method for Preparation of Mesoporous TiO₂ for Energy and Environmental Applications.* Materials, 2014. **7**(4): p. 2697-2746.

2.   AlSalka, Y., F. Karabet, and S. Hashem, *Development and optimisation of quantitative analytical method to determine BTEX in environmental water samples using HPLC-DAD.* Analytical Methods, 2010. **2**(8): p. 1026-1035.

3.   Li, R., et al., *Achieving overall water splitting using titanium dioxide-based photocatalysts of different phases.* Energy & Environmental Science, 2015. **8**(8): p. 2377-2382.

4.   Sachs, M., et al., *Evaluation of surface state mediated charge recombination in anatase and rutile TiO₂.* The journal of physical chemistry letters, 2016. **7**(19): p. 3742-3746.

5.   Knorr, F.J., C.C. Mercado, and J.L. McHale, *Trap-state distributions and carrier transport in pure and mixed-phase TiO₂: influence of contacting solvent and interphasial electron transfer.* The Journal of Physical Chemistry C, 2008. **112**(33): p. 12786-12794.

6.   Sing, K.S.S., *Reporting Physisorption Data for Gas/Solid Systems with Special Reference to the Determination of Surface Area and Porosity.* 1982, Brunel University: UK. p. 2201—2218.

7.   van de Krol, R., *Principles of Photoelectrochemical Cells*, in *Photoelectrochemical Hydrogen Production*, R. van de Krol and M. Grätzel, Editors. 2012, Springer US: Boston, MA. p. 13-67.

8.   Asahi, R., et al., *Electronic and optical properties of anatase TiO₂.* Physical Review B, 2000. **61**(11): p. 7459-7465.

9.   Liu, N., et al., *Hydrogenated Anatase: Strong Photocatalytic Dihydrogen Evolution without the Use of a Co-Catalyst.* Angewandte Chemie International Edition, 2014. **53**(51): p. 14201-14205.

10. Pan, X., et al., *Defective TiO₂ with oxygen vacancies: synthesis, properties and photocatalytic applications.* Nanoscale, 2013. **5**(9): p. 3601-3614.

11. Xiong, L.-B., et al., *in the Surface of Titanium Dioxide: Generation, Properties and Photocatalytic Application.* Journal of Nanomaterials, 2012. **2012**: p. 13.

12. Wang, S., et al., *Titanium-Defected Undoped Anatase TiO₂ with p-Type Conductivity, Room-Temperature Ferromagnetism, and Remarkable Photocatalytic Performance.* Journal of the American Chemical Society, 2015. **137**(8): p. 2975-2983.

13. Murakami, Y., et al., *Femtosecond Diffuse-Reflectance Spectroscopy of Various Commercially Available TiO₂ Powders.* Spectroscopy Letters, 2011. **44**(2): p. 88-94.

14. Wang, X., et al., *Transient Absorption Spectroscopy of Anatase and Rutile: The Impact of Morphology and Phase on Photocatalytic Activity.* The Journal of Physical Chemistry C, 2015. **119**(19): p. 10439-10447.

15. Bahnemann, D.W., M. Hilgendorff, and R. Memming, *Charge Carrier Dynamics at TiO₂ Particles: Reactivity of Free and Trapped Holes.* The Journal of Physical Chemistry B, 1997. **101**(21): p. 4265-4275.

16. Schneider, J., et al., *Improved charge carrier separation in barium tantalate composites investigated by laser flash photolysis.* Physical Chemistry Chemical Physics, 2016. **18**(16): p. 10719-10726.

17. Kong, M., et al., *Tuning the Relative Concentration Ratio of Bulk Defects to Surface Defects in TiO₂ Nanocrystals Leads to High Photocatalytic Efficiency.* Journal of the American Chemical Society, 2011. **133**(41): p. 16414-16417.

18. Ohtani, B., *Titania Photocatalysis beyond Recombination: A Critical Review.* Catalysts, 2013. **3**(4): p. 942-953.

19. Katoh, R., M. Murai, and A. Furube, *Transient absorption spectra of nanocrystalline TiO₂ films at high excitation density.* Chemical Physics Letters, 2010. **500**(4): p. 309-312.

20. Nosaka, Y. and A.Y. Nosaka, *CHAPTER 7 Kinetic Processes in the Presence of Photogenerated Charge Carriers*, in *Photocatalysis: Fundamentals and Perspectives.* 2016, The Royal Society of Chemistry. p. 163-184.

21. Zhijiao, W., et al., *Effects of bulk and surface defects on the photocatalytic performance of size-controlled TiO₂ nanoparticles.* Nanotechnology, 2017. **28**(27): p. 275706.

22. Rothenberger, G., et al., *Charge carrier trapping and recombination dynamics in small semiconductor particles.* Journal of the American Chemical Society, 1985. **107**(26): p. 8054-8059.

23. Naldoni, A., et al., *Photocatalysis with reduced TiO₂: from black TiO₂ to cocatalyst-free hydrogen production.* ACS catalysis, 2019. **9**(1): p. 345-364.

24. Chen, X., et al., *Increasing Solar Absorption for Photocatalysis with Black Hydrogenated Titanium Dioxide Nanocrystals.* Science, 2011. **331**(6018): p. 746-750.

25. Liu, N., et al., *Black Magic in Gray Titania: Noble-Metal-Free Photocatalytic H₂ Evolution from Hydrogenated Anatase.* ChemSusChem, 2017. **10**(1): p. 62-67.

26. Wu, Q., et al., *Ultra-small yellow defective TiO₂ nanoparticles for co-catalyst free photocatalytic hydrogen production.* Nano Energy, 2016. **24**: p. 63-71.

27. Zhang, K., et al., *An order/disorder/water junction system for highly efficient co-catalyst-free photocatalytic hydrogen generation.* Energy & Environmental Science, 2016. **9**(2): p. 499-503.

28. Bilmes, S.A., et al., *Surface and Electronic Structure of Titanium Dioxide Photocatalysts.* The Journal of Physical Chemistry B, 2000. **104**(42): p. 9851-9858.

29. Justicia, I., et al., *Designed Self-Doped Titanium Oxide Thin Films for Efficient Visible-Light Photocatalysis.* Advanced Materials, 2002. **14**(19): p. 1399-1402.

30. Chen, X., L. Liu, and F. Huang, *Black titanium dioxide (TiO₂) nanomaterials.* Chemical Society Reviews, 2015. **44**(7): p. 1861-1885.

31. Cai, J., et al., *In Situ Formation of Disorder-Engineered TiO₂(B)-Anatase Heterophase Junction for Enhanced Photocatalytic Hydrogen Evolution.* ACS Applied Materials & Interfaces, 2015. **7**(45): p. 24987-24992.

32. Fu, Y., et al., *XPS characterization of surface and interfacial structure of sputtered TiNi films on Si substrate.* Materials Science and Engineering: A, 2005. **403**(1): p. 25-31.

33. Peng, W.-C., et al., *Tunability of p- and n-channel TiO$_x$ thin film transistors.* Scientific Reports, 2018. **8**(1): p. 9255.

34. Farber, M. and A.J. Darnell, *The Disproportionation and Vapor Pressure of TiCl₃.* The Journal of Physical Chemistry, 1955. **59**(2): p. 156-159.

35. Hashimoto, S. and A. Tanaka, *Alteration of Ti 2p XPS spectrum for titanium oxide by low-energy Ar ion bombardment.* Surface and Interface Analysis, 2002. **34**(1): p. 262-265.

36. Zhou, X., N. Liu, and P. Schmuki, *Ar⁺-ion bombardment of TiO₂ nanotubes creates co-catalytic effect for photocatalytic open circuit hydrogen evolution.* Electrochemistry Communications, 2014. **49**: p. 60-64.

37. Nowotny, J., *Titanium dioxide-based semiconductors for solar-driven environmentally friendly applications: impact of point defects on performance.* Energy & Environmental Science, 2008. **1**(5): p. 565-572.

38. Nowotny, J., et al., *Defect chemistry and defect engineering of TiO₂-based semiconductors for solar energy conversion.* Chemical Society Reviews, 2015. **44**(23): p. 8424-8442.

39. Pei, D.-N., et al., *Defective titanium dioxide single crystals exposed by high-energy {001} facets for efficient oxygen reduction.* Nature Communications, 2015. **6**(1): p. 8696.

40. Xing, M., et al., *Self-doped Ti³⁺-enhanced TiO₂ nanoparticles with a high-performance photocatalysis.* Journal of Catalysis, 2013. **297**: p. 236-243.

41. Zuo, F., et al., *Self-Doped Ti³⁺ Enhanced Photocatalyst for Hydrogen Production under Visible Light.* Journal of the American Chemical Society, 2010. **132**(34): p. 11856-11857.

42. Swaminathan, J., R. Subbiah, and V. Singaram, *Defect-Rich Metallic Titania (TiO₁.₂₃)—An Efficient Hydrogen Evolution Catalyst for Electrochemical Water Splitting.* ACS Catalysis, 2016. **6**(4): p. 2222-2229.

43. Jacobs, K., *F. A. Kröger. The Chemistry of Imperfect Crystals. 2nd Revised Edition, Volume 1: Preparation, Purification, Crystal Growth And Phase Theory.* Kristall und Technik, 1974. **9**(7): p. K67-K68.

44. Kamat, P.V., N.M. Dimitrijevic, and A.J. Nozik, *Dynamic Burstein-Moss shift in semiconductor colloids.* The Journal of Physical Chemistry, 1989. **93**(8): p. 2873-2875.

45. Feng, N., et al., *Unravelling the Efficient Photocatalytic Activity of Boron-induced Ti^{3+} Species in the Surface Layer of TiO_2.* Scientific Reports, 2016. **6**(1): p. 34765.

46. Ern, V. and A.C. Switendick, *Electronic Band Structure of TiC, TiN, and TiO.* Physical Review, 1965. **137**(6A): p. A1927-A1936.

47. Chen, Z.Z., Wei; Liang, Zhutian; Li, Weiqian; He, Guannan; Wang, Yinzhen, *Photocatalytic Activity Enhancement of Anatase TiO_2 by Using TiO.* Journal of Nanomaterials, 2014. **2014**: p. 9.

48. Greiner, M.T., et al., *Transition Metal Oxide Work Functions: The Influence of Cation Oxidation State and Oxygen Vacancies.* Advanced Functional Materials, 2012. **22**(21): p. 4557-4568.

49. Koleżyński, A. and K. Tkacz-Śmiech, *From the Molecular Picture to the Band Structure of Cubic and Tetragonal Barium Titanate.* Ferroelectrics, 2005. **314**(1): p. 123-134.

50. Swaminathan, J. and S. Ravichandran, *Insights into the Electrocatalytic Behavior of Defect-Centered Reduced Titania ($TiO_{1.23}$).* The Journal of Physical Chemistry C, 2018. **122**(3): p. 1670-1680.

51. Zhu, T. and S.-P. Gao, *The Stability, Electronic Structure, and Optical Property of TiO_2 Polymorphs.* The Journal of Physical Chemistry C, 2014. **118**(21): p. 11385-11396.

52. Wheeler, D.A., et al., *Probing the Nature of Bandgap States in Hydrogen-Treated TiO_2 Nanowires.* The Journal of Physical Chemistry C, 2013. **117**(50): p. 26821-26830.

53. Li, Y., G. Lu, and S. Li, *Photocatalytic hydrogen generation and decomposition of oxalic acid over platinized TiO_2.* Applied Catalysis A: General, 2001. **214**(2): p. 179-185.

54. Kosanić, M.M., *Photocatalytic degradation of oxalic acid over TiO_2 power.* Journal of Photochemistry and Photobiology A: Chemistry, 1998. **119**(2): p. 119-122.

55. Rossetti, I., *Hydrogen Production by Photoreforming of Renewable Substrates.* International Scholarly Research Network, 2012. **2012**: p. 21.

56. Sakaguchi, N., et al., *Effect of dissolved oxygen and lanthanide ions in solution on TiO_2 photocatalytic oxidation of 2-propanol.* Research on Chemical Intermediates, 2006. **32**(2): p. 95-101.

57. Shibata, H., et al., *Hydroxyl Radical Generation Depending on O_2 or H_2O by a Photocatalyzed Reaction in an Aqueous Suspension of Titanium Dioxide.* Bioscience, Biotechnology, and Biochemistry, 1998. **62**(12): p. 2306-2311.

58. Brezonik, P.L. and J. Fulkerson-Brekken, *Nitrate-Induced Photolysis in Natural Waters: Controls on Concentrations of Hydroxyl Radical Photo-Intermediates by Natural Scavenging Agents.* Environmental Science & Technology, 1998. **32**(19): p. 3004-3010.

59. Puga, A.V., *Photocatalytic production of hydrogen from biomass-derived feedstocks.* Coordination Chemistry Reviews, 2016. **315**: p. 1-66.

60. Li, Y., G. Lu, and S. Li, *Photocatalytic production of hydrogen in single component and mixture systems of electron donors and monitoring adsorption of donors by in situ infrared spectroscopy.* Chemosphere, 2003. **52**(5): p. 843-850.

61. Sun, Y., et al., *An Unexpected Fluctuating Reactivity for Odd and Even Carbon Numbers in the TiO_2-Based Photocatalytic Decarboxylation of C_2-C_6 Dicarboxylic Acids.* Chemistry – A European Journal, 2014. **20**(7): p. 1861-1870.

62. Yamada, Y., et al., *Photocatalytic hydrogen evolution from carbon-neutral oxalate with 2-phenyl-4-(1-naphthyl)quinolinium ion and metal nanoparticles.* Physical Chemistry Chemical Physics, 2012. **14**(30): p. 10564-10571.

63. Kandiel, T.A., I. Ivanova, and D.W. Bahnemann, *Long-term investigation of the photocatalytic hydrogen production on platinized TiO_2: an isotopic study.* Energy & Environmental Science, 2014. **7**(4): p. 1420-1425.

64. AlSalka, Y., et al., *Understanding the degradation pathways of oxalic acid in different photocatalytic systems: Towards simultaneous photocatalytic hydrogen evolution.* Journal of Photochemistry and Photobiology A: Chemistry, 2018. **366**: p. 81-90.

65.   Bamwenda, G.R., et al., *Photoassisted hydrogen production from a water-ethanol solution: a comparison of activities of Au-TiO₂ and Pt-TiO₂.* Journal of Photochemistry and Photobiology A: Chemistry, 1995. **89**(2): p. 177-189.

66.   Tanaka, A., et al., *Preparation of Au/TiO₂ with Metal Cocatalysts Exhibiting Strong Surface Plasmon Resonance Effective for Photoinduced Hydrogen Formation under Irradiation of Visible Light.* ACS Catalysis, 2013. **3**(1): p. 79-85.

67.   Gallo, A., et al., *Bimetallic Au–Pt/TiO₂ photocatalysts active under UV-A and simulated sunlight for H₂ production from ethanol.* Green Chemistry, 2012. **14**(2): p. 330-333.

68.   Michaelson, H.B., *The work function of the elements and its periodicity.* Journal of Applied Physics, 1977. **48**(11): p. 4729-4733.

69.   Schneider, J., T.A. Kandiel, and D.W. Bahnemann, *Solar Photocatalytic Hydrogen Production: Current Status and Future Challenges*, in *Materials and Processes for Solar Fuel Production*, B. Viswanathan, V. Subramanian, and J.S. Lee, Editors. 2014, Springer New York: New York, NY. p. 41-74.

70.   Kamat, P.V., *Manipulation of Charge Transfer Across Semiconductor Interface. A Criterion That Cannot Be Ignored in Photocatalyst Design.* The Journal of Physical Chemistry Letters, 2012. **3**(5): p. 663-672.

71.   Nørskov, J.K., et al., *Trends in the exchange current for hydrogen evolution.* Journal of The Electrochemical Society, 2005. **152**(3): p. J23-J26.

72.   Dong, H., et al., *Three-dimensional nitrogen-doped graphene supported molybdenum disulfide nanoparticles as an advanced catalyst for hydrogen evolution reaction.* Scientific reports, 2015. **5**: p. 17542.

73.   Jakob, M., H. Levanon, and P.V. Kamat, *Charge Distribution between UV-Irradiated TiO₂ and Gold Nanoparticles: Determination of Shift in the Fermi Level.* Nano Letters, 2003. **3**(3): p. 353-358.

74.   Subramanian, V., E.E. Wolf, and P.V. Kamat, *Green Emission to Probe Photoinduced Charging Events in ZnO−Au Nanoparticles. Charge Distribution and Fermi-Level Equilibration.* The Journal of Physical Chemistry B, 2003. **107**(30): p. 7479-7485.

75.   Huber, G.W., et al., *Aqueous-phase reforming of ethylene glycol over supported Pt and Pd bimetallic catalysts.* Applied Catalysis B: Environmental, 2006. **62**(3-4): p. 226-235.

76.   Hu, M., et al., *Hydrogen adsorption on platinum–gold bimetallic nanoparticles: A density functional theory study.* The Journal of Physical Chemistry C, 2013. **117**(29): p. 15050-15060.

77.   Kmetykó, Á., et al., *Photocatalytic H₂ production using Pt-TiO₂ in the presence of oxalic acid: Influence of the noble metal size and the carrier gas flow rate.* Materials, 2014. **7**(10): p. 7022-7038.

78.   Yamada, Y., et al., *Photocatalytic hydrogen evolution from carbon-neutral oxalate with 2-phenyl-4-(1-naphthyl) quinolinium ion and metal nanoparticles.* Physical Chemistry Chemical Physics, 2012. **14**(30): p. 10564-10571.

79.   Nakaoka, Y. and Y. Nosaka, *ESR investigation into the effects of heat treatment and crystal structure on radicals produced over irradiated TiO₂ powder.* Journal of Photochemistry and Photobiology A: Chemistry, 1997. **110**(3): p. 299-305.

80.   Howe, R.F. and M. Gratzel, *EPR study of hydrated anatase under UV irradiation.* Journal of Physical Chemistry, 1987. **91**(14): p. 3906-3909.

81.   Livraghi, S., et al., *On the nature of reduced states in titanium dioxide as monitored by electron paramagnetic resonance. I: the anatase case.* The Journal of Physical Chemistry C, 2011. **115**(51): p. 25413-25421.

82.   Chiesa, M., et al., *Charge trapping in TiO₂ polymorphs as seen by Electron Paramagnetic Resonance spectroscopy.* Physical Chemistry Chemical Physics, 2013. **15**(24): p. 9435-9447.

83.   Howe, R.F. and M. Gratzel, *EPR observation of trapped electrons in colloidal titanium dioxide.* The Journal of Physical Chemistry, 1985. **89**(21): p. 4495-4499.

84.   Micic, O., et al., *Photoinduced hole transfer from titanium dioxide to methanol molecules in aqueous solution studied by electron paramagnetic resonance.* The Journal of Physical Chemistry, 1993. **97**(50): p. 13284-13288.

85.   Ohtani, B., *Photocatalysis A to Z—What we know and what we do not know in a scientific sense.* Journal of Photochemistry and Photobiology C: Photochemistry Reviews, 2010. **11**(4): p. 157-178.

86.   Serpone, N., et al., *Turnovers and photocatalysis: A mathematical description.* Journal of Photochemistry and Photobiology A: Chemistry, 2000. **130**(2-3): p. 83-94.

87.   Sun, Y., et al., *An Unexpected Fluctuating Reactivity for Odd and Even Carbon Numbers in the TiO_2-Based Photocatalytic Decarboxylation of C_2-C_6 Dicarboxylic Acids.* Chemistry–A European Journal, 2014. **20**(7): p. 1861-1870.

88.   Wang, Y. and P. Zhang, *Photocatalytic decomposition of perfluorooctanoic acid (PFOA) by TiO_2 in the presence of oxalic acid.* Journal of hazardous materials, 2011. **192**(3): p. 1869-1875.

89.   Marriott, P.R., M.J. Perkins, and D. Griller, *Spin trapping for hydroxyl in water: a kinetic evaluation of two popular traps.* Canadian Journal of Chemistry, 1980. **58**(8): p. 803-807.

90.   Ervens, B., S. Gligorovski, and H. Herrmann, *Temperature-dependent rate constants for hydroxyl radical reactions with organic compounds in aqueous solutions.* Physical Chemistry Chemical Physics, 2003. **5**(9): p. 1811-1824.

91.   Buettner, G.R., *Spin Trapping: ESR parameters of spin adducts 1474 1528V.* Free Radical Biology and Medicine, 1987. **3**(4): p. 259-303.

92.   Bauer, N.A., et al., *Detection of the formyl radical by EPR spin-trapping and mass spectrometry.* Free Radical Biology and Medicine, 2018. **116**: p. 129-133.

93.   Mendive, C.B., et al., *Oxalic acid at the TiO_2/water interface under UV (A) illumination: Surface reaction mechanisms.* Journal of catalysis, 2015. **322**: p. 60-72.

94.   Mendive, C.B., M. Curti, and D. Bahnemann, *CHAPTER 3 Current Issues Concerning the Mechanism of Pristine TiO_2 Photocatalysis and the Effects on Photonic Crystal Nanostructures*, in *Photocatalysis: Fundamentals and Perspectives*. 2016, The Royal Society of Chemistry. p. 51-79.

95.   Doudrick, K., et al., *Nitrate reduction in water using commercial titanium dioxide photocatalysts (P25, P90, and Hombikat UV100).* Journal of Environmental Engineering, 2011. **138**(8): p. 852-861.

96.   Mora-Sero, I., et al., *Photoelectrochemical behavior of nanostructured TiO_2 thin-film electrodes in contact with aqueous electrolytes containing dissolved pollutants: A model for distinguishing between direct and indirect interfacial hole transfer from photocurrent measurements.* The Journal of Physical Chemistry B, 2005. **109**(8): p. 3371-3380.

97.   Hakki, A., J. Schneider, and D. Bahnemann, *CHAPTER 2 Understanding the Chemistry of Photocatalytic Processes*, in *Photocatalysis: Fundamentals and Perspectives*. 2016, The Royal Society of Chemistry. p. 29-50.

98.   Mulazzani, Q.G., et al., *Interaction of formate and oxalate ions with radiation-generated radicals in aqueous solution. Methylviologen as a mechanistic probe.* The Journal of Physical Chemistry, 1986. **90**(21): p. 5347-5352.

99.   Kanoufi, F. and A.J. Bard, *Electrogenerated chemiluminescence. 65. An investigation of the oxidation of oxalate by tris (polypyridine) ruthenium complexes and the effect of the electrochemical steps on the emission intensity.* The Journal of Physical Chemistry B, 1999. **103**(47): p. 10469-10480.

100.   Flyunt, R., M.N. Schuchmann, and C. von Sonntag, *A Common Carbanion Intermediate in the Recombination and Proton-Catalysed Disproportionation of the Carboxyl Radical Anion, $CO_2^{\cdot -}$, in Aqueous Solution.* Chemistry–A European Journal, 2001. **7**(4): p. 796-799.

101.   Chen, C., J.F. Khosrowabadi Kotyk, and S.W. Sheehan, *Progress toward Commercial Application of Electrochemical Carbon Dioxide Reduction.* Chem, 2018. **4**(11): p. 2571-2586.

102.   Gao, R., A. Safrany, and J. Rabani, *Fundamental reactions in TiO₂ nanocrystallite aqueous solutions studied by pulse radiolysis.* Radiation Physics and Chemistry, 2002. **65**(6): p. 599-609.

103.   Dimitrijevic, N.M., et al., *Revealing the Nature of Trapping Sites in Nanocrystalline Titanium Dioxide by Selective Surface Modification.* The Journal of Physical Chemistry B, 2003. **107**(30): p. 7368-7375.

104.   Safrany, A., R. Gao, and J. Rabani, *Optical Properties and Reactions of Radiation Induced TiO₂ Electrons in Aqueous Colloid Solutions.* The Journal of Physical Chemistry B, 2000. **104**(24): p. 5848-5853.

105.   Hykaway, N., et al., *Current-doubling reactions on titanium dioxide photoanodes.* The Journal of Physical Chemistry, 1986. **90**(25): p. 6663-6667.

106.   Nogami, G., *Investigation of "Current Doubling" Mechanism of Organic Compounds by the Rotating Ring Disk Electrode Technique.* Journal of The Electrochemical Society, 1989. **136**(9): p. 2583.

107.   Melin, G.A. and R.J. Madix, *Energy accommodation during hydrogen atom recombination on metal surfaces.* Transactions of the Faraday Society, 1971. **67**(0): p. 2711-2719.

108.   Joo, J.B., et al., *Promotion of atomic hydrogen recombination as an alternative to electron trapping for the role of metals in the photocatalytic production of H₂.* Proceedings of the National Academy of Sciences, 2014. **111**(22): p. 7942-7947.

109.   Walenta, C.A., et al., *Why co-catalyst-loaded rutile facilitates photocatalytic hydrogen evolution.* Physical Chemistry Chemical Physics, 2019. **21**(3): p. 1491-1496.

110.   Karim, W., et al., *Catalyst support effects on hydrogen spillover.* Nature, 2017. **541**(7635): p. 68-71.

111.   Nash, T., *The colorimetric estimation of formaldehyde by means of the Hantzsch reaction.* Biochemical Journal, 1953. **55**(3): p. 416.

112.   Bagotzky, V.S. and N.V. Osetrova, *Investigations of hydrogen ionization on platinum with the help of micro-electrodes.* Journal of Electroanalytical Chemistry and Interfacial Electrochemistry, 1973. **43**(2): p. 233-249.

113.   Gossenberger, F., T. Roman, and A. Groß, *Hydrogen and halide co-adsorption on Pt(111) in an electrochemical environment: a computational perspective.* Electrochimica Acta, 2016. **216**: p. 152-159.

114.   Rowley, J. and G.J. Meyer, *Reduction of I₂/I₃⁻ by Titanium Dioxide.* The Journal of Physical Chemistry C, 2009. **113**(43): p. 18444-18447.

115.   Neta, P., R.E. Huie, and A.B. Ross, *Rate Constants for Reactions of Inorganic Radicals in Aqueous Solution.* Journal of Physical and Chemical Reference Data, 1988. **17**(3): p. 1027-1284.

Publications

Journal Publications:

- AlSalka, Y.; Al-Madanat, O.; Curti, M.; Hakki, A.; Bahnemann, W. D., Photocatalytic H_2 Evolution from Oxalic Acid: Effect of Co-catalysts and Carbon Dioxide Radical Anion on the Surface Charge Transfer Mechanisms, ACS Applied Energy Materials (Just Accepted Manuscript), DOI: 10.1021/acsaem.0c00826. Copyright 2020 American Chemical Society.

- Al-Madanat, O.; AlSalka, Y.; Curti, M.; Dillert R.; Bahnemann, W. D., Mechanistic Insights into Hydrogen Evolution by Photocatalytic Reforming of Naphthalene, ACS Catalysis 2020, 10, 7398–7412, (DOI: 10.1021/acscatal.0c01713).

- AlSalka, Y.; Granone, I., L.; Ramadan, W.; Hakki A.; Dillert R.; Bahnemann, W. D., Iron-based Photocatalytic and Photoelectrocatalytic Nano-structures: Facts, Perspectives, and Expectations, Applied Catalysis B: Environmental 2019, 244, 1065-1095, (DOI: 10.1016/j.apcatb.2018.12.014).

- AlSalka, Y.; Hakki, A.; Schneider, J.; Bahnemann, W. D., Co-catalyst-free Photocatalytic Hydrogen Evolution on TiO_2: Synthesis of Optimized Photocatalyst through Statistical Material Science, Applied Catalysis B: Environmental 2018, 238, 422-433, (DOI: 10.1016/j.apcatb.2018.07.045).

- AlSalka, Y.; Hakki, A.; Fleisch, M.; Bahnemann, W. D., Understanding the Degradation Pathways of Oxalic Acid in Different Photocatalytic Systems: Towards Simultaneous Photocatalytic Hydrogen Evolution, Journal of Photochemistry and Photobiology A: Chemistry 2018, 366, 81-90, (DOI: 10.1016/j.jphotochem.2018.04.008).

- Melchers, S.; AlSalka, Y.; Schneider, J.; Bahnemann, W. D., Studies on the Adsorption and Photocatalytic Degradation of an $Eu^{III}(TTFA)_3(MePhTerpy)$ Complex on the TiO_2 Surface, Journal of Photochemistry and Photobiology A: Chemistry 2018, 364, 303-308, (doi: 10.1016/j.jphotochem.2018.06.016).

- Belhadj, H.; AlSalka, Y.; Robertson, P.K.J.; Bahnemann, W. D., In situ ATR-FTIR Investigation of the Effects of H_2O and D_2O Adsorption on the TiO_2 Surface, ECS Transactions 2017, 75, 101-113, (DOI: 10.1149/07550.0101ecst).

- Friehs, E.; AlSalka, Y.; Jonczyk, R.; Lavrentieva, A.; Jochums, A.; Walter, J.; Stahl, F.; Scheper, T; Bahnemann, W. D., Toxicity, Phototoxicity and Biocidal Activity of Nanoparticles Employed in Photocatalysis, Journal of Photochemistry and Photobiology C: Photochemistry Reviews 2016, 29, 1-28, (DOI: 10.1016/j.jphotochemrev.2016.09.001).

- AlSalka, Y.; Lehnberg, K.; Al-Halbouni, D.; Karabet, F.; Hashem, S., A Sonication Extraction Method to Determine PAHs in Activated Sludge (Supernatant and Solid) for the Monitoring of Aerobic Biodegradation, Asian Journal of Water, Environment and Pollution 2012, 9, 11-23.

- AlSalka, Y.; Karabet, F.; Hashem, S., Removal Efficiency of Polycyclic Aromatic Hydrocarbons from Synthetic Water Samples by Electrocoagulation Processes, Damascus University journal for Basic Sciences 2011, 27, 65-80e.

- AlSalka, Y.; Karabet, F.; Hashem, S., Evaluation of Electrochemical Processes for the Removal of Several Target Aromatic Hydrocarbons from Petroleum Contaminated Water, Journal of Environmental Monitoring 2011, 13, 605-613, (DOI: 10.1039/C0EM00450B).

- AlSalka, Y.; Karabet, F.; Hashem, S., Development and Optimisation of Quantitative Analytical Method to Determine BTEX in Environmental Water Samples Using HPLC-DAD, Analytical Methods 2010, 2, 1026-1035, (DOI: 10.1039/C0AY00285B).

Book Chapters:

- AlSalka, Y.; Mendive, C.B.; Ubogui, J.; Dos Santos Claro, P.C.; Bahnemann, W. D., Hydrogen Production by Heterogeneous Photocatalysis, in Encyclopedia of Interfacial Chemistry: Surface Science and Electrochemistry 2018, Editor: Wandelt, K., Elsevier, 413-419, (DOI: 10.1016/B978-0-12-409547-2.13795-3).

- AlSalka, Y.; Daghestani, M.; Karabet, F., Arabic Translation of the Handbook of Analytical Validation 2013, Arab Center for Arabization, Translation, Authorship and Publication.

Oral Presentations:

- AlSalka, Y.; Bahnemann, W. D., "Photocatalytic Reforming of Oxalic Acid on TiO_2 Surfaces", 7th German-Russian Workshop, National University of St. Petersburg, October 2019, St. Petersburg, Russia.

- AlSalka, Y.; Bahnemann, W. D., "Understanding the Photocatalytic Reforming of Oxalic Acid: towrds Efficient Systems for the Conversion of Organic Pollutants to Molecular Hydrogen", 6th European Conference on Environmental Applications of Advanced Oxidation Processes (EAAOP-6), June 2019, Portoroz-Portorose, Slovenia.

- AlSalka, Y.; Bahnemann, W. D., "Noble Metal-Free TiO_2 for Photocatalytic Hydrogen Evolution: The Statistically Significant Role of Precursor", 6th German-Russian Workshop, Leibniz Universität Hannover, September 2018, Hannover, Germany.

- AlSalka, Y.; Bahnemann, W. D., "Synthesis of Effective Bare TiO_2 for Photocatalytic Hydrogen Evolution Using an Optimised EISA Method", 4th Photocatalytic and Superhydrophilic Surfaces Workshop, Museum of Science and Industry, Manchester, UK, December 2017, Manchester, UK.

- AlSalka, Y.; Bahnemann, W. D., "Mesoporous Based Titanium Dioxide for Efficient Solar Photocatalytic Hydrogen Production", 1st International Conference on New Photocatalytic Materials for Environment, Energy & Sustainability, June 2016, Göttingen, Germany.

Poster Presentations:

- AlSalka, Y.; Bahnemann, W. D., "Defective Titanium Dioxide as a Noble-Metal-Free Material for Photocatalytic Fuel Generation: Role of The Precursor", 14th International conference on materials chemistry (MC14), Birmingham University, July 2019, Birmingham, UK.

- AlSalka, Y.; Hakki, A.; Schneider, J.; Bahnemann, W. D., "Co-catalyst-free Photocatalytic Hydrogen Evolution: Optimizing the Synthesis of TiO_2 *via* Statistical Approach", Nano-Day 2018, Leibniz Universität Hannover, September 2018, Hannover, Germany.

- AlSalka, Y.; Bahnemann, W. D., "Mechanism of Oxalic Acid Photoreforming on TiO_2: Effect of Noble Metal Modification", 6th International Conference on Semiconductor Photochemistry (SP6), Carl von Ossietzky University, September 2017, Oldenburg, Germany.

- AlSalka, Y.; Bahnemann, W. D., "Oxalic Acid Photoreforming with Simultaneous Hydrogen Evolution: Kinetic Aspects", 28th International Conference on Photochemistry (ICP2017), Strasbourg Convention & Exhibition Centre, July 2017, Strasburg, France.

- AlSalka, Y.; Bahnemann, W. D., "Solar Photocatalytic Hydrogen Production and Photoelectrochmical Behavior of Self-prepared Titanium Dioxide Modified with Different Noble Metals", Advances in Semiconductors & Catalysts for Photoelectrochemical Fuel Production (SolarFuel-16), September 2016, Berlin, Germany.

Curriculum Vitae

Personal Data

Name:	AlSalka, Yamen
Address:	Holzmarkt 6, 30159 Hannover, Germany
E-mail:	alsalka@iftc.uni-hannover.de
Date & place of birth:	22.04.1980, Damascus, Syria
Nationality:	Syrien
Marital status:	Married, two children

Work Experience

02.2017 – 06.2018 **Research assistant to support staff in research tasks**
Institut für Technische Chemie, Leibniz Universität Hannover, Germany

01.2009 – 05.2015 **Representative for scientific support and training**
Modern Labs Co. (importer of scientific equipment), Damascus, Syria

09.2002 – 05.2015 **Lecturer in chemistry**
Department of Chemistry, Faculty of Sciences, Damascus University, Syria

01.2005 – 12.2008 **Marketing coordinator for laboratory equipment**
Modern Labs Co., Damascus, Syria

01.2003 – 11.2003 **Analyst in a quality control laboratory**
Al-Fares for pharmaceutical industries, Damascus, Syria

Education

10.2015 – present **Doctoral candidate - DAAD scholarship holder**
Institut für Technische Chemie, Leibniz Universität Hannover, Germany

- Photocatalytic hydrogen production and simultaneous degradation of organic pollutants.

02.2007 – 06.2011 **Master's degree in "Chemistry", analytical and environmental chemistry**
Department of Chemistry, Faculty of Sciences, Damascus University, Syria

- Determination and treatment of aromatic hydrocarbons pollutants in water.

10.2003 – 09.2004 **Professional Master "Science of Danger - Risk Management"**
University of Poitiers, France (in collaboration with Damascus University
- Project: Food safety, HACCP application in communal restaurants in France

09.1998 – 06.2002 **Bachelor's degree "Chemical Sciences – Applied Chemistry"**
Department of Chemistry, Faculty of Sciences, Damascus University, Syria

- Bachelor thesis: Separation of aromatic hydrocarbons from kerosene by column chromatography followed by determination of concentration by UV spectrophotometer.

Internship

11.2009 – 12.2009 **Biological degradation of PAHs in water**
Institute for Hygiene and Environmental Medicine, RWTH Aachen University, Germany

05.2004 – 07.2004 **Food security (HACCP) in collective restaurants in France**
Centre Européen de Prévention des Risques, Niort, France

08.2001 – 09.2001 **Intern in the quality control laboratory**
AVENZOR for pharmaceutical industries, Damascus, Syria

Further Education

2016–2017 Design thinking, intercultural awareness and leadership training (Konstanz Uni.)

2016–2017 Democratic understanding of society, peace agreements & public security (Konstanz Uni.)

2015   Projectcycle management (European Institute for Cooperation and Development, SY)

2011   Laser diffraction for particle size distribution (SYMPATEC GmbH, Clausthal-Zellerfeld)

2011   Writing in the Sciences, Stanford University, USA (Online-platform)

2009   Gel Permeation Chromatography: Molecular Weight of Polymers (KNAUER, Berlin)

2009   Acetaldehyde analyzer for PET bottles (PIOVAN, Santa Maria di Sala, Venice, Italian)

2008   FT-NIR Instrument: Analysis of pharmaceutical raw materials (HIJAZ, Amman, Jordan)

2005   Ion Chromatography (IC): Analysis of ions and organic acids (KNAUER, Berlin, DE)

2005   Marketing training of scientific equipment (HIJAZ for deliveries, Amman, Jordan)

2003   ISO / IEC 17025: 1999 (AEC & Al-Fares for pharmaceutical industries, SY)

Awards

2019   Travel Grant to Participate at Conferences, Graduate Academy of Leibniz Universität Hannover (two international conferences in Slovenia and UK).

2016   DAAD scholarship for a one-year program (Leadership for Syria) on "Democratic understanding of society and personal competence" at the Uni. of Konstanz, Germany.

2015   DAAD scholarship (4.5 years) for the completion of a PhD study at Leibniz Universität Hannover, Germany.

2009   DAAD scholarship for a one-month internship at the Institute for Hygiene and Environmental Medicine, RWTH Aachen University, Germany.

Special Knowledge

Language

German: good knowledge.   English: very good knowledge.

French: very good knowledge.   Arabic: Mother language.

EDV

Microsoft Windows®, Microsoft Office® (ECDL/ICDL4.0 Certificate), and Adobe Photoshop®.

Special EDV: OriginLab®, Chemdraw®, Effivalidation®, DOE++® and SPSS®.

Voluntary Work

2013 – 2015   Trainer in the Syrian Chemical Society (SCS), Damascus, Syria
                   - Training SCS members on HPLC and validation processes.

2010 – 2015   Secretary of the Syrian Chemical Society (SCS), Damascus, Syria
                   - Organization of agendas and minutes, correspondence and archiving.